RARE-EARTH-DOPED KNN-BASED CERAMICS FOR PHOTOLUMINESCENT AND ELECTRO-OPTIC APPLICATIONS

WU XIAO

Ph.D

The Hong Kong Polytechnic University

2015

The Hong Kong Polytechnic University
Department of Applied Physics

Rare-earth-doped KNN-based Ceramics for Photoluminescent and Electro-optic Applications

Wu Xiao

A thesis submitted in partial fulfillment of the requirements for
the degree of Doctor of Philosophy

September 2014

CERTIFICATE OF ORIGINALITY

I hereby declare that this thesis is my own work and that, to the best of my knowledge and belief, it reproduces no material previously published or written, nor material that has been accepted for the award of any other degree or diploma, except where due acknowledgement has been made in the text.

__________________________________ (Signed)

Wu Xiao (Name of student)

Abstract

The photoluminescence (PL) properties in various rare-earth (RE) doped materials have been extensively investigated. Visible (Vis) up-conversion emission and near-infrared (NIR)/middle-infrared (MIR) emissions have attracted considerable attention due to their applications in biological/medical imaging and data storage, as well as optical communications, medical and military areas. Er^{3+} is the most popular activator among the RE ions used for up-conversion PL. When the PL properties are combined with other properties such as ferroelectricity into a single entity, multifunctional performance can be realized. The corresponding multifunctional material has potential application in the optoelectronic fields.

This work aims to develop new lead-free RE-doped $(K_{0.5}Na_{0.5})NbO_3$ (KNN)-based multifunctional ceramics with good PL, ferroelectric, piezoelectric and electro-optic (EO) properties. The mechanisms and influencing factors of PL have been systematically studied. Our results have shown that the PL performances of the Er-doped KNN-based ceramics can be effectively adjusted by regulating the concentration of activator (i.e. Er^{3+}), changing the host structural properties (e.g. lattice distortion by Li^{+}-doping, local asymmetry induced by phase transition or polarization switching), controlling the homogeneity and grain size of ceramics, and introducing sensitizers (e.g. Pr^{3+}, Yb^{3+}).

Er-doped KNN ceramics (abbreviated as KNN:Er-x, where x is mol% of Er^{3+}) have first been prepared by the solid state reaction (SSR) method. Raman results reveal that the ceramics have low phonon energy (~860 cm^{-1}) and thus slow multi-phonon relaxation rate. The PL properties, including the up-conversion Vis emission, down-conversion NIR and MIR emissions, emission colors and lifetimes as well as the energy transfer processes have been systemically investigated. The relationship between the intensity of Vis up-conversion PL and laser power indicates an efficient two-photon process when $x \leq 2$. The Er-doping also induces a phase transition from orthorhombic to cubic-like at $x = 2$, and inhibits the grain growth due to the donor-type nature. Both the change of crystallographic structures and the concentration quenching effect induced by Er^{3+} ions have great influences on PL properties. The resulting effects on the dielectric, ferroelectric and piezoelectric properties have also been investigated. At large x, the ceramic transforms normal ferroelectric to relaxor-like. At $x = 1$ and $x = 2$, the ceramics manifest relatively good piezoelectric properties (d_{33}), high remanent polarizations (P_r) and dielectric constants (ε_r), low dielectric losses (tan δ), as well as outstanding PL performances.

The effects of Li-doping on dielectric, ferroelectric and PL properties of the Er-doped KNN ceramics have then been investigated. The samples are 2 mol% Er-doped $(K_{0.5}Na_{0.5})_{1-x}Li_xNbO_3$ (Er-KNLN-x) ceramics and fabricated by the SSR method. At $x < 0.06$, the ceramics possess a single-phase perovskite structure. At larger x, the crystal structure transforms from orthorhombic to tetragonal. Under an excitation of 980-nm laser, the ceramics exhibit intense up-conversion emissions as well as strong down-conversion emissions in NIR and MIR regions. The optimum doping level of Li for up-conversion PL is 0.08. Probably due to the induced structure distortion and reduced local symmetry, the PL intensities of the green, red as well as MIR emissions are enhanced by the doping of Li^+. The Li-doping is effective in establishing a dynamic circulatory energy process to further enhance the PL intensity of the MIR emission at the expense of the NIR emission. At the optimum doping level of Li^+ (x = 0.06), the full bandwidth at half maximum of the MIR emission reaches a very large value of ~250 nm, demonstrating that the ceramic is a promising candidate for high-power 2.7-μm ceramic lasers. The Er-KNLN-*x* ceramics also exhibit good ferroelectric properties, and thus they should have great potential for multifunctional optoelectronic applications.

A sol-gel method has been applied to prepare the KNN:Er-*x* and Er-KNLN-0.08 ceramics for enhancing the PL emissions. As compared to the SSR method, the sol-gel process can reduce the sintering temperature, producing ceramics with better compositional homogeneity and uniform grains. All these are beneficial for improving both the up-conversion and luminescent efficiencies of the ceramics, and thus leading to very strong green emissions even at a low quenching concentration of 2 mol%. The sol-gel-derived Er-KNLN-0.08 ceramics have better up-conversion PL properties (higher emission intensity) than the KNN:Er-2 (Li-free) and SSR-derived Er-KNLN-0.08 ceramics.

KNN ceramics codoped with Er^{3+}/Pr^{3+} or Er^{3+}/Yb^{3+} have also been studied. The SSR method has been used to prepare both the KNN codoped with 2 mol% Er and y mol% Pr (Er-KNN-Pr-y) and KNN codoped with 1 mol% Er and z mol% Yb (Er-KNN-Yb-z) ceramics. The relationships between Vis up-conversion emissions, NIR and MIR emissions of Er^{3+} have been studied by 980-nm excitation. The effects of Pr^{3+} and the energy transfer processes between Er^{3+} and Pr^{3+} have been investigated. By selecting appropriate excitation wavelength, simultaneous Vis down-conversion emissions of both Er^{3+} and Pr^{3+} can be obtained. Moreover, the PL intensity of the ceramics can be enhanced by the remanent polarization resulting from by the poling process. Our results also show that Yb^{3+} is a superior sensitizer to significantly enhance the Vis up-conversion emissions (one order of magnitude higher) and partly improve the MIR emissions (at low Yb content).

The transparent ceramics $(K_{0.5}Na_{0.5})_{1-x}Li_xNb_{1-x}Bi_xO_3$ (KNN-LB-*x*) and 1 mol% Er-doped $(K_{0.5}Na_{0.5})_{1-x}Li_xNb_{1-x}Bi_xO_3$ (Er-KNN-LB-*x*) have been successfully manufactured by pressureless sintering through the same SSR method. Due to the effective suppression of grain growth by Bi-doping, the ceramics possess fine and cubic crystalline grains with dense structure. The ceramics are optical transparent, exhibiting high optical transmittance (~70% for KNN-LB-*x* and ~50% for Er-KNN-LB-*x*) in the NIR region (~900 nm). The good optical transparency may also be derived from the cubic-like crystal structure and relaxor-like characteristics. Both the transparent ceramics exhibit strong EO response, giving a large effective linear EO coefficient, i.e. 120-200 pm/V. The PL and ferroelectric properties of the Er-KNN-LB-*x* transparent ceramics have also been investigated for exploring the multifunctional photonic applications, such as optical-electro integrated materials and devices.

List of Publications

Peer-reviewed Journals

1. **Wu, X.**, Kwok, K. W. and Li, F. L. "Upconversion fluorescence studies of sol-gel-derived Er-doped KNN ceramics," *Journal of Alloys and Compounds* 580, 88, 2013.
2. **Wu, X.** and Kwok, K. W. "Mid-IR to visible photoluminescence, dielectric, and ferroelectric properties of Er-doped KNLN ceramics," *Journal of the American Ceramic Society* 97, 1504, 2014.
3. **Wu, X.**, Lau, C. M. and Kwok, K. W. "Effect of phase transition on photoluminescence of Er-doped KNN ceramics," *Journal of Luminescence* 155, 343, 2014.
4. **Wu, X.**, Lau, C. M. and Kwok, K. W. "Photoluminescence properties of Er/Pr-doped $K_{0.5}Na_{0.5}NbO_3$ ferroelectric ceramics," *Journal of the American Ceramic Society*, accepted.
5. Lau, C. M. **Wu, X.** and Kwok, K. W. "Photoluminescence, ferroelectric, dielectric and piezoelectric properties of Er-doped BNT-BT multifunctional ceramics," *Applied Surface Science*, in press.
6. Sun, H. L., Zheng, Q. J., Wan, Y., Li, Q., Chen, Y., **Wu, X.**, Kwok, K. W., Chan, H. W. L. W. and Lin, D. M. "Microstructure, electrical properties and electric field-induced transitions in $NaNbO_3$-$LiTaO_3$ lead-free ceramics," *Physica Status Solidi A* 211, 869, 2014.
7. Lin, M., Chen, Y. M., Chen, B. L., **Wu, X.**, Kam, K. F., Lu, W., Chan, H. L. W. and Yuan, J. K. "Morphology-controlled synthesis of self-assembled $LiFePO_4$/C/RGO

for high-performance Li-ion batteries," *ACS Applied Materials & Interfaces* 6, 17556, 2014.

Presentations in international conferences

1. **Wu, X.**, Lin, M., Lau, C. M. and Kwok, K. W. "Photoluminescence, ferroelectric, dielectric and piezoelectric properties of sol-gel-derived Er-doped KNN-LN lead-free multifunctional ceramics," *CIMTEC 2014: 13th International Ceramics Congress*, published by Trans Tech Publications Ltd, Kreuzstrasse 10, CH-8635 Zurich-Durnten, Switzerland.
2. Lin, M., **Wu, X.**, Chen, B. L. and Yuan, J. K. "Hydrothermal synthesis of corn cob-like $LiFePO_4/C$ as high performance cathode material for lithium ion batteries," *CIMTEC 2014: 6th Forum on new materials*, published by Trans Tech Publications Ltd, Kreuzstrasse 10, CH-8635 Zurich-Durnten, Switzerland.

Acknowledgements

I would like to express my sincere appreciation to my chief supervisor Dr. K. W. Kwok for his patience, advice and constant encouragement throughout my years of research work. With his broad knowledge, academic insight, enthusiastic and painstaking guidance, I can finish my PhD study quickly, smoothly and successfully.

I also need to thank Dr. J. H. Hao for the photoluminescence measurements. I gratefully acknowledge the technical support provided by the Materials Research Centre of the Hong Kong Polytechnic University. Without their help, I can not finish my experimental work readily.

I would also like to thank all members in Dr. Kwok's group, especially Dr. Faliang Li, Mr. Ximing Fan, Miss Hailing Sun, Mr. M. T. Wong, Miss C. M. Lau, Mr. T. H. Chung, Miss M. T. Chan, and Mr. H. K. Chan, for their friendship, help and valuable discussions on my experiments. In addition, I would like to give my sincere thanks to my colleagues in our department, Miss Mei Lin (also my girlfriend), Mr. Gongxun Bai, Dr. Yan Chen, Mr. Zhiyong Bao, Miss Wenjing Jie, Mr. Huajing Fang, and Mr. Vincent Chan, for their great help and assistance.

Last but not the least, I am deeply indebted to my family and friends for their understanding, constant support and encouragement.

Table of Contents

Chapter 6 Er/Pr-Doped KNN and Er/Yb-Doped KNN Ceramics 112

Chapter 7 Er-Doped KNN-LB Transparent Ceramics 132

List of Figures

List of Tables

List of Symbols

Symbol	Description
λ_{ex}	excitation wavelength
λ_{em}	emission wavelength
L	total orbital quantum number in spectroscopic notation
J	total angular momentum
2S+1	maximum number of different possible states of J for a given (L, S) combination
k	decay rate constant
k_r	radiative decay rate constant
k_{nr}	sum of decay rate constants of non-radiative processes
τ	lifetime
$n^* (t)$	number of excited ions at time t
$n^* (0)$	initial number of excited ions
$f (t)$	an arbitrary function of the time
$I (t)$	luminescence intensity at time t
$I (0)$	luminescence intensity at $t = 0$
α_i	fractions
$\overline{\tau}$	mean lifetime
W_p	multi-phonon relaxation rate
W_o	constant of multi-phonon relaxation
α	constant dependent on the host materials
ΔE	energy gap between the populated level and the next lower level
$\hbar\omega_{max}$	maximum phonon energy of the host material
T_c	Curie temperature
d_{33}	piezoelectric constant
k_{33}	electromechanical coupling coefficient

E_{c}	Electrical coercive field
k_{p}	planar coupling coefficient
T_{N}	Néel temperature
Q_{m}	mechanical quality factor
$T_{\mathrm{O-T}}$	orthorhombic-tetragonal phase transition temperature
k_{t}	thickness coupling coefficient
d_{hkl}	interplanar spacing of the {hkl} set of lattice planes
θ_{hkl}	incident angle of the beam
k'	order of diffraction
λ	wavelength of the X-ray
v_0	frequency of the incident photon
hv	energy interval between two energy states
C	capacitance
$\tan\delta$	dielectric loss
ε_{r}	dielectric constant
ε_0	permittivity of the vacuum
d	thickness of sample
ε'	real part of the dielectric constant
ε''	imaginary part of the dielectric constant
P_{s}	spontaneous polarization
P_{sat}	saturation polarization
P_{r}	remnant polarization
E_{c}	electric coercive field
$\mathrm{C_F}$	ferroelectric capacitor
$\mathrm{C_R}$	reference capacitor
$\mathrm{V_0}$	output voltage
$\mathrm{V_i}$	input voltage
P	polarization
A	area of electrode on the both surfaces of the sample
E_{in}	polarization amplitude of the laser beam
ω	angular frequency of the laser beam

Γ	phase retardation
E_A	polarization component
I_A	the intensity of laser beam arriving at the photodetector
G	a constant determined by the photodetector
n_e	extraordinary refractive index
n_o	ordinary refractive index
n	refractive index
r_{pk}	first-order EO matrix
r_c	effective linear EO coefficient
$\mathrm{R_{wp}}$	reliability factor
S	goodness-of-fit indicator
n	number of laser photons needed
P	pump laser power
I	PL intensity
ρ	density
T	sintering temperature
Ω	PL intensity parameter
R_c	critical distance
V	volume of the unit cell
$\mathrm{X_c}$	critical concentration of the activator
Z	number of host cations in the unit cell
T	transmittance
a, b, c, β	lattice parameters
c/a	tetragonality
T_m	the temperature of maximum ε_r
$\mathrm{g_c}$	polarization-related quadratic EO coefficient

List of Acronyms

Acronyms	**Description**
UV	ultraviolet
Vis	visible
IR	infrared
PL	photoluminescence
RE	rare-earth
Ln	lanthanide
NIR	near-infrared
MIR	middle-infrared
SHG	second harmonic generation
GSA	ground state absorption
ESA	excited state absorption
ETU	energy transfer up-conversion
PA	photon avalanche
OPO	optical parametric oscillator
P-E loop	polarization-electric field hysteresis loop
PT	$PbTiO_3$
PZT	$PbZr_xTi_{1-x}O_3$
PLZT	$(Pb, La)(Zr, Ti)O_3$
PMN-PT	$(1-x)Pb(Mg_{1/3}Nb_{2/3})O_3$-$xPbTiO_3$
BT	$BaTiO_3$
BST	$Ba_xSr_{1-x}TiO_3$
KNN	$K_{0.5}Na_{0.5}NbO_3$
BNT	$Bi_{0.5}Na_{0.5}TiO_3$
BFO	$BiFeO_3$
SBN	$Sr_xBa_{1-x}Nb_2O_6$
SNN	$Sr_2NaNb_5O_{15}$

KBLN	$K_{6-x}Ba_xLi_{4-x}Nb_{10}O_{30}$
BTO	$Bi_4Ti_3O_{12}$
CBT	$CaBi_4Ti_4O_{15}$
BBT	$BaBi_2Ta_2O_9$
MPB	morphotropic phase boundary
EU-RoHS	European Restriction of Hazardous Substances
HP	hot pressing
SPS	spark plasma sintering
HIP	hot isostatic pressing
RTGG	reactive-templated grain growth
KNLN	$(K_{0.5}Na_{0.5})_{1-x}Li_xNbO_3$
KNN-LB	$(K_{0.5}Na_{0.5})_{1-x}Li_xNb_{1-x}Bi_xO_3$
SSR	solid state reaction
PVA	polyvinyl alcohol
dc	direct-current
XRD	X-ray diffraction
SEM	scanning electron microscope
PLE	photoluminescence excitation
EO	electro-optic
PMT	photomultiplier tubes
ac	alternating current
ET	energy transfer
CN	coordination number
CIE	Commission Internationale de L’Eclairage
MPR	multi-phonon relaxation
CR	cross relaxation
FWHM	full bandwidth at half maximum
DI water	distilled water
PAET	phonon-assisted energy transfer

Chapter 1 Introduction

1.1 Definition and classification of luminescence

The term “luminescence” was first introduced in 1888 by Wiedemann (Wiedemann, 1888). Luminescence, different from incandescence, is a form of cold body radiation with emission of light by a substance not resulting from heat. It can be excited by external energy, such as photon, electron, chemical reactions, stress or subatomic motions. The wavelength range of emission is very wide, not only in the visible (Vis) region from 390 to 780 nm, but also in the ultraviolet (UV) and infrared (IR) regions (Vij, 1998). Based on the luminescent duration (or lifetime), luminescence is classified as fluorescence (lifetime shorter than 10^{-8} s) or phosphorescence (lifetime longer than 10^{-8} s). Depending on the external energy source, there are many forms of luminescence, such as photoluminescence, cathodoluminescence and electroluminescence. Table 1.1 summarizes various luminescence processes and corresponding excitation methods (Mahesh, 1989). In this work, photoluminescence from solid materials will be investigated.

With the rapid development of science and technology, luminescence excited with different energy sources such as cathode ray, X ray, optical, acoustic, chemical or biochemical reaction and mechanical energy have been intensely studied and the luminescent materials have been applied in a number of high technology fields, including ultra-thin televisions, mini-monitors, high load fluorescent lamps, plasma or liquid crystal displays, precise instruments, probes, and so on (Rong, 2004).

Table 1.1 Various luminescence processes and corresponding excitation methods.

Luminescence process	**Excitation methods**
Photoluminescence	Absorption of photons (UV, Vis light, IR light, etc.)
Cathodoluminescence	High energy electron beam
Electroluminescence	Electric current passed through a substance
Radioluminescence	Bombardment by ionizing radiation (X, α, β and γ rays, protons, neutrons, etc.)
Triboluminescence	Mechanical or frictional forces
Chemiluminescence	Chemical reaction
Thermoluminescence	Heating (a stimulating cause)
Bioluminescence	Biochemical reaction by a living organism
Crystalloluminescence	During crystallization
Sonoluminescence	Imploding bubbles in a liquid when excited by sound

1.2 Photoluminescence

Photoluminescence (abbreviated as PL) describes the phenomenon of light emission from any form of matter after the excitation by photons (Henderson, 1989). It typically undergoes various relaxation processes to re-radiate the photons, including absorption, energy transfer and light emission. Among the processes, absorption and emission occurs between the energy states and ground state, while the energy transfer is ascribed to the transitions among the excited states.

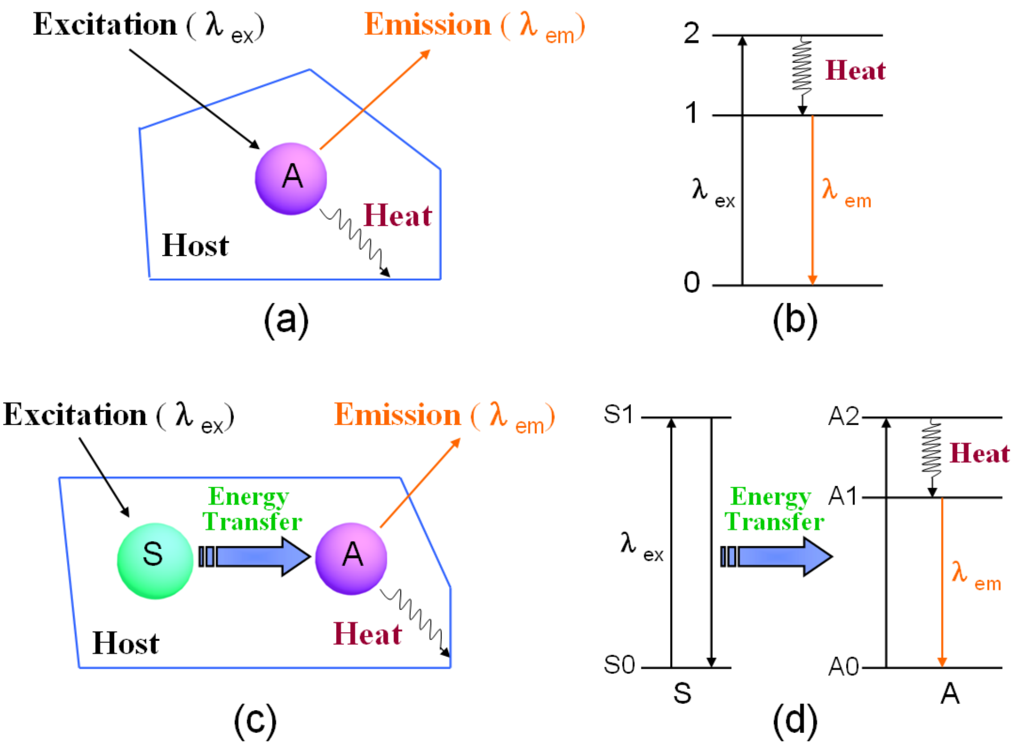

Figure 1.1 (a) PL behavior in a crystal lattice, A is activator. (b) Energy level diagram of the activator and the PL mechanism. (c) PL process with energy transferred from sensitizer to activator, S is sensitizer. (d) Energy level diagram of the sensitizer and activator and the corresponding PL process.

There are three main possible PL processes which are illustrated in Fig. 1.1. For he first PL process, the ion labeled as “A” embedded in the host is an activator (luminescent center). The mechanisms and energy levels of “A” are described in Figs. 1.1a and 1.1b. The excitation radiation (at wavelength λ_{ex}) is absorbed by the activator, raising it from the ground state “0” to the excited state “2”. The electron at the excited state “2” will subsequently relax non-radiatively to the nearest lower excited state “1”, generating heat to the host. Finally the electron at the excited state “1” will emit a photon (with a longer wavelength λ_{em}) and return to the ground state “0” by a radiative way (Blasse, 1994). As λ_{em} is longer than λ_{ex}, this PL process is defined as down-conversion PL.

The first PL process is the simplest mode because only the activator is involved. For the other possible processes, the host lattice or another luminescent center will participate in the PL processes. Fig. 1.1c shows the second possible process for which the host contains two different dopant ions. The dopant ion labeled as “S” is a sensitizer for absorbing the excitation energy and subsequently transferring it to the neighbouring activator “A” (Blasse, 1994). Then “A” will emit radiation simultaneously with non-radiative transition generating heat to the host. The function of host is simply holding the ions “S” and “A”. Fig. 1.1d shows the energy levels of “S” and “A” and the luminescent mechanism. The electron in the ground state “S0” first absorbs the excitation energy and jumps to the excited state “S1”. The absorbed energy by the sensitizer ion “S” will be transferred to the activator “A” due to the equal energy difference between “S0→S1” and “A0→A2”. The subsequent emission process is the same as that of the first possible PL process. In the third possible PL process, the host lattice, instead of the sensitizer or activator, will absorb the excitation energy, and transfer to the activator following similar mechanism of the sensitizer.

1.3 Rare-earth ions

1.3.1 Rare-earth ions doped luminescent materials

Rare-earth (RE) elements play an important role in human development and technological advancement. RE elements are commonly used as matrix components as well as activators, co-activators, sensitizers or dopants for luminescent materials. RE-doped luminescent materials have superior luminous efficiency and color properties as compared with luminescent materials doped with other ions. There are 17 members in the family of RE elements, including 15 lanthanides (La, Ce, Pr, Nd, Pm, Sm, Eu, Gd, Tb, Dy, Ho, Er, Tm, Yb, Lu), Sc and Y (Yen, 2007). These RE elements were discovered later than other common elements since they have similar outer shell electron configurations and active chemical properties. They also show a number of physical and chemical features, such as high electrovalence, large radius, strong polarization force, good hydrolysis property and superior metal activity (Su, 2001).

Table 1.2 shows the electron shell structure and electron configurations of lanthanide (Ln) elements. For the Ln^{3+} ions, the 6s, 5p and 5s orbits of the outer shells are filled with electrons, while the 5d orbit is empty or occupied with one electron. So the outer electron shell structures of Ln^{3+} ions are very similar. However, the characteristics of Ln^{3+} ions are determined by the partially filled 4f electrons, which are shielded from external electric field by the outer 5s and 5p electrons. The interaction between 4f electrons are mainly the spin-spin and spin-orbit interactions. Practically, the energy level is represented by Russell-Saunders term symbol (Russell, 1925) predicted by Hund’s rules in the form of $^{2S+1}L_J$, where S is the total spin quantum number, L is the total orbital quantum number in spectroscopic notation, J is the total angular momentum, 2S+1 is the maximum number of different possible states of J for a given (L, S) combination.

Table 1.2 The electron shell structures and electronic configurations of the Ln elements.

Atomic number	**Element**	**Electron shell structure**					**4f electrons of RE^{3+} ions**	**S**	**L**	**J**
		4f	**5s**	**5p**	**5d**	**6s**				
57	La	0	2	6	1	2	$4f^0$	0	0	0
58	Ce	1	2	6	1	2	$4f^1$	1/2	3	5/2
59	Pr	3	2	6	0	2	$4f^2$	1	5	4
60	Nd	4	2	6	0	2	$4f^3$	3/2	6	9/2
61	Pm	5	2	6	0	2	$4f^4$	2	6	4
62	Sm	6	2	6	0	2	$4f^5$	5/2	5	5/2
63	Eu	7	2	6	0	2	$4f^6$	3	3	0
64	Gd	7	2	6	1	2	$4f^7$	7/2	0	7/2
65	Tb	9	2	6	0	2	$4f^8$	3	3	6
66	Dy	10	2	6	0	2	$4f^9$	5/2	5	15/2
67	Ho	11	2	6	0	2	$4f^{10}$	2	6	8
68	Er	12	2	6	0	2	$4f^{11}$	3/2	6	15/2
69	Tm	13	2	6	0	2	$4f^{12}$	1	5	6
70	Yb	14	2	6	0	2	$4f^{13}$	1/2	3	7/2
71	Lu	14	2	6	1	2	$4f^{14}$	0	0	0

According to the electron configuration and the resulting spectroscopic properties, RE^{3+} ions can be divided into three categories:

1. Sc^{3+}, Y^{3+}, La^{3+}, Lu^{3+}. There are no electrons or full of electrons in the outer 4f orbit so that the 4f-4f transition cannot be achieved and no luminescence can be obtained.
2. Sm^{3+}, Eu^{3+}, Tb^{3+}, Dy^{3+}. There are around 7 electrons in the outer 4f orbit, and thus having high energy transfer efficiencies and strong fluorescence intensities.
3. Ce^{3+}, Pr^{3+}, Nd^{3+}, Pm^{3+}, Ho^{3+}, Er^{3+}, Tm^{3+}, Yb^{3+}. The outer 4f orbits of these ions are

partial filled. Their fluorescence properties are weaker than those of the RE^{3+} ions in the second category because of the higher possibilities of non-radiatively transition.

For the RE^{3+} ions from Pr^{3+} to Tm^{3+}, the emission and absorption bands are mainly resulted from the electron transitions between the energy levels in the 4f orbit and hence are narrow. On the other hand, electron transitions between the energy levels in the 4f orbit and outer orbits (such as 5s and 5p) are allowed for Ce^{3+} and Yb^{3+} ions. Thus their emission and absorption bands are wide and continuous. In general, the electron transitions between f orbits are forbidden by the Laporte rule. Nevertheless, the 4f-4f transitions can be motivated by the excitation of a bound “antenna” ligand, which leads to sharp emission bands in the Vis, near-infrared (NIR) and middle-infrared (MIR) range and with a relatively long luminescence lifetime (Werts, 2005).

1.3.2 Er^{3+} ion

Erbium (Er) is the 11th element of the lanthanide series and has a $1s^22s^2p^63s^2p^6d^{10}4s^2p^6d^{10}f^{12}5s^2p^66s^2$ electron configuration. It commonly exists as a stable trivalent ion (Er^{3+}) with a $1s^22s^2p^63s^2p^6d^{10}4s^2p^6d^{10}f^{11}5s^2p^6$. The ladder-like arranged 4f energy levels of a free Er^{3+} ion as well as an Er^{3+} ion in a host are shown schematically in Fig. 1.2. Other RE^{3+} ions in the second and third categories also possess similar ladder-like arranged 4f energy levels. As illustrated by the Stark effect, the 4f energy levels are split into several sub-levels by the crystal field of the host. The number of sub-levels is determined by the symmetry of the crystal field around Er^{3+}. When Er^{3+} ion is doped into a host, the 16-fold degeneracy of the atomic state is partly lifted by the crystal field (Chu, 2004). As a result, the 4f-4f transitions become realizable in Er-doped materials.

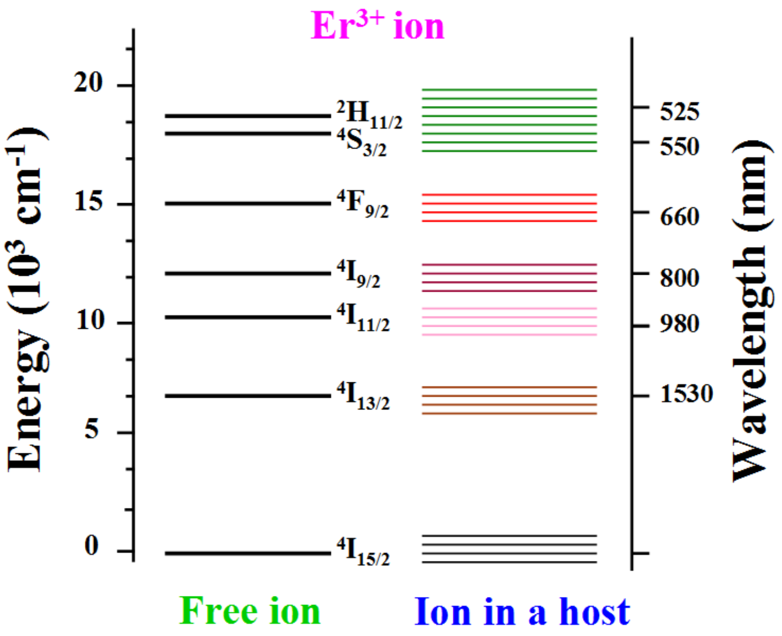

Figure 1.2 Energy levels of Er^{3+}, both for the Er^{3+} free ion, and for Er^{3+} in a host.

Recently, the spectroscopic performances in various Er-doped materials, e.g., phosphors, glasses, ceramics and crystals, have been extensively investigated. As an important spectroscopic probe, Er^{3+} ions show Vis up-conversion ($\lambda_{ex} > \lambda_{em}$, to be introduced in the following section) PL at 550 nm (green emission) and 660 nm (red emission), which has great potential for practical applications such as optical storage, printing, medicine and display technology (Möbert, 1997). The transition from $^4I_{13/2}$ level (first excited state) to $^4I_{15/2}$ level (ground state) produces the ~1.5 μm (NIR) emission, while the $^4I_{11/2} \rightarrow {}^4I_{13/2}$ transition produces the ~2.7 μm (MIR) emission (Gomes, 2011). Accordingly, Er^{3+} ions are commonly used for IR to Vis up-convertors, NIR amplifiers and MIR photonics (to be introduced in the following section). Besides, the Er^{3+} ions can also be used to probe physical effects, such as point defects, radiation defects, network structure, excitons, optical density of states, photonic band structure, and so on (Polman, 2001).

1.3.3 Pr^{3+} ion

Praseodymium (Pr) is a member of the lanthanide group, having a $1s^22s^2p^63s^2p^6d^{10}4s^2p^6d^{10}f^35s^2p^66s^2$ electron configuration, which becomes $1s^22s^2p^63s^2p^6d^{10}4s^2p^6d^{10}f^25s^2p^6$ for the Pr^{3+} ion. Fig. 1.3 shows the energy level diagram of (free) Pr^{3+} ion. The color of its emissions is strongly dependent on the characteristics of the host. Under the excitation of blue or UV light, red and green emissions may be obtained attributed to the transitions of $^3P_0 \rightarrow {}^3F_2/{}^3H_6$ and $^1D_2 \rightarrow {}^3H_4$, and transition $^3P_1/{}^3P_0 \rightarrow {}^3H_5$, respectively (Fig. 1.3a).

Different from other RE^{3+} ions, Pr^{3+} ion has a unique electronic structure, resulting from the close energy separation between the $^1S_0$ level and the lowest edge of the 4f5d configuration (Fig. 1.3b) (You, 2007). Under the excitation of vacuum ultraviolet (VUV) light, the emission wavelength of Pr^{3+} strongly depends on the position of 4f5d configuration, which is influenced by the host. If the lowest 4f5d state locates above the $^1S_0$ level (Fig. 1.3b), electron in the 4f5d state can relax non-radiatively to the $^1S_0$ level, and then efficient cascade emission takes place, which is ascribed to the two-step $4f^2$-$4f^2$ transitions, i.e. $^1S_0 \rightarrow {}^3P_{2,1,0}$ followed by $^3P_0 \rightarrow {}^3F_2/{}^3H_{6,5,4}$ (Fig. 1.3a) or $^1S_0 \rightarrow {}^1D_2$ followed by $^1D_2 \rightarrow {}^3H_{6,5,4}$ (Piper, 1974, Huang, 2003). On the other hand, if the lowest 4f5d state locates below $^1S_0$ level (Fig. 1.3c), a wide-band emission of parity-allowed inter-configurational 4f5d-$4f^2$ transitions occur. The emissions from the 4f5d-$4f^2$ have been observed in many hosts, such as $LiYF_4$, KYF_4, LaF_3, YPO_4, YBO_3 and $CaMgAl_{14}O_{23}$ (You, 2007).

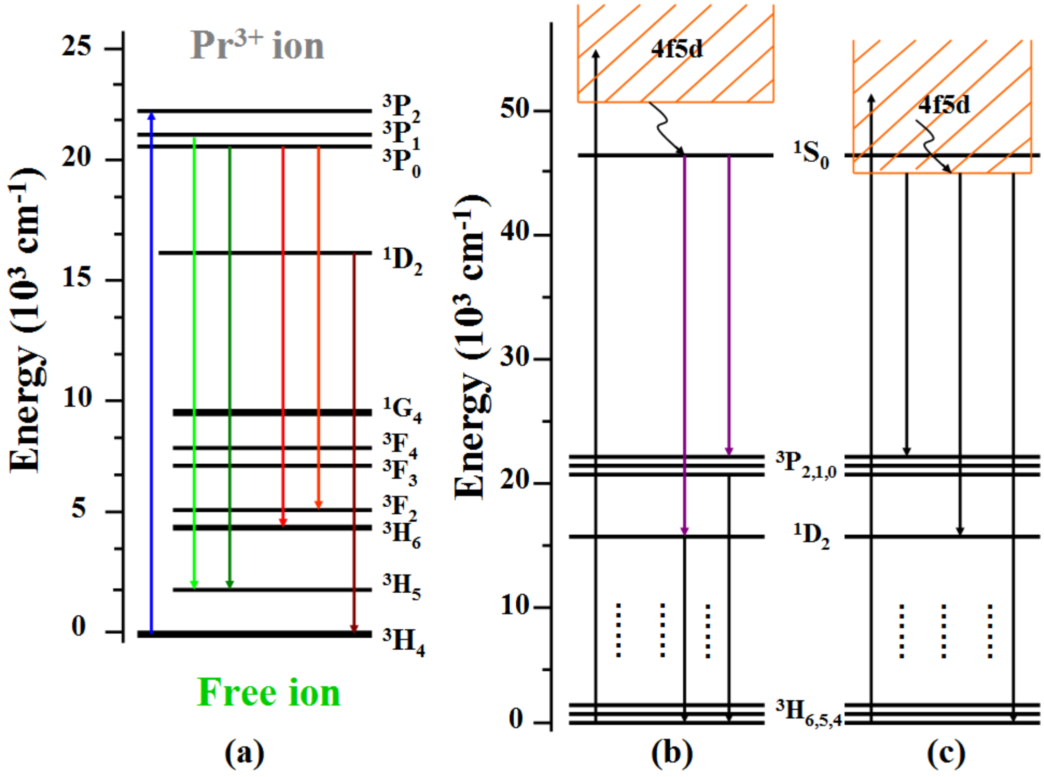

Figure 1.3 Energy levels diagram of (free) Pr^{3+} ion.

Owing to the diverse emission regions and different excitation sources, Pr^{3+} ions are applied in numerous areas, including luminescent probes in bio-molecule structure and phase transition (Zhou, 2012, Jia, 2003), single mode fiber optical amplifiers (similar to Er^{3+} ions) in Pr-doped fluoride glasses (Jha, 1995), and also mechanoluminescence studies on electro-mechano-optical conversions in Pr-doped $BaTiO_3$-$CaTiO_3$ ceramics (Wang, 2005).

1.3.4 Yb^{3+} ion

Ytterbium (Yb) is the 14th and penultimate element in the lanthanide group. Similar to the other lanthanides, the most common oxidation state is +3 in its oxide (Yb_2O_3), halides (YbX_3, X = F, Cl, Br, I) and other compounds. Fig. 1.4 shows the energy levels diagram of Yb^{3+} ion (in a host). Yb^{3+} has a simple electron shell structure, consisting of the ground state (lower $^2F_{7/2}$ level) and the excited state (upper $^2F_{5/2}$ level). Due to the Stark effect, the two levels are split into several sub-levels. The large gap between the upper and lower levels will prevent the non-radiative transition and increase the lifetime of upper $^2F_{5/2}$ level. In addition, because of the small quantum defect, Yb^{3+} ions can easily be introduced into the host material for making lasers with high efficiency, long lifetimes and short pulses (Ostby, 2007). The Yb-based lasers radiate in the range of 1.06-1.12 μm, when pumped at 0.9-1 μm.

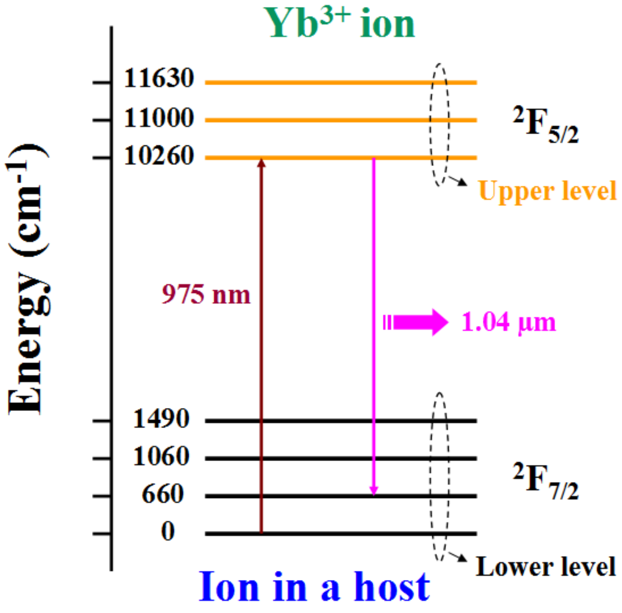

Figure 1.4 Energy levels diagram of Yb^{3+} ion (in a host).

Owing to the larger cross section of absorption (2.5×10^{-24} m^2 vs 2×10^{-25} m^2 near 975 nm) and the efficient energy inter-transfer, Yb^{3+} ions are commonly codoped as sensitizers with Er^{3+} ions for enhancing the pumping and then PL efficiencies (Babu, 2007, Liu, 2007). Various Er^{3+}/Yb^{3+} codoped luminescent materials have been developed and applied in various applications, such as up-conversion phosphor powders (Singh, 2013), nanocrystals (Wang, 2009), fiber distributed-feedback lasers (Kringlebotn, 1994), glass lasers with pulsed and continuous wave laser actions (Hsu, 1995), and ion-exchanged waveguide amplifiers (Donzella, 2010).

1.4 Up-conversion luminescence

1.4.1 Up-conversion process

Up-conversion luminescence is a nonlinear process in which the sequential absorption of two or more (incident) photons leads to an emission of photon with a shorter wavelength (Auzel, 2004). It is an anti-Stoke type emission and different from the multi-photon (e.g. two-photon) process and second harmonic generation (SHG), where the absorption of photons takes place simultaneously (Suyver, 2005). A typical example is the conversion of NIR light to Vis light. Owing to the lower energy, the NIR excitation light can greatly minimize the background auto-fluorescence, photo-bleaching, and photo-damage to specimens (Wang, 2009), and hence is preferable to the UV excitation light in producing PL emissions in the Vis region via the up-conversion process. Generally, the NIR-to-Vis process can be realized by an economic way, sucha as utilizing a low-power (1-10^3 W/cm^2) continuous wave laser instead of an expensive high-intensity (10^6-10^9 W/cm^2) pulsed laser (Wang, 2009).

There are three basic processes (Liu, 2013) as shown in Fig. 1.5. Type (a) is the simplest process in which a single activator ion will absorb the incident photons in sequence (Fig. 1.5a). If the energy of incident photons equals the inter energy difference between the ground state G and metastable states E1 and E2, the ion will absorb the photons and the E1 level will be populated via a process called ground state absorption (GSA). The ion will then absorb another photon and the higher energy level E2 will be populated. The process is called excited state absorption (ESA). The excited ion will eventually relax radiatively to G, generating an (up-conversion) emission at wavelength half of that of the incident photon (Gamelin, 2000). The ESA is easy to take place when the concentration of the RE ions is low.

Similar to Type (a), the second up-conversion process Type (b) involves the sequential absorption of two incident photons (Fig. 1.5b). However, unlike Type (a), the two incident photons are not absorbed by a single activator ion. Instead, both the activator and sensitizer (S) ions will absorb the incident photons and their E1 levels will be populated simultaneously. The excited sensitizer ion will then relax to the ground state G via the transfer of energy to the neighboring excited activator, of which the higher energy level E2 is thus populated. This is called energy transfer up-conversion (ETU) process. Similarly, the excited activator will eventually relax radiatively to G, generating an (up-conversion) emission at wavelength half of that of the incident photon. ETU process is resulted from the ion-ion interactions and thus strongly depends on the concentration of the RE ions (both activator and sensitizer ions).

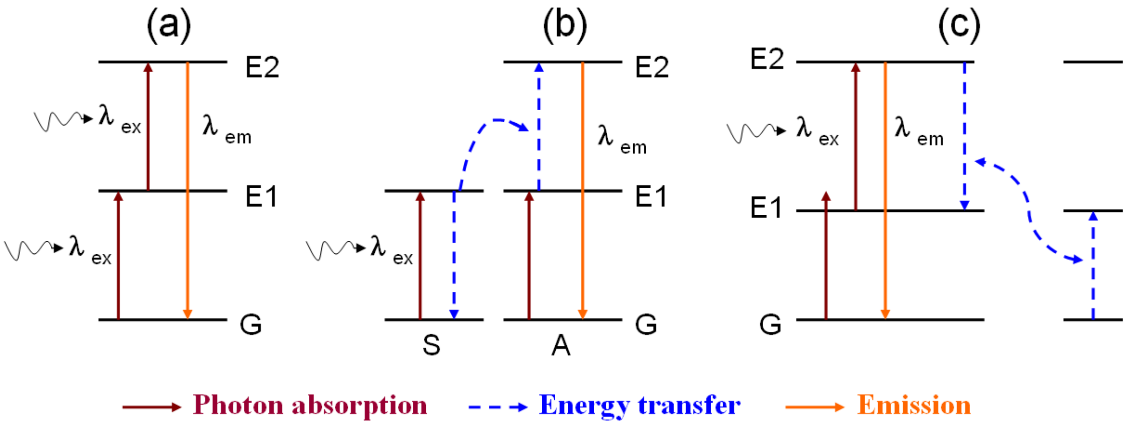

Figure 1.5 Simplified energy level diagram showing the basic up-conversion processes.

Type (c) is a photon avalanche (PA) process (Fig. 1.5c), which was first reported by Chivan in Pr^{3+}-based infrared quantum counters (Chivian, 1979). A high pump intensity (critical intensity) is required for inducing the PA process (Joubert, 1999). Below it, up-the pump light is hardly absorbed by the material and the up-conversion emission is weak. When the pump intensity is higher than the critical intensity, the pump light absorption increases considerably and the up-conversion emission becomes very strong, with an increase in intensity by orders of magnitude (Joubert, 1999). The PA process begins with a weak non-resonant GSA process (the energy of pump photons is slightly larger than that required) to populate the intermediate level E1, followed by a resonant ESA process or energy transfer process from a neighboring ion (i.e. ETU) to populate the higher energy level E2, from which weak up-conversion emission may occur. After that, cross-relaxation energy transfer occurs between an excited ion (at E2) and a neighboring unexcited ion, leading to the population of E1 level for both the ions. Then the feedback looping of ESA (or ETU) and cross-relaxation processes will exponentially increase the population of both E1 and E2, thus eventually producing strong up-conversion emission (Wang, 2009, Zheng, 2014). For the PA process, the concentration of RE ions should be high enough for the ion-ion interactions to produce efficient cross-relaxation process (Joubert, 1999).

Since the f-f transition in RE ions is forbidden according to the selection rules (Judd, 1962), RE-doped luminescent materials usually exhibit low luminescent efficiency, especially for the up-conversion process. The three up-conversion processes have different luminescent efficiencies. ESA in type (a) has the lowest efficiency while PA has the highest one. However, there are some drawbacks for the PA process, such as high pump-power dependence, slow response to excitation induced by many looping cycles of ESA, and a number of cross-relaxation processes. By contrast, the ETU process, which is fast and independent of pump-power, has been utilized in the development of many advanced up-conversion materials over the past decades (Auzel, 2004).

1.4.2 Up-conversion materials

In 1966, Auzel (Auzel, 1966) found that when Yb^{3+} ion was introduced in the $NaY(WO_4)_2$ glasses, the Vis emission of Er^{3+}, Ho^{3+} and Tm^{3+} ions pumped by IR light enhanced significantly (~ two orders of magnitude higher). Thereupon, the concept of “up-conversion” was introduced, which greatly promoted numerous research studies on new up-conversion materials. Nowadays, the main up-conversion materials are single RE doped or Yb/RE-doped materials, in which RE^{3+} ions are activators (typically Er, Tm, Ho, Tb, Pr, etc.) and Yb^{3+} ion is sensitizer. The host materials include fluorides, oxides, oxyfluorides, chlorides and sulfides.

Bulk Yb/Er-doped $NaYF_4$ is a high efficient up-conversion material, having almost the highest up-conversion quantum efficiency among all the bulk up-conversion phosphor materials (Phillips, 2000). Under the NIR excitation, Er^{3+} ions in Yb/Er-doped $NaYF_4$ show strong green emission with a very high efficiency. On the other hand, Tm^{3+} ions in Yb/Tm-doped $NaYF_4$ show efficient blue emission (Heer, 2004). The sensitizing effect of Yb^{3+} plays a key role in enhancing the luminescent efficiencies and PL intensities of both Er^{3+} and Tm^{3+} ions. Er-doped ZBLAN ($53ZrF_4$, $20BaF_2$, $4LaF_3$, $3AlF_3$, 20NaF) glass is a good up-conversion material, which can be applied in high-density optical recording equipments and efficient diode pumped waveguide green integrated lasers (Gottmann, 2008). De Wild et al. have applied the up-convertor Yb/Er-doped Gd_2O_2S in wide band-gap solar cells due to the high spectral response in the emission range (400-700 nm) (De Wild, 2011). The promising achievement in laser output shows that after utilizing up-conversion materials, such as fluoride crystals, the laser operation can be realized in the fibers even at low temperature (down to the liquid nitrogen temperature) and the optical-to-optical conversion efficiency still remains high, up to 1.4% (Zhu, 2010). Hence, the up-conversion bulk materials in use with NIR excitation have great potential for applications in display, optical computing and information processing areas.

Recently, RE-doped nanomaterials have attracted much attention for applications in up-conversion PL. The size of nanoparticles greatly influences the optical performances, such as nonlinear optical properties, light absorption, light reflection and energy loss during the transmission. M. Haase and H. Schäfer (Haase, 2011) have summarized the studies on RE-doped nanocrystalline and macrocrystalline up-conversion phosphors, which are regarded as the promising alternatives to organic fluorophosphors and quantum dots in medical imaging. Furthermore, RE-doped nanocrystalline thin films have been prepared, focusing for the application of RE-based up-convertors in combination with wide band-gap solar cells (Van Sark, 2013).

1.5 NIR and MIR emissions

NIR at ~1.5 μm is located in the "eye safe" spectral region and has applications in laser range finders, optical communication networks and atmospheric communication systems (Kanth, 2004). As the optical technologies become more and more significant, wide bandwidth is the future trend in optical communication because the rates of data information transfer and processing must be orders of magnitude higher than those of electronic technologies. For example, a 1.5-μm optical signal with 8 nm bandwidth has a corresponding optical frequency bandwidth of 10^{12} Hz. Hence, in order to meet the demand of high frequencies, new materials should be exploited for the generation, guiding, switching, and amplification of light (Polman, 1997).

Er-doped glasses, such as tungstate, tellurite, germanate and borosilicate glasses (Luo, 2006, Sun, 2006), have been reported for exhibiting a broad 1.5-μm emission band. When fabricated as fiber amplifier, they exhibit a wide and flat gain spectrum which is necessary for dense wavelength division multiplexing (employing multiple light wavelengths to transmit signals over a single optical fiber) optical network applications (Chen, 2005). The 1.5-μm emission of Er^{3+} ions is attributed to the intra-4f transition from the first excited state ($^4I_{13/2}$) to the ground state ($^4I_{15/2}$), as shown in Fig. 1.2. The Er-concentration should be optimized for the emission. At low Er concentration, the emission efficiency is low and the PL intensity is weak. However, at high Er concentration, the interionic distance between Er^{3+} ions becomes shorter and the electric dipole-dipole interactions will reduce the gain performance of the amplifier (Polman, 1997). A continuous wave laser (980 nm) is commonly used as the excitation source. There are other advantages of Er-doped fiber amplifiers, such as linear gain response, temperature and polarization insensitivity, and low noise (Desurvire, 1994).

In recent years, lasers operating at ~2.7 μm (a typical wavelength in the MIR region) have attracted considerable attention due to promising potentials in various applications such as military countermeasures, medical surgery, remote sensing, atmosphere pollution monitoring and optical parametric oscillators (Gomes, 2011, Dickinson, 2001). Optical parametric oscillator (OPO) is the typical laser system with tunability in the spectral range of directional IR counter-measures (Zhang, 2011). Owing to the requirement of nonlinear crystals and matching with pump laser, the design and construction of OPO is very complicated. A simple and feasible solution is to use MIR solid state lasers which require suitable activators (i.e. Ho^{3+}, Er^{3+}, Tm^{3+}, Dy^{3+} and Pr^{3+} ions) and host (with comparatively low phonon energy and stable physical and chemical properties).

Among the RE ions, Er^{3+} ions have been extensively studied for exhibiting MIR emission, which is attributed to the $^4I_{11/2} \rightarrow {}^4I_{13/2}$ transition (Fig. 1.2), in various glasses, glass ceramics and single crystals. The typical examples are Er^{3+}/Pr^{3+}-codoped germanate glasses (Xu, 2011), Nd^{3+}/Er^{3+}-codoped sodium tellurite glasses (Guo, 2011),

$Er^{3+}/Tm^{3+}/Pr^{3+}$ triply doped fluoride glasses (Tian, 2011a), single Er^{3+}-doped oxyfluoride transparent glass-ceramics (Tikhomirov, 2006) and Er^{3+}-doped BaY_2F_8 laser crystals (Pollnau, 1996). The luminous efficiency of the MIR emission is affected by a number of factors. One of them is that the host materials should have minimal absorption coefficient in the typical H_2O absorption band near 2.7 μm because the hydroxyl groups (OH^-) will absorb and degrade the MIR emission (Gao, 2009).

1.6 Luminescence lifetime

When a RE ion in the host absorbs a certain amount of energy, a number of de-excitation processes take place, including vibrational relaxation (loss of energy in the absence of light emission), intersystem crossing (a non-radiative process involving a transition between two electronic states), and radiative transition with emission (luminescence) (Berezin, 2010). The probability for the de-excitation processes to occur is characterized by a decay rate constant (k), which is the sum of the decay rate constants of all possible de-excitation processes:

$$k = k_r + k_{nr} \tag{1.1}$$

where k_r is the radiative decay rate constant and k_{nr} the sum of decay rate constants of non-radiative processes. The lifetime (τ) that is the time for the RE ion remaining in the excited state before returning to the ground state and is inversely proportion to k:

$$\tau = \frac{1}{k} = \frac{1}{k_r + k_{nr}} \tag{1.2}$$

Obviously, the lifetime for different excited RE ions will be different. The variation of the number of excited RE ions, after switching off the excitation source, can be expressed as:

$$\frac{dn^*(t)}{dt} = -kn^*(t) + f(t) \tag{1.3}$$

where $n^*(t)$ is the number of excited ions at time t. The solution of Eq. 1.3 gives:

$$n^*(t) = n^*(0)\exp(-kt) = n^*(0)\exp(-\frac{t}{\tau}) \tag{1.4}$$

On the other hand, the decrease in the number of excited RE ions via radiative processes is related to the (observed) PL intensity $I(t)$:

$$I(t)\,? \quad \frac{dn^*}{dt} = k_r n^*(t) \tag{1.5}$$

The variation of PL intensity with time, i.e., the decay profiles, is then given as:

$$I(t) = I(0)\exp(-\frac{t}{\tau}) \tag{1.6}$$

Accordingly, the lifetime τ can be determined as the time required for the intensity (or the number of excited ions) to decrease to 1/e of its initial value. As indicated by Eqs. 1.1-1.6, the observed I and then τ are affected by both the luminescence and non-radiative processes. Nevertheless, the observed τ is commonly called the luminescence lifetime.

For most of the luminescent materials with a single emission center (activator), the observed I decreases exponentially with time, i.e., giving a single-exponential luminescence decay curve as shown in Fig. 1.6a. In general, the (overall) decay time is much longer than the excitation pulse. If there are more than one emission center or significant ion-ion interactions (such as up-conversion process), the luminescence decay curve will become a multi-exponential curve because of the multiple lifetimes (Fig. 1.6b). The multi-exponential decay can be represented by the following equation:

$$I(t) = I(0)\sum_i \alpha_i \exp(-\frac{t}{\tau_i}) \qquad (1.7)$$

The individual lifetimes τ_i and fractions α_i can be determined by experimentally fitting the data to Eq. 1.7. A maximum entropy method is commonly used to determine a mean lifetime $\overline{\tau}$ as:

$$\overline{\tau} = \frac{\int_0^\infty I(t)tdt}{\int_0^\infty I(t)dt} = \frac{\sum_i \alpha_i \tau_i^2}{\sum_i \alpha_i \tau_i} \qquad (1.8)$$

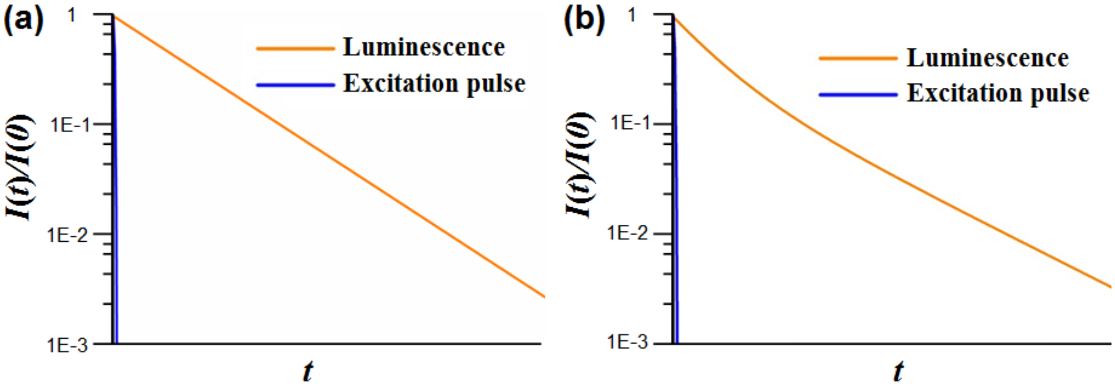

Figure 1.6 Luminescence decay curves of RE ions in a host after excitation, (a) single-exponential decay curve and (b) multi-exponential decay curve.

The luminescence lifetime is an intrinsic property for emission center and hence does not depend on the method of measurement, excitation energy, duration of light exposure, single- or multi-photon excitation and photo-bleaching (Chen, 2004). As mentioned, the de-excitation processes may include non-radiative processes such as electron redistribution and reorganization of the surrounding ions. Those non-radiative processes will lead to the loss of absorbed energy to the host, and are collectively called quenching. The observed (luminescence) lifetime is hence usually shorter than the intrinsic lifetime since quenching is inevitable to certain extent (Berezin, 2010). Lifetime is an important parameter for practical applications in PL, such as luminescence resonance energy transfer, lifetime imaging on small animal, cell, yeast, bacteria and virus in biotechnology and medicine (Bhatta, 2008), and material sciences and engineering applications.

1.7 Host selection

Selection of a right host material is especially important for obtaining high up-conversion efficiency as well as tailoring the luminescence lifetime and emission color. The luminescent features of an activator ion will be varied when it is doped in different host materials. There are two main effects: cloud expanding (nephelauxetic) effect and crystal field effect, which affect the luminescent characteristics.

The cloud expanding effect is caused by the properties of covalent bond. When the bond strength between anionic ligands and metal cations increases, the electronic interaction will be weakened, and hence affecting the energy for electronic transition. For a host lattice having higher covalency, the energy spacing between the multiplet electronic states will be smaller, and thus leading to the decrease of energy for electronic transition. The crystal field theory is very complicated and can be specifically interpreted by the Judd-Ofelt theory (Judd, 1962, Ofelt, 1962). The crystal field effect can be considered as the electric field arising from the environment (neighboring ions) around the activator ion. Different host lattices have different crystal field parameters, resulting in different crystal field splits. Based on this effect, the emission center, i.e. activator ion, can be applied as the structure probe to detect the chemical environment in the host.

The ideal host materials should have close matches of lattices with dopant ions, low phonon energies, stability and non-toxicity (Wang, 2009). The inorganic compounds are often selected as the host materials when applied in the Vis up-conversion PL, NIR and MIR emissions. In general, the alkaline earth ions (Ca^{2+}, Sr^{2+}, and Ba^{2+}) and transition metal ions (Ti^{4+} and Zr^{4+}) have similar size to RE ions, so they are frequently contained in the inorganic host materials. However, as most of them are replaced by RE^{3+} ions, metal ion vacancies or oxygen vacancies will be generated for maintaining the charge neutrality, and thus affecting the luminescent characteristics of the materials. The defect vacancies can be eliminated for the host materials containing transition metal ions Al^{3+} and Ga^{3+} (Rodriguez, 2009).

Low phonon energy is one of the major factors leading to good PL properties. According to the Miyakawa-Dexter theory, the multi-phonon relaxation rate W_P is given as (Van Dijk, 1983)

$$W_p = W_o \exp(-\alpha \Delta E / \hbar\omega_{max}) \tag{1.9}$$

where W_o and α are constants dependent on the host materials, ΔE is the energy gap between the populated level and the next lower level, and $\hbar\omega_{max}$ is the maximum phonon energy of the host material. Although phonons with other energies can be emitted in the relaxation process, the one emitting the fewest number of phonons (i.e., the smallest $\Delta E/\hbar\omega_{max}$) will predominate, and hence $\hbar\omega_{max}$ is used. As illustrated by Eq. 1.9, a lower $\hbar\omega_{max}$ leads to a slower W_p, and thus decreasing the non-radiative energy loss and increasing the populations of some excited levels and then the probability of radiative emission. Heavy metal halides, especially fluorides of which the phonon energy is lower than 300 cm^{-1}, have been widely studied as the host materials for both Vis up-conversion PL and MIR PL applications (Peng, 2013, Tran, 1984). However, the practical applications of halides are limited by the low laser-induced damage threshold, low thermal-shock resistance, poor chemical stability, fragility and manufacture difficult (Hou, 2010). In addition, moisture sensitivity is also a major consideration for selecting the host material as the OH^- group will degrade the 2.7-μm MIR emissions. So there are urgent needs for highly efficient and stable host materials.

The oxide materials with high chemical, mechanical and thermal stabilities, superior environmental durability, as well as intermediate phonon energy are then the promising hosts for PL applications. The simplest host materials are mono-metal oxides, such as ZnO (Wang, 2007), Al_2O_3 (Fan, 2011), Y_2O_3 (Capobianco, 2002), La_2O_3 (Zhang, 2012), ZrO_2 (Patra, 2003), TiO_2 (Hu, 2010), and Ta_2O_5 (Kazuo, 1995). Multi-metal oxides, such as $NaY(WO_4)_2$ (Cheng, 2002), $Sr_3Y_2(BO_3)_4$ (Shyichuk, 2011), $CaLa_2ZnO_5$ (Bandi, 2012), $CaMoO_4$ (Chung, 2012), Ln_2BaZnO_5 (Ln = Y, Gd) (Etchart, 2010), and $Lu_3Ga_5O_{12}$ (Mahalingam, 2008), have also been intensely studied for PL applications.

1.8 Ferroelectrics

Ferroelectricity is a property of certain materials (i.e., ferroelectric materials) in which spontaneous polarization (i.e., separation of the centre of positive and negative electric charge, making one side positive and the opposite side negative) exists and can be reversed or switched by applying an external electric field (Xu, 1991). In 1921, Valasek discovered the phenomenon of ferroelectricity and studied the dielectric properties of Rochelle salt ($NaKC_4H_4O_6 \cdot 4H_2O$) (Valasek, 1921). Ferroelectric materials contain spontaneous polarization and domain structure only at temperatures below the Curie point (T_c). Above this temperature they demonstrate paraelectricity, which is an ability (possessed by many materials, specifically ceramics and crystals) to become polarized under an applied electric field. Induced by the displacement of ions, spontaneous polarizations are formed below T_c. The switching of the spontaneous polarization under an external electric field will generate an observable polarization-electric field (P-E) hysteresis loop.

There are hundreds of ferroelectric materials, including ceramics, single crystals, thin films, liquid crystals, polymers and nanoscale ferroelectrics. The common and significant ferroelectrics can be divided into the following three categories:

1. Perovskite-type compounds, such as $PbTiO_3$ (PT), $PbZr_xTi_{1-x}O_3$ (PZT), $BaTiO_3$ (BT), $(1-x)Pb(Mg_{1/3}Nb_{2/3})O_3$-$xPbTiO_3$ (PMN-PT), $K_{0.5}Na_{0.5}NbO_3$ (KNN), $Bi_{0.5}Na_{0.5}TiO_3$ (BNT), $Ba_xSr_{1-x}TiO_3$ (BST), $BiFeO_3$ (BFO), $LiNbO_3$, $LiTaO_3$.
2. Tungsten bronze type compounds, such as $Sr_xBa_{1-x}Nb_2O_6$ (SBN), $PbNb_2O_6$, $Sr_2NaNb_5O_{15}$ (SNN), $K_{6-x}Ba_xLi_{4-x}Nb_{10}O_{30}$ (KBLN), $K(Nb/Ta)W_2O_9$.

3. Bi-layered structure compounds, such as $Bi_4Ti_3O_{12}$ (BTO), $CaBi_4Ti_4O_{15}$ (CBT), $BaBi_2Ta_2O_9$ (BBT), $Ca_xSr_{1-x}Bi_2Ta_2O_9$, $Bi_4Gd_2Ti_3Fe_2O_{18}$.

In general, perovskite-type compounds can be used for sensors, non-volatile memories, medical ultrasound imaging devices, actuators and transducers; tungsten bronze type compounds can be used for electro-optic (EO) devices, optical storage systems and photorefractive devices; Bi-layered structure compounds can be used for high-temperature sensors, resonators and filters (Xu, 1991, Wang, 2003).

1.8.1 Electrical properties of ferroelectrics

In the past decades, perovskite-type ferroelectric materials, especially lead-based compounds have been extensively studied and used in numerous applications because of their outstanding piezoelectric, dielectric, pyroelectric, ferroelectric and elastic properties, as well as the excellent coupling of electro-mechanical, electro-thermal and EO properties. The PZT-based ceramics are the dominating materials with a piezoelectric constant $d_{33} \sim 600$ pC/N, electromechanical coupling coefficient $k_{33} \sim 70$ % and electric field-induced strain ~0.15 % (Park, 2002). As the fast development of single crystals, the PZT ceramics and corresponding devices have been gradually replaced by PMN-PT single crystals, which exhibit ultrahigh piezoelectric responses. For the [001]-oriented crystals with the composition near the morphotropic phase boundary (MPB), $d_{33} \sim 2500$ pC/N, $k_{33} \sim 94$ % and strain ~ 1.8% (Fu, 2000, Feng, 2003, Park, 1997).

In 2006, the European Restriction of Hazardous Substances (EU-RoHS) directive aimed to restrict lead-based substances used in electronic equipments because the lead oxides and their high vapor pressure during processing show detrimental effect on both human body and environment. From the perspective of environmental protection, there is urgent demand for researching alternative lead-free ferroelectric materials. BT is a typical lead-free ferroelectric material having a cubic perovskite structure but with tetragonal-type distortion. It has a low Curie temperature ($T_c = 120$ ℃), resulting from a ferroelectric tetragonal to paraelectric cubic phase transition (Merz, 1949). Wada et al. have found that an external electric field can induce phase transitions at room temperature, i.e., changing from tetragonal to monoclinic phase at 1 kV/mm and then to rhombohedral phase at 3 kV/mm (Wada, 1999). The observed d_{33} for BT in the form of ceramics is about 190 pC/N, and changes to 86 pC/N for single crystals (Berlincourt, 1958). Although the piezoelectric properties of BT are not very outstanding, they show extraordinary non-piezoelectric properties such as colossal permittivity, which can be up to ~10^6 for BT nanocrystalline ceramics (Fritsch, 2008), and large reversible strain, which can be up to ~0.8 % resulting from the switching of defect-mediated domains (Ren, 2004). BT is also served as the model ferroelectric for fundamental investigations.

BNT is a promising ferroelectric material with a high Curie temperature T_c of 325 ℃, remanent polarization P_r of 38 μC/cm^2, coercive field E_c of 7.3 kV/mm and d_{33} of 73 pC/N at room temperature (Pronin, 1980). However, BNT has some drawbacks such as high coercive field and relatively large conductivity (Ge, 2009), which makes the poling difficult and thus resulting in poor piezoelectric properties. BNT also exhibits a low depolarization temperature (~187 ℃) limiting its applications at high temperatures (Hiruma, 2009). Sakata et al. have reported that the depolarization is resulted from an intermediate antiferroelectric phase existed in BNT (Sakata, 1974). However, the suggestion of antiferroelectric phase is still an issue of disputes (Aparna, 2006).

KNN is a ferroelectric system formed by orthorhombic ferroelectric $KNbO_3$ and orthorhombic antiferroelectric $NaNbO_3$ (Ahtee, 1976). It has a high Curie temperature T_c of 420 ℃, high planar coupling k_p of 45%, moderate dielectric constant of 470, and remnant polarization P_r of 33 $\mu C/cm^2$ (Haertling, 1967). But it also has several drawbacks hindering its applications. It is hard to prepare dense KNN ceramics due to the high volatility of alkaline metal elements. According to the phase diagram of $KNbO_3$ and $NaNbO_3$, the phase stability of KNN ceramics is limited to 1140 ℃ (Egerton, 1959). Li et al. have applied the spark plasma sintering technique to successfully fabricate dense KNN ceramics with a high d_{33} of 148 pC/N (Li, 2006). On the other hand, the d_{33} of KNN prepared by the conventional solid-state method is about 90 pC/N (Guo, 2004). For improving the sinterability and then the properties of KNN, three ways are commonly used. The first way is to use special sintering method to replace the conventional solid-state method, such as hot pressing (HP) (Ringgaard, 2005), spark plasma sintering (SPS) (Wang, 2002), hot isostatic pressing (HIP) (Jaeger, 1962), and reactive-templated grain growth (RTGG) (Yilmaz, 2003). The second way is to use sintering aids or dopants, such as Li^+, Cu^{2+}, Zn^{2+}, Mn^{4+}, Fe^{3+}, Ta^{5+} and Sb^{5+}. The third way is to form new solid solutions with other ferroelectrics, such as $LiNbO_3$, $LiTaO_3$, $LiSbO_3$, $SrTiO_3$, BT, BNT, BFO and $BiScO_3$. The research status and potential applications of the KNN-based ceramics will be further introduced in Chapter 1.9.

BFO is a lead-free candidate exhibiting both ferroelectric and ferromagnetic properties. The orientation of the ferroelectric domains can be changed by a magnetic field, and the ferromagnetic orientation can be changed by an electric field (Chu, 2009). It has a bulk rhombohedral symmetry at room temperature. The BFO single crystals show very high Curie temperature (T_c = 830 ℃) and large remnant polarization (P_r = 100 μC/cm^2) (Teague, 1970). However, due to defects, secondary phases and porosity arisen from the preparation process, only a few works are successful in preparing BFO ceramics with good properties (Gheorghiu, 2010). From the magnetic point of view, BFO has an antiferromagnetic order (Néel temperature T_N ~ 370 ℃ and magnetic Curie temperature T_c ~600 ℃) (Neaton, 2005). Although BFO has shown great potential for practical use, there are still numerous drawbacks, such as poor dielectric and ferroelectric properties, lossy and unsaturated (*P*-*E*) hysteresis loops. Furthermore, BFO has unanswered questions of its behavior, such as the lack in reading of the BFO phase diagram and switching processes (Catalan, 2009).

As discussed in the previous sections, most of the above-mentioned lead-free ferroelectrics have their own drawbacks. For developing new ferroelectric materials with improved piezoelectric, dielectric and ferroelectric properties, new solutions have been formed from two or three above-mentioned systems, with a composition near the MPB region. The binary systems include BNT-KNN (Kounga, 2008), BNT-BT (Takenaka, 1991), BNT-BFO (Nagata, 1999), KNN-BT (Ahn, 2007). The ternary systems have also been investigated, such as 0.92NBT-0.06BT-0.02KNN ceramics, which show the largest strain (~0.45 %) in all the polycrystalline lead-free ceramics (Zhang, 2008). As more attentions have been paid to the lead-free systems, more and more complex solid solutions will be explored for enhancing the ferroelectric-related performances and pursuing extraordinary properties.

1.8.2 Photoluminescence studies of ferroelectrics

PL effect has been reported in pure ferroelectrics. The PL mechanism in highly disordered (amorphous) ferroelectrics (PT, PZT, BT, BST) has been theoretically studied (Pizani, 2000, Orhan, 2005, Cavalcante, 2008). The charge transfer process responsible for the observed light emission is from the defected BO_5 (B = Ti, Zr) clusters to the normal BO_6 clusters. The PL is mainly from the interface between the crystalline and amorphous region. In BFO nanotubes, the strong Vis PL has also been observed, which is caused by the oxygen vacancy (Miriyala, 2013). However, the disordered structure or defects such as oxygen vacancies will greatly degrade the ferroelectric properties. Thereupon, new ways should be utilized to develop PL properties in ferroelectrics while retaining the ferroelectric functions.

When the ferroelectric hosts are doped with RE ions, multifunction will be realized. The multifunctional materials that possess two or more desirable properties (e.g. ferroelectric and PL properties) in a single entity should have great potentials in sensors, optical-electro integration, coupling devices and other multifunctional optoelectronic applications. The new materials should have high luminescent efficiency as well as stable chemical, thermal, and mechanical properties.

Lead-based ferroelectrics can be easily doped with RE ions. Er-doped PLZT exhibits efficient PL at 1.55 μm in the NIR region, which is a good candidate for EO devices in optical communication networks (Ballato, 2000). The up-conversion PL has been investigated in Er-doped PMN-PT transparent ceramics with different Er^{3+} concentrations. And the up-conversion mechanism has been discussed together with the energy transfer processes (Zeng, 2012).

There are also a number of PL studies on lead-free RE-doped ferroelectrics in the literatures. Dopant site location has been found to influence the relative PL intensities in Sm-doped BT (Makishima, 1965) and Pr-doped BT (Okamoto, 2002). The vibronic structures and the effects of soft-mode lattice vibration have been investigated in the PL spectra of Pr/Eu/Tb-doped BT (Yamamoto, 1967). Pr-doped $CaTiO_3$ has been reported as a potential red phosphor for the display applications (Vecht, 1994) and the origin of red emission from Pr^{3+} ions have been explained (Diallo, 1997). The Vis up-conversion PL has been investigated in Er-doped BST ceramics, and the results have shown that phase structure could affect both the shape and the intensities of PL spectra (Chen, 2012). In Er-doped NBT ceramics, strong green and red up-conversion emissions have been obtained and the concentration quenching has been discussed (Chen, 2007).

Multifunction combined with electrical and optical properties have also been reported in lead-free RE-doped ferroelectric systems. In Pr-doped NBT ceramics, the ferroelectric remanent polarization can enhance the PL intensities remarkably by ~35 %, attributed to the decrease of crystal symmetry in the host after poling (Tian, 2013). The relationships between PL spectra and the poling electric field and time have been systematically investigated in Er-doped $KNbO_3$ ceramics, demonstrating that the Stark splitting is produced by the dipole moment of Er^{3+} ions interacting with the internal local electric field induced by polarization (Chu, 2004). It has also been shown for Er-doped SBN glass ceramics that some optical transitions are sensitive to the change in the ferroelectric properties (González, 2011). The Er-doped CBT bismuth layer structured ceramics exhibit bright Vis up-conversion PL and simultaneously show increased T_c, enhanced ferroelectric and piezoelectric properties (Peng, 2013). As a multifunctional material, Er-doped CBT has great potential in sensor, EO integration, and coupling device applications. Tm/Pr/Er-doped $LiNbO_3$ crystals have been studied for applications in optical switches, modulators and waveguide amplifier materials (Thiel, 2012), as well as applications in mode-locked, Q-switched, or tunable waveguide lasers owing to its electro-optical properties (Brinkmann, 1991). In RE-doped binary systems, such as Pr-doped NBT-$CaTiO_3$ and Pr-doped BT-$CaTiO_3$ ceramics, the PL performances can be enhanced greatly by poling, resulting from the change of band gap of host by the local electric field (Du, 2013a, Zou, 2013). The Eu- or Pr-doped NBT-BT ceramics exhibit enhanced ferroelectric, piezoelectric, dielectric properties as well as strong PL effects, and thus having great potential in applications as sensors and electro-mechano-optical integration (Yao, 2013).

1.9 Lead-free KNN-based ceramics

As mentioned in the previous section, KNN ceramics have a number of drawbacks, which greatly influence the sinterability and performances. Other oxides or ferroelectrics have been used to develop new KNN-based ceramics for improving the properties. CuO has been used as a novel sintering aid to decrease the sintering temperature (~150 ℃ lower) and increase the relative density (up to ~97.5%) (Matsubara, 2004). BaO has also been added to decrease the grain size and increase the density of KNN ceramics. KNN ceramics added with 2 mol% BaO have a relative density of ~95%, dielectric constant of 760, dielectric loss of 0.024, and d_{33} of 115 pC/N

(Ahn, 1987). Similarly, the doping of Bi_2O_3 can increase the relative density of KNN ceramics to above 99% and improve the properties. For the KNN ceramics doped with 1 mol% Bi, d_{33} = 164 pC/N, k_p = 0.47, and mechanical quality factor Q_m = 120 (Du, 2007a). Murty et al. have reported that after the addition of RE ions, such as Eu^{3+} and La^{3+} ions, the grain sizes of KNN ceramics decrease and T_c reduce, giving a low T_c of 355°C and 342°C for the Eu-doped KNN and La-doped KNN, respectively (Murty, 1989, Murty, 1988). Similarly, the Eu-doping can reduce the orthorhombic-tetragonal transition temperature by 20 ℃.

The binary, ternary or even quaternary systems of KNN have been investigated. For the KNN-$LiNbO_3$, the densification is improved, giving a significant decrease in pore size. Moreover, the T_c is shifted to a higher temperature while the orthorhombic-tetragonal phase transition temperature $T_{O–T}$ is shifted to a lower temperature. The MPB region between the orthorhombic and tetragonal phases has been found in the compositional range $0.05 < x < 0.07$ for (1-x)KNN-x$LiNbO_3$ ceramics (Guo, 2004). Similar results have also been obtained in KNN-$LiTaO_3$ ceramics (Guo, 2005). Li and Bi co-modified KNN ceramics have been studied, and the results have shown that the grain growth can be inhibited by the doping of Bi, giving a uniform and fine-grained microstructure. The optimum piezoelectric properties for the ceramics are d_{33} = 185 pC/N, k_p = 0.43 and k_t = 0.45 (Du, 2007b). Lin et al. have systematically investigated the structure, phase transition, ferroelectric, dielectric and piezoelectric properties of a series of KNN-based ceramics, such as CuO-modified KNN-$Ba(Ti_{0.95}Zr_{0.05})O_3$ (Lin, 2007a), KNN-$LiSbO_3$ (Lin, 2007b), KNN-$LiTaO_3$-$LiSbO_3$ (Lin, 2007c), CuO-modified KNN-BT (Lin, 2007d), MnO_2- and CuO-modified KNN (Lin, 2008a), etc.

By using the reactive templated grain growth technique, Saito et al. have developed the most popular KNN-based ceramics: textured $(K_{0.44}Na_{0.52}Li_{0.04})(Nb_{0.84}Ta_{0.10}Sb_{0.06})O_3$ (KNN-$LiTaO_3$-$LiSbO_3$) (Saito, 2004). Owing to the MPB composition, the un-textured KNN-$LiTaO_3$-$LiSbO_3$ ceramic already exhibits a high d_{33} of ~300 pC/N. After texturing, d_{33} and k_p increases to a peak value of 416 pC/N and 0.61, respectively, making the ceramic become comparable to the widely used PZT ceramics. The textured material shows temperature-independent field induced strain characteristics. Recently, the transparent KNN-based ceramics have been successfully fabricated by the hot-press sintering method (Li, 2013a). The optical transmittance of the ceramics reaches a high value of 60% in the NIR region. They exhibit strong linear EO response, giving a large effective linear electro-optic coefficient in the range of 120-200 pm/V. The transparent ceramics have great potential in optoelectronic, such as optical filters, switches, modulators and data processing devices.

Sun et al. has reported the Pr-doped KNN ceramics with strong green (528 nm) and red (617 nm and 650 nm) emissions (Sun, 2012). Wei et al. has reported the dual-enhancement of ferroelectric and PL performances in Pr-doped KNN ceramics (Wei, 2014). Recently, Jia et al. has used Eu^{3+} ions as the PL structural probe to investigate the compositional changes in $K_{1-x}Na_xNbO_3$ (x = 0.42-0.56) ceramics (Jia, 2014). However, to the best of my knowledge, there is no other work studying PL properties of RE-doped KNN-based materials. Therefore, it has great value to study the RE-doped KNN-based ceramics because as a multifunctional material, they may take an important role in various research and application fields.

1.10 Motivation of research

PL effects, including Vis up-conversion PL, down-conversion NIR and MIR emissions, emission colors and lifetimes, play an important role on optical researches and applications. The combination of both PL and ferroelectrics in a single entity can provide a multifunctional material for the optoelectronic applications. In this thesis, we aim to develop new lead-free multifunctional ceramics with good PL, ferroelectric and EO properties. Accordingly, three groups of multifunctional ceramics will be prepared: RE-doped KNN ceramics, RE-doped Li-modified KNN ceramics, and RE-doped Bi/Li-comodified KNN transparent ceramics. The work will focus on preparing both up-conversion and down-conversion PL ceramics via the doping of Er^{3+}, Pr^{3+} or Yb^{3+} ions. The PL mechanism of various RE-doped KNN-based ceramics will be elaborated. The sol-gel method will be used to prepare the ceramics for studying the effects of microstructure on PL properties. The effects of phase transition as well as ferroelectric polarization will also be investigated. The relationship among PL, ferroelectric and EO properties will be elucidated in Er-doped KNN-based transparent ceramics.

1.11 Scope of work

The main objective of present work is to study the PL and electrical properties of lead-free RE-doped KNN-based ceramics. The thesis consists of eight chapters:

Chapter 1 gives an introduction of luminescence, rare-earth ions, ferroelectrics and corresponding materials, as well as the motivation and objectives of the present work.

Chapter 2 introduces the fabrication methods for RE-doped KNN-based ceramics. The characterization instruments and techniques, including XRD, SEM, Raman, PL, ferroelectric, dielectric, optical and EO properties are described.

Chapter 3 discusses the PL properties of Er-doped KNN ceramics, including the up-conversion Vis emissions, down-conversion NIR and MIR emissions, emission colors, lifetimes of Er^{3+} ions and the energy transfer processes. The dielectric, ferroelectric and piezoelectric properties of the ceramics are studied.

Chapter 4 reports the PL (both up- and down-conversion) and ferroelectric properties of 2 mol% Er-doped $(K_{0.5}Na_{0.5})_{1-x}Li_xNbO_3$ (KNLN) ceramics. The effects of Li^+ on PL from Vis to MIR region and on phase transition are investigated.

Chapter 5 presents the fabrication and properties of the sol-gel-derived Er-doped KNN and KNLN ceramics. Their microstructure, PL, piezoelectric and dielectric performances are compared with those of the ceramics prepared by the solid state reaction method.

Chapter 6 shows the PL properties of Er/Pr-doped KNN ceramics and Er/Yb-doped KNN ceramics. The effects of Pr^{3+} and Yb^{3+} ions on the PL properties of Er^{3+} and the relationship between PL intensity and electrical poling are investigated.

Chapter 7 introduces the $(K_{0.5}Na_{0.5})_{1-x}Li_xNb_{1-x}Bi_xO_3$ (KNN-LB) and 1 mol% Er-doped KNN-LB transparent ceramics fabricated by pressureless sintering through the solid-state reaction method. The EO, dielectric, ferroelectric and PL properties of the Er-doped KNN-LB transparent ceramics are investigated for exploring the multifunctional photonic applications.

Chapter 8 gives the conclusions.

Chapter 2 Fabrication and Characterization

2.1 Fabrication of ceramics

2.1.1 Classification of ceramics in the thesis

In this study, six groups of ceramic samples were fabricated by either the conventional solid state reaction (SSR) method or the sol-gel method:

(a) x mol% Er-doped $K_{0.5}Na_{0.5}NbO_3$ with x = 0, 1, 2, 3, 4, 5. The samples are abbreviated as KNN:Er-x.

(b) 2 mol% Er-doped $(K_{0.5}Na_{0.5})_{1-x}Li_xNbO_3$ with x = 0, 0.02, 0.04, 0.06, 0.08, 0.10. The samples are abbreviated as Er-KNLN-x.

(c) 2 mol% Er and y mol% Pr-codoped $K_{0.5}Na_{0.5}NbO_3$ with y = 0, 0.25, 0.5, 1. The samples are abbreviated as Er-KNN-Pr-y.

(d) 1 mol% Er and z mol% Yb-codoped $K_{0.5}Na_{0.5}NbO_3$ with z = 0, 1, 2, 3, 4, 5, 6. The samples are abbreviated as Er-KNN-Yb-z.

(e) $(K_{0.5}Na_{0.5})_{1-x}Li_xNb_{1-x}Bi_xO_3$ with x = 0.01, 0.02, 0.03, 0.04, 0.05, 0.06, 0.07, 0.08, 0.09, 0.10. The samples are abbreviated as KNN-LB-x.

(f) 1 mol% Er-doped $(K_{0.5}Na_{0.5})_{1-x}Li_xNb_{1-x}Bi_xO_3$ with x = 0.04, 0.05, 0.06, 0.07, 0.08. The samples are abbreviated as Er-KNN-LB-x.

2.1.2 Fabrication procedure of ceramics

The main SSR fabrication procedure is summarized in Fig. 2.1. The starting raw chemicals are K_2CO_3 (99.9%), Na_2CO_3 (99.5%), Nb_2O_5 (99.99%), Li_2CO_3 (99%), Bi_2O_3 (99.9%), Er_2O_3 (99.99%), Pr_6O_{11} (99.9%) and Yb_2O_3 (99.9%). These powders were weighed according to the stoichiometric ratio of the compositions using electronic balance. The mixing and grinding processes are achieved by ball-milling using zirconia balls for 12 h in ethanol as medium. The mixture was then baked to remove moisture and calcined at 850°C for 4 h in an alumina crucible. The aim of calcination is to form a chemically and crystallographically uniform structure by making the ions interact with each other through the inter-diffusion process. After that, the calcined powders were ball-milled again for 8 h, baked, and then mixed thoroughly with a 5 wt% polyvinyl alcohol (PVA) binder solution for shaping and strengthening the dry forms. After being pressed into disks with 12 mm-diameter under ~300 MPa of pressure, the binders in the samples are completely burned out at 800°C for 2 h with a slow increasing temperature. Finally the disk samples were sintered at 1050-1150°C for 4 h in air to obtain dense ceramics.

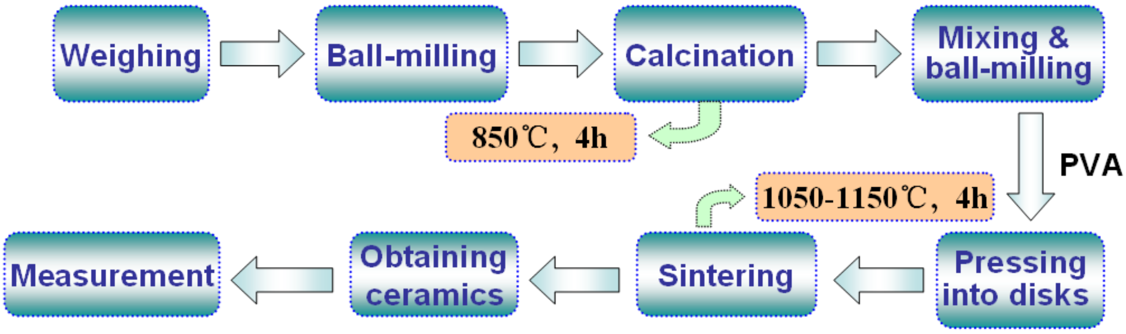

Figure 2.1 Flow diagram of the ceramics' fabrication procedure.

2.1.3 Poling

After sintering, the ceramics were polished to different thicknesses to achieve flat and smooth surfaces for different measurements. In the microcosmic field of these ceramics, the dipoles nearby tend to align in regions called ferroelectric domains, which are usually randomly oriented so that the materials are isotropic. However, these domains can be aligned through the process of poling, by which an external electric field is applied across the material. The poled ceramics are anisotropic, possessing a net permanent polarization. Fig. 2.2 shows the schematic diagram of poling system.

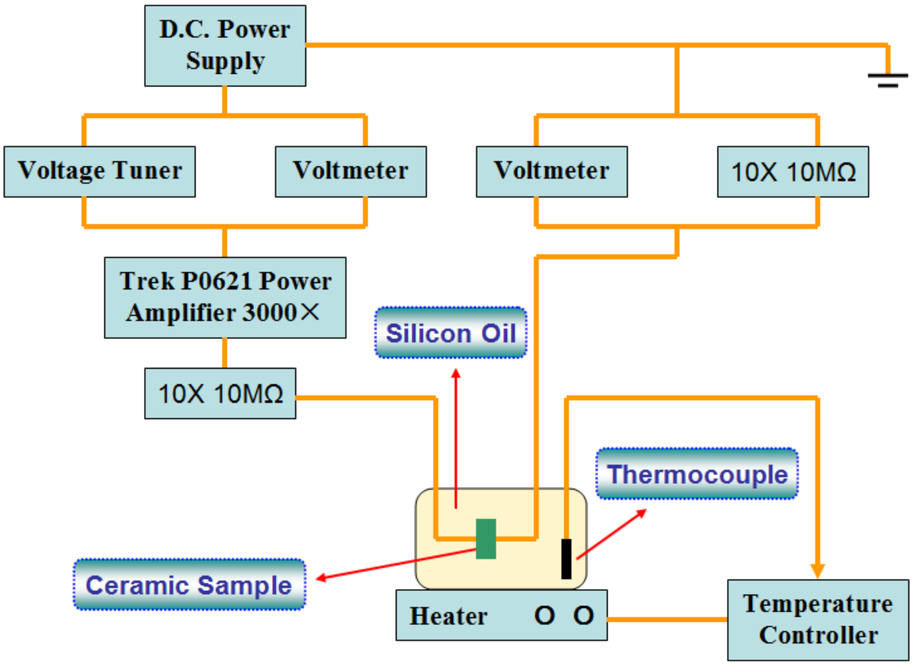

Figure 2.2 Schematic diagram of poling system.

The ceramic sample was first painted with silver paste and fired at 750°C for 15 min to form silver electrode. During the poling process, the sample was heated in silicon oil to a temperature of 150°C. Then a direct-current (dc) electric field of 5.0 kV/mm was applied along the thickness direction for 30 min to fully polarize the sample. After that, the sample was cooled down to room temperature with the electric field kept on.

2.2 Characterization of ceramics

The characterization methods for the structural, thermal, optical, electrical, and EO properties of the ceramics are described as follows, including X-ray diffraction (XRD), scanning electron microscope (SEM), Raman, PL, photoluminescence excitation (PLE), luminescence decay curves, optical transmittance, dielectric properties, ferroelectric hysteresis loops (*P*-*E* loops), and linear EO coefficients.

2.2.1 Structural characterization

2.2.1.1 XRD

XRD is an analytical technique looking at X-ray scattering from crystalline materials. Each crystalline material produces a unique X-ray fingerprint of X-ray intensity versus scattering angle. In this study, the crystalline structures of ceramics were examined using the XRD analysis with CuK_α ($\lambda = 0.154$ nm) radiation (SmartLab; Rigaku Co., Japan). The common θ-2θ scan was conducted to reveal the crystalline planes, 2θ angles, crystalline phases and lattice parameters of the ceramics.

The scattering of X-ray is resulted from the interaction between X-rays and crystal lattices of the ceramics. The X-rays diffracted from crystalline planes at each angle interfere with each other, producing a variation of intensity that is called XRD pattern. According to the Bragg's Law, the intensity reaches maximum at certain incident angle:

$$2d_{hkl}\sin\theta_{hkl} = k'\lambda \tag{2.1}$$

where h, k, l are Miller indices, d_{hkl} is the interplanar spacing of the {hkl} set of lattice planes, θ_{hkl} is the incident angle of the beam, k' is the order of diffraction, and λ is the wavelength of the X-ray.

2.2.1.2 SEM

The microstructures of ceramics, such as morphologies and crystalline grain sizes, were examined by SEM (JSM-6490, JEOL Ltd., Japan), which can produce high resolution images of the surface structure of a sample. A schematic diagram of the SEM equipment is shown in Fig. 2.3.

The SEM equipment can be considered as a combination of three systems: (1) an electron-optical column with associated electronic circuit for controlling lens currents, etc. (2) a vacuum system, stage air-lock etc. (3) a signal detection and display system. During the operation, a narrow beam of accelerated electrons from an electron gun is passed through a magnetic lens and focused on the specimen surface. As the electron beam scans the surface, the collector current changes due to the changes in composition, texture or surface orientation. Then three kinds of radiations will be obtained: secondary electrons, backscattered electrons and characteristic X-rays. Among them, the secondary electrons will be collected by the scintillating detector of SEM. These electrons usually have low energy and only those originated within a few nanometers can be collected to form an image, manifesting morphology and topography of a sample.

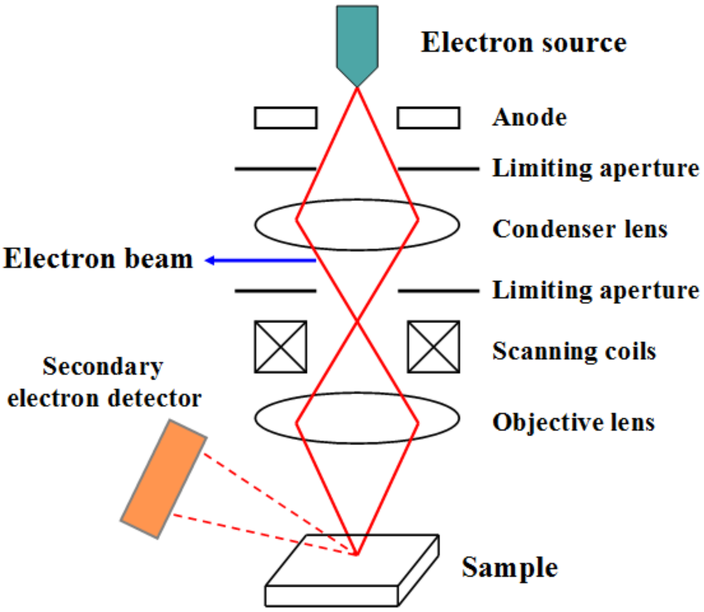

Figure 2.3 Schematic diagram of SEM equipment.

2.2.1.3 Raman

Raman spectroscopy is a useful spectroscopic technique to analyze the vibrational, rotational, and other low-frequency modes in a system (Gardiner, 1989). Strong monochromatic light (e.g. laser) is usually applied in the Raman measurement because it is fast, simple, repeatable and no damage to samples for the qualitative and quantitative analysis. According to quantum theory, when the incident photon (at frequency of v_0) interacts with a molecule, both elastic and inelastic scatterings may take place. In the elastic scattering process, there is no energy exchange and only the moving direction of photon changes. This scattering way is called Rayleigh scattering.

Whereas in the inelastic scattering process, there is energy exchange between photon and molecule. The moving direction of photon changes followed with energy transfer, leading to a change in photon frequency. The frequency decreases with the lost of photon energy, which is called Stokes Raman scattering; whereas the frequency increases with the gain of photon energy, which is called anti-Stokes Raman scattering.

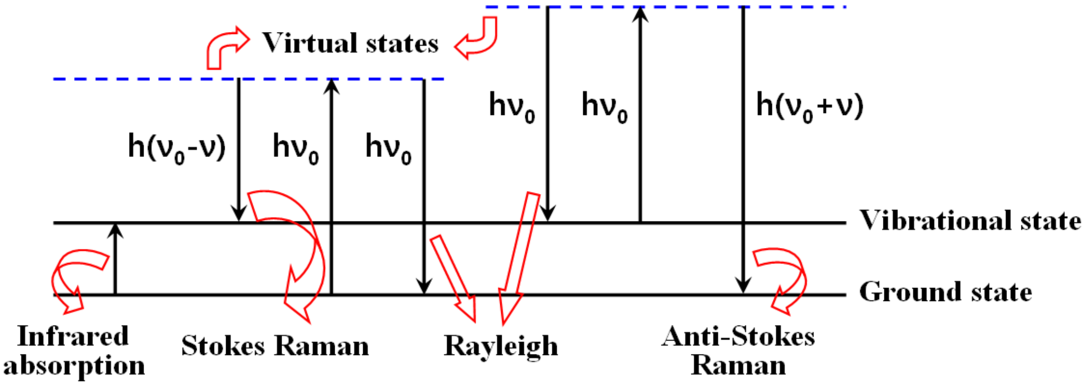

Figure 2.4 Energy level diagram of Raman scattering effect.

Fig. 2.4 shows the energy level diagram of Raman scattering effect. It should be noted the virtual states do not exist. The energy interval between the vibrational state and ground state is $h\nu$. The energy difference between Stokes Raman line and Rayleigh line is $h(\nu_0-\nu)-h\nu_0 = -h\nu$, meanwhile the energy difference between anti-Stokes Raman and Rayleigh line is $h(\nu_0+\nu)-h\nu_0 = h\nu$. This means that the Raman spectra are distributed symmetrically on both sides of the Rayleigh line. Generally, the vibration energy of molecule is much larger than that of the molecular kinetic thermal energy. According to the Boltzmann distribution law, the number of molecules in the vibrational state is far less than those in the ground state. Therefore, the Stokes line is stronger than the anti-Stokes line.

In this study, the Raman spectra for the ceramics were measured in backscattering geometry using the 488-nm line of an Ar ion laser (Spectra-Physics) as the excitation source. Spectra were recorded by a grating spectrometer (Jobin-Yvon Horiba HR800, France). The micro-Raman spectroscopy technique was used as the laser spot which was reduced to ~1 μm in diameter by the high-magnification microscopic objectives. In the Raman measurement, a laser light beam is incident on the sample surface, inducing energy exchange with the material via the creation or annihilation of phonons. The scattered light then loses or gains certain amount of energy depending on whether a phonon is created or annihilated. By measuring the energy change of the light beam, the characteristic value of the vibrational energy (scattering peak in the Raman spectra) for the sample is obtained.

2.2.2 Optical characterization

2.2.2.1 Luminescence measurement

The luminescence properties (PL, PLE and lifetime) of the rare earth-doped KNN-based ceramics were characterized by a commercial PL spectrometer (FLSP920, Edinburgh Instruments, UK). Fig. 2.5 shows both the photograph and schematic diagram of the PL system.

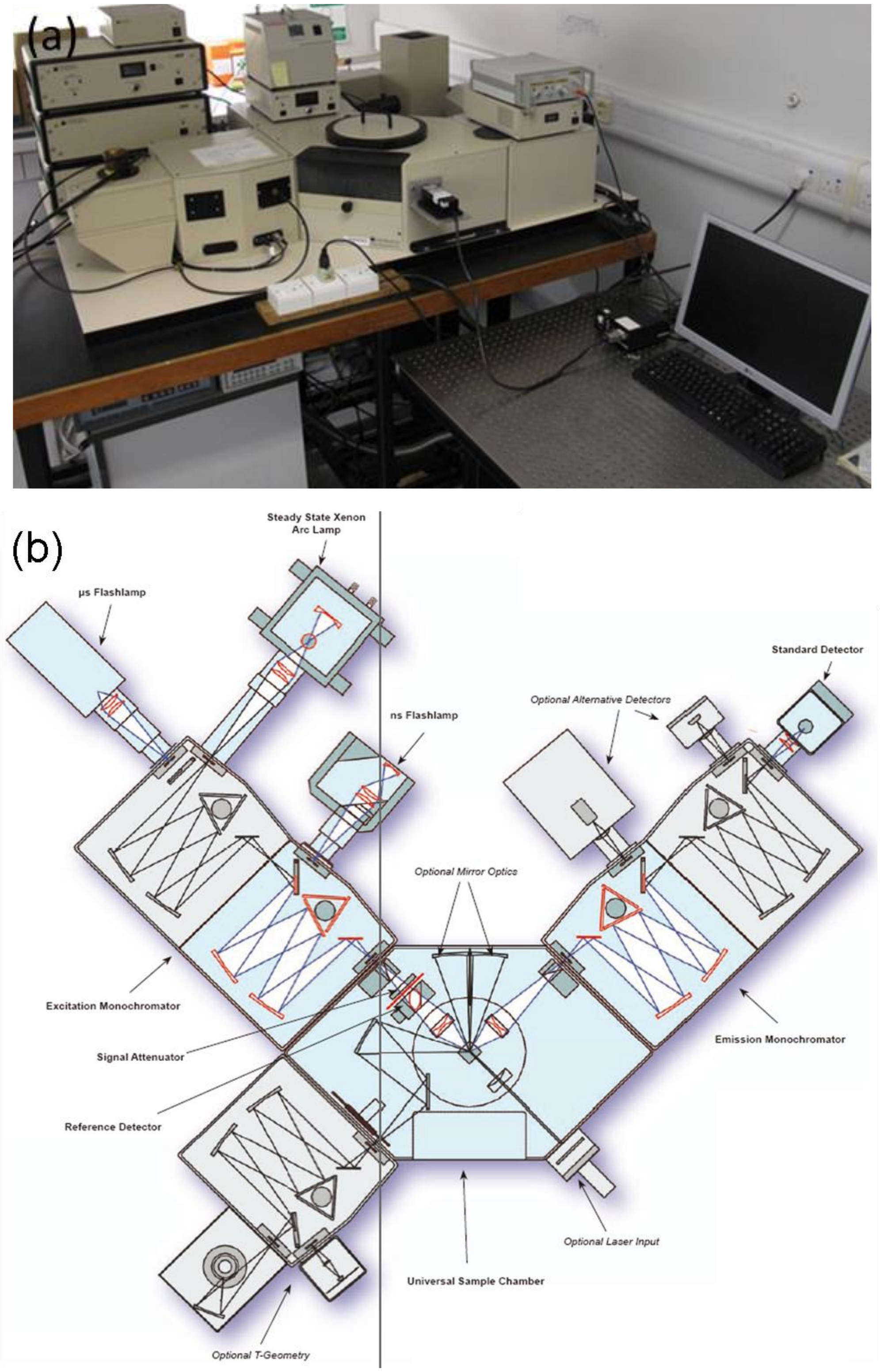

Figure 2.5 (a) Photograph of the PL spectrometer system. (b) Interior structure of the PL spectrometer system (FLSP920 n.d.).

The PL spectrometer can be used for both steady state and time resolved measurements. It combines high sensitivity with high spectral resolution and good stray light rejection. Depending on the light sources and detectors, the PL spectra can be measured in a wide range from UV to MIR. The main parts employed in this study are listed as follows:

1. A 450-W steady state xenon arc lamp (Xe900) equipped with ozone generating lamp emits radiation from 200 nm to 2.6 μm, which is used as the excitation source during the measurements of Vis down-conversion PL and PLE spectra.
2. A continuous 980 nm diode laser (MDL-III, CNI Optoelectronics Tech. Co., China) with the maximum power output of 2 W is used for the measurements of Vis up-conversion PL, down-conversion NIR and MIR emissions.
3. A function generator (AFG3251, Tektronix, USA) is used to generate a Transistor-Transistor Logic (TTL) signal with a rep-rate of 100 Hz and duty circle of 10 % for controlling the 980-nm diode laser to generate pulsed signals in the measurements of emission decay curves (lifetimes).
4. A red sensitive photomultiplier tubes (PMT) is used to measure the PL spectra from UV to NIR range, i.e. 200-900 nm. Peltier-cooled housings (low to -25°C) are used to reduce the dark noise.
5. A NIR PMT is used to measure the PL spectra in the range of 400 nm to 1.7 μm. A cooling system is used to keep the PMT temperature at approximately -80 ℃.
6. A MIR PMT is used to measure the PL spectra in the range of 2.0 to 3.0 μm. Liquid nitrogen is used to cool the MIR PMT for reducing the noise effect.

2.2.2.2 Optical transmittance measurement

For measuring the optical transmittance, the KNN-based transparent ceramics were polished to a thickness of about 0.3 mm using 1-μm diamond compound. The optical transmittance was measured in the range of 300-900 nm using a UV-Vis spectrophotometer (UV-2550, Shimadzu Co., Japan), which is in double-beam configuration. The initial beam was split into two beams before reaching the ceramic sample: one acted as a reference beam and was assumed to be 100% transmission, and the other was sent to the sample. The observed transmittance was the net intensity of the two beams.

2.2.3 Electrical characterization

2.2.3.1 Dielectric measurement

The dielectric properties of the ceramic samples (with top and bottom electrodes), including the capacitance (C) and the dielectric loss (tan δ), were measured as a function of temperature using an impedance analyzer (HP 4194A; Agilent Technologies Inc., Palo Alto, CA). The dielectric constant (ε_r) is given as:

$$C = \frac{\varepsilon_0 \varepsilon_r A}{d} \tag{2.2}$$

where ε_0 is the permittivity of the vacuum, A is the electrode area of sample, and d is the thickness of sample. ε_r can be expressed as $\varepsilon_r = \varepsilon' - \varepsilon''$, where ε' is the real part of the dielectric constant and ε'' the imaginary part. The dielectric loss is defined as:

$$\tan\delta = \frac{\varepsilon''}{\varepsilon'} \qquad (2.3)$$

The experimental setup is schematically shown in Fig. 2.6. The ceramic sample connected to the impedance analyzer was placed inside a Carbolite furnace, in which the temperature could be varied from 25 to 480 ℃. The exact temperature in the tube furnace was measured by a thermocouple connected to a Keithley multimeter. The data from both the impedance analyzer and the multimeter were collected and analyzed by a computer.

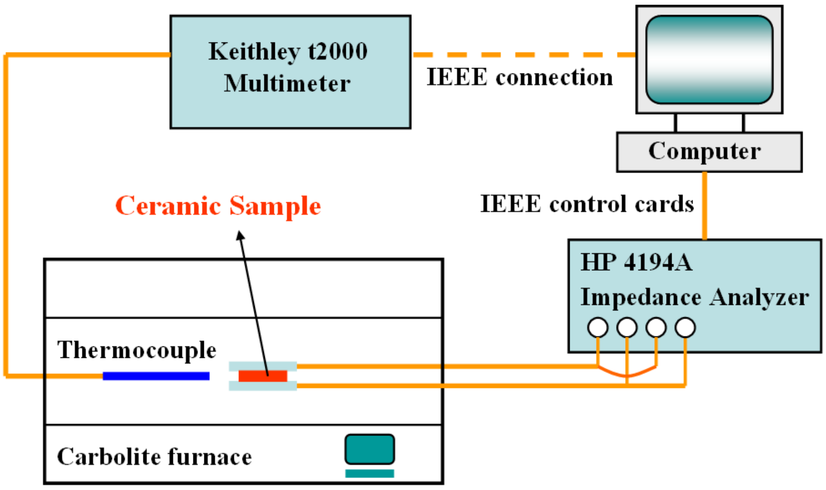

Figure 2.6 Schematic diagram of the dielectric experimental setup.

2.2.3.2 Ferroelectric measurement

The ferroelectric *P*-*E* loops illustrates the relationship between the applied electric field and the net macroscopic polarization of a ferroelectric material. From the *P*-*E* loop, ferroelectric parameters such as spontaneous polarization (P_s), saturation polarization (P_{sat}), remnant polarization (P_r) and electric coercive field (E_c) can be determined. In this study, a modified Sawyer-Tower circuit was used to measure the *P*-*E* loops at 100

Hz (Sawyer, 1930). Fig. 2.7 shows the experimental setup for the *P-E* loop measurement. There are two capacitors in the Sawyer-Tower circuit: ferroelectric capacitor (C_F) of ceramic sample and reference capacitor (C_R). The C_R value should be much larger (over 1000 times) than that of C_F so that the voltage drop at C_R can be neglected. The ceramic sample with electrodes was immersed in a silicone oil bath for preventing electrical breakdown in the air. An alternating current (ac) voltage signal was generated by a HP8116A function generator, and then amplified by a high voltage amplifier (Trek 609D-6) and applied to the sample. A digital oscilloscope (HP54645A) was used to measure the output voltage V_0 across C_R and input voltage V_i applied to the sample. The data were recorded by a computer, and the polarization P was given as:

$$P = \frac{C_R V_0}{A} \tag{2.4}$$

where *A* is the area of electrode.

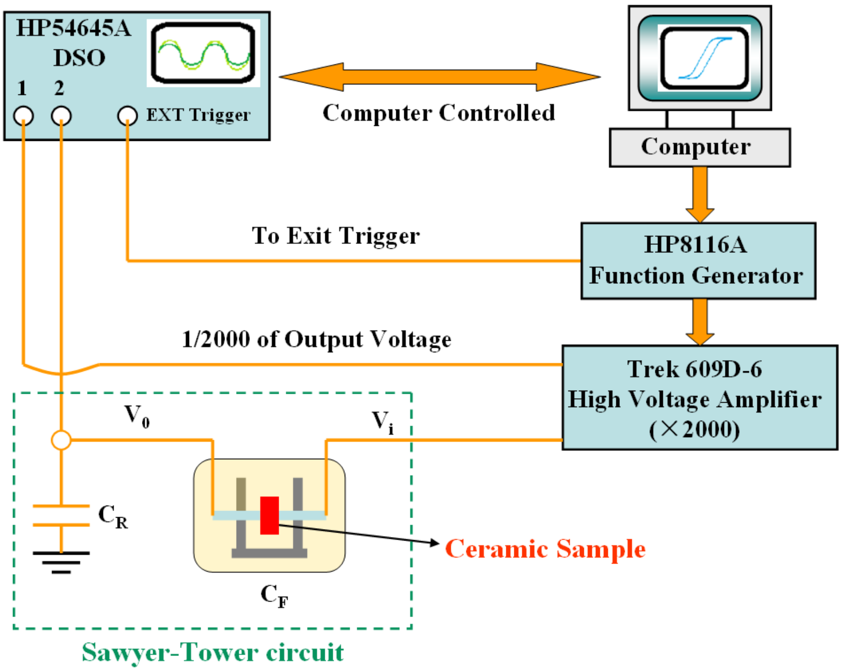

Figure 2.7 Experimental setup of *P-E* loop measurement.

2.2.4 EO characterization

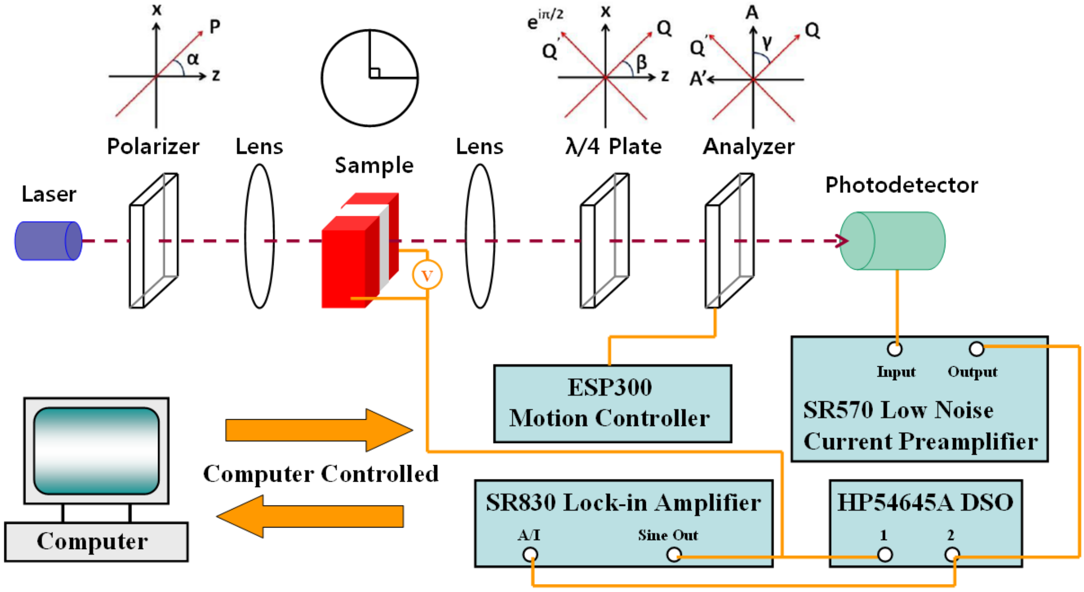

Figure 2.8 Schematic arrangement of the experimental setup in the modified Sénarmont system.

The EO coefficients of the KNN-based transparent ceramics were measured by a modified Sénarmont setup. Coplanar Au/Cr electrodes were sputtered on both the top and bottom surfaces of ceramics with a parallel spacing of 1 mm for the poling and EO measurement. Fig. 2.8 shows the schematic diagram of the experimental setup (Wan, 2005). In the EO measurement, a 2-mW frequency- and intensity-stabilized He-Ne laser (Model 117A, Spectra-Physics) is used as a light source. The ceramic sample is placed in the light path with the polarization direction along the z-axis (Fig. 2.8). A small ac voltage (E_0) with the frequency of 1 kHz is applied across the sample. The polarizer and quarter-wave (λ/4) plate are oriented with their optical axes (P and Q) making an angle of α and β, respectively, with the z-axis. The analyzer is rotated by an ESP300 motion controller at any azimuthal angle γ. A 633-nm laser beam propagates along the y-axis through the polarizer, sample, quarter-wave plate, analyzer, reaching a photodetector which is connected with a SR570 low noise current preamplifier. The demodulated output voltage of the photodetection is fed to a digital oscilloscope (HP54645A). The experimental setup is automatically controlled by a computer and the data is acquired from a SR830 lock-in amplifier.

Let the amplitude of the incident light beam equal E_{in}. The two components of the light beam incident normally on the ceramic sample are given as:

$$E_x = E_{in} \sin\alpha e^{i(ky-\omega t)},\ E_z = E_{in} \cos\alpha e^{i(ky-\omega t)} \tag{2.5}$$

where ω is the angular frequency of the light beam and t is the time. After passing the sample which is subjected to an electric field E along the z-direction, the components become:

$$E_x = E_{in} \sin\alpha e^{ikn_1(E)L} e^{i(ky-\omega t)},\ E_z = E_{in} \cos\alpha e^{ikn_3(E)L} e^{i(ky-\omega t)} \tag{2.6}$$

where L is the thickness of sample (along the y-direction). Then define the phase retardation Γ as:

$$\Gamma = k[n_3(E) - n_1(E)]L \tag{2.7}$$

Eq. 2.6 becomes:

$$E_z = E_{in} \cos\alpha e^{in_1(E)L} e^{i\Gamma} e^{i(ky-\omega t)} \tag{2.8}$$

After passing the λ/4 plate, the light beam, represented in terms of the components along and normal to the optical axis of the λ/4 plate, Q and Q', respectively, becomes:

$$E_Q = E_{in}[\sin\alpha \sin\beta + \cos\alpha \cos\beta \bullet e^{i\Gamma}] \bullet e^{i(ky-\omega t)+kn_1(E)L} \tag{2.9}$$

$$E_{Q'} = E_{in}[\sin\alpha\cos\beta - \cos\alpha\sin\beta \bullet e^{i\Gamma}] \bullet e^{i\pi/2} e^{i(ky-\omega t)+kn_1(E)L} \tag{2.10}$$

The light beam component which can pass through the analyzer and arrive at the photodetector is given as:

$$\begin{aligned} E_A = E_{in}[&\sin\alpha\sin\beta\cos\gamma + \cos\alpha\cos\beta\cos\gamma \bullet e^{i\Gamma} + \sin\alpha\cos\beta\sin\gamma \bullet e^{i\pi/2} \\ &- \cos\alpha\sin\beta\sin\gamma \bullet e^{i(\Gamma+\pi/2)}] \bullet e^{i(ky-\omega t)+kn_1(E)L} \end{aligned} \tag{2.11}$$

In the experiment, α and β are set as 45 °. Then Eq. 2.11 becomes:

$$E_A = \frac{E_{in}}{2}[\cos\gamma + \cos\gamma \bullet e^{i\Gamma} + \sin\gamma \bullet e^{i(\Gamma+\pi/2)}] \bullet e^{i(ky-\omega t)+kn_1(E)L} \tag{2.12}$$

Using Euler's formula, Eq. 2.12 can be written as:

$$E_A = \frac{E_{in}}{2}\{[\cos\gamma + \cos(\Gamma-\gamma)] + i \bullet [\sin\gamma + \sin(\Gamma-\gamma)]\} \bullet e^{i(ky-\omega t)+kn_1(E)L} \tag{2.13}$$

The intensity of the light beam (which is proportional to E^2) is then given as:

$$I_A = \frac{I_{in}}{4}\{2[1+\cos\gamma\cos(\Gamma-\gamma)] + \sin\gamma\sin(\Gamma-\gamma)\} = \frac{I_{in}}{2}[1+\cos(\Gamma-2\gamma)] \tag{2.14}$$

A photodetector signal is:

$$V_s = \frac{GI_{in}}{2}[1+\cos(\Gamma-2\gamma)] \tag{2.15}$$

where G is a constant depending on the properties of the photodetector.

The fully poled KNN-based transparent ceramics possess uniaxial symmetry with the optical axis aligned along the poling direction (i.e. z-direction). In the absence of an applied electric field, the equation of the optical indicatrix for the ceramics can be written as:

$$\frac{x^2}{n_o^2} + \frac{y^2}{n_o^2} + \frac{z^2}{n_e^2} = 1 \tag{2.16}$$

where (x, y, z) coordinate is the principal-axis coordinate system, n_o and n_e are the ordinary and extraordinary refractive index. When an electric field is applied to the ceramics along the z-axis (Fig. 2.8), the optical indicatrix will be modified, which is linearly proportional to the electric field. This linear EO effect is called the Pockels effect. The change in the refractive indexes (*n*) for this EO effect is given as:

$$\Delta(\frac{1}{n_p^2}) = r_{pk}E_k \tag{2.17}$$

where p = 1, 2, 3, 4, 5, 6 and r_{pk} is the first-order EO matrix. For the ceramics with uniaxial symmetry, the r_{pk} has the form as:

$$\left(r_{pk}\right) = \begin{pmatrix} 0 & 0 & r_{13} \\ 0 & 0 & r_{13} \\ 0 & 0 & r_{33} \\ 0 & r_{51} & 0 \\ r_{51} & 0 & 0 \\ 0 & 0 & 0 \end{pmatrix} \tag{2.18}$$

Under the electric field E_0 on the ceramics along the z-axis, Eq. 2.16 becomes:

$$(\frac{1}{n_o^2} + r_{13}E_o)x^2 + (\frac{1}{n_o^2} + r_{13}E_o)y^2 + (\frac{1}{n_e^2} + r_{33}E_o)z^2 = 1 \tag{2.19}$$

The new indicatrix has different dimensions, but is not rotated. For the light beam propagating along the y-axis, the refractive indexes n_o(E) and n_e(E) are given as:

$$\begin{aligned} \frac{1}{n_o^2(E)} &= \frac{1}{n_o^2} + r_{13}E_o \\ \frac{1}{n_e^2(E)} &= \frac{1}{n_e^2} + r_{13}E_o \end{aligned} \tag{2.20}$$

or

$$\begin{aligned} n_o(E) &= n_o - \frac{1}{2}n_o^3 r_{13}E \\ n_e(E) &= n_e - \frac{1}{2}n_e^3 r_{33}E \end{aligned} \tag{2.21}$$

Approximations $r_{13}E \ll 1/n_o^2$ and $r_{33}E \ll 1/n_e^2$ have been used in Eq. 2.21.

The difference between the two indexes (Δn, birefringence) is expressed as:

$$\Delta n = n_e - n_o \tag{2.22}$$

As shown in Fig. 2.8, the light beam travels along the y-axis incident normally on the sample, i.e. normal to the optical axis of the sample. The refractive indexes for the waves travelling in the ceramic sample n_1 and n_3 are determined to be $n_o(E)$ and $n_e(E)$, respectively. Therefore, the phase retardation Γ becomes:

$$\Gamma = \frac{2\pi L}{\lambda}(n_3 - n_1) = \frac{2\pi L}{\lambda}[(n_e - n_o) - \frac{1}{2}(n_e^3 r_{33} - n_o^3 r_{13})E_o] \tag{2.23}$$

Define the effective EO coefficient r_c as (Aillerie, 2000):

$$r_c = r_{33} - r_{13} \cdot n_o^3 / n_e^3 \tag{2.24}$$

Eq. 2.23 becomes:

$$\Gamma = \frac{2\pi L}{\lambda}[(n_e - n_o) - \frac{1}{2} r_c n_e^3 E_o] \tag{2.25}$$

To improve the precision, a lock-in detection technique is utilized during the measurement. A small AC voltage is applied to the sample:

$$E_o = \frac{V_o}{d}\sin \omega t \tag{2.26}$$

where V_o is the amplitude of applied voltage and d is the gap between coplanar electrodes. Then Γ can be given by:

$$\Gamma = \Gamma_0 - \Gamma_m \sin \omega t \tag{2.27}$$

where

$$\Gamma_0 = \frac{2\pi L}{\lambda}(n_e - n_o), \quad \Gamma_m = \frac{\pi L}{\lambda}\frac{n_e^3 r_c V_o}{d} \tag{2.28}$$

The detect signal is then:

$$V_s = \frac{GI_{in}}{2}[1+\cos(2\gamma-\Gamma_0+\Gamma_m\sin\omega t)] = \frac{GI_{in}}{2}[1+\cos(2\gamma'+\Gamma_m\sin\omega t)] \tag{2.29}$$

where $2\gamma' = 2\gamma - \Gamma_0$. According to the Jacobi-Anger expansion and Bessel functions, Eq. 2.29 can be approximated as:

$$V_s = \frac{GI_{in}}{2}(1+\cos 2\gamma' - \Gamma_m \sin 2\gamma' \sin\omega t) \tag{2.30}$$

Then the dc component $V_{s,dc}$ and ac component $V_{s,ac}$ of the detected signal are:

$$\begin{aligned} V_{s,dc} &= \frac{GI_{in}}{2}(1+\cos 2\gamma') = GI_{in}\cos^2\gamma' \\ V_{s,ac} &= -\frac{GI_{in}}{2}\Gamma_m \sin 2\gamma' \sin\omega t = V_{s,ac,o}\sin\omega t \end{aligned} \tag{2.31}$$

In the measurement, the analyzer will be rotated by 360°, in a step of 2°, i.e. γ as well as γ' will vary from 0 to 360°. By the measurements of the difference between the maximum and minimum values of $V_{s,dc}$:

$$\begin{aligned} V_{s,dc,p-p} &= V_{s,dc,\max} - V_{s,dc,\min} = GI_{in} \\ V_{s,ac,p-p} &= V_{s,ac,\max} - V_{s,ac,\min} = GI_{in}\Gamma_m \end{aligned} \tag{2.32}$$

Finally Γ_m is obtained and the effective EO coefficient r_c is calculated as:

$$r_c = \frac{\lambda d}{\pi L n_e^3 V_o}\frac{V_{s,ac,p-p}}{V_{s,dc,p-p}} \tag{2.33}$$

where λ is the wavelength of laser, d is the electrode spacing, L is the thickness of sample and V_o is the applied voltage.

Chapter 3 Er-Doped KNN Ceramics

3.1 Introduction

Er-doped $K_{0.5}Na_{0.5}NbO_3$ (KNN:Er-x, x = 0, 1, 2, 3, 4, 5) ceramics have been successfully fabricated by the SSR method as introduced in chapter 2. The optimum sintering temperature for obtaining dense KNN:Er-x ceramics is 1120°C. KNN ceramics are chosen as the host material because of high chemical, mechanical and thermal stability (Lin, 2007e), as well as the similar ionic size between K^+, Na^+ and Er^{3+} ions. Ln-doping (such as Er) is of great importance in controlling the crystallographic phases (Wang, 2010a) and tuning PL properties of the luminescent materials (Heer, 2004). The variation of crystal structure of the host changes the crystal field around the dopant ions, resulting in influencing the optical properties (Patra, 2003, Yi, 2004).

In this chapter, the PL properties of KNN:Er-x ceramics, including the up-conversion Vis emissions, down-conversion NIR and MIR emissions, emission colors, lifetimes of each energy level of Er^{3+} ions and energy transfer (ET) processes have been systemically investigated. By adjusting the Er contents and different combinations between Er and KNN host, the crystallographic phases, emission spectra, ET processes, emission colors and emission lifetimes can be effectively modulated in the ceramics. As a kind of lead-free ferroelectrics, the dielectric, ferroelectric and piezoelectric properties of KNN:Er-x ceramics have also been studied.

3.2 Structural properties

3.2.1 XRD

Fig. 3.1a shows the XRD patterns of KNN:Er-*x* (*x* = 0, 1, 2, 3, 4, 5) ceramics. All the ceramics possess the perovskite structure, indicating that Er^{3+} ions have successfully diffused into the KNN host lattice. A small amount of impurity phases $K_{5.75}Nb_{10.85}O_{30}$ (JCPDS No. 38-0297) and $ErNbO_4$ (JCPDS NO. 22-1095) exist in the ceramics especially for $x \geq 4$. The $K_{5.75}Nb_{10.85}O_{30}$ phase may be due to the "deficiency" of Er^{3+} ions. For maintaining the charge neutrality, one Er^{3+} is substituted for three A-site ions. According to the ionic radius: K^+ (1.51 Å, coordination number (CN) = 8), Na^+ (1.18 Å, CN = 8) and Er^{3+} (1.004 Å, CN = 8), Er^{3+} may preferentially occupy the Na^+ sites rather than the K^+ sites. So K^+ and Nb^{5+} may then become "excessive", and thus leading to the formation of the impurity $K_{5.75}Nb_{10.85}O_{30}$ phase (Shannon, 1976). When at high Er concentration ($x \geq 4$), Er^{3+} ions can not totally diffuse into the host, leaving excess Er^{3+} together with Nb^{5+} to form the $ErNbO_4$ phase.

The enlarged (220) and (002) peaks of 2θ around 45.5 °of the KNN:Er-*x* are shown in Fig. 3.1b. At $x \leq 2$, the ceramics have an orthorhombic phase showing two distinct diffraction peaks. For the ceramics with $x > 3$, the two diffraction peaks merge together, indicating that the ceramics may transform to another phase. The lattice constants of the ceramics have then been refined using all the diffraction peaks shown in Fig. 3.1a by the Rietveld method. Both the orthorhombic and monoclinic unit cells have been used for the refinement of the KNN cell parameters, and only a small difference between the two structures is noted. In this work, a better fit between the observed and calculated diffraction patterns using the monoclinic model is obtained, giving the results together with the reliability factor R_{wp} and goodness-of-fit indicator S listed in Table 3.1. The low R_{wp} (< 15 %) and S (< 2) values denote a good fit between the observed and calculated patterns (MAUD n.d.). As *x* increases, the c/a value increases gradually and reaches a maximum value of 0.9946 at *x* = 3, suggesting that the crystal structure has transformed to a pseudo-cubic (cubic-like) phase. Similar results have been reported for La-doped KNN ceramics (Gao, 2009a).

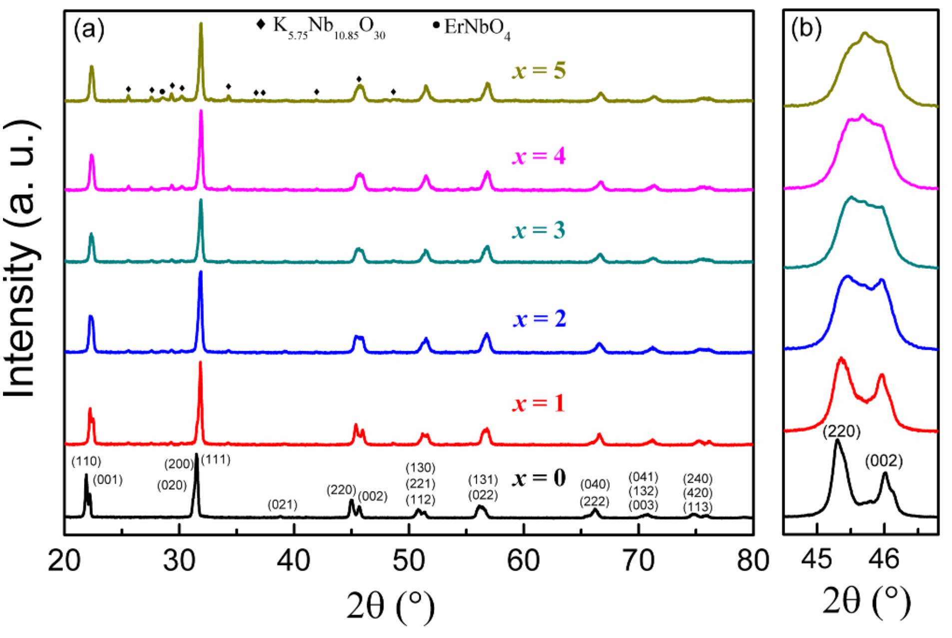

Figure 3.1 (a) XRD patterns of KNN:Er-*x* ceramics. (b) Enlarged XRD patterns.

Table 3.1 Lattice constants of KNN:Er-*x* ceramics.

x	a (Å)	b (Å)	c (Å)	β (°)	c/a	R_{wp} (%)	S
0	4.0217	3.9491	3.9775	89.90	0.9890	15.01	1.2704
1	4.0141	3.9491	3.9748	89.82	0.9902	13.46	1.4117
2	4.0024	3.9485	3.9720	89.66	0.9924	12.84	1.4306
3	3.9925	3.9486	3.9709	89.70	0.9946	13.68	1.4159
4	3.9929	3.9485	3.9642	89.68	0.9928	12.15	1.3711
5	3.9890	3.9454	3.9595	89.69	0.9926	12.90	1.4713

3.2.2 SEM

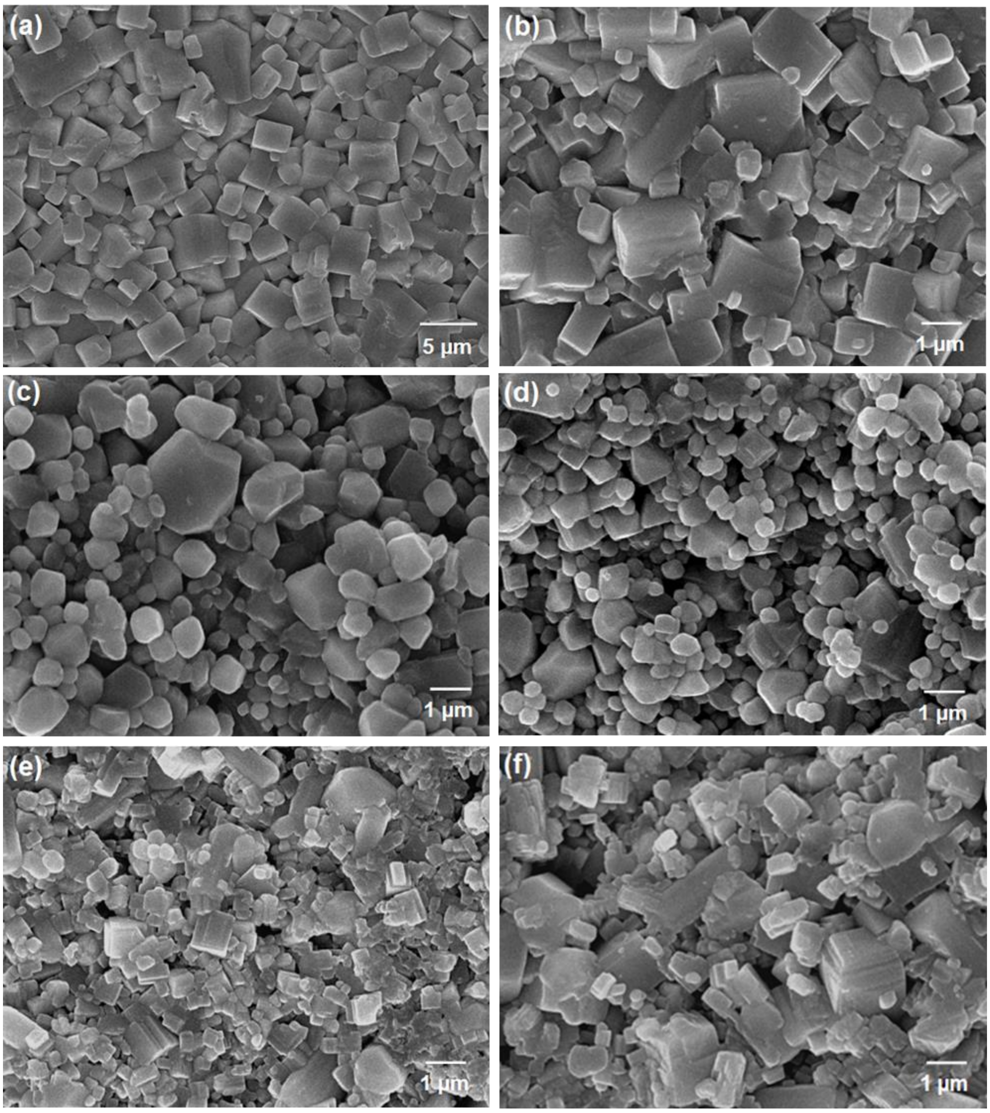

Figure 3.2 SEM micrographs of the KNN:Er-x ceramics. (a) x = 0, (b) x = 1, (c) x = 2, (d) x = 3, (e) x = 4, (f) x = 5.

The SEM micrographs of KNN:Er-x ceramics are shown in Fig. 3.2. Table 3.2 lists the average crystalline grain sizes. The pure KNN (x = 0) ceramic is well densified, having large and rectangular grains of size ~2.6 μm (Fig. 3.2a). After doping with Er^{3+} ions ($x \leq 3$), the grains become round gradually and the size decrease significantly to

~900 nm at $x = 1$, ~660 nm at $x = 2$ and ~450 nm at $x = 3$, respectively (Figs. 3.2b-d). This should be attributed to the effects arisen from the donor-type nature of Er^{3+} on inhibiting the grain growth (Ramam, 2006). Owing to the higher valence, Er^{3+} ion acts as a donor to produce space charge (e.g. $Er_A^{\bullet\bullet}$, A = K or Na) when replacing the A-site in the KNN lattice. Cation vacancies (V_K' or V_{Na}') are then generated to balance the charge disequilibrium and bound to the impurity ion Er^{3+}. As a result, the lattice diffusion coefficient is decreased, the mass transportation is weakened, and the grain growth is suppressed (Gao, 2009a). However, as x increases to 4 and 5 (Fig. 3.2e and Fig. 3.2f), the grain size slightly increases to ~620 nm and ~670 nm and some grains combine with each other to form clusters, leaving some pores in the ceramics (especially for the ceramic with $x = 5$). This should probably be due to the impurity phase $K_{5.75}Nb_{10.85}O_{30}$ with a tetragonal tungsten bronze structure.

Table 3.2 Average grain sizes of KNN:Er-x ceramics.

x	0	1	2	3	4	5
Grain size (nm)	2600	900	660	450	620	670

3.2.3 Raman

Based on the theoretical Raman analysis of KNN ceramics and films by Kakimoto et al. (Kakimoto, 2005) and Nakashima et al. (Nakashima, 2007), the KNN crystal has the space group of $Amm2\text{-}C_{2v}^{14}$ with Raman-active optical modes of $4A_1 + 4B_1 + 3B_2 + A_2$. According to the model by Ross (Ross, 1970), the vibration modes of NbO_6

octahedron consist of $1A_{1g}$ (Raman) + $1E_g$ (Raman) + $2F_{1u}$ (infrared) + F_{2g} (Raman) + F_{2u} (inactive), which can be deeply decomposed into two pure bond stretching of symmetry A_{1g} (ν_1) and E_g (ν_2), two inter-bond angle bending vibration of F_{2g} (ν_5) and F_{2u} (ν_6), and two F_{1u} stretching (ν_3) and bending (ν_4) vibration modes.

The Raman spectra of the KNN:Er-*x* ceramics are shown in Fig. 3.3. All the ceramics exhibits three main scattering peaks at 258 cm^{-1} (ν_5), 614 cm^{-1} (ν_1) and 860 cm^{-1} ($\nu_1 + \nu_5$), respectively. Probably due to the similar ionic radius of Er^{3+} and Na^+, the scattering peak ν_1 does not shift towards higher frequencies (Kakimoto, 2005). Moreover, no splitting of the coupled peak (ν_1 + ν_5) is observed, suggesting that the secondary phases detected in XRD measurement are of insignificant amount (Ahn, 2010). Raman-active optical modes of KNN comprise translational modes of cations and internal modes of NbO_6 octahedra. It has been shown that a substitution of A-site ions with a smaller (lighter) ion will shorten the distance between Nb^{5+} and its coordinated oxygen atoms, causing an increase in the binding strength and then a shift of the ν_1 stretching mode to higher frequencies (Kakimoto, 2005). On the other hand, impurity phases will induce a splitting of the coupled peak (ν_1 + ν_5) (Ahn, 2010). In addition, weak scattering peaks can also be observed at 427 cm^{-1} when $x > 0$, which are arisen from the $^2H_{11/2} \rightarrow {}^4I_{15/2}$ hypersensitive transition ($\Delta J = 2$) of the Er^{3+} ions that will be discussed later (Wen, 2008).

As also shown in Fig. 3.3, the maximum phonon energy for the KNN:Er-*x* ceramics is 860 cm^{-1}, which is lower than those of borate (1400 cm^{-1}), phosphate (1200 cm^{-1}), silicate (1100 cm^{-1}), and germinate (900 cm^{-1}) (Pollnau, 2008). According to the Eq. 1.9, the multi-phonon relaxation rate W_p is determined by the maximum phonon energy of the host. A lower $\hbar\omega_{max}$ leads to a slower W_p, and thus increasing the populations of some excited levels and then the probability of radiative emission from those excited levels. Therefore, KNN host is a good candidate for achieving superior PL properties when doped with RE ions.

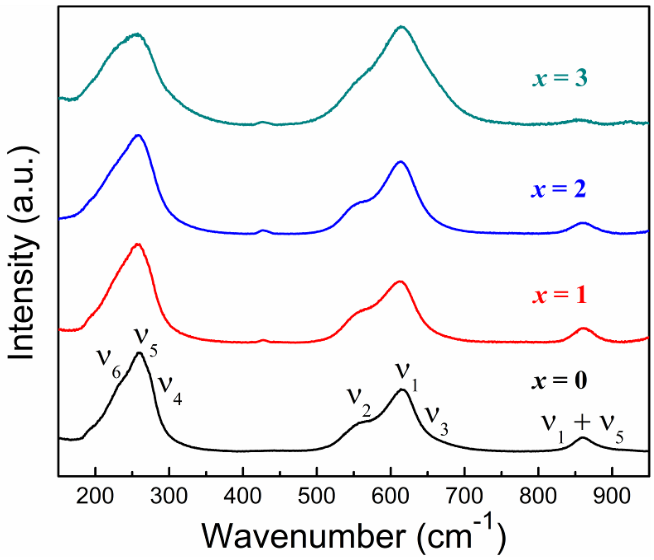

Figure 3.3 Raman spectra of KNN:Er-x (x = 0, 1, 2, 3) ceramics excited by 488 nm.

3.3 PL properties

3.3.1 Vis emissions

Fig. 3.4 shows the Vis up-conversion emission spectra of the KNN:Er-x (x = 1, 2, 3, 4, 5) ceramics under the 980 nm at power ranging from 0.19 to 1.4 W. There are three emission bands for all the ceramics: green emissions in 510-537 nm, green emissions in 537-585 nm, and red emissions in 640-690 nm, which are attributed to the transitions $^2H_{11/2} \rightarrow {}^4I_{15/2}$, $^4S_{3/2} \rightarrow {}^4I_{15/2}$ and $^4F_{9/2} \rightarrow {}^4I_{15/2}$, respectively (Figs. 3.4a-e). At each power, the PL spectra varies slightly in shape as x increases from 1 to 2 (Fig. 3.4a and Fig.

3.4b), and then significantly at higher *x* (Figs. 3.4c-e). This should be attributed to the change of the crystal field around Er^{3+} arisen from the orthorhombic to cubic-like phase transformation. The intensity for each emission band has been integrated and plotted as a function of the pumping power in the insets of Fig. 3.4. Based on the theoretical consideration of the multi-photon absorption process, the relationship between the intensity I and pumping power P can be represented by a power law (Pollnau, 2000):

$$I \propto P^n \tag{3.1}$$

where n is the number of photons required for the up-conversion process. For each ceramic, a straight line with a positive slope (i.e., n) is obtained for each emission band in the log-log plot shown in the insets of Fig. 3.4. As shown in the inset of Figs. 3.4a and 3.4b, the observed n for the two green emission bands of the ceramics with $x \leq 2$ is close to 2.0, indicating a two-photon process of the up-conversion PL (Auzel, 2004). However, it decreases to nearly 1.0 at higher *x* (insets of Figs. 3.4c-e). Similar results have been reported for Er-doped $YAlO_3$ (Szachowicz, 2006), Er-doped fluorozirconate glasses (Henke, 2010) and Er-doped PMN-PT transparent ceramics (Zeng, 2012). This should be ascribed to the concentration-quenching effect and the orthorhombic to cubic-like phase transformation of the host material. Probably due to the weaker asymmetry, the cubic-like crystal structure may not be favor for the two-photon process. For all the ceramics, the observed n for the red emission is smaller than those for the green emission bands, suggesting that the red emission is a mixture of the one- and two-photon processes, with the one-photon process being dominant (Chen, 2012).

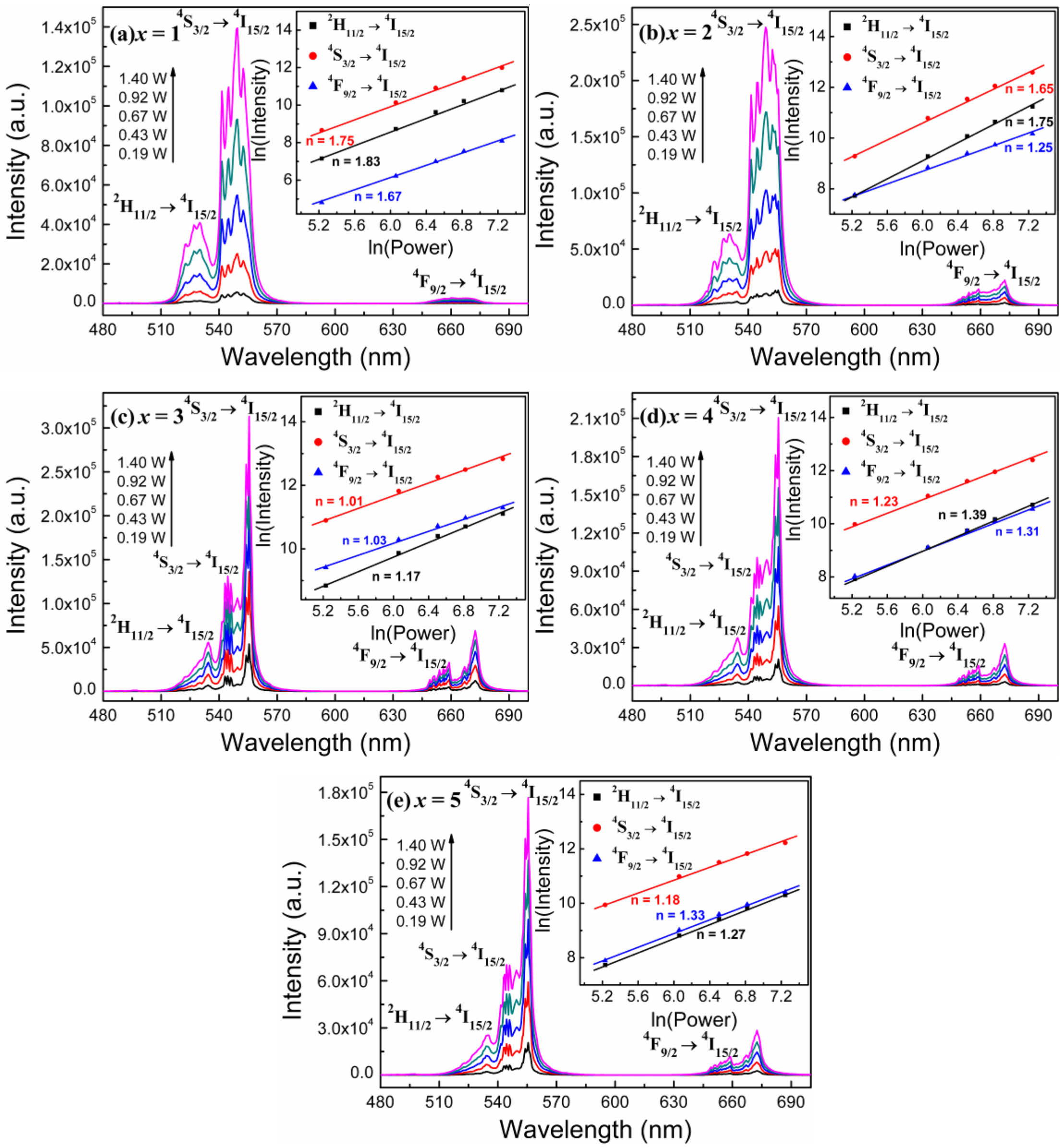

Figure 3.4 Vis up-conversion emission spectra of the KNN:Er-*x* ceramics under the 980 nm laser excitation with powers ranging from 0.19 to 1.4 W. (a) *x* = 1, (b) *x* = 2, (c) *x* = 3, (d) *x* = 4, (e) *x* = 5. The insets of each figure are emission intensities log-log plotted against the laser powers.

The Commission Internationale de L'Eclairage (CIE) color coordinates (X, Y) of the KNN:Er-*x* ceramics calculated from the up-conversion emission spectra at 1.4 W are shown in Fig. 3.5. The CIE coordinate of all the ceramics locates in the yellowish green region, and shows a red shift from (0.267, 0.7163) at x = 1 to (0.3048, 0.6827) at x = 5. It has been shown that the color of the up-conversion emission is primarily based on the combination of the host and dopant (i.e., KNN and Er) (Yi, 2006), the dopant concentration (i.e., x) (Yang, 2009), and the physical size of the host (i.e., the grain size of the ceramics) (Bai, 2007).

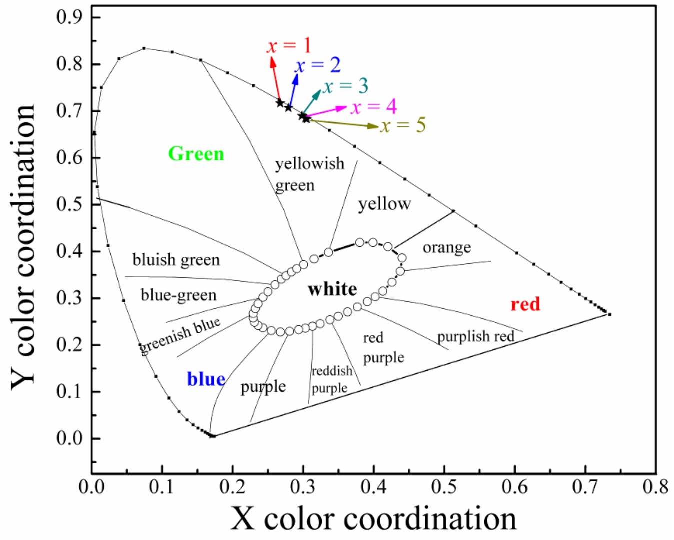

Figure 3.5 CIE color coordinates of the KNN:Er-x ceramics calculated from the up-conversion emission spectra.

The decay curves of up-conversion PL originating from the energy levels $^2H_{11/2}$, $^4S_{3/2}$ and $^4F_{9/2}$ of Er^{3+} ions are shown in Fig. 3.6. Probably due to the energy transfer process, the fluorescence decay curves become slightly non-exponential. Nevertheless, the average luminescent lifetime $\overline{\tau}$ can be calculated based on the following equation:

$$\overline{\tau} = \frac{\int_0^\infty I(t)tdt}{\int_0^\infty I(t)dt} \tag{3.2}$$

where I(t) is the PL intensity at a time t after the cutoff of the 980-nm excitation, The calculated $\bar{\tau}$ of the KNN:Er-*x* ceramics are listed in Table 3.3. It can be seen that the calculated $\bar{\tau}$ for the two green emission bands (Fig. 3.6a and Fig. 3.6b) is close to 100 μs without large change, while that for the red emission band (Fig. 3.6c) changes greatly between 100 and 200 μs. It has been reported that the lifetime can be reduced significantly via the enhanced energy transfer process between the dopant ions resulting from the increase of the dopant concentration (Ting, 2013). However, as shown in Fig. 3.6d, the calculated $\bar{\tau}$ for all the three emission bands increases abruptly as *x* increases from 2 to 3. This should be attributed to the phase transformation of the ceramics from orthorhombic at $x \leq 2$ to cubic-like at $x \geq 3$, suggesting that the crystal structure is a decisive factor for the decay lifetime. Similar results have been reported for the Eu-doped zirconia samples (Hui, 2013).

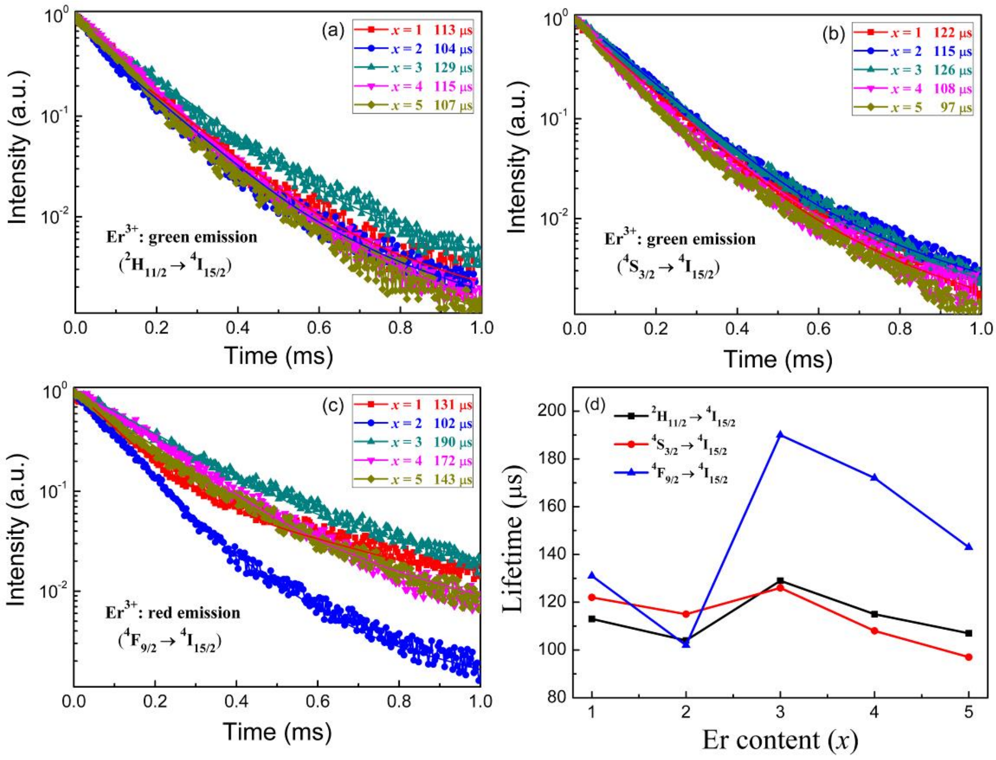

Figure 3.6 Up-conversion PL decay curves originating from different energy levels of Er^{3+} ions. (a) Green emissions of $^2H_{11/2} \rightarrow {}^4I_{15/2}$. (b) Green emissions of $^4S_{3/2} \rightarrow {}^4I_{15/2}$. (c) Red emissions of $^4F_{9/2} \rightarrow {}^4I_{15/2}$. (d) Er content dependence on decay lifetimes of KNN:Er-*x* ceramics for the three emissions.

Table 3.3 Decay times obtained by 980 nm laser for the excitation and by monitoring the emissions for KNN:Er-*x* ceramics.

x	Green emissions		Red emission	NIR emission
	$^2H_{11/2} \rightarrow {}^4I_{15/2}$	$^4S_{3/2} \rightarrow {}^4I_{15/2}$	$^4F_{9/2} \rightarrow {}^4I_{15/2}$	$^4I_{13/2} \rightarrow {}^4I_{15/2}$
1	113 μs	122 μs	131 μs	16.8 ms
2	104 μs	115 μs	102 μs	8.0 ms
3	129 μs	126 μs	190 μs	5.1 ms
4	115 μs	108 μs	172 μs	6.2 ms
5	107 μs	97 μs	143 μs	7.3 ms

3.3.2 NIR emissions

Fig. 3.7 shows the NIR emission spectra and decay curves of the KNN:Er-*x* ceramics. For each ceramic, the emission band locates at ~ 1.55 μm and exhibits clear spitting due to the Stark effect (Fig. 3.7a). The ceramics with $x = 2$ and 3 exhibit the highest PL intensities, while the KNN:Er-1 ceramic shows an emission spectra of different shapes. This should be attributed to the enhanced energy transfer processes between Er^{3+} ions arisen from the shortening of the interionic distance in the ceramics with higher *x*. The broadband emission is reabsorbed by the neighboring Er^{3+} ions, and thus increasing the PL intensity and changing the shape of the spectra (Wu, 2007). All the decay curves of the ceramics shown in Fig. 3.7b can be fitted to a single exponential decay function by Eq. 1.6. As x increases from 1 to 3, the calculated τ decreases from 16.8 ms to 5.1 ms, and then increases slightly to 7.3 ms at $x = 5$. The NIR emissions have long rise and decay times. The exponential characteristics of decay kinetics signify that the energy migration among Er^{3+} ions is noteworthy (Lisiecki, 2011). Although Er^{3+} ions are incorporated into different crystalline phases (orthorhombic or cubic-like phases), the decay behavior still follows the single exponential function. It can then be inferred that the total relaxation rates of the optically active Er^{3+} ions are similar in various crystalline structures of the KNN host.

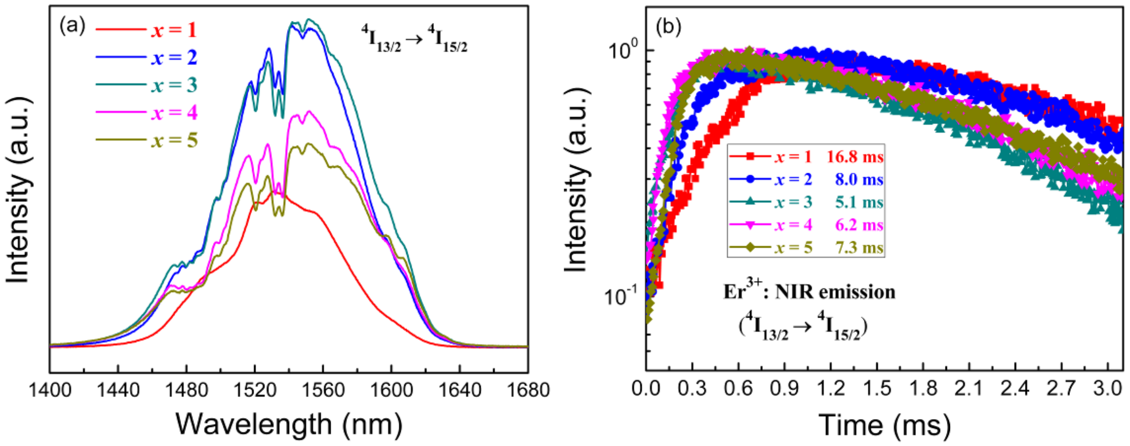

Figure 3.7 (a) NIR emission spectra of the KNN:Er-x ceramics. (b) NIR emission decay curves of the KNN:Er-x ceramics.

3.3.3 MIR emissions

The MIR emission spectra of the KNN:Er-x ceramics are shown in Fig. 3.8. All the emission bands are broad and split into a number of components (four for the ceramics with x = 1 to 2 and five for those with x = 3 to 5). The KNN:Er-2 ceramic has the highest PL intensity. Probably due to the change of the crystal field around Er^{3+} induced by the phase transformation, the emission peaks at ~2638 nm and ~2679 nm become more obvious for the ceramics with $x \geq 3$.

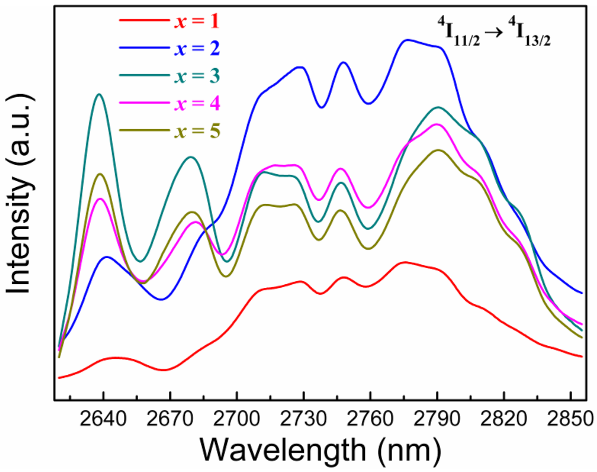

Figure 3.8 MIR emission spectra of the KNN:Er-x ceramics.

3.3.4 PL mechanism

As evidenced by the above results, the considerable decrease in the Er-Er distance as well as the change of the crystalline structure (in the ceramics with higher x) is beneficial for the energy transfer processes and then enhancing the PL properties of the KNN:Er-x ceramics. Fig. 3.9 shows the energy level diagram of Er^{3+} ions and the relevant energy transfer (ET) mechanism. Upon the pumping with a 980-nm laser, Er^{3+} ions are first excited from the $^4I_{15/2}$ ground state to the $^4I_{11/2}$ level by the ground state absorption (GSA) process. Some of the Er^{3+} ions in the $^4I_{11/2}$ level will undergo an excited state absorption (ESA) process to populate the $^4F_{7/2}$ level. Subsequently, multi-phonon relaxation (MPR) occurs, resulting in the populations of the $^2H_{11/2}$, $^4S_{3/2}$, and $^4F_{9/2}$ levels, and thus leading to the up-conversion green emissions ($^2H_{11/2}/^4S_{3/2} \rightarrow {}^4I_{15/2}$) and red emission ($^4F_{9/2} \rightarrow {}^4I_{15/2}$) by radiatively relaxation. These mechanisms are consistent with the two-photon process of producing the up-conversion green and red emissions, especially for the materials with a low dopant concentration (Adhikari, 2014). In addition, the $^4F_{9/2}$ level can be further populated for enhancing the red emission by a cross relaxation (CR1) process: $^4F_{7/2} + {}^4I_{11/2} \rightarrow {}^4F_{9/2} + {}^4F_{9/2}$ (Kishi, 2005). Some Er^{3+} ions in the $^4I_{11/2}$ level will relax to the $^4I_{13/2}$ level non-radiatively or radiatively via the generation of the 2.7-μm MIR emission. Most of the Er^{3+} ions in the $^4I_{13/2}$ level will eventually relax radiatively to the $^4I_{15/2}$ level, generating the 1.55-μm NIR emission.

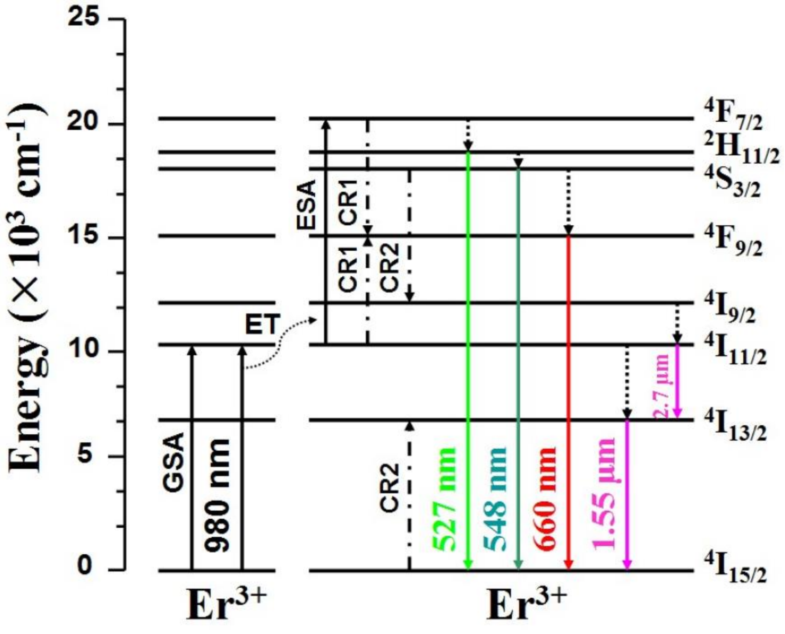

Figure 3.9 Energy levels diagram of Er^{3+} ions.

Fig. 3.10 compares the relative integrated intensities of the green, red, NIR and MIR emission bands at different Er contents for the KNN:Er-*x* ceramics. For all the emission bands, the observed intensity increases and then decreases with increasing x, reaching a maximum value at $x = 2$ (green and MIR) or 3 (red and NIR). Probably due to the increased population of the $^4F_{9/2}$ level arisen from the CR1 process (Fig. 3.9), the intensity enhancement of the red emission band becomes the largest, reaching more than 10 times at $x = 3$. The decrease in the PL intensity should be due to the concentration-quenching effect, revealing the enhanced non-radiative energy transfer process induced by the shortening distance between Er^{3+} ions in the ceramics with high x. For the ceramics with low Er concentrations (e.g., $x = 1$), the interionic distance between Er^{3+} ions is large and the ESA process is preferable, and thus leading to a high population of the $^4F_{7/2}$ level and then the strong $^2H_{11/2} \rightarrow {}^4I_{15/2}$ green emission. As most of the Er^{3+} ions are further excited to the higher energy levels, the populations of the $^4I_{11/2}$ or $^4I_{13/2}$ levels are small. In addition to the low photon transition probability and quantum efficiency, both the NIR and MIR emissions become very weak.

For the ceramics with high x (e.g., $x = 3$), the CR1 process becomes more important, and thus leading to a further increase of the red emission intensity at the expense of the two green emissions. On the other hand, the CR2 process ($^4S_{3/2} + {}^4I_{15/2} \rightarrow {}^4I_{9/2} + {}^4I_{13/2}$, Fig. 3.9) populates the $^4I_{9/2}$ and $^4I_{13/2}$ levels, and subsequently enhances the NIR and MIR emissions. As a result, the PL intensities of the NIR and MIR emission bands remain high even for the ceramics with concentrations higher than the quenching concentration (2 mol%). The continuous pumping of the $^4I_{13/2}$ level may also cause the observed lifetime of the NIR emission band become artificially longer, giving the abnormal increase at $x \geq 3$.

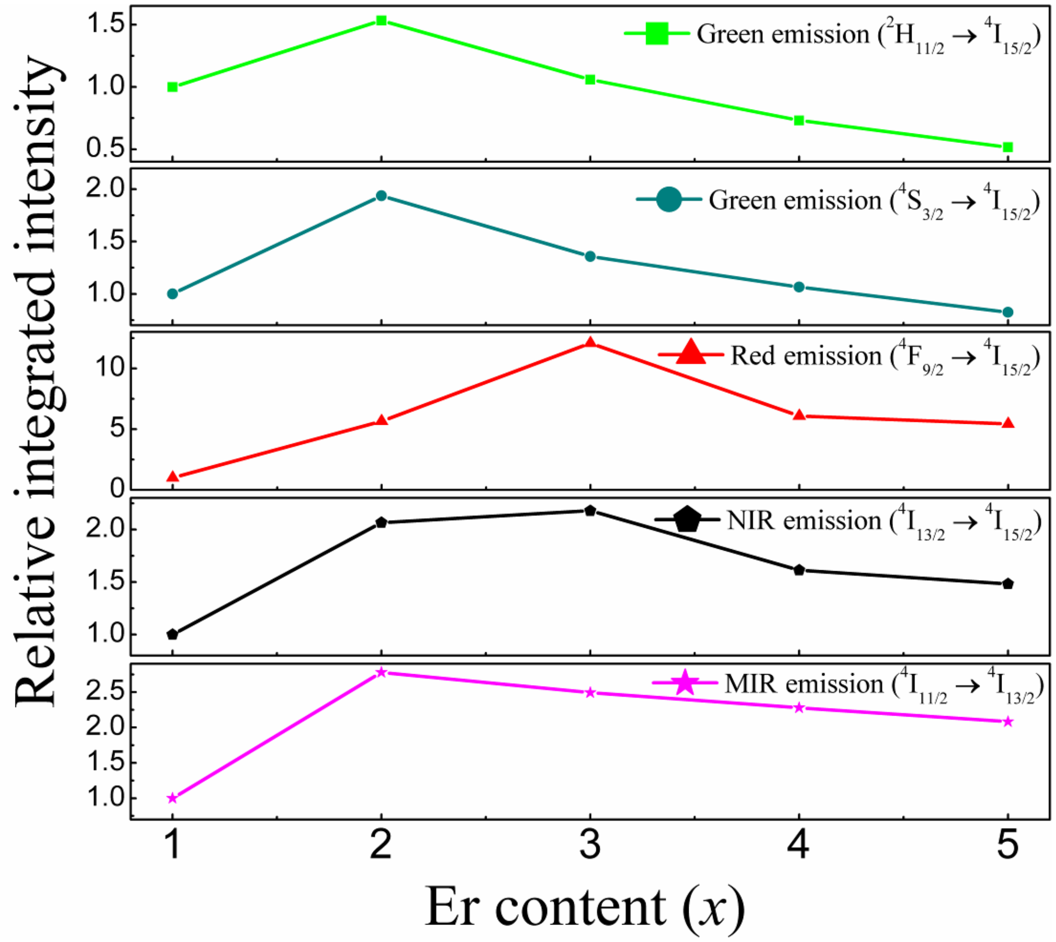

Figure 3.10 Variations of relative integrated intensities of the green, red, NIR and MIR emission bands with different Er contents for the KNN:Er-*x* ceramics.

The PL intensity, energy transfer processes, emission colors and lifetimes of a PL material are generally governed by the concentration-quenching effect and the symmetry of the local crystal field at the lattice sites of activators (Ting, 2013). The Er^{3+} dopants in the KNN:Er-*x* ceramics serves mainly as the activators for the emissions at various wavelengths. The PL emissions of Er^{3+} ions arise primarily from the intra-configurational $4f^n$-$4f^n$ electronic transitions. Owing to the shielding provided by the filled $5s^2$ and $5p^6$ electronic shells, the 4f electrons hardly experience interactions with the host materials (Wang, 2010b). These transitions are forbidden by the selection rules, and become allowed if the crystal symmetry of the host materials is lowered or the local symmetry around Er^{3+} is reduced (Judd, 1962). In these cases, the crystal field shifts the 5d energy level of Er^{3+}, allowing the stronger 4f-4f emissions to occur. The observed phase-dependent PL properties of the the KNN:Er-x ceramics (Fig. 3.4) should then be ascribed to the change in the crystal fields around Er^{3+} ions arisen from the phase transformation of the host material. As compared to the ceramics with $x \geq 3$ which have a cubic-like phase, the ceramics with $x \leq 2$ having an orthorhombic phase would exert a crystal field containing more uneven components because of the lower symmetry. The crystal field then enhances the electronic coupling between the 4f levels and higher electronic configurations of Er^{3+}, leading to an increase in the f-f transition probabilities (Blasse, 1994).

3.4 Electrical properties

Apart from the outstanding PL properties, KNN:Er-x ceramics also exhibit good electrical properties. Fig. 3.11 shows the temperature dependence of the dielectric constant and dielectric loss measured at 100 kHz for the KNN:Er-x ceramics. The pure KNN ceramics exhibit a sharp cubic-tetragonal transition peak at ~400°C (T_c) and a tetragonal-orthorhombic transition peak at 222°C ($T_{O\text{-}T}$). With increasing Er content (x), the normal ferroelectric ($x = 0$) gradually change to relaxor-like ferroelectric ($x \geq 2$) as indicated by the two broadened transition peaks. Probably due to the local compositional fluctuation arisen from similar radii of A-site ions (Er^{3+}, 1.004 Å; K^+, 1.51 Å; and Na^+, 1.18 Å), diffuse phase transitions are induced in the KNN:Er-x ($x \geq 2$) ceramics, exhibiting broadened cubic-tetragonal and tetragonal-orthorhombic transition peaks. The relaxor-like characteristics of the ceramic may also be arisen from the charge imbalance produced by the substitution of Er^{3+} for $(K_{0.5}Na_{0.5})^+$. The Curie temperature T_c decreases with x increases, from 420°C ($x = 0$) to 380°C ($x = 5$), as shown in Table 3.4.

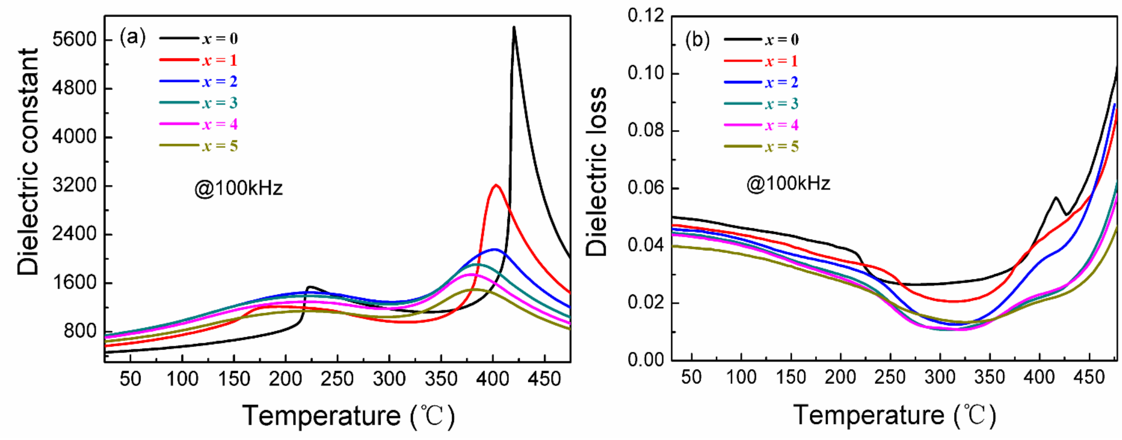

Figure 3.11 Temperature dependence of dielectric constants (a) and dielectric loss (b) measured at 100 kHz for the KNN:Er-x ceramics.

Fig. 3.12 shows the *P*-*E* loops of the KNN:Er-x ceramics measured under an electric field of 4 kV/mm at 100 Hz. KNN ceramic is a normal ferroelectric with the standard shape of polarization hysteresis loop. The remnant polarization P_r is 10.3 μC/cm^2 and coercive field E_c is 0.9 kV/mm. After doping with a small amount of Er^{3+}, i.e. KNN:Er-1 ceramic, the shape of *P*-*E* loop remains the same but P_r increase to 12.4 μC/cm^2 and E_c slight increase to 1 kV/mm. At $x \geq 2$, the ceramics exhibit flattened, slant and unsaturated polarization hysteresis loops, indicating the relaxor-like characteristics. As x increases, E_c almost remains the same while P_r decreases greatly to 4 μC/cm^2 at x =

5. The results are consistent with those as shown in Fig. 3.11, suggesting that Er-doping is effective in inducing relaxor-like characteristics in KNN ceramics.

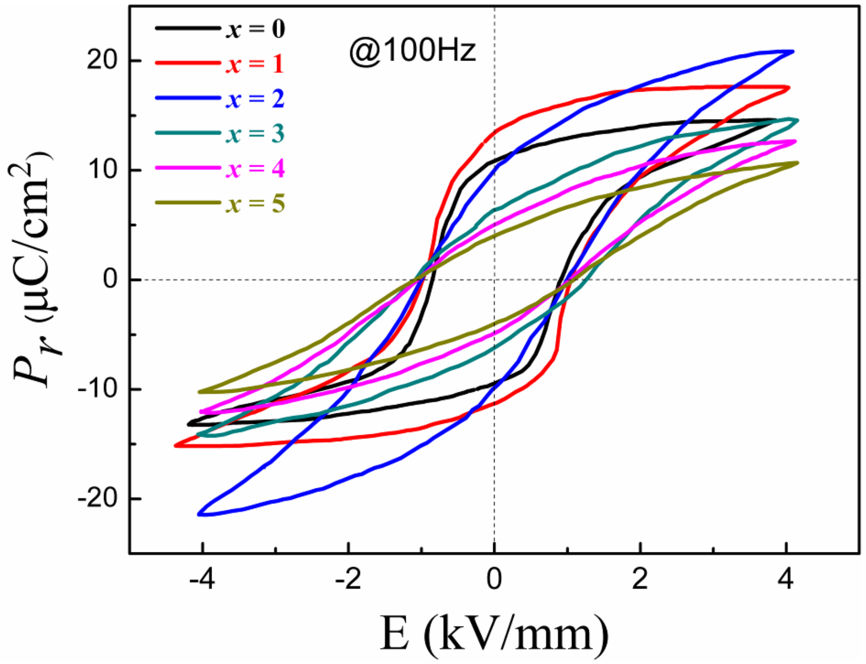

Figure 3.12 *P-E* loops for the KNN:Er-*x* ceramics measured at 100 Hz.

Table 3.4 gives the material parameters of the KNN:Er-*x* ceramics, including densities, dielectric properties and piezoelectric properties. All the ceramics have high densities (> 97.5%) except for the KNN:Er-5 ceramic, which may be due to a few pores in the ceramic as shown in the SEM image (Fig. 3.2f). The dielectric properties (ε_r and tan δ) were measured at room temperature. As x increases, ε_r increases and reaches a maximum value of 771 at $x = 3$, then decreases, while tan δ gradually decreases. Similar to tan δ, the d_{33} also decreases with increasing x, but showing a sudden drop at $2 < x < 3$. Although Er-doping has weakened the piezoelectric properties, the ceramics with $x \leq 2$ still exhibit good piezoelectric properties as well as excellent PL performances, which should find potential in the applications of optoelectronic field.

Table 3.4 Density and electrical properties for KNN:Er-*x* ceramics.

x	ρ (g/cm^3)	Relative density (%)	ε_r @1kHz	tan δ @1kHz	T_c (°C)	d_{33} (pC/N)
0	4.45	98.7	480	0.049	420	92
1	4.50	98.2	648	0.045	401	85
2	4.51	97.8	731	0.042	399	76
3	4.59	98.2	771	0.041	383	32
4	4.64	98.4	735	0.039	380	28
5	4.59	96.4	656	0.034	380	25

3.5 Conclusions

x mol% Er-doped $K_{0.5}Na_{0.5}NbO_3$ ceramics have been prepared and their luminescence and electrical properties have been studied. The ceramics possess an orthorhombic perovskite structure at $x \le 2$ and a cublic-like phase at $x \ge 3$. The Er-doping is effective in inhibiting the grain growth and reducing the grain size. Under an excitation of 980 nm, the ceramics exhibit up-conversion green and red emissions, as well as down-conversion NIR and MIR emissions. The relationships between the Vis up-conversion PL and laser power indicate an efficient two-photon process at $x \le 2$. The concentration quenching effect of Er^{3+} occurs at $x \ge 3$. As x increases, the lifetimes reduce significantly except for a sudden increase at $x = 3$ because of the formation of a cubic-like phase. Both the concentration-quenching effect and phase transition affect the energy transfer processes and PL properties, including emission intensities, colors and lifetimes. The Er-doping is also effective in inducing relax-like characteristics in KNN ceramics. At $x \leq 2$, the ceramic exhibits relatively good d_{33}, high P_r and ε_r, low tan δ, as well as outstanding PL performances. The application of them should have great potential in the optoelectronic field.

Chapter 4 Er-Doped KNLN Ceramics

4.1 Introduction

As introduced in Chapter 3, 2 mol% Er-doped KNN ceramics exhibit relatively good d_{33}, high P_r and ε_r, low tan δ, as well as PL performances. However, the properties of ceramics do not reach the optimal level and still require further improvement. Li^+ is a widely used dopant for KNN ceramics to improve their dielectric and piezoelectric properties (Guo, 2004, Singh, 2010). It has also been shown that the up-conversion emission intensities in Er-doped PL materials, such as Er-doped ZnO powders (Bai, 2008), Er-doped Sb_2O_3-Na_2O-SiO_2 glasses (Liu, 2010), and Er-doped GaAs (Uki, 2007) can be increased significantly by the co-doping of Li^+. Nevertheless, the doping effect of Li on PL properties of Er^{3+} doped ferroelectrics has seldom been reported.

In this chapter, 2 mol% Er-doped $(K_{0.5}Na_{0.5})_{1-x}Li_xNbO_3$ ceramics with x varying from 0 to 0.10 (abbreviated as Er-KNLN-x) have been prepared by the SSR method. Their PL properties, both up-conversion and down-conversion, have been studied. The effects of Li^+ on PL emissions from Vis to MIR region have been investigated. Besides for potential applications in high-power MIR solid-state lasers, these ceramics, as a multifunctional material, should be of great importance for the fundamental study of electro-mechano-optical couplings (Park, 1999) in many application fields, including future EO integrated materials and devices, photo-ferroelectric and mechanical-ferroelectric devices.

4.2 Structural properties

4.2.1 XRD

The XRD patterns of the Er-KNLN-x ceramics are shown in Fig. 4.1a. Although small amounts of secondary phases such as $K_3LiNb_6O_{17}$ (JCPDS NO. 36-0533) and $ErNbO_4$ (JCPDS NO. 22-1095) are observed, all the ceramics are of the perovskite structure, suggesting that Er^{3+} and Li^+ have diffused into the KNN lattices. Probably due to insignificant amounts, the diffraction peaks of the secondary phases for the ceramics with $x < 0.06$ are very weak. $K_3LiNb_6O_{17}$ has a completely-filled tungsten-bronze like structure (Tanaka, 1982), while $ErNbO_4$ has a fergusonite-like structure (Zhang, 2004). Unlike KNN that has a perovskite structure with a space group of Amm2-C_{2v}^{14}, $LiNbO_3$ has a heavily distorted perovskite-type structure with a space group of R_{3C} (C_{3v}^{6}) (Guo, 2004). The existence of two structures may hence affect the stability of the Er-KNLN-x phase, leading to the formation of $K_3LiNb_6O_{17}$ secondary phase, which has also been reported in other KNLN ceramics (Kim, 2011). As shown in Fig. 4.1b (the enlarged XRD patterns near 45.5°), the crystal structure of the ceramics shows a tendency of transforming from orthorhombic to tetragonal with increasing x, which should be ascribed to the large distortion caused by Li^+. Similar results have been observed for the Li-doped KNN-based ceramics (Guo, 2004). The small peaks at ~45.6° for the ceramics with $x \geq 0.06$ are attributed to the $K_3LiNb_6O_{17}$ secondary phase.

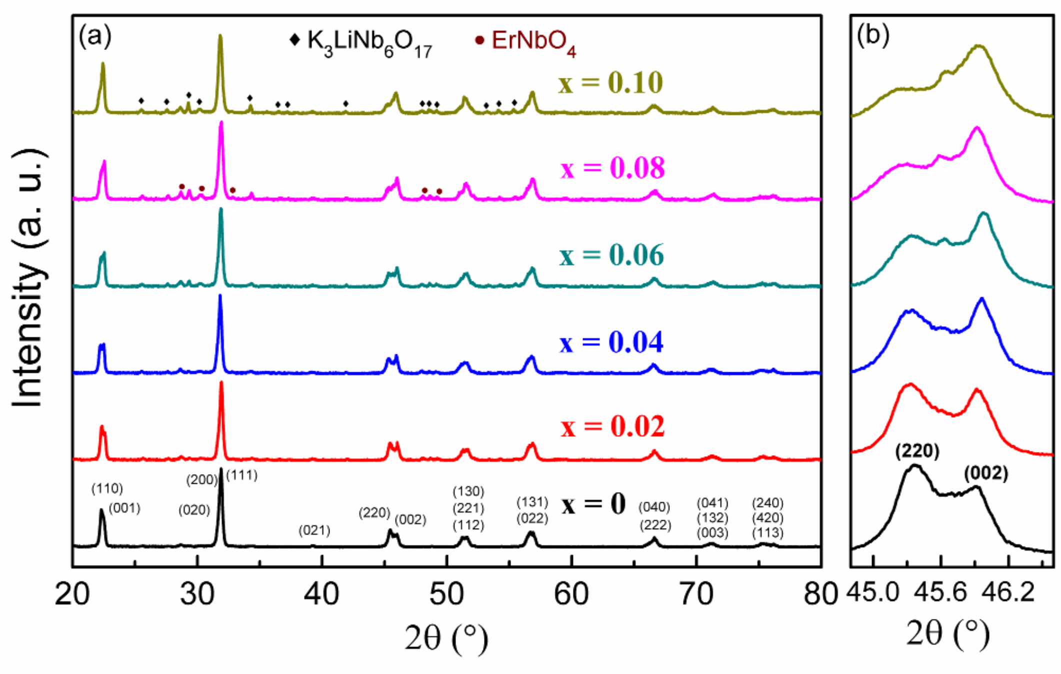

Figure 4.1 (a) XRD patterns of the Er-KNLN-x ceramics. (b) Enlarged XRD patterns near 45.5 °.

4.2.2 SEM

The SEM micrographs of Er-KNLN-x ceramics are shown in Fig. 4.2. The Li-free Er-KNLN-0 ceramic shows round crystalline grains with the grain size of 0.3-2 μm and average size of ~650 nm (Fig. 4.2a). The addition of Li transforms the grain shape to rectangular and increases the average size to ~1.5 μm (for x = 0.02 to 0.08 in Figs. 4.2b-e). With increasing the Li content, the ceramics do not exhibit obvious changes in both grain shapes and sizes, except for x = 0.10 which may be caused by the secondary phases as shown in the XRD results.

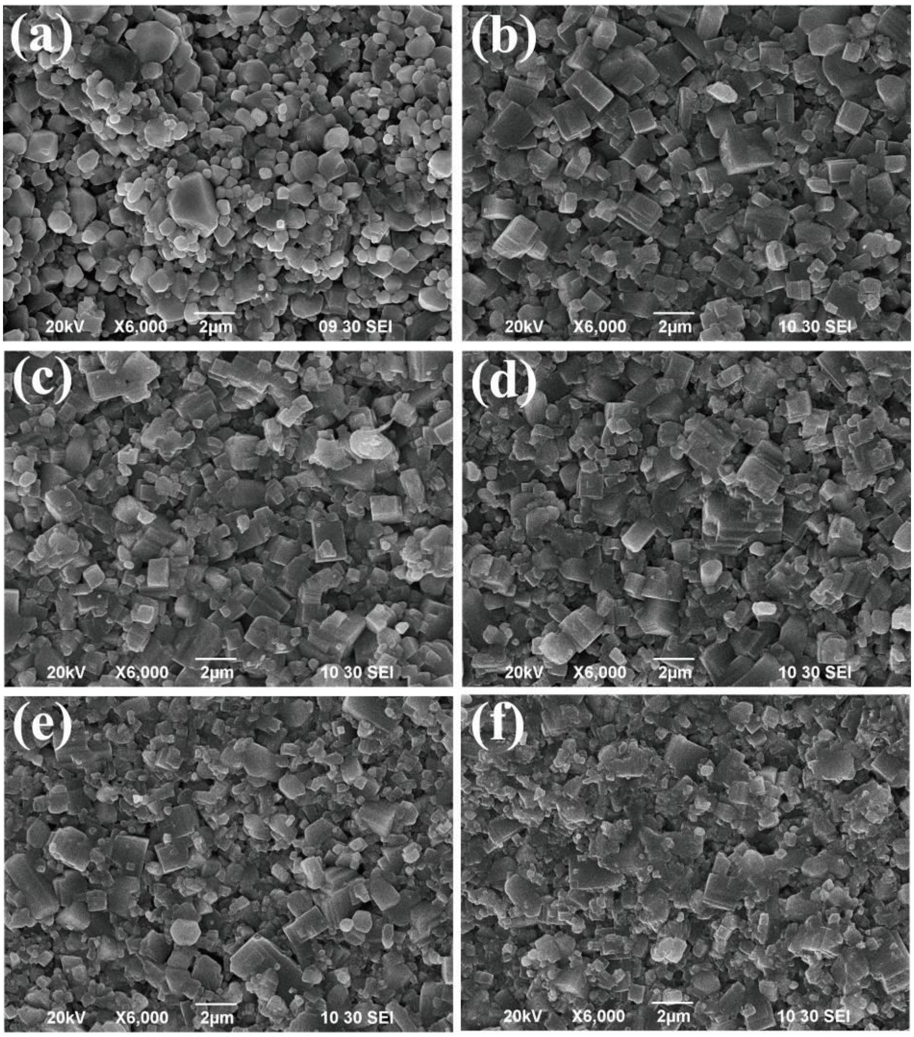

Figure 4.2 SEM micrographs of the Er-KNLN-x ceramics. (a) x = 0, (b) x = 0.02, (c) x = 0.04, (d) x = 0.06, (e) x = 0.08, (f) x = 0.10.

Table 4.1 Optimum sintering temperatures (*T*) and densities of Er-KNLN-x ceramics.

x	0	0.02	0.04	0.06	0.08	0.10
T (°C)	1120	1100	1090	1080	1070	1060
ρ (g/cm^3)	4.51	4.42	4.38	4.34	4.39	4.28
Relative density (%)	97.4	96.1	95.8	95.6	97.3	95.5

Table 4.1 gives the optimum sintering temperatures and densities of the Er-KNLN-

x ceramics. The optimum sintering temperature of the ceramics is slightly reduced by the doping of Li^+. The relative densities of Er-KNLN-x ceramics are lower than those of KNN:Er-*x* ceramics shown in Table 3.4. This is probably due to the inhomogeneity of grains and pores as illustrated in the SEM micrographs.

4.3 PL properties

4.3.1 Vis up-conversion PL spectra

The Vis up-conversion PL emission spectra of the Er-KNLN-x ceramics are shown in Fig. 4.3. Similar to the KNN:Er-*x* ceramics and other Er-doped PL materials (Chen, 2007, Zhang, 2004), all the Er-KNLN-x ceramics exhibit two green emission bands (515-537 nm and 537-570 nm) and one red emission band (640-685 nm) under the excitation of 980 nm, which are attributed to the transitions $^2H_{11/2} \rightarrow {}^4I_{15/2}$, $^4S_{3/2} \rightarrow {}^4I_{15/2}$ and $^4F_{9/2} \rightarrow {}^4I_{15/2}$, respectively (Fig. 4.4). Clear Stark-splitting is observed, revealing the interaction between Er^{3+} ions and the host. No shifting of the split peaks is observed. It has been observed that the intensity of the emission band centered at 550 nm is very strong and a bright green spot on the irradiated surface of the ceramics can be easily observed by naked eyes during the measurements.

The mechanism of up-conversion PL has been elaborated in Chapter 3, including GSA, ESA, MPR, CR1 and emission processes. However, the emission wavelengths of Er-KNLN-x ceramics are a bit different from that of the KNN:Er-*x* ceramics. As the energy gap between $^2H_{11/2}$ and $^4S_{3/2}$ is the smallest, the MPR rate for $^2H_{11/2} \rightarrow {}^4S_{3/2}$ is the fastest (Zhao, 2005), and thus resulting in the largest number of Er^{3+} ions in the $^4S_{3/2}$

level and the highest PL intensity of the green emission (537-570 nm). On the other hand, the MPR rate for $^4S_{3/2} \rightarrow {}^4F_{9/2}$ is the lowest, and then the PL intensity of the resulting red emission should be very weak. However, CR1 process may occur to populate the $^4F_{9/2}$ level, leading to certain red emission.

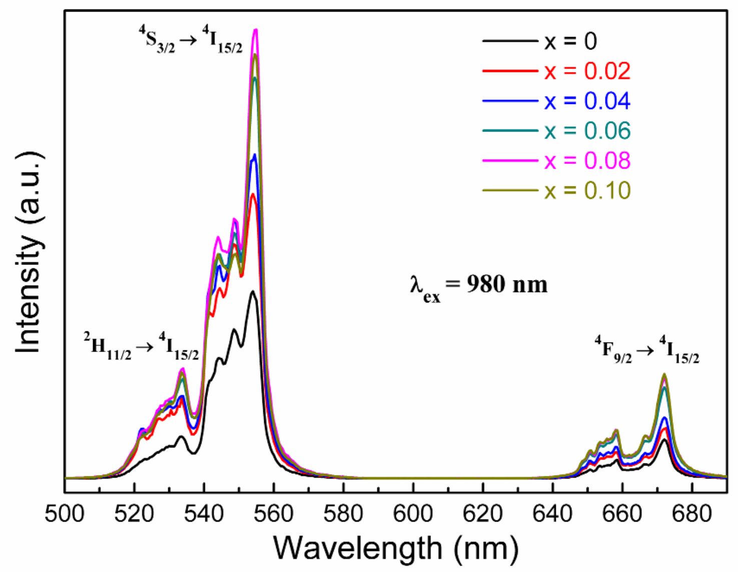

Figure 4.3 Vis up-conversion PL spectra of Er-KNLN-x ceramics by 980 nm excitation.

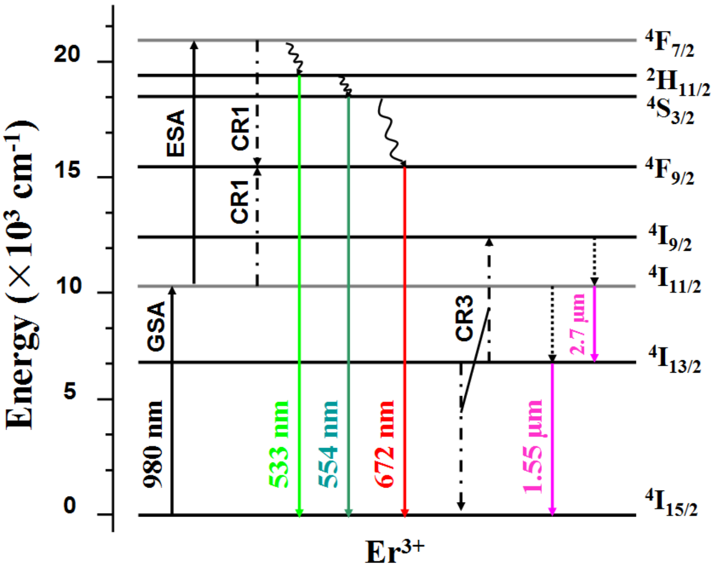

Figure 4.4 The schematic diagram for the PL mechanism of Er^{3+} ions in the Er-KNLN-x ceramics.

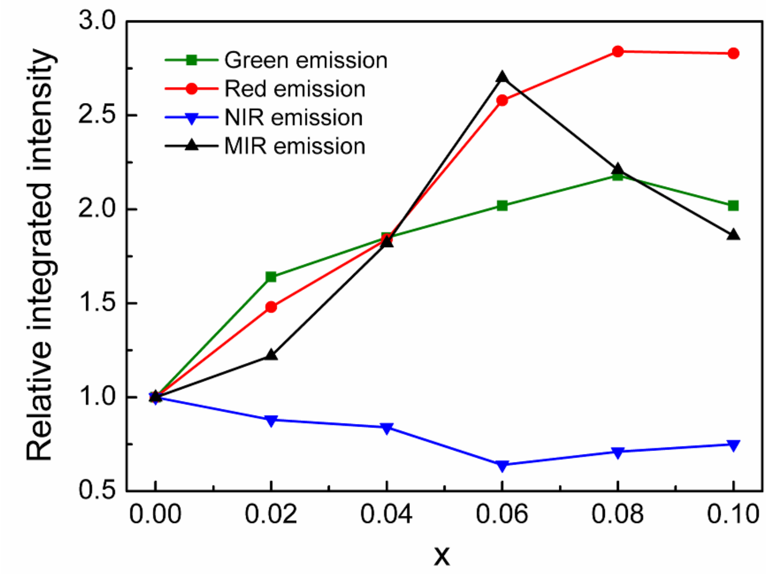

Figure 4.5 The variations of the relative integrated intensities of emission bands with x (molar fraction of Li) for the Er-KNLN-x ceramics under 980 nm excitation.

The Li-doping is effective in enhancing the Vis up-conversion PL of the Er-KNLN-x ceramics. The variations of the relative integrated intensities of the green (515-570 nm) and red (640-685 nm) emission bands with x (molar fraction of Li) for the Er-KNLN-x ceramics are shown in Fig. 4.5. The intensities of both the green and red emission bands increase with increasing x, and become almost saturated at $x \geq 0.08$. It can also be seen that the enhancement in the red emission is stronger, in particular at $x > 0.04$, than that in the green emission. These may be due to the change in the crystal field around Er^{3+} ions arisen from the doping of Li^+ (Bai, 2008). According to the Judd-Ofelt theory developed for explaining the ligand field of rare earth ions (Judd, 1962, Ofelt, 1962), the probabilities and then the PL intensities of the two green emissions $^2H_{11/2} \rightarrow {}^4I_{15/2}$ and $^4S_{3/2} \rightarrow {}^4I_{15/2}$ for Er^{3+} are dependent on intensity parameter Ω_2 and Ω_6, respectively (Weber, 1967) while those of the red emission $^4F_{9/2} \rightarrow {}^4I_{15/2}$ are determined by two intensity parameters Ω_4 and Ω_6 (Weber, 1967). Jorgensen and Reisfeld have shown that Ω_2 can be increased by decreasing the symmetry between Er^{3+} ions and the ligand field, while Ω_6 is increased by decreasing the covalence between Er^{3+} ions and the hosts (Jorgensen, 1983). On the other hand, it has been reported that the bond length of Er-O can be increased by Li^+ ions (Liu, 2010). The Li-doping may also change the dimensions of the other bonds, such as K-O, Na-O and Nb-O. The local environment of Er^{3+} ions in the host may hence be distorted, leading to a decrease in the symmetry between Er^{3+} ions and the ligand field as well as a decrease in the covalence between Er^{3+} ions and the host. The changes obviously increase with increasing the molar fraction of Li. These are consistent with the XRD results that reveal a structure transformation induced by the large distortion arisen from the Li-doping (Fig. 4.1b). As a result of the decreases in the symmetry and covalence, both Ω_2 and Ω_6 increase, causing the enhancements in the PL intensities of the green as well as the red emission bands.

4.3.2 Vis down-conversion PL spectra

For comparison purpose, the Vis down-conversion PL emission spectra of the Er-KNLN-x ceramics have been measured, giving the results shown in Fig. 4.6. Similar to the up-conversion spectra, the green emission ($^4S_{3/2} \rightarrow {}^4I_{15/2}$) has the highest intensity and the optimum doping level of Li is 0.08. However, it is noted that the observed intensities of the other green emission ($^2H_{11/2} \rightarrow {}^4I_{15/2}$) and red emission ($^4F_{9/2} \rightarrow {}^4I_{15/2}$)

are very weak. Similar results have been observed for Er-doped PMN-PT ceramics (Zeng, 2012). Under an excitation of 490 nm, Er^{3+} ions are excited directly to the $^4F_{7/2}$ level (Fig. 4.4). Due to the fastest MPR rate, most the excited Er^{3+} ions relax non-radiatively to the $^4S_{3/2}$ level and then radiatively to the $^4I_{15/2}$ ground level. Unlike the up-conversion process (under an excitation of 980 nm), no Er^{3+} ion is excited to the $^4I_{11/2}$ level, and hence CR1 will not occur to increase the number of ions in the $^4F_{9/2}$ level as well as the intensity of the red emission.

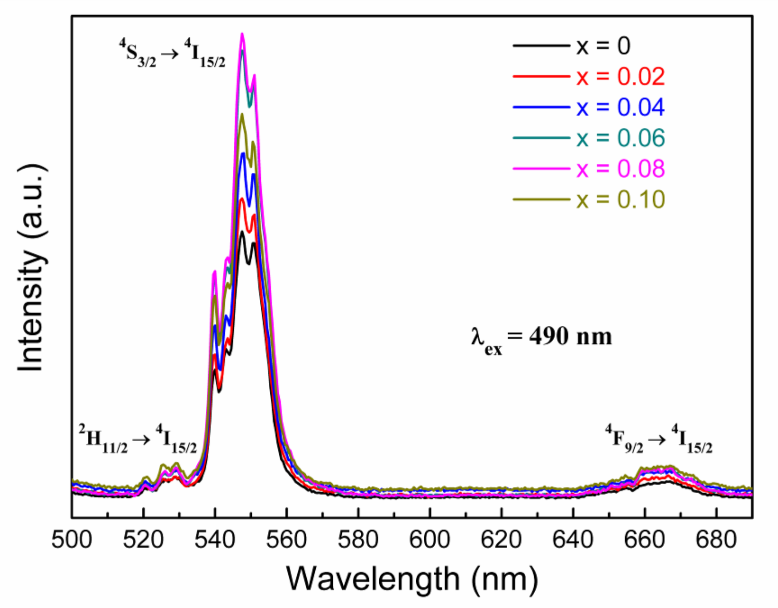

Figure 4.6 Vis down-conversion PL emission spectra of Er-KNLN-x ceramics under 490 nm excitation.

The PLE spectrum of the Er-KNLN-0.08 ceramic monitoring at the green emission (547 nm) is shown in Fig. 4.7. A series of peaks attributed to the excitation of Er^{3+} ions from the $^4I_{15/2}$ ground level to the $^4G_{11/2}$, $^2H_{9/2}$, $^4F_{3/2}$, $^4F_{5/2}$, $^4F_{7/2}$, and $^2H_{11/2}$ excited levels, respectively, are observed. This confirms that the green emissions observed in the Er-doped KNLN ceramics are originated from the excitation of Er^{3+} ions rather than the other ions in the KNLN lattices. It can also be seen that the highest peak occurs at ~490 nm, suggesting that the most efficient excitation source for Er-doped PL materials should be of 490 nm and 980 nm for down-conversion and up-conversion processes, respectively.

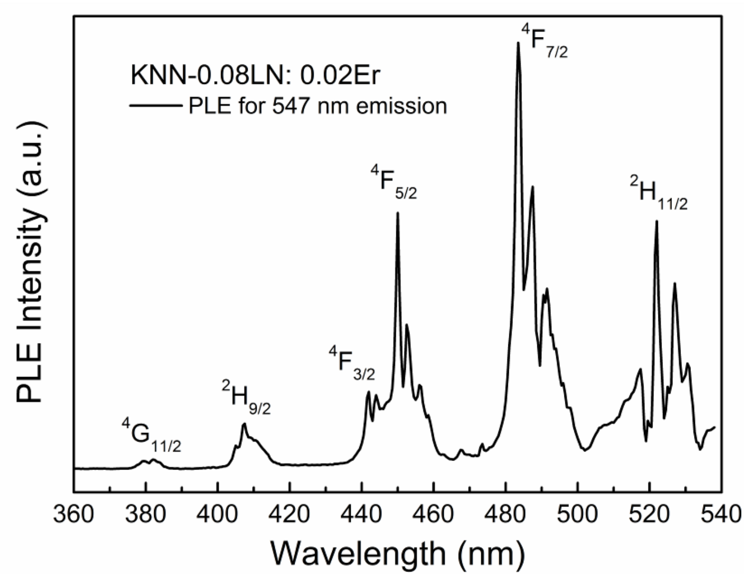

Figure 4.7 Photoluminescence excitation spectrum of the Er-KNLN-0.08 ceramic for monitoring the 547 nm green emission.

4.3.3 NIR and MIR emissions

The MIR (down-conversion) PL emission spectra for the Er-KNLN-x ceramics are shown in Fig. 4.8. A broad emission band ranging from 2.6 to 2.85 μm is observed for all the ceramics. It is attributed to the $^4I_{11/2} \rightarrow {}^4I_{13/2}$ transition of Er^{3+} ions, and the splitting is due to the Stark effect. Although the intensity is the weakest among the others, the emission band of the Er-KNLN-0 (i.e. Er-KNN) ceramic is clear and can be detected easily, suggesting that KNN (without any sensitizers) is a promising host for MIR luminescence. As x increases, the PL intensity increases and the emission band becomes split into four components instead of three components. Unlike the Vis up-conversion PL, the optimum doping level of Li for MIR emission is 0.06. As discussed previously and revealed by the XRD patterns (Fig. 4.1), the doping of Li^+ would reduce the local symmetry between Er^{3+} ions and the ligand field, and induce a structure transformation of the ceramics. It has been known that the PL emissions of Er^{3+} are resulted from electronic transitions between the partially filled 4f levels, which are well shielded by the filled 5s and 5p electron shells and have negligible interaction with the host. These transitions are forbidden in a host material with inversion symmetry, and become allowed if the crystal symmetry of the host material is lowered or the local symmetry around Er^{3+} is reduced (Judd, 1962). Accordingly, the enhancement in the MIR emission of the Er-KNLN-x ceramics should be partly due to the reduction of local symmetry arisen from the Li-doping. The structure transformation also induces a change in the crystal field around Er^{3+} that shifts the 5d energy level and enhances the 4f-4f emissions (Kang, 2009). The enhancement in the MIR emission may also be due to the good ability to resist moisture in the Er-KNLN-x ceramics. The OH^- group will participate in the energy transfer of Er^{3+} ions and then reduce the intensity of emission (Xu, 2011, Bai, 2012). As the typical H_2O absorption band occurs around 3 μm, the presence of OH^- group will also absorb the 2.7-μm emission and make it become undetectable (Chai, 2013).

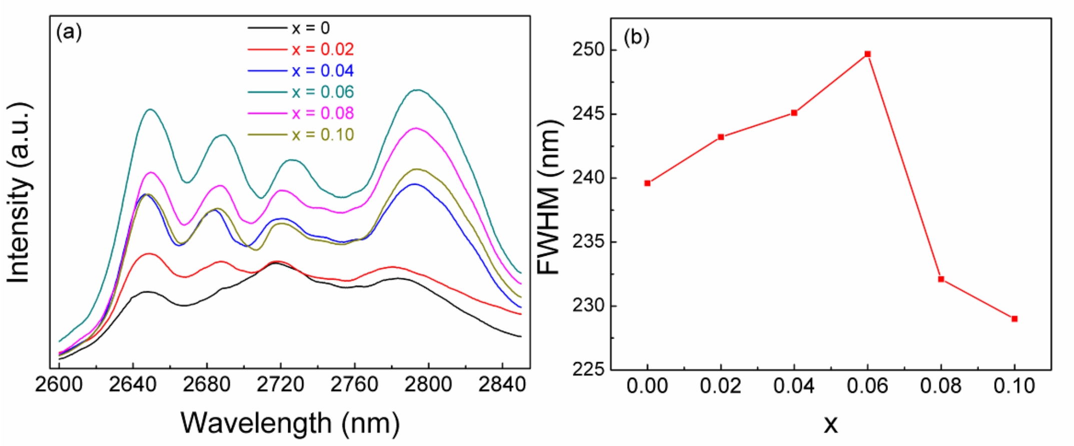

Figure 4.8 (a) MIR emission spectra of the Er-KNLN-x ceramics. (b) Change of FWHM values with x.

The full bandwidth at half maximum (FWHM) of the MIR emission band has been evaluated for the Er-KNLN-x ceramics, giving the results shown in Fig. 4.8b. At x = 0.06, the ceramic exhibits not only the highest PL intensity but also the largest FWHM (~250 nm), which is larger than those of Er-doped germanate glasses (~100 nm) (Xu, 2011), Er-doped oxysulfide glasses (~130 nm) (Vila, 2002), Er-doped fluorotellurite glasses (~163 nm) (Zhan, 2012) and Er-doped PLZT transparent ceramics (230 nm) (De Camargo, 2005). A large FWHW is advantageous for applications in widening the wavelength range of laser sources. The Er-KNLN-x ceramics, especially for those with x = 0.06, are hence promising candidates for high-power 2.7-µm ceramic lasers, which are of great importance for medical applications, hazardous chemical detection, remote atmospheric sensing and pollution monitoring (Sanamyan, 2011).

For understanding the PL mechanism of MIR mission, the NIR PL emission spectra of the Er-KNLN-x ceramics have been measured, giving the results shown in Fig. 4.9. It can be seen that, under an excitation of 980 nm, all the ceramics exhibit a broad emission band ranging from 1.40 to 1.65 μm. The emission is attributed to the $^4I_{13/2} \rightarrow {}^4I_{15/2}$ transition of Er^{3+} ions, and similarly the splitting is due to the Stark effect. Unlike the MIR as well as green and red emissions, the observed PL intensity for the NIR emission decreases after the doping of Li^+. This can be clearly exemplified by Fig. 4.5 in which the relative integrated intensities of the NIR emission band for the Er-KNLN-x ceramics are compared with those of the MIR, green and red emission bands.

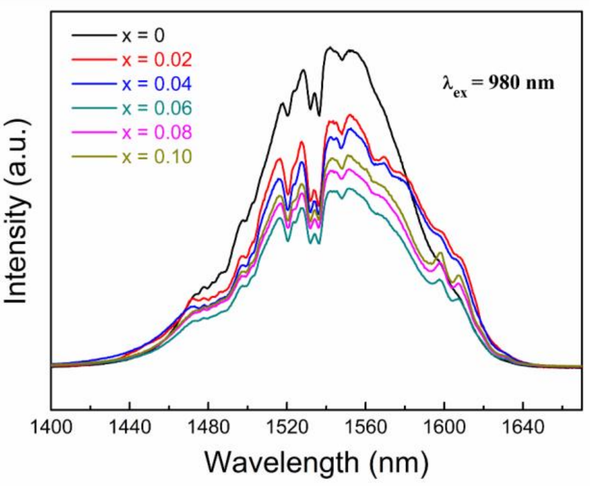

Figure 4.9 NIR emission spectra of the Er-KNLN-x ceramics.

As illustrated in Fig. 4.4, Er^{3+} in the $^4I_{11/2}$ excited level (via absorption of 980-nm incident photons) may relax radiatively to the $^4I_{13/2}$ level, generating the MIR emission (2.6-2.85 μm) as shown in Fig. 4.8. Some of the excited Er^{3+} may also relax non-radiatively to the $^4I_{13/2}$ level. Subsequently, Er^{3+} in the $^4I_{13/2}$ level may relax radiatively to the $^4I_{15/2}$ ground level, giving the NIR emission (1.40-1.65 μm). Indeed, some adjacent Er^{3+} in the $^4I_{13/2}$ level may interact with each other, inducing a CR3 process between the two transitions $^4I_{13/2} \rightarrow {}^4I_{9/2}$ and $^4I_{13/2} \rightarrow {}^4I_{15/2}$. This will obviously decrease the population of Er^{3+} in the $^4I_{13/2}$ level and then the PL intensity of the NIR emission.

As the excited Er^{3+} in the $^4I_{9/2}$ level will relax non-radiatively to the $^4I_{11/2}$ level rapidly, the CR3 process also increases the population of Er^{3+} in the $^4I_{11/2}$ level, and thus facilitating a population inversion between the $^4I_{11/2}$ and $^4I_{13/2}$ levels and enhancing the MIR emission. Our results suggest that, probably due to the reduced local symmetry and the change in crystal field, the Li-doping is effective in establishing such a dynamic circulatory energy process to enhance the MIR PL intensity at the expense of the NIR emission (Fig. 4.5).

4.4 Electrical properties

4.4.1 Dielectric properties

Fig. 4.10a shows the temperature dependence of ε_r measured at 100 kHz for the Er-KNLN-x ceramics. The relaxor-like characteristics of the ceramic may be arisen from the doping of Er^{3+} as discussed in Chapter 3. The Er-KNLN-0 ceramic exhibits two broadened peaks at ~400°C (T_c) and ~220°C ($T_{O\text{-}T}$). After the doping of Li^+, both the transition peaks remain broadened and shift to different temperatures. As x increases, T_c increases while $T_{O\text{-}T}$ decreases (Fig. 4.10c). Similar results have been observed for the KNLN ceramics (Lin, 2007e, Guo, 2004). As Li^+ (0.68 Å) has a much smaller radius than K^+ (1.51 Å) and Na^+ (1.18 Å), the tolerance factor (t) of the perovskite structure decreases as x increases. It has been shown that as the tolerance factor decreases below t = 1, T_c would increase (Eitel, 2001). The doping of Li^+ would not enhance the diffuseness in the cubic-tetragonal phase transition because Li^+ has the same valence as K^+ and Na^+. On the other hand, the transition peak at $T_{O\text{-}T}$ continues to broaden and shifts to lower temperatures as x increases. This may be attributed to the lattice distortion induced by the doping of Li^+. As revealed by the XRD results (Fig. 4.1b), the ceramics with $x \geq 0.06$ should have the tetragonal phase while the ceramic with x = 0.04 contains both the orthorhombic and tetragonal phases. However, as the transition peak for the ceramics with $x \geq 0.04$ are very broad and weak, it is suggested that the two phases may coexist in the ceramics over a very wide temperature range (Lobo, 1995, Chattopadhyay, 1995), and the amount of orthorhombic phase in the ceramics with $x \geq 0.06$ is small and decreases with increasing x. The coexistence of the two phases may also lead to the enhancement in PL intensity as shown in Figs. 4.3, 4.6 and 4.8, because of the resulting reduction in local symmetry.

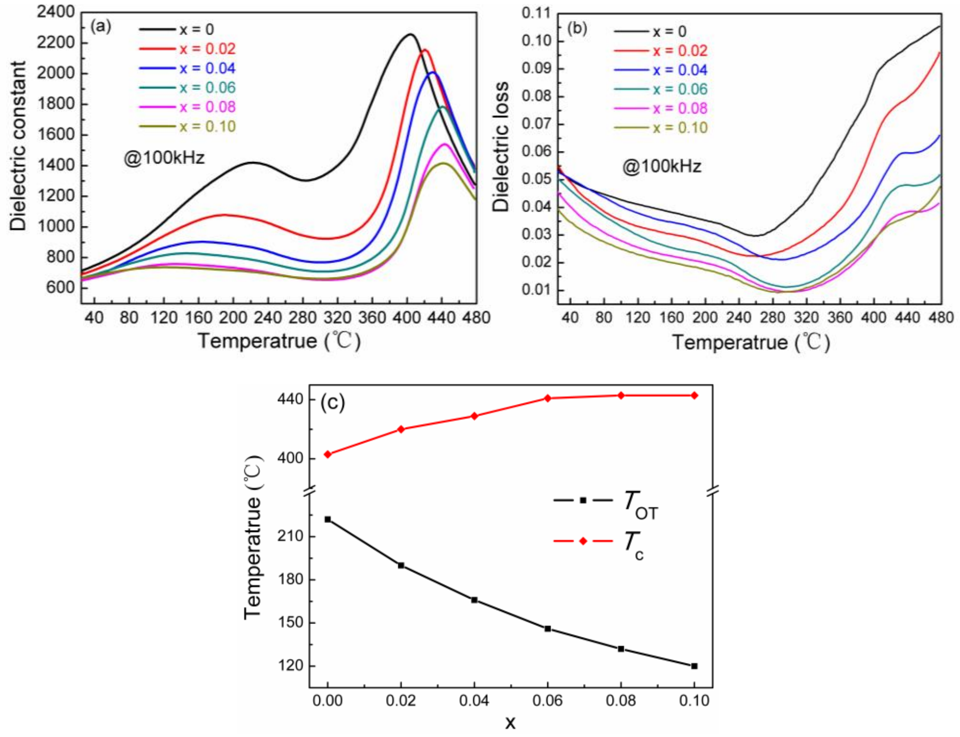

Figure 4.10 Temperature dependence of relative dielectric constant (a) and dielectric loss (b) measured at 100 kHz for the Er-KNLN-x ceramics. (c) Variations of phase transition temperatures with x.

4.4.2 Ferroelectric properties

Fig. 4.11a shows the *P*-*E* loops of the Er-KNLN-x ceramics measured under an electric field of 4 kV/mm, while the variations of the remanant polarization P_r and coercive field E_c with x are shown in Fig. 4.11b. The ceramics will electrically break down if a higher electric field is applied. All the ceramics exhibit a flattened, slant and unsaturated polarization hysteresis loop. As x increases, the observed E_c increases and reaches a maximum value of 1.36 kV/mm at x = 0.06. The observed P_r remains almost unchanged at $x \leq 0.02$, and then decreases from 8.23 to 2.38 μC/cm^2 as x increases to 0.10. Similar results have been reported for the other Li-doped KNN-based ceramics (Lin, 2007c). Although the ferroelectricity is weakened by the Li-doping, the Er-KNLN-x ceramics are a multi-functional material exhibiting good ferroelectric as well as PL properties.

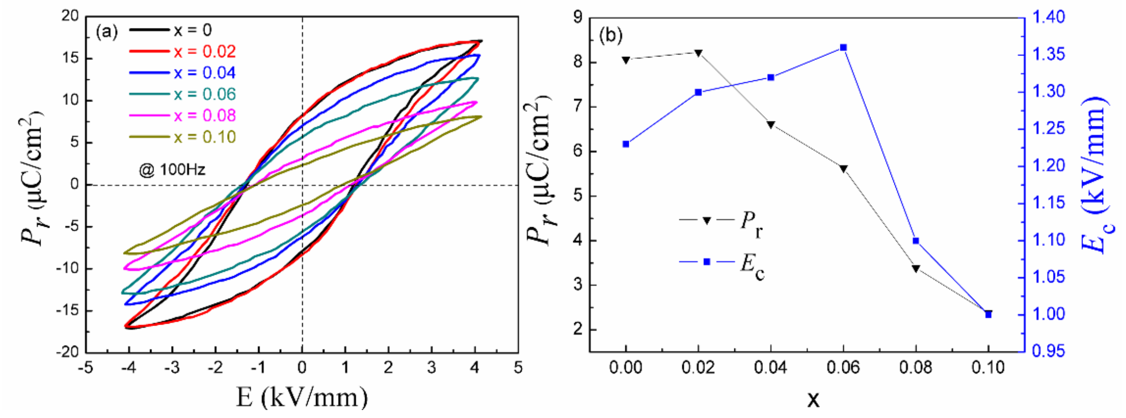

Figure 4.11 (a) *P*-*E* loops of Er-KNLN-x ceramics. (b) Variations of P_r and E_c with x.

4.5 Conclusions

2 mol% Er-doped $(K_{0.5}Na_{0.5})_{1-x}Li_xNbO_3$ ceramics have been prepared and their dielectric, ferroelectric and PL properties have been investigated. The ceramics possess a single-phase perovskite structure at $x < 0.06$. As x increases from 0 to 0.06, the perovskite structure transforms from orthorhombic to tetragonal symmetry. Under an excitation of 980 nm, the ceramics exhibit up-conversion luminescent emission bands at 527 nm (green), 548 nm (green), 660 nm (red) as well as down-conversion emission bands at 1.55 μm (NIR) and 2.7 μm (MIR), which are attributed to the transitions $^2H_{11/2} \rightarrow {}^4I_{15/2}$, $^4S_{3/2} \rightarrow {}^4I_{15/2}$, $^4F_{9/2} \rightarrow {}^4I_{15/2}$, $^4I_{13/2} \rightarrow {}^4I_{15/2}$ and $^4I_{11/2} \rightarrow {}^4I_{13/2}$, respectively. Probably due to the induced structure distortion and reduced local symmetry, the PL intensities of the green, red as well as MIR emissions are enhanced by the doping of Li^+. Our results show that the Li-doping is effective in establishing a dynamic circulatory energy process to further enhance the PL intensity of the MIR emission at the expense of the NIR emission. At the optimum doping level of Li^+ (~6 mol%), the FWHM of the MIR emission also reaches a very large value of ~250 nm, demonstrating that the ceramic is a promising candidate for high-power 2.7-μm ceramic lasers. In addition to the good ferroelectric properties, the 2 mol% Er-doped $(K_{0.5}Na_{0.5})_{1-x}Li_xNbO_3$ ceramics should also have great potential for multifunctional optoelectronic applications.

Chapter 5 Sol-gel-derived Er-Doped KNN and KNLN Ceramics

5.1 Introduction

As discussed in Chapter 3 and 4, Er-doped KNN and KNLN ceramics have been fabricated by the SSR method. Their PL performances and corresponding mechanisms, as well as ferroelectric, dielectric and piezoelectric properties have been systematically investigated. However, those SSR-derived ceramics have some drawbacks, such as inhomogeneous grains and inferior piezoelectric properties. Thereupon, sol-gel method is applied to fabricate these KNN-based ceramics in order to obtain compositional homogeneity, fine grains and good crystallinity, which are essential for simultaneously improving the ferroelectric-related properties and enhancing the PL intensity (Bandi, 2012, Guo, 2011).

In this chapter, a sol-gel method has been used to fabricate x mol% Er-doped KNN (KNN:Er-x, x = 0, 0.5, 1, 2, 3) and 2 mol% Er-doped KNLN (Er-KNLN-x, x = 0.08) powders. And the corresponding ceramics have been prepared by the SSR method. As the precursors are mixed at the molecular level, the sol-gel process can provide a high degree of homogeneity and effective doping of activators. It can also produce ceramics with a dense and fine-grained structure. These sol-gel-derived ceramics show better performances than the SSR-based ceramics.

5.2 Sol-gel process

Fig. 5.1 shows the flow chart of the sol-gel process. Er-doped KNN and KNLN ceramics were prepared from the sol-gel-derived fine powders. The starting materials in this study were Nb_2O_5 (99.9%), KOH (95%), Na_2CO_3 (99%), K_2CO_3 (99.9%), Li_2CO_3 (99%), $Er(NO_3)_3 \cdot 5H_2O$ (99.9%), oxalic acid ($(COOH)_2 \cdot 2H_2O$, 99.5%), citric acid ($C_6H_8O_7 \cdot H_2O$, 99.5 %), nitric acid (HNO_3, 70%), and ammonia solution ($NH_3 \cdot H_2O$, 25.0%). A niobium precursor solution was first prepared from Nb_2O_5 and KOH. The powders were mixed thoroughly and heated at 350°C for 2 h to obtain water-soluble K_3NbO_4, which was then dissolved in distilled (DI) water and titrated with nitric acid (controlling PH = 3) to form a $Nb(OH)_5$ precipitate. After washing several times by DI water to remove the residual K^+, the precipitate was chelated with oxalic acid to form the niobium precursor solution. After that, stoichiometric amounts of K_2CO_3, Na_2CO_3, Li_2CO_3 and $Er(NO_3)_3 \cdot 6H_2O$ were dissolved in a mixture of the niobium precursor solution and dilute citric acid. After vigorous stirring, the solution could be homogeneous and stable. Fig. 5.2a is the photograph of the as-prepared white solution. The mixture was then stirred vigorously for 4 h and heated at 120°C for 24 h to form a dried light brown gelatin, as shown in Fig. 5.2b. After that the dried gel was calcined at 800°C for 5 h with the heating rate of 1 °C/min. The resulting ultrafine powders were granulated with PVA binder and pressed into pellets, then compacted to disc specimens. Finally, the disk samples were sintered at different temperatures for 4 h to obtain dense ceramics. Table 5.1 gives the optimum sintering temperatures comparing with the sol-gel-derived and SSR-derived ceramics. It is obvious that sol-gel method is beneficial for reducing the sintering temperature.

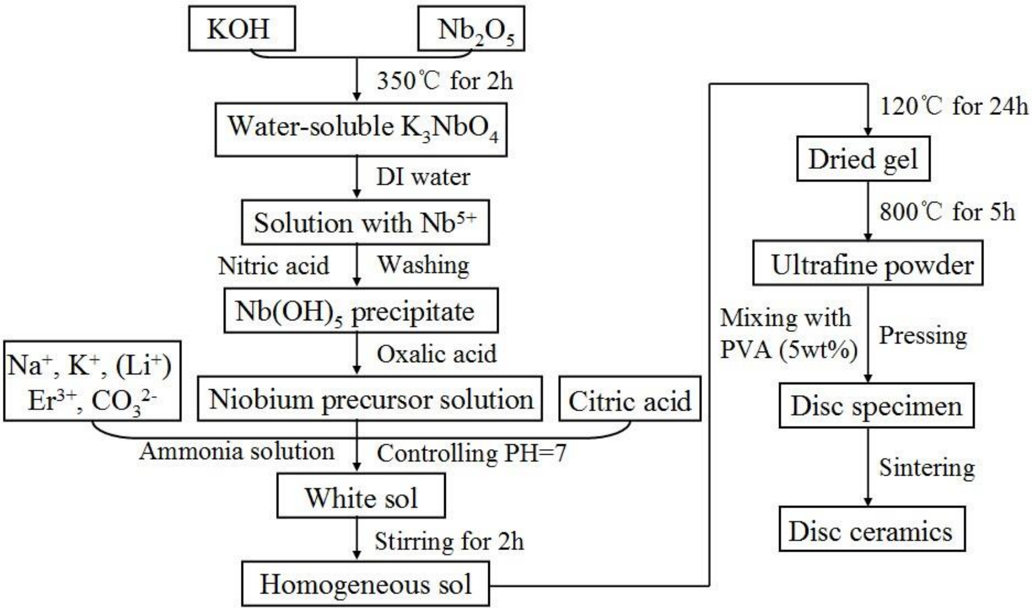

Figure 5.1 The flow chart of sol-gel process.

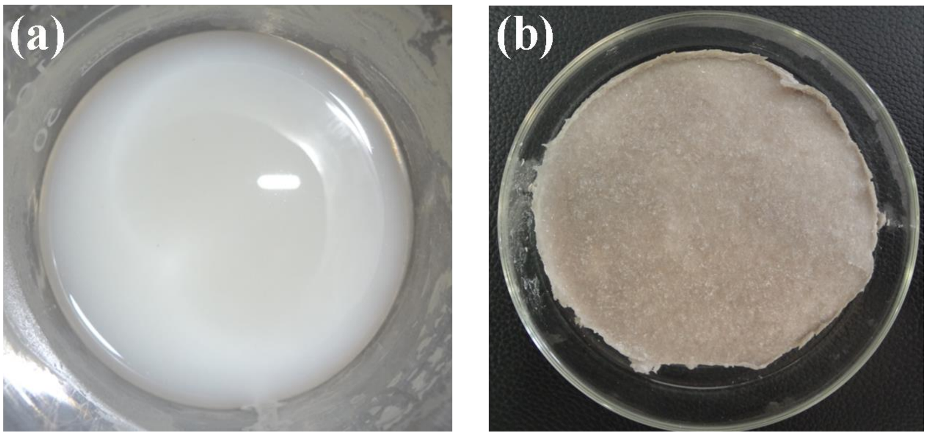

Figure 5.2 (a) Photograph of as-prepared solution. (b) Photograph of dried gelatin.

Table 5.1 The optimum sintering temperatures for KNN-based ceramics.

Sample name Preparing method	KNN:Er-0	KNN:Er-1	KNN:Er-2	KNN:Er-3	Er-KNLN-0.08
Sol-gel	1060°C	1060°C	1065°C	1065°C	1000°C
SSR	1100°C	1110°C	1120°C	1120°C	1070°C

5.3 Er-doped KNN ceramics

5.3.1 XRD

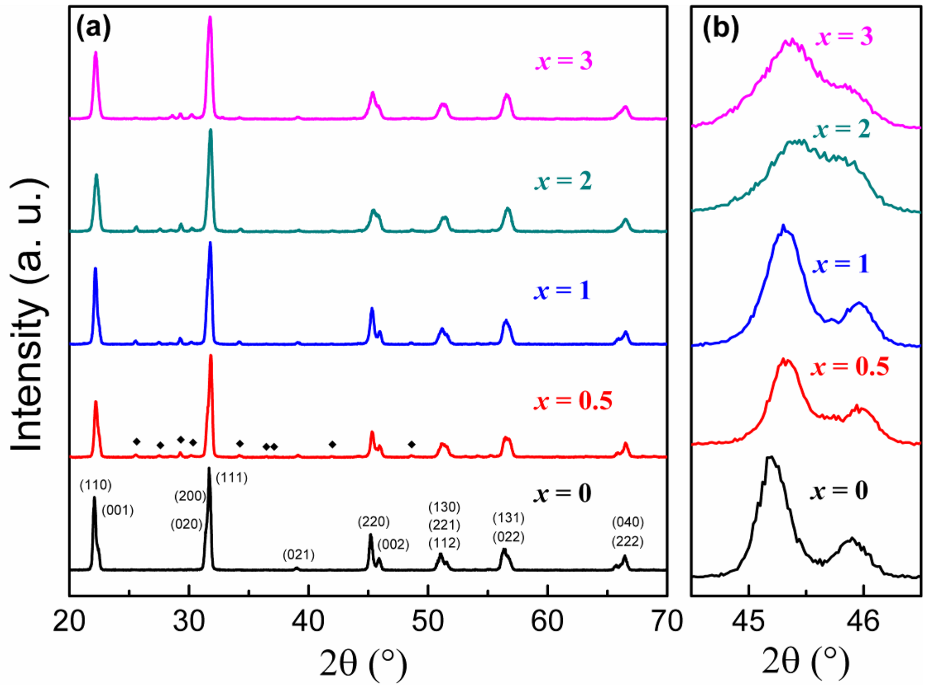

Figure 5.3 XRD patterns of the KNN:Er-x ceramics.

The XRD patterns of the KNN:Er-x ceramics are shown in Fig. 5.3a. All the ceramics possess an orthorhombic perovskite structure, suggesting that Er^{3+} has diffused into the KNN lattices. Similar to the SSR-derived KNN:Er-x ceramics in Chapter 3, a small amount of impurity phase $K_{5.75}Nb_{10.85}O_{30}$ (JCPDS No. 38-0297) is also observed in the sol-gel-derived ones. Probably due to the lattice shrinkage arisen from the replacement of large K^+ (CN = 8, 1.51 Å) and Na^+ (CN = 8, 1.18 Å) with small Er^{3+} (CN = 8, 1.004 Å) (Shannon, 1976), the diffraction peaks shift toward higher angles with increasing x (Fig. 5.3b). As also shown in Fig. 5.3b, the two diffraction peaks (220) and (002) near 45.5 °become merged together, forming a broadened peak at $x \geq 2$. This suggests that the lattice constants of the ceramics become close to each other. Similar results have been observed for other KNN-based ceramics, e.g., La-doped KNN and Ta-modified KNN ceramics (Gao, 2009a, Lin, 2008b).

5.3.2 PL properties

The up-conversion PL emission spectra of the KNN:Er-*x* ceramics are shown in Fig. 5.4. The up-conversion mechanism of sol-gel-derived Er-doped ceramics is similar to that of SSR-derived one, which has been discussed in Fig. 3.9. Under an excitation of 980 nm, all the ceramics exhibit two strong green emission bands at 548 and 527 nm, which are attributed to the transitions $^4S_{3/2} \rightarrow {}^4I_{15/2}$ and $^2H_{11/2} \rightarrow {}^4I_{15/2}$, respectively (Fig. 5.4a). Clear stark-splitting is observed, revealing the interaction between Er^{3+} and the host. No shifting of the split peaks with increasing x is observed. The observed PL intensity increases with increasing x, and reaches a maximum at $x = 2$. It has been observed that the emission intensity of the KNN:Er-2 ceramic is very strong, giving a very bright green spot on the sample during the measurement (Fig. 5.4a). Probably due to the increase in the defect density and concentration-quenching effect (Inokuti, 1965), the PL intensity decreases when $x > 2$. Above the critical concentration for quenching (i.e., 2 mol% for the KNN:Er-*x* ceramics), the inter-distance of Er^{3+} becomes shorter and the transfer of non-radiative energy from one to the others becomes easier, having a probability larger than that of the radiative emission. As a result, the radiative emission is quenched and the PL intensity decreases.

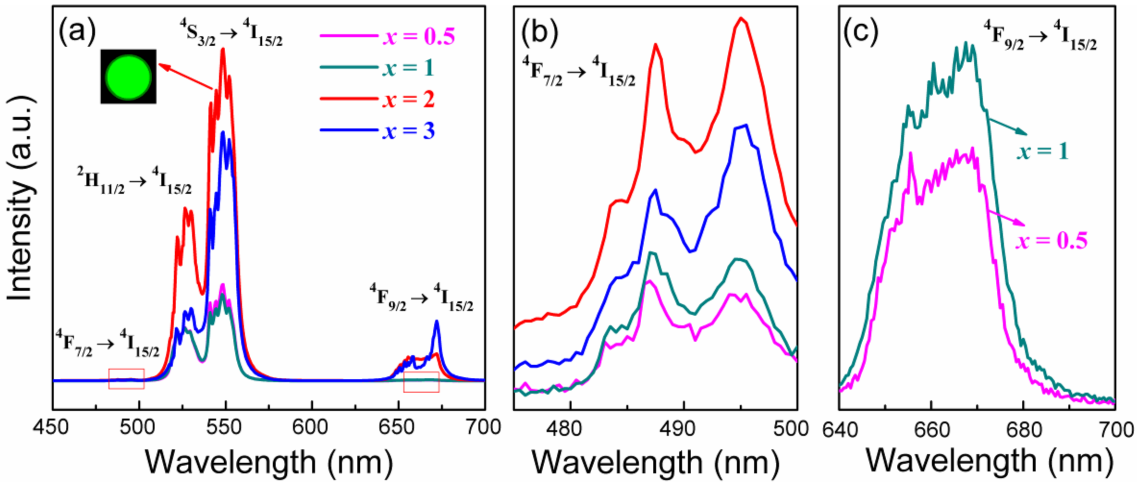

Figure 5.4 Up-conversion PL spectra of the KNN:Er-*x* ceramics.

As shown in the enlarged PL spectra (Fig. 5.4b and 5.4c), the KNN:Er-*x* ceramics also exhibit two emission bands at 487 nm (blue) and 660 nm (red), which are attributed to the transitions $^4F_{7/2} \rightarrow {}^4I_{15/2}$ and $^4F_{9/2} \rightarrow {}^4I_{15/2}$, respectively. Unlike the green emission bands, the intensities of these two bands are low, in particular for the blue emission band that has rarely been reported for the Er-doped systems. Due to the small energy gaps (Fig. 3.9), the excited Er^{3+} in the $^4F_{7/2}$ level will decay non-radiatively to the $^2H_{11/2}$ and then $^4S_{3/2}$ level very quickly by MPR. As a result, the probability for the excited Er^{3+} relaxing radiatively from the $^4F_{7/2}$ level directly to the $^4I_{15/2}$ ground level becomes very low. The corresponding emission is then very weak and hard to be observed unless the population of Er^{3+} in the $^4F_{7/2}$ level is very large or the overall PL intensity is very strong. Accordingly, the observation of the blue emission band in this work attests the strong PL intensity of the sol-gel-derived KNN:Er-*x* ceramics. It should be noted that the quenching concentration of Er^{3+} for producing such a strong PL intensity is only 2 mol%, which is lower than those for the other Er-doped ferroelectrics, e.g. 3 mol% for

Er-doped $KNbO_3$ polycrystalline (Wen, 2004), 3 mol% for Er-doped $BaTiO_3$ films (Zhang, 2000), and 5 mol% for Er-doped $0.75Pb(Mg_{1/3}Nb_{2/3})O_3$-$0.25PbTiO_3$ transparent ceramics (Zeng, 2012). This suggests that the KNN:Er-x ceramics have a higher pumping efficiency, which should be partly due to the uniform distribution of Er^{3+}.

On the other hand, due to the large band gap between $^4S_{3/2}$ and $^4F_{9/2}$ (Fig. 3.9), there is only a small amount of Er^{3+} in the $^4F_{9/2}$ level, and thus leading to the weak emission band at 660 nm for the KNN:Er-x ceramics with $x \leq 1$. As x increases, the inter-distance of Er^{3+} decreases and the CR1 process becomes more effective. For example, Er^{3+} in the $^4F_{7/2}$ level may interact with those in the $^4I_{11/2}$ level, inducing a CR1 process between the two transitions $^4F_{7/2} \rightarrow {}^4F_{9/2}$ and $^4I_{11/2} \rightarrow {}^4F_{9/2}$. As a result, the population of Er^{3+} in the $^4F_{9/2}$ level increases and the red emission at 660 nm is enhanced. The results also suggest that the large increase in PL intensity of the green bands at $x = 2$ should be partly attributed to the effective energy transfer between different Er^{3+} ions.

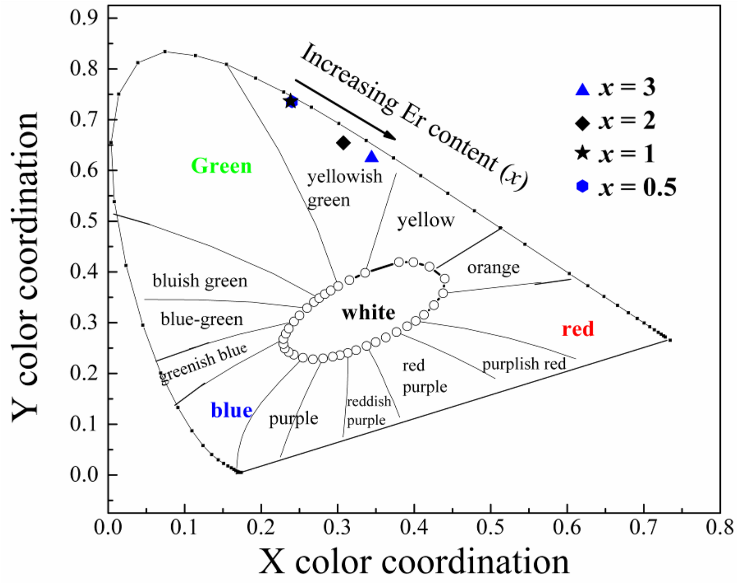

Figure 5.5 CIE chromaticity coordinates (X, Y) of the KNN:Er-x ceramics.

Owing to the enhancement of the red emission, the CIE chromaticity coordinates (X, Y) of the KNN:Er-x ceramics show a red shift (Fig. 5.5), changing from (0.2402, 0.7355) at x = 0.5 to (0.3443, 0.6245) at x = 3. Nevertheless, the color remains as yellowish green because of the strong green emission.

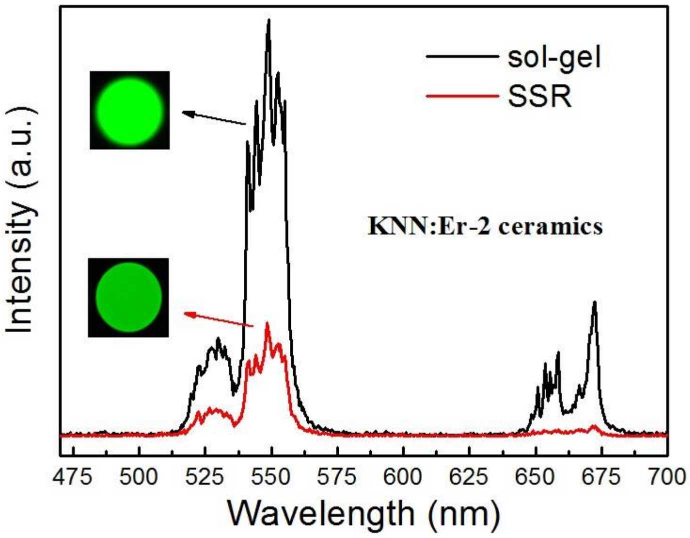

Figure 5.6 Up-conversion PL spectra of the KNN:Er-2 ceramics prepared by the sol-gel and SSR method.

Fig. 5.6 compares the up-conversion PL intensities of the KNN:Er-2 ceramics prepared by the sol-gel and SSR method. It is clearly seen that the observed PL intensity for the SSR-derived ceramic is much lower. It should be noted that the experimental conditions, e.g., the power of the diode laser, were kept the same for all the PL measurements. The difference in PL intensities, which is also demonstrated by the green spots observed on the two ceramics during the measurements (inset of Fig. 5.6), should be partly attributed to the better compositional homogeneity of the host material and dopants in the sol-gel-derived ceramics.

Fig. 5.7 compares the NIR and MIR emission intensities of the KNN:Er-2 ceramics prepared by the sol-gel and SSR method. The NIR emission spectra with some splitting peaks are centered at 1.55 μm (Fig. 5.7a). The PL intensity of sol-gel-derived ceramic is higher than that of SSR-derived one. Similar to the NIR emissions, the PL intensity of MIR emission of sol-gel-derived ceramic is higher. The MIR emission bands in the range of 2.6-2.85 μm split into three peaks and the strongest one is at ~2.72 μm. It can be seen that the emission intensities from Vis to MIR range of the sol-gel-derived KNN:Er-2 ceramic are all stronger than those of the SSR-derived ceramic.

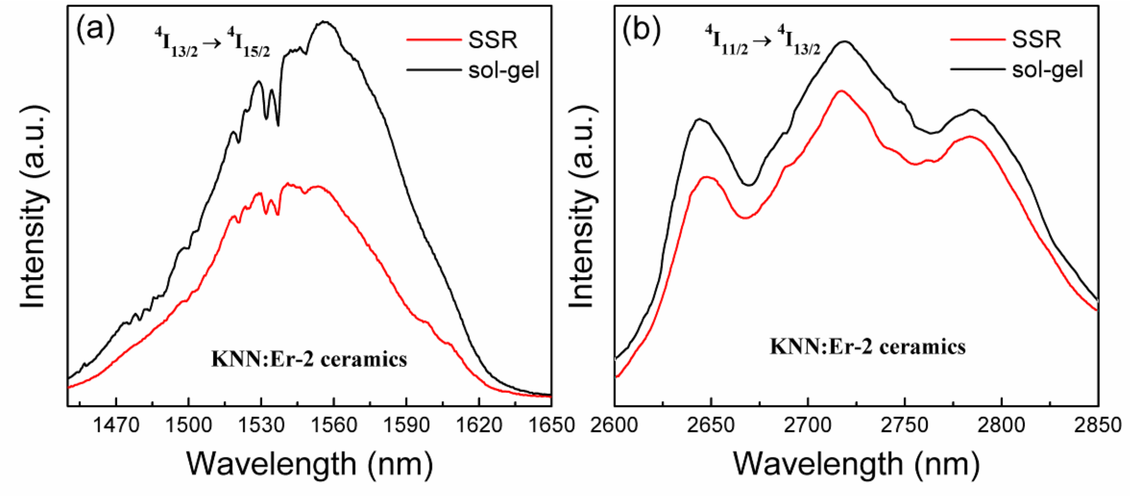

Figure 5.7 NIR and MIR emission spectra of the KNN:Er-2 ceramics prepared by the sol-gel and SSR method.

5.3.3 SEM

The SEM micrographs of the sol-gel-derived and SSR-derived KNN:Er-*x* ceramics are shown in Fig. 5.8. All the sol-gel-derived ceramics possess a dense structure. As shown in Figs. 5.8a-c, the grain growth of the ceramics is suppressed effectively by the

Er-doping. The average grain size decreases from 3 μm to 0.7 μm with increasing *x* from 0 to 2. Similar results have been reported for La-doped and Ce-doped KNN ceramics (Gao, 2009a, Gao, 2009b). This should be attributed to the donor-type nature of Er. For PZT-based ceramics, donor doping generally causes an inhibition of grain growth (Lee, 2006, Pereira, 2001). Owing to the higher valence of Er^{3+}, cation vacancies are generated after the replacement of the A-site K^+ or Na^+. The vacancies concentrate near the grain boundaries and decrease their mobility during densification. As a result, the mass transportation becomes weakened and the grain growth is then inhibited.

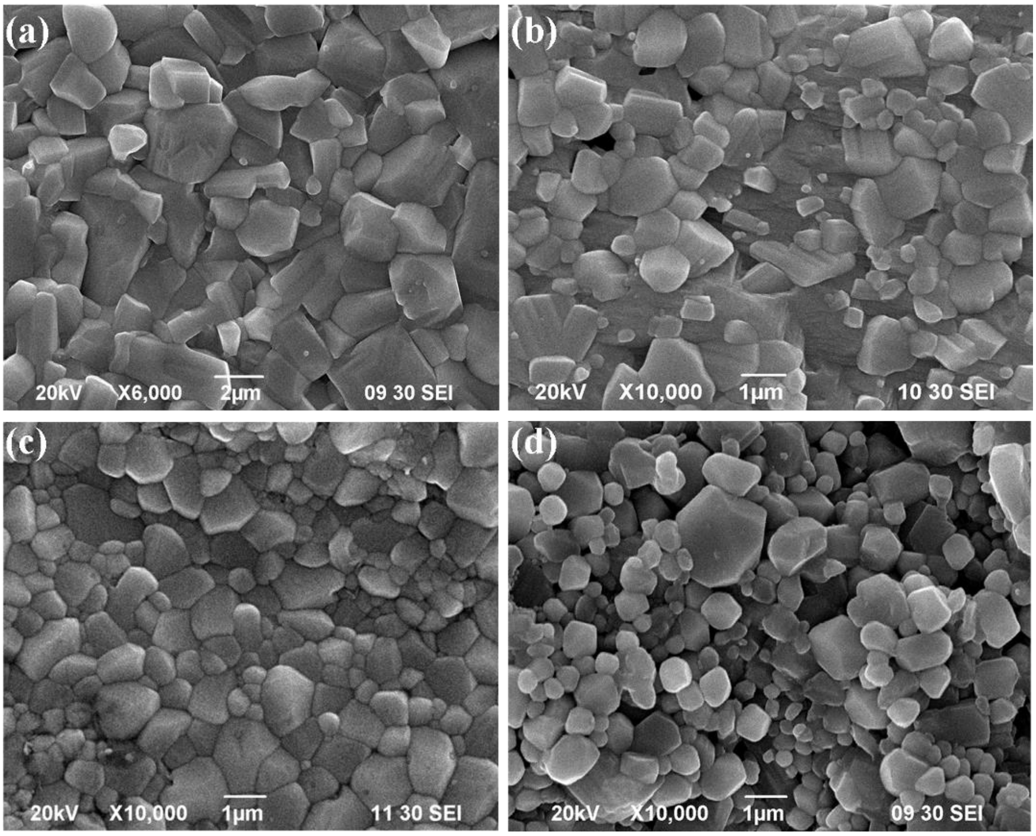

Figure 5.8 SEM micrographs of the KNN:Er-*x* ceramics, (a) sol-gel, *x* = 0, (b) sol-gel, *x* = 1, (c) sol-gel, *x* = 2, and (d) SSR, *x* = 2.

It can also be seen that the grains of the sol-gel-derived ceramics are generally finer and more uniform than that those of the SSR-derived ceramic (Figs. 5.8c and 5.8d). In the sol-gel process, the precursors are mixed at the molecular level, so the homogeneity of the compositions is improved significantly and the diffusion of the elements during the sintering process becomes shorter in range and effective, and thus leading to the finer and more uniform grains with higher density (Wang, 2008). These are advantageous for enhancing the PL intensity (Bandi, 2012, Pang, 2005, Guo, 2011) as shown in Figs. 5.6 and 5.7.

5.4 Er-doped KNLN ceramics

5.4.1 XRD

As the sol-gel method is effective in improving the homogeneity of crystalline grains and enhancing the PL properties of Er-doped KNN ceramics, it has been applied to fabricate the Er-KNLN-0.08 ceramic for comparing with the sol-gel-derived ceramic.

Fig. 5.9 shows the XRD patterns of Er-KNLN-0.08 ceramics prepared by the sol-gel and SSR methods. The main diffraction peaks agree with those of KNN (JCPDS NO. 32-0822), suggesting that the ceramics have the perovskite structure, and Er^{3+} and Li^{+} ions have successfully diffused into the KNN lattices. A small amount of secondary phase $K_3LiNb_6O_{17}$ (JCPDS NO. 36-0533) exists in the SSR-derived Er-KNLN-0.08 ceramic while the sol-gel-derived ceramic is almost free of the impurity phase. This is probably due to the improved homogeneity of the composition offered by the sol-gel process.

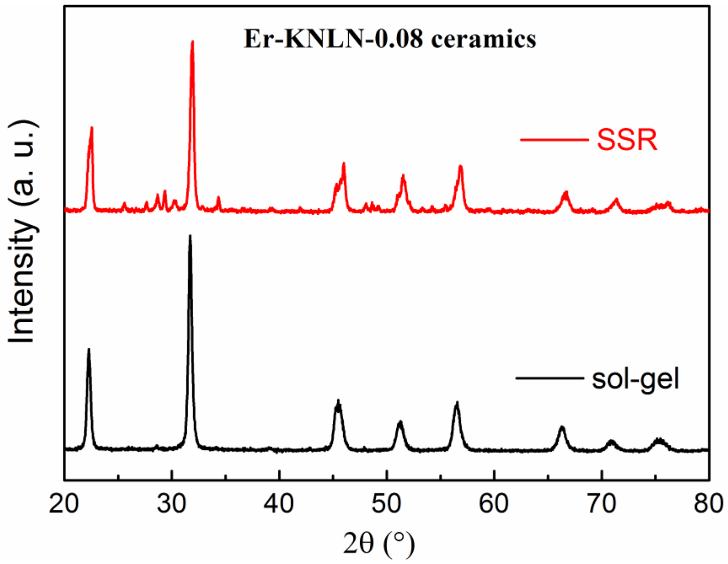

Figure 5.9 XRD patterns of the Er-KNLN-0.08 ceramics prepared by the sol-gel and SSR methods.

5.4.2 SEM

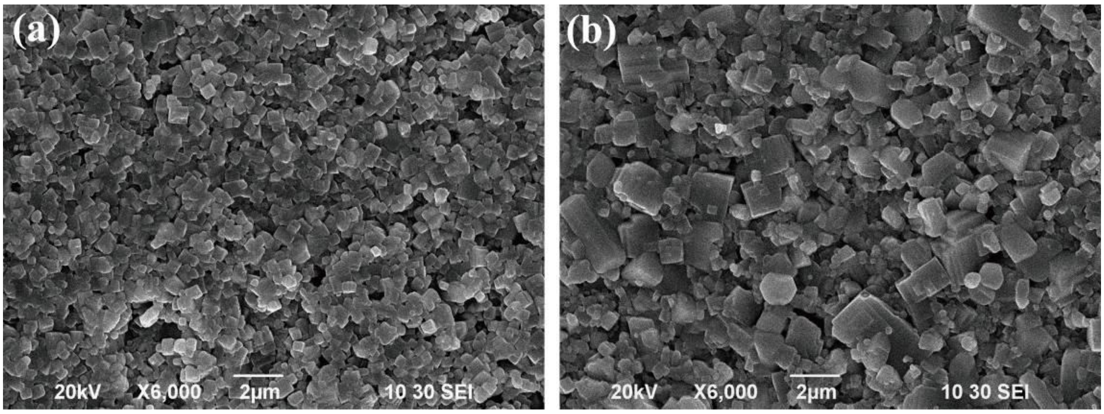

Figure 5.10 SEM micrographs of the Er-KNLN-0.08 ceramics, (a) sol-gel, (b) SSR.

Fig. 5.10 shows the SEM micrographs of the sol-gel-derived and SSR-derived Er-KNLN-0.08 ceramics. The sol-gel-derived ceramic possesses homogeneous cubic-like grains with an average size of ~600 nm (Fig. 5.10a). On the other hand, the grains of the

SSR-derived ceramic are larger and irregular, having the size in the range of 1-5 μm (Fig. 5.10b).

5.4.3 PL properties

Fig. 5.11 shows the PL properties of sol-gel-derived Er-KNLN-0 (i.e. KNN:Er-2 as mentioned above) and Er-KNLN-0.08 ceramics. Three emissions bands: 510-537 nm green emissions, 537-585 nm green emissions and 640-685 nm red emissions are observed in the Vis up-conversion emissions spectra (Fig. 5.11a). After the doping of Li^+, the emission intensity of the Er-KNLN-0.08 ceramic, especially the green emission, is higher than that of the Er-KNLN-0 ceramic. The CIE chromaticity coordinates (Fig. 5.11b) indicate an obvious green shift because of the great enhancement of the green emission induced by Li. But the emission color still remains in the yellowish green region. The NIR emission bands of both the ceramics are in the range of 1450-1650 nm (Fig. 5.11c), but their shapes are different probably due to the doping of Li. The emission intensity of the Er-KNLN-0.08 ceramic is lower than that of the Er-KNLN-0 ceramic. The MIR emission bands of the ceramics are in the same range, i.e., 2600-2870 nm (Fig. 5.11d), but the emission intensity of the Er-KNLN-0.08 ceramic is slightly higher than that of the Er-KNLN-0 ceramic. These PL results are almost consistent with those of the SSR-derived Er-KNLN-x ceramics.

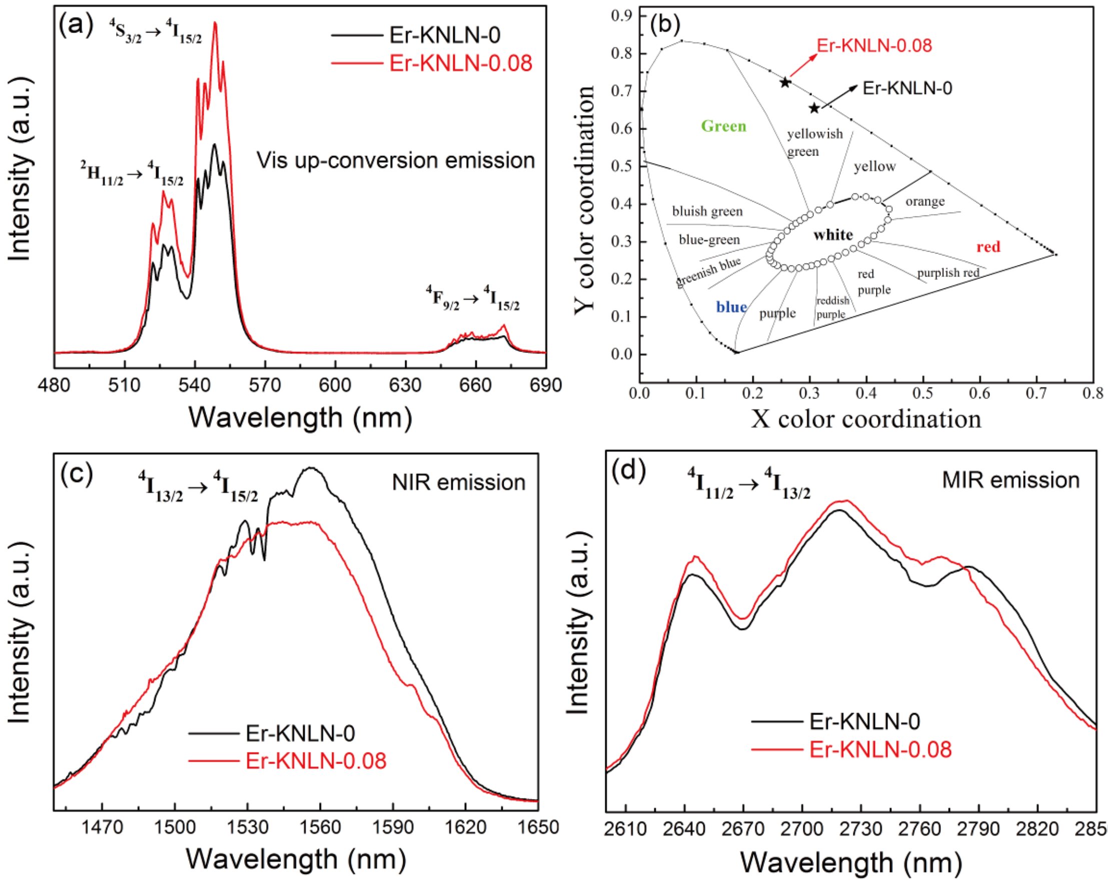

Figure 5.11 PL properties of sol-gel-derived Er-KNLN-0 and Er-KNLN-0.08 ceramics. (a) Vis up-conversion emissions, (b) CIE chromaticity coordinates, (c) NIR emissions and (d) MIR emissions.

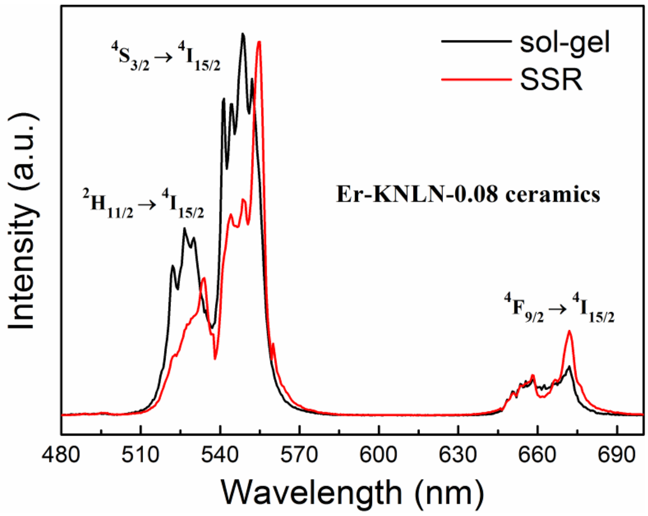

Figure 5.12 Up-conversion PL spectra of the Er-KNLN-0.08 ceramics prepared by the sol-gel and SSR method.

Fig. 5.12 compares the PL spectra of the Er-KNLN-0.08 ceramics prepared by the sol-gel and SSR methods. Both of them exhibit two green emission bands and one red emission band, attributed to the $^2H_{11/2} \rightarrow {}^4I_{15/2}$, $^4S_{3/2} \rightarrow {}^4I_{15/2}$ and $^4F_{9/2} \rightarrow {}^4I_{15/2}$ transitions, respectively. However, the spectrum shapes of each emission bands and emission intensities of each emission band are different, suggesting that the splitting effect is different although the ceramics have the same composition. This may be due to the different phase structures (Fig. 5.9) or different sizes and homogeneity of crystalline grains, which are resulted from the fabrication methods (i.e. SSR and sol-gel).

5.4.4 Electrical properties

Apart from the outstanding PL performances, the sol-gel-derived ceramics possess better ferroelectric and dielectric properties. Fig. 5.13a shows the *P-E* loops of the sol-gel-derived Er-KNLN-0 and Er-KNLN-0.08 ceramics under an electric field of 6 kV/mm. They exhibit similar ferroelectric properties, showing a flattened, slant and unsaturated *P-E* loops which may be attributed to the relaxor-like characteristics induced by the Er-doping. The remnant polarization P_r is ~9 μC/cm^2 and coercive field E_c is ~1.5 kV/mm. Fig. 5.13b shows the temperature dependence of dielectric constant (ε_r) measured at 100 kHz. Two broadened transition peaks resulting from the tetragonal-cubic and orthorhombic-tetragonal phase transition are observed. For the Er-KNLN-0 ceramic, the observed T_c is 380°C and the observed $T_{O\text{-}T}$ is ~200°C. For the Er-KNLN-0.08 ceramic, T_c increases to 415°C and $T_{O\text{-}T}$ shifts to low temperature and becomes further broadened, suggesting that both the orthorhombic and tetragonal phases may coexist over a very wide temperature range. It is clear that the addition of Li is effective in inducing the relaxor-like ferroelectric characteristics in the Er-KNLN-0.08 ceramic.

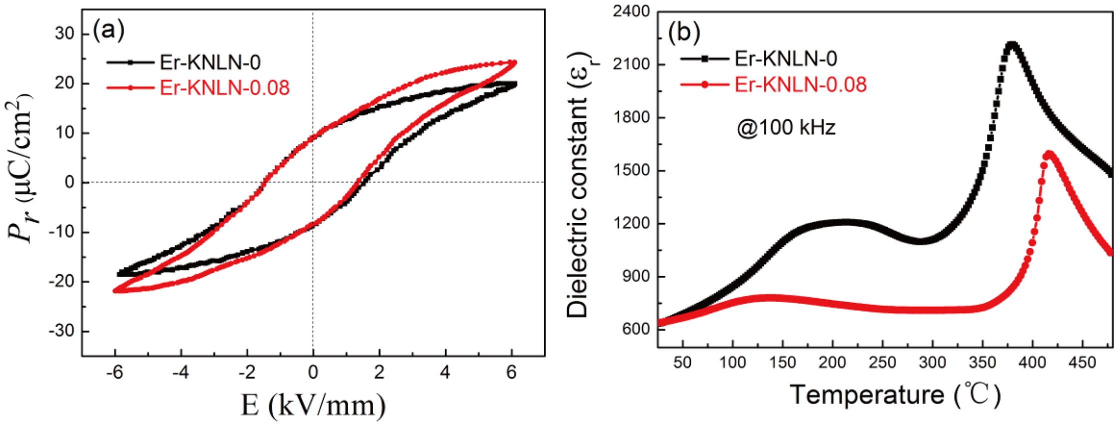

Figure 5.13 Electrical properties of the sol-gel-derived Er-KNLN-0 and Er-KNLN-0.08 ceramics. (a) *P-E* loops, (b) Temperature dependence of ε_r.

Table 5.2 The piezoelectric and dielectric properties of Er-KNN-based ceramics prepared by SSR and sol-gel method.

Sample name	Preparing method	d_{33} (pC/N)	ε_r @1kHz	tan δ @1kHz
Er-KNLN-0	SSR	39	837	0.039
	Sol-gel	49	732	0.031
Er-KNLN-0.08	SSR	42	708	0.045
	Sol-gel	56	722	0.041

The piezoelectric and dielectric properties of Er-KNLN-x ceramics prepared by the SSR and sol-gel methods have been measured and compared in Table 5.2. The sol-gel-derived ceramics have larger d_{33} and lower tan δ than those of the SSR-derived ceramics, which is probable due to the finer and more uniform grains as mentioned in the SEM results (Figs. 5.8 and 5.10). In addition, the sol-gel-derived Er-KNLN-0.08 ceramic has the highest d_{33} of 56 pC/N.

5.5 Conclusions

Er-doped KNN and 2 mol% Er-doped KNLN ceramics have been successfully prepared using a sol-gel method. The ceramics possess perovskite structure, good compositional homogeneity, fine and uniform grains, resulting from the sol-gel process. For the KNN:Er-x ceramics, both the up-conversion emissions and luminescent efficiencies are improved, leading to very strong green emissions at a low quenching concentration of 2 mol% (x = 2). For the Er-KNLN-0.08 ceramic, the PL intensities of Vis up-conversion (especially green) and MIR emissions are higher than those of Er-KNLN-0 ceramic. As compared to the SSR-derived ceramics, the sol-gel-derived ceramics can be well-densified at a lower sintering temperature, and exhibit higher PL intensities, better d_{33} and lower tan δ. A moderate Li content is effective in enhancing Vis up-conversion emissions, d_{33} and T_c. The multifunctional performances of the sol-gel-derived Er-KNLN-0.08 ceramic could be applied for the design of new materials with optical and electric multifunction.

Chapter 6 Er/Pr-Doped KNN and Er/Yb-Doped KNN Ceramics

6.1 Introduction

As discussed in the previous chapters, Er^{3+} ions can be used as activators, without using any sensitizers, in KNN ferroelectric ceramics for exhibiting PL emissions. Although the outstanding PL properties of Er^{3+} have been systematically investigated in the Er-doped KNN ceramics, the pumping and emission efficiencies (especially the up-conversion luminescence efficiency) are not very high due to the weak ground state absorption of Er^{3+}. Yb^{3+} ions are often used as sensitizers for increasing the pumping efficiency of Er^{3+} because of the efficient energy transfer from Yb^{3+} to Er^{3+} ions (Liu, 2007, Gerner, 2005). In addition, the MIR emissions of Er^{3+} are not very strong because the emission lifetime of $^4I_{11/2}$ level is commonly shorter than that of $^4I_{13/2}$ level (Allain, 1991). Thereupon, codoping of Pr^{3+} with Er^{3+} ions has been considered as an effective approach to quench the lower $^4I_{13/2}$ level, thus increasing the MIR emissions (Pollnau, 2001, Zhu, 2007).

Modification of PL in RE-doped materials is a prospective technology to improve the properties of optoelectronic devices (Hao, 2011). The common approach is to modify the compositions of activators, sensitizers or hosts (Heer, 2003, Ye, 2010) so as to tune the distance between the dopant ions, vary the host symmetry and crystal field, or increase the probabilities of energy transfer from sensitizer to activator ions. However, these conventional chemical approaches are irreversible and ex-situ, and the changes in PL can only take place in different specimens. Apparently, it is of great significance to realize the modulation of PL in the same sample. Recently, Hao et al. have reported that the electric field-induced enhancement and modulation of up-conversion PL can be realized in epitaxial ferroelectric Yb/Er-codoped $BaTiO_3$ thin films in an in-situ and real-time manner (Hao, 2011). After the poling (i.e., the alignment of the ferroelectric polarization by an external electric field), the PL intensity of Pr-doped $Bi_{0.5}Na_{0.5}TiO_3$ ceramics has been shown to increase remarkably by about 35% (Tian, 2013). Similar results have also been obtained in Er-doped $Bi_{0.5}Na_{0.5}TiO_3$ and Pr-doped $BaTiO_3$-$CaTiO_3$ ceramics (Du, 2013b, Zou, 2013). It has been suggested that the enhancement of PL performances after poling is attributed to the change of the band gap of host by the local electric field (Zou, 2013).

In this chapter, 2 mol% Er and y mol% Pr codoped KNN (Er-KNN-Pr-y) ceramics and 1 mol% Er and z mol% Yb codoped KNN (Er-KNN-Yb-z) ceramics have been fabricated by the SSR method. The sintering temperatures of these ceramics are 1110-1150°C. The effects of Pr^{3+} and Yb^{3+} ions on the PL properties of Er^{3+} have been investigated respectively. The relationships between Vis up-conversion emissions, NIR and MIR emissions of Er^{3+} ions under the excitation of 980 nm have been studied and elucidated in terms of the effects of Pr^{3+} ions and energy transfer processes between Er^{3+} and Pr^{3+} ions. The PL intensities of the ceramics can be enhanced by poling and the corresponding mechanism has been discussed. Yb^{3+} ions are used as the sensitizer to codope with Er^{3+} in the KNN host to improve the emission efficiency as well as PL intensities. The relationship between Yb^{3+} content and emission intensities of Er^{3+} have been studied in detail.

6.2 Er/Pr-doped KNN ceramics

6.2.1 XRD

The XRD patterns of the Er-KNN-Pr-y ceramics are shown in Fig. 6.1. All the ceramics are of the perovskite structure, suggesting that Er^{3+} and Pr^{3+} ions have diffused into the KNN lattice. No obvious impurity phase has been detected in the ceramics except for Er-KNN-Pr-1 (y = 1), which has the impurity phase of $PrNbO_4$ (JCPDS No. 23-1379) as shown between 25 °-30 ° in Fig. 6.1. As y (the content of Pr) increases, the diffraction peaks around 45.5 ° remain the same, indicating that the doping of Pr^{3+} ions does not change the phase structure of the KNN host.

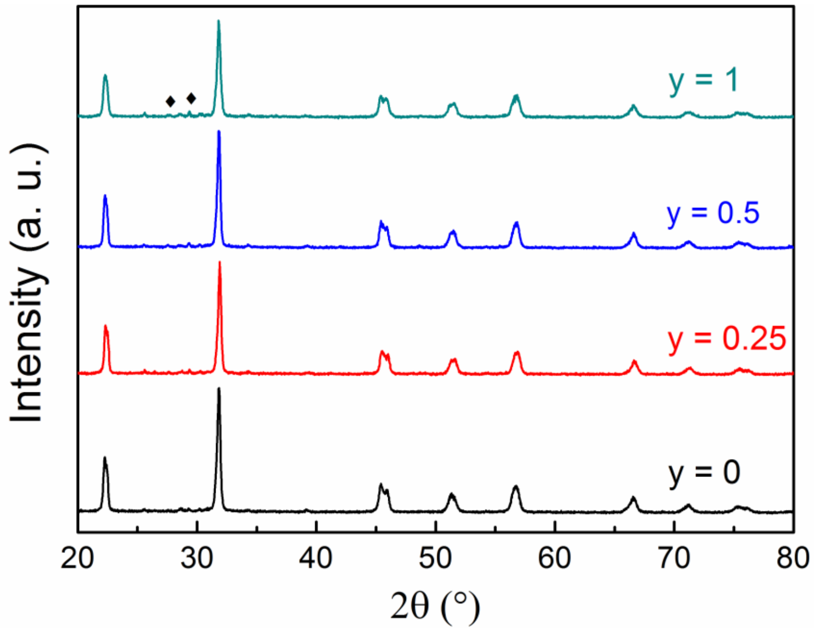

Figure 6.1 XRD patterns of the Er-KNN-Pr-y ceramics.

6.2.2 PL properties

6.2.2.1 Emissions from Er^{3+}

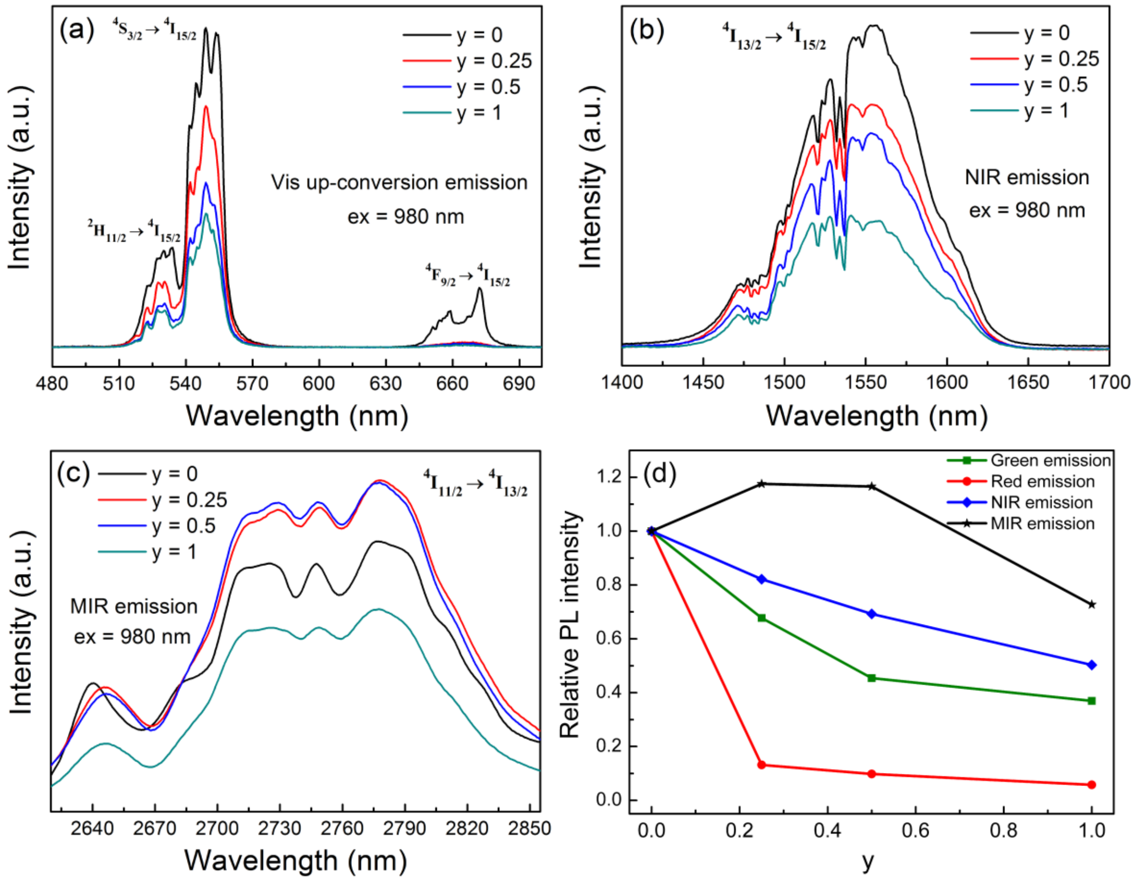

Figure 6.2 PL spectra of the Er-KNN-Pr-y ceramics under the excitation of 980 nm. (a) Vis up-conversion emissions, (b) NIR emissions, (c) MIR emissions, (d) Variations of the relative (integrated) PL intensities.

Fig. 6.2 shows the PL emission spectra of the Er-KNN-Pr-y ceramics under the excitation of 980 nm. All the ceramics exhibit three Vis up-conversion emission bands in 510-537 nm (green), 537-585 nm (green) and 640-690 nm (red), and two down-conversion emission bands in 1.4-1.7 μm (NIR) and 2.6-2.85 μm (MIR). The Vis emission bands are attributed to the transitions $^2H_{11/2} \rightarrow {}^4I_{15/2}$, $^4S_{3/2} \rightarrow {}^4I_{15/2}$ and $^4F_{9/2} \rightarrow$

$^4I_{15/2}$ of Er^{3+}, respectively, while the infrared emission bands are attributed to the transitions $^4I_{13/2} \rightarrow {}^4I_{15/2}$ and $^4I_{11/2} \rightarrow {}^4I_{13/2}$, respectively. Each emission band is split into several peaks because of the Stark effect induced by the crystal field in the KNN host. As shown in Fig. 6.2d, the relative (integrated) PL intensities of the green, red and NIR emission bands decrease with increasing y. Among them, the PL intensity of the red emission band decreases most significantly and becomes almost zero after the doping of Pr^{3+} (Fig. 6.2a). On the other hand, the spectral shape of the MIR emission changes slightly after the doping of Pr^{3+} ions, and the PL intensity increases by ~20% as y increases to 0.25 and 0.5 (Fig. 6.2d).

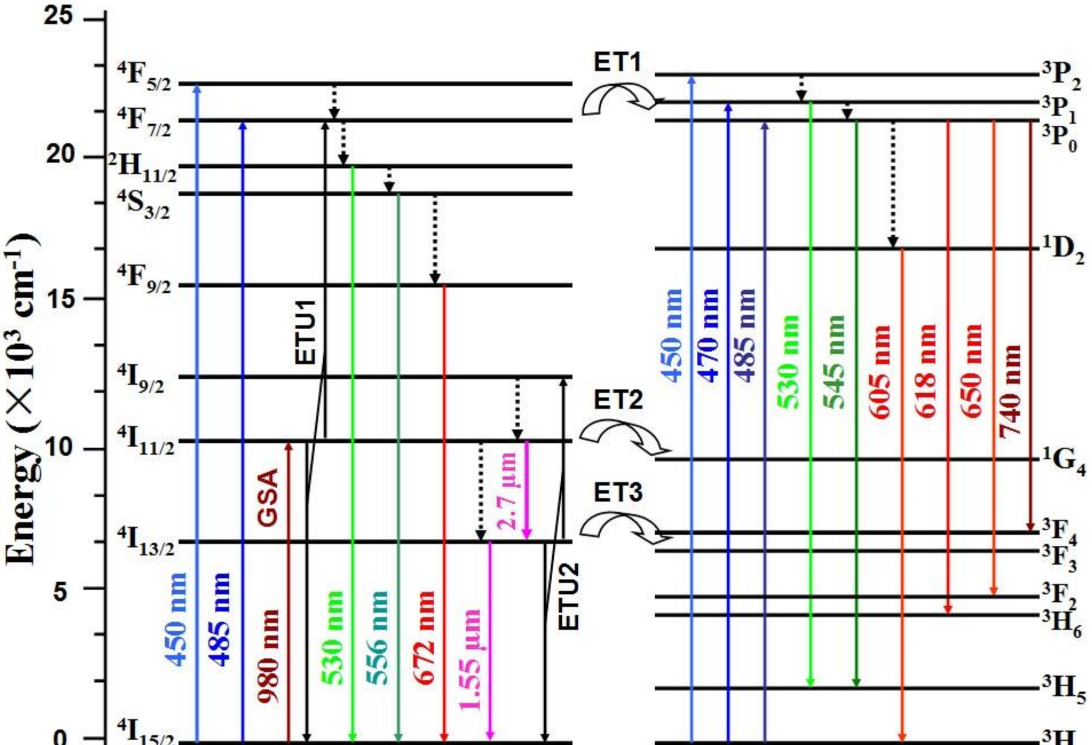

Figure 6.3 Energy levels diagram of Er^{3+} and Pr^{3+} ions.

Fig. 6.3 shows the energy level diagrams of Er^{3+} and Pr^{3+} ions together with the relevant energy transfer mechanisms. Upon pumping at 980 nm, Er^{3+} ions are first excited from the $^4I_{15/2}$ ground state to the $^4I_{11/2}$ level by the GSA process. Some of the excited Er^{3+} ions in the $^4I_{11/2}$ level may undergo the ETU1 process to populate the $^4F_{7/2}$ level. Then, MPR processes occur, populating the $^2H_{11/2}$, $^4S_{3/2}$, and $^4F_{9/2}$ levels in sequence and then generating the green ($^2H_{11/2}/^4S_{3/2} \rightarrow {}^4I_{15/2}$) and red ($^4F_{9/2} \rightarrow {}^4I_{15/2}$) emissions by radiative relaxation. Due to the small energy gap between the $^2H_{11/2}$ and $^4S_{3/2}$ levels and large energy gap between the $^4S_{3/2}$ and $^4F_{9/2}$ levels, the green emissions at 530 nm and the red emissions at 672 nm are weak, meanwhile the green emissions at 556 nm become very strong, as shown in Fig. 6.2a. The addition of Pr^{3+} ions will increase the maximum emission cross section of the Er-KNN-Pr-y ceramics (Jackson, 2000, Xu, 2011), which is favor for the ET process between Er^{3+} and Pr^{3+} ions. Owing to the similar energy levels, some of the excited Er^{3+} ions in the $^4F_{7/2}$ level may relax non-radiatively to the $^4I_{15/2}$ ground state via transferring energy (ET1) to excite Pr^{3+} ions from the $^3H_4$ ground state to the $^3P_1$ or $^3P_0$ level. As a result, the green and red emissions of Er^{3+} ions are suppressed. Nevertheless, the excited Pr^{3+} ions may relax to the ground state via similar mechanisms to generate green (530 nm and 545 nm) and red (605 nm, 618 nm and 650 nm) emissions (Fig. 6.3). Probably due to the wider emission range and lower efficiencies (most of them do not relax to the ground state), the Vis emission of Pr^{3+} ions cannot completely compensate the quenched emissions of Er^{3+} ions, and thus leading to the decreases in the observed PL intensities. As illustrated in Fig. 6.3, there is another energy transfer process ET2 that is more efficient than ET1 and should be the major cause for the significant decreases in the observed PL intensities of the Vis emission bands, in particular the red emission (Fig. 6.2d). As the populations of the $^4I_{11/2}$ as well as $^4F_{7/2}$ levels are reduced because of ET2, the probabilities of the transitions $^2H_{11/2}/^4S_{3/2}/^4F_{9/2} \rightarrow {}^4I_{15/2}$ are decreased, and thus weakening the corresponding green and red emissions. As the excited Pr^{3+} ions in the $^1G_4$ level will not generate any Vis emissions, the observed PL intensities for the Vis emission bands remain decreased. Clearly, the decreases in the PL intensities would increase with increasing concentration of Pr^{3+} (Fig. 6.2d).

Owing to ET2, ETU1 process is suppressed and the population of the $^4I_{11/2}$ level then remains large, and thus favoring the infrared emissions (Fig. 6.3) (Tian, 2011b). Some of the excited Er^{3+} ions in the $^4I_{11/2}$ level may relax radiatively to the $^4I_{13/2}$ level, generating the MIR emission as shown in Fig. 6.2c. Some of the excited Er^{3+} ions may also relax to the $^4I_{13/2}$ level non-radiatively. The resulting Er^{3+} ions in the $^4I_{13/2}$ level then relax radiatively to the $^4I_{15/2}$ ground level, producing the NIR emission (Fig. 6.3b). As illustrated in Fig. 6.3, the excited Er^{3+} ions in the $^4I_{13/2}$ level may relax via the energy transfer process ET3 or ETU2 ($^4I_{13/2} + {}^4I_{13/2} \rightarrow {}^4I_{9/2} + {}^4I_{15/2}$), both resulting in the reduction in the NIR emission (Pollnan, 1997). ET3 is much more efficient than ET2 because of its remarkably larger oscillator strength (Golding, 2000). The excited Pr^{3+} ions in the $^3F_3$ or $^3F_4$ level (resulting from ET3) will relax back to the $^3H_4$ ground level non-radiatively, producing no PL emission. On the other hand, ETU2 process would enhance the MIR emission via the continuous pumping of the $^4I_{9/2}$ and then $^4I_{11/2}$ levels. As a result, the observed PL intensity of the MIR emission increases while that of the NIR emission decreases with increasing concentration of Pr^{3+} as shown in Fig. 6.2d.

6.2.2.2 Emissions from both Er^{3+} and Pr^{3+}

The PLE spectra of the Er-KNN-Pr-y ceramics monitoring at 556 nm (emitting wavelength of Er^{3+} ions are shown in Fig. 6.4a, while their Vis down-conversion PL emission spectra are shown in Fig. 6.4b. A series of peaks attributed to the excitation of Er^{3+} ions from the $^4I_{15/2}$ ground level to the $^4G_{11/2}$, $^2H_{9/2}$, $^4F_{3/2}$, $^4F_{5/2}$ and $^4F_{7/2}$ levels, respectively, are observed (Fig. 6.4a). There are also a few weak peaks attributed to the excitation of Pr^{3+} ions found in the range of 450-480 nm. This confirms that the green emission observed in the Er-KNN-Pr-y ceramics is mainly originated from the excitation of Er^{3+} ions rather than Pr^{3+} ions or other ions in the KNN lattice. Among the peaks, the one located at 485 nm is the strongest, indicating that the most efficient excitation source for the ceramics should be of 485 nm for down-conversion processes. As shown in Fig. 6.4b, the ceramics exhibit a total of seven down-conversion emission bands under the excitation of 485 nm. The two green emissions at 530 and 556 nm and red emission at 672 nm are attributed to the transitions of Er^{3+} ions, while the other four red emissions are attributed to the transitions of Pr^{3+} ions. Although the down-conversion emission bands of Er^{3+} ions occur at similar wavelengths to their up-conversion emission bands, there are discrepancies between their spectra shapes as well as relative PL intensities due to their distinct PL mechanisms.

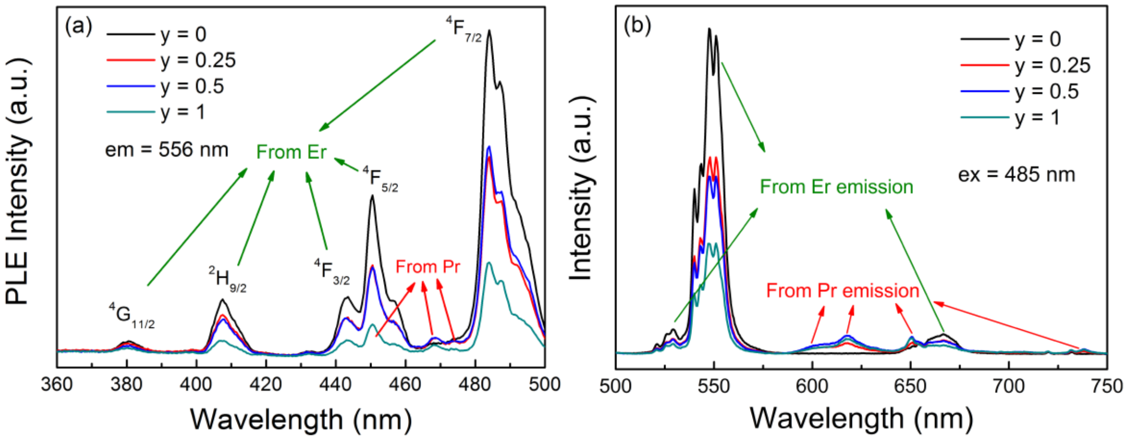

Figure 6.4 (a) PLE spectra of the Er-KNN-Pr-y ceramics monitoring at 556 nm, (b) Vis down-conversion emission spectra of the Er-KNN-Pr-y ceramics under the excitation of 485 nm.

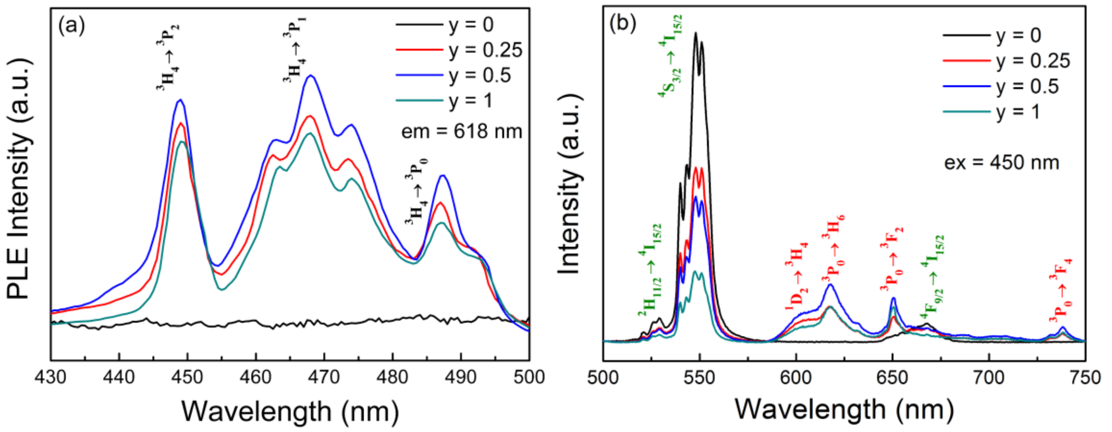

Figure 6.5 (a) PLE spectra of the Er-KNN-Pr-y ceramics monitoring at 618 nm, (b) Vis down-conversion emission spectra of the Er-KNN-Pr-y ceramics under the excitation of 450 nm.

To study the PL characteristics of Pr^{3+} ions, the PLE spectra of the Er-KNN-Pr-y ceramics monitoring at the emitting wavelength of Pr^{3+} (618 nm, Fig. 6.3) have also been measured, giving the results shown in Fig. 6.5a. Clearly, because of the absence of

Pr^{3+} ions, no excitation peak is observed for the Er-KNN-Pr-0 ceramic. Three excitation bands attributed to the transitions $^3H_4 \rightarrow {}^3P_2$, $^3H_4 \rightarrow {}^3P_1$, and $^3H_4 \rightarrow {}^3P_0$ of Pr^{3+} ions are observed at 450 nm, 470 nm and 485 nm, respectively, for the ceramics with $y > 0$. Although the excitation band at 470 nm is the strongest, 470-nm light cannot activate the PL characteristics of Er^{3+} ions (Fig. 6.3) and then should not be used as the excitation source for the ceramics. Accordingly, for activating both Er^{3+} and Pr^{3+} ions, the excitation source at 450 nm is used for measuring the down-conversion emission spectra (Fig. 6.5b). Similar to the emission spectra measured under the excitation of 485 nm, a total of seven emission bands attributed to the transitions $^2H_{11/2} \rightarrow {}^4I_{15/2}$ (Er^{3+}), $^4S_{3/2} \rightarrow {}^4I_{15/2}$ (Er^{3+}), $^1D_2 \rightarrow {}^3H_4$ (Pr^{3+}), $^3P_0 \rightarrow {}^3H_6$ (Pr^{3+}), $^3P_0 \rightarrow {}^3F_2$ (Pr^{3+}), $^4F_{9/2} \rightarrow {}^4I_{15/2}$ (Er^{3+}) and $^3P_0 \rightarrow {}^3F_4$ (Pr^{3+}) are observed. Among them, the emission band attributed to the transition $^4S_{3/2} \rightarrow {}^4I_{15/2}$ (556 nm) of Er^{3+} is the strongest. Although the excited Pr^{3+} ions may emit green photons at 530 and 545 nm resulting from the transitions $^3P_1 \rightarrow {}^3H_5$ and $^3P_0 \rightarrow {}^3H_5$ (Fig. 6.3), the green emission (556 nm) of Er^{3+} ions is very strong and hence remains dominant.

Similar to the up-conversion PL emissions (Fig. 6.2a), the observed PL intensities of the green emission bands (for the down-conversion emissions under both the excitation of 485 and 450 nm) decrease with increasing concentration of y. These should also be due to the suppression of the Vis emissions of Er^{3+} ions arisen from the energy transfer process ET1 (Fig. 6.3). Owing to the small energy gap, most of the excited Pr^{3+} ions in the $^3P_1$ level (both from GSA and ET1) will relax rapidly to the $^3P_0$ level non-radiatively, and then relax radiatively to the $^3H_5$, $^3H_6$, $^3F_2$ or $^3F_4$ levels, giving the green (545 nm) or red (605-740 nm) emissions. As a result, unlike the up-conversion emissions, the PL intensities of the red emission bands generally increase and then decrease with increasing y, reaching a maximum at y = 0.5. It seems that the (relative) changes in the red emissions of the ceramics irradiated with 450-nm light are stronger than those under the excitation of 485 nm. This may be due to the weaker emissions of Er^{3+} ions resulted from the less efficient excitation at 450 nm.

On the basis of the emission spectra shown in Figs. 6.4b and 6.5b, the CIE color coordinates of the Er-KNN-Pr-y ceramics have been calculated, giving the results shown in Fig. 6.6. Under the excitation of 485 nm, the emission color changes only slightly toward the red color and remains mainly in yellowish green region with increasing y. On the other hand, due to the larger changes in the red emissions (Figs. 6.4 and 6.5), the emission color of the ceramics irradiated with 450-nm light exhibit a clear red shift, changing from yellowish green to yellow as y increases.

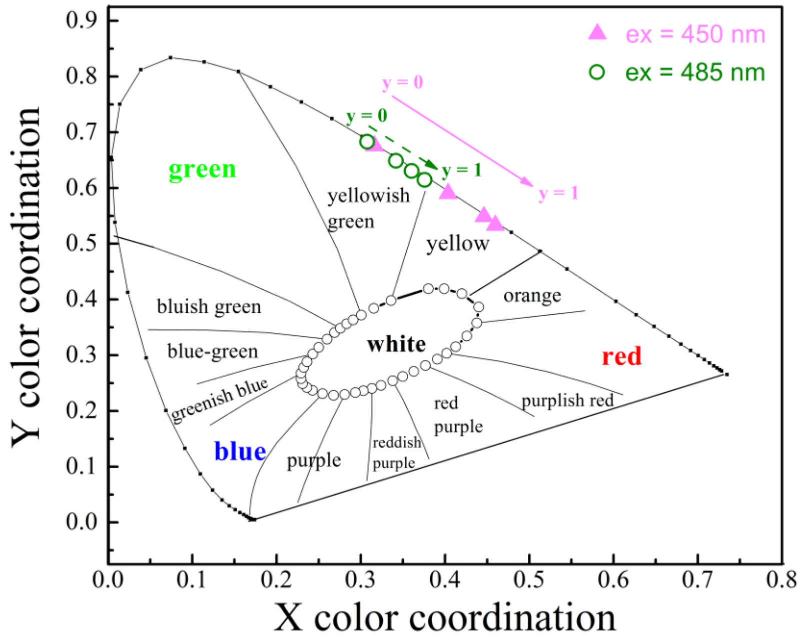

Figure 6.6 The CIE color coordinates of the Er-KNN-Pr-y ceramics under the excitation of 485 nm and 450 nm.

6.2.2.3 Poling effect on PL properties

For studying the poling effect, silver electrodes were fired on the top and bottom surfaces of the samples, and then the samples were poled under a dc field of 5 kV/mm along the thickness direction at 120°C in silicone oil for 30 min. After that, the electrodes were removed carefully to ensure that the surfaces were as smooth as those of the un-poled samples for the PL measurements.

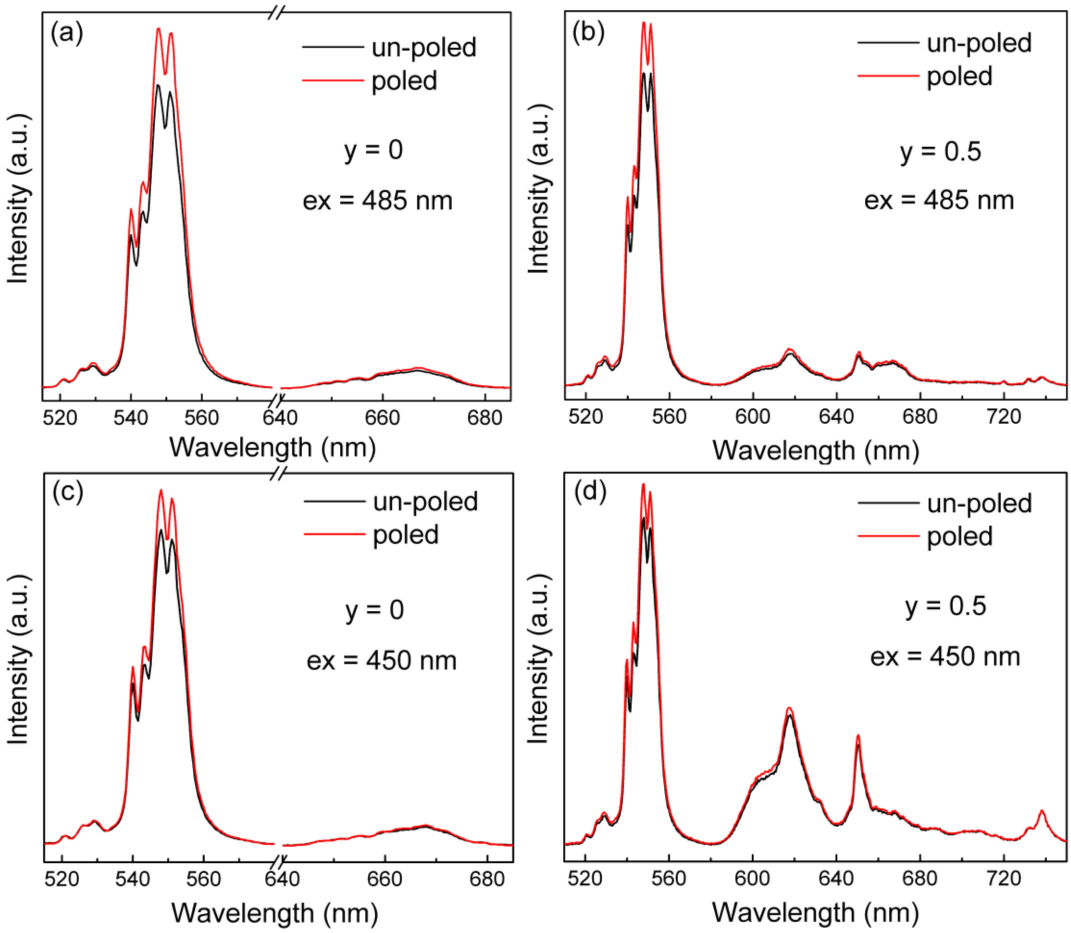

Figure 6.7 Vis down-conversion emission spectra of the un-poled and poled Er-KNN-Pr-y ceramics under the excitation of different wavelengths: (a) y = 0, 485 nm; (b) y = 0.5, 485 nm; (c) y = 0, 450 nm; (d) y = 0.5, 450 nm.

Fig. 6.7 compares the Vis down-conversion emission spectra of the un-poled and poled Er-KNN-Pr-y ceramics under the excitation of 485 and 450 nm, while their variations of the relative (integrated) PL intensity of the green and red emissions are shown in Fig. 6.8. It can be seen that all the poled ceramics exhibit stronger Vis emissions, in particular the green emissions. For each excitation, the enhancements in the green emissions are larger than those in the red emissions. On the other hand, the enhancements in both emissions for the ceramics under the excitation of 485 nm are greater. These should be mainly attributed to the unique structure of the ferroelectric KNN host. After poling, remanent polarization and then strain are induced in the ferroelectric host, and thus resulting in lattice distortion and structural asymmetry (or lower symmetry) around Er^{3+} and Pr^{3+} ions. The resulting uneven crystal field components can mix opposite-parity states into the 4f configurational levels and then increase the 4f-4f electric dipole transition probabilities of the dopant ions (Hao, 2011).

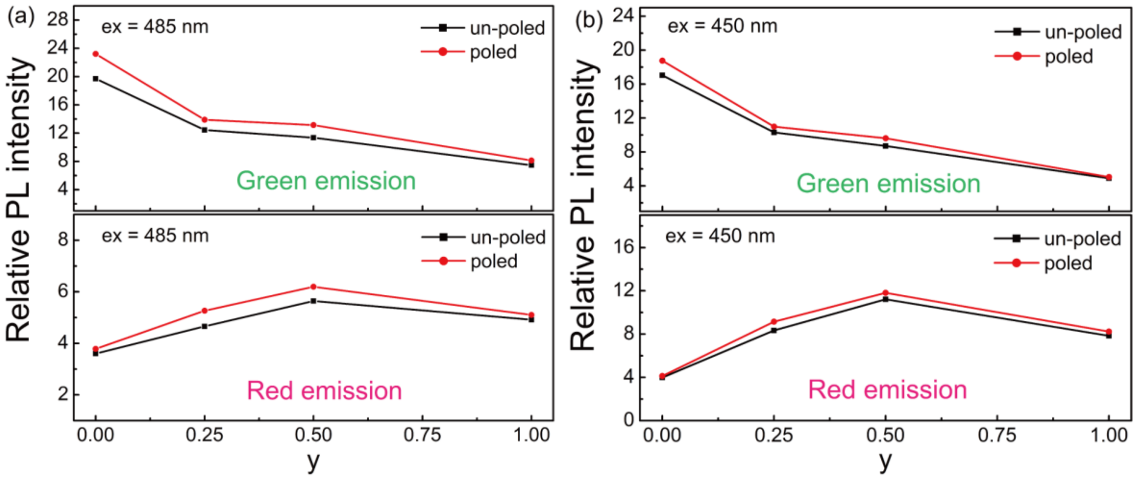

Figure 6.8 Variations of the relative PL intensities for the un-poled and poled Er-KNN-Pr-y ceramics under the excitation of (a) 485 nm and (b) 450 nm.

6.3 Er/Yb-doped KNN ceramics

6.3.1 XRD

Fig. 6.9 shows the XRD patterns of the Er-KNN-Yb-z ceramics. All the ceramics are of perovskite structure, suggesting that Er^{3+} and Yb^{3+} ions have diffused into the KNN lattice. For the ceramics with $z \geq 4$, a small amount of impurity phase $YbNbO_4$ (JCPDS No. 23-1480) is observed. The diffraction peaks around 45.5 ° remain almost the same, indicating that all the ceramics own the same orthorhombic phase and the microstructure is not affected by the doping of Yb.

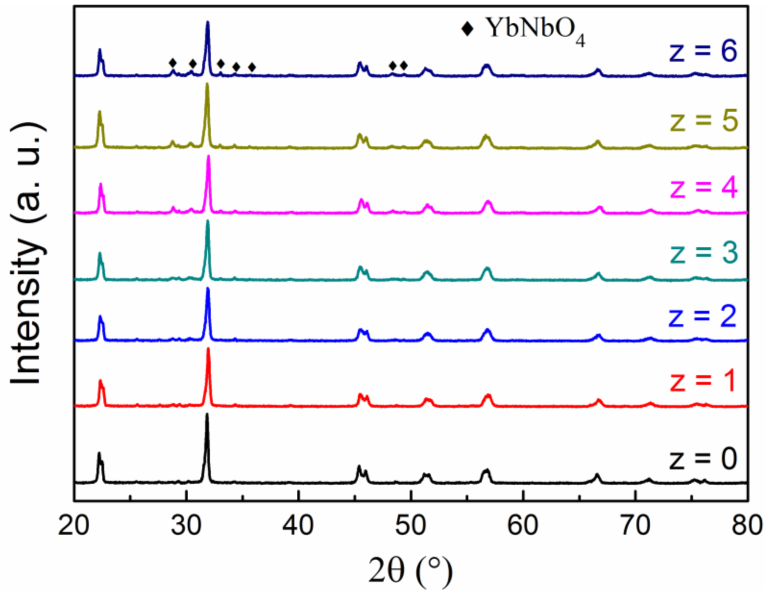

Figure 6.9 XRD patterns of the Er-KNN-Yb-z ceramics.

6.3.2 Vis up-conversion emissions

Fig. 6.10 shows the Vis up-conversion emissions of the Er-KNN-Yb-z ceramics. All the emission bands are attributed to the Er^{3+} ions in the ceramics, including four main emission bands in 510-537 nm (green), 537-580 nm (green), 640-690 nm (red) (Fig. 6.10a) and 480-500 nm (weak blue) (Fig. 6.10b). As mentioned in Chapter 5, the blue emission of Er^{3+} ions is only obtained in sol-gel-derived Er-doped KNN ceramics on the condition that the overall PL intensity is very strong. As shown in Fig. 6.10b, the blue emission can also be observed in the SSR-derived Er/Yb-doped KNN ceramics, indicating that the overall PL intensities of the ceramics are enhanced significantly after codoping of Yb^{3+} ions.

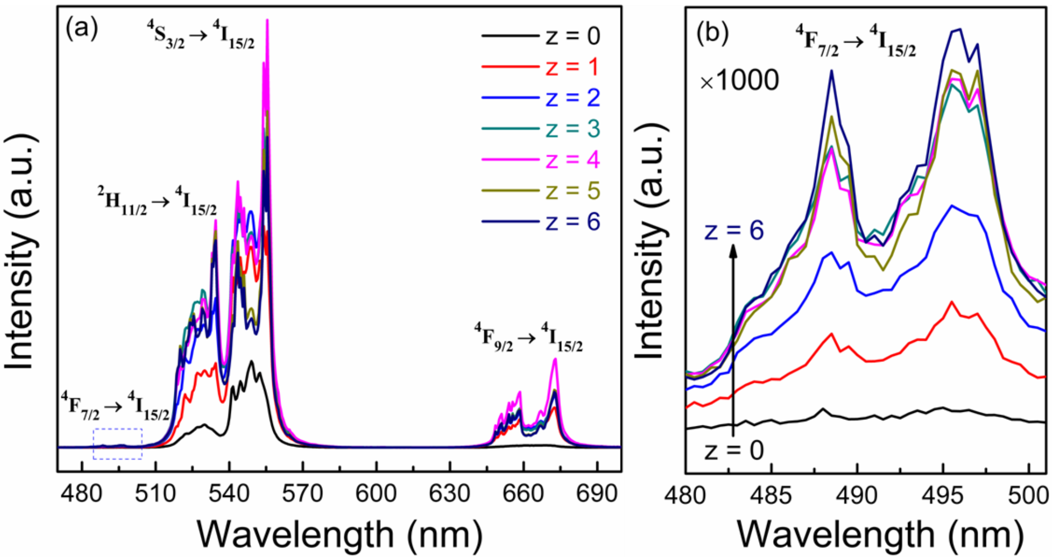

Figure 6.10 Vis up-conversion emissions of the Er-KNN-Yb-z ceramics. (a) Green and red emissions, (b) Enlarged blue emissions.

6.3.3 NIR and MIR emissions

The NIR emissions of Er-KNN-Yb-z ceramics are shown in Fig. 6.11. The emission band centered at 1.53 μm is attributed to the $^4I_{13/2} \rightarrow {}^4I_{15/2}$ transition of Er^{3+}. The emission intensity decreases with increasing z (the Yb content), followed with a gradual change in the spectral shape. The MIR emission of the ceramics is shown in Fig. 6.12. The emission is attributed to the transition $^4I_{11/2} \rightarrow {}^4I_{13/2}$. The emission intensity increases with increasing z and reaches a maximum at z = 4. Probably due to the different levels of splitting induced by the codoping of Yb, emission peaks of different shapes are observed.

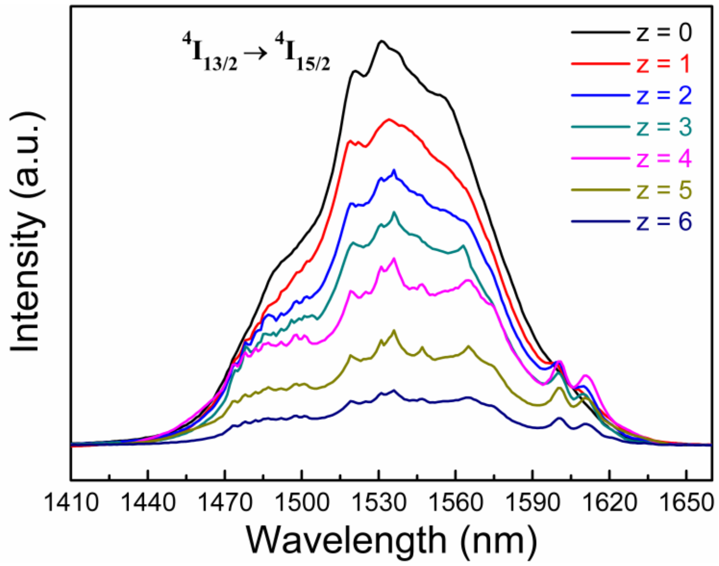

Figure 6.11 NIR emissions of the Er-KNN-Yb-z ceramics.

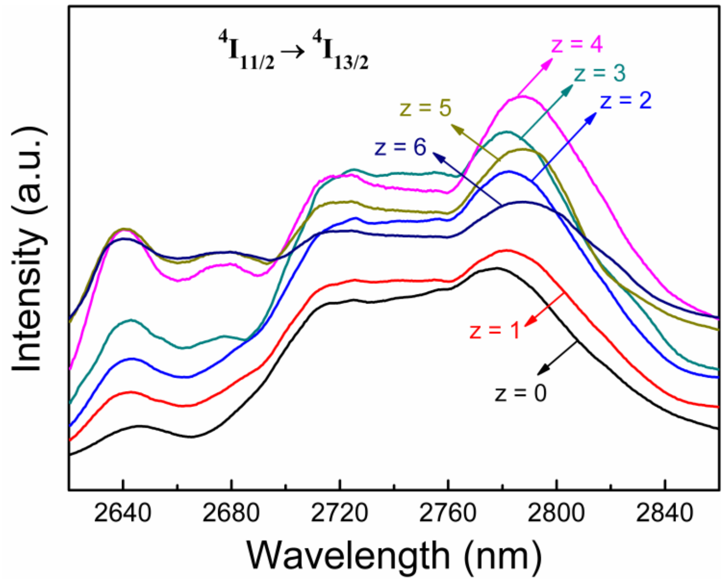

Figure 6.12 MIR emissions of the Er-KNN-Yb-z ceramics.

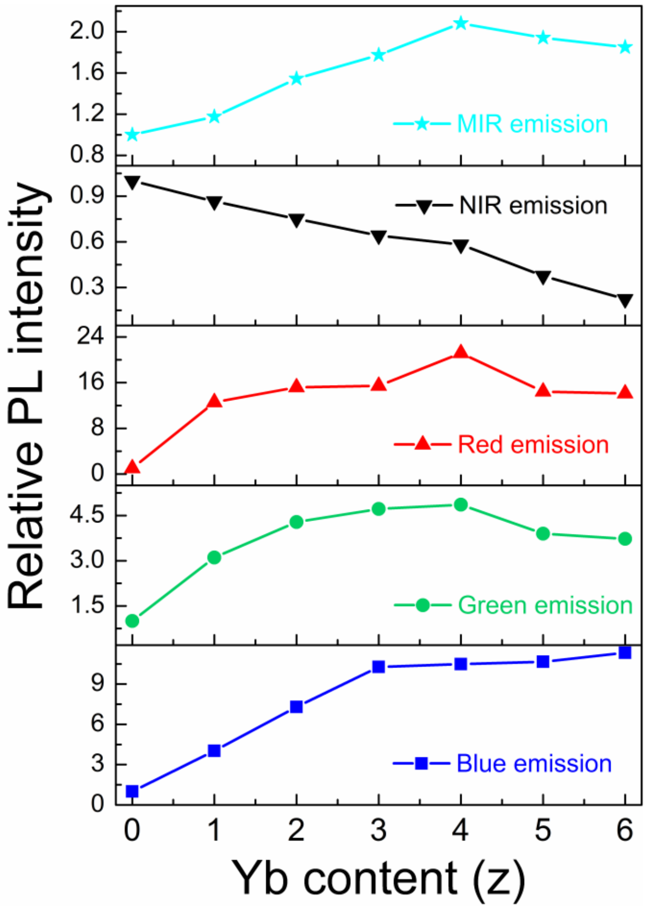

Figure 6.13 Variations of the relative PL intensities of the Er-KNN-Yb-z ceramics.

The variations of the relative (integrated) PL intensities of the blue (480-500 nm), green (510-580 nm), red (640-680 nm), NIR (1.41-1.65 μm) and MIR (2.62-2.85 μm) emission bands with the Yb content for the Er-KNN-Yb-z ceramics are shown in Fig. 6.13. The PL intensitiy of blue emission band increases with increasing z, and becomes almost saturated at z = 3. The PL intensities of green, red and MIR emission bands exhibit similar dependences on z. Among them, the enhancement for the red emission is the largest (at z = 4), about 20 times larger than that of Er-doped KNN (i.e., z = 0). The great enhancement of Vis up-conversion (both red and green) emissions have also been reported for Er^{3+}/Yb^{3+}-codoped $KNbO_3$ phosphors (Balakrishnaiah, 2009). However, unlike the Vis and MIR emissions, the PL intensity of the NIR emission decreases as z increases.

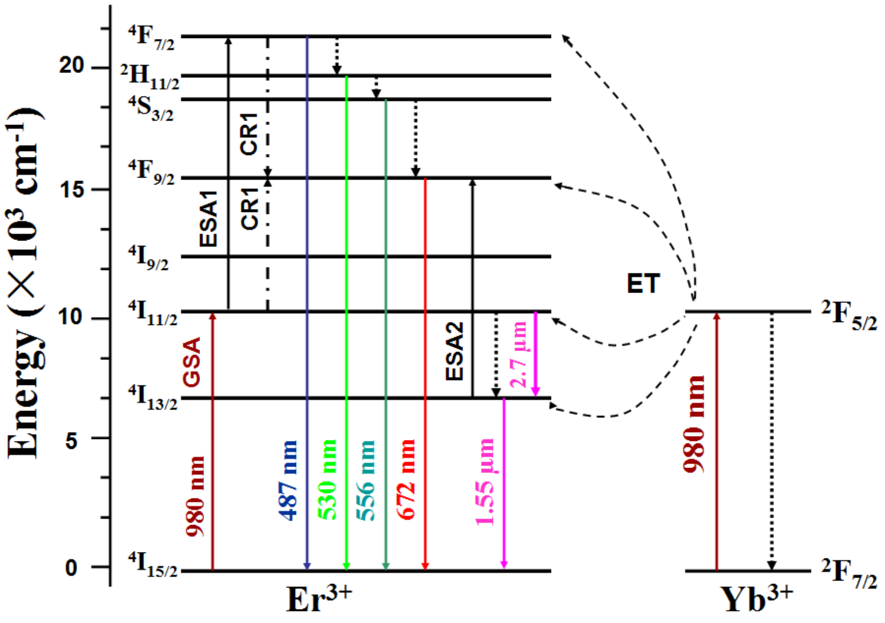

Figure 6.14 Energy levels diagram of Er^{3+} and Yb^{3+} ions.

The energy levels diagram of Er^{3+} and Yb^{3+} ions are illustrated in Fig. 6.14. The up-conversion emission mechanism for the Er-doped KNN ceramics has been discussed in the previous chapters. With the incorporation of Yb^{3+} ions in the Er-KNN-Yb-z ceramics, an efficient ET process from Yb^{3+} to Er^{3+} ($^2F_{5/2}(Yb^{3+})$ + $^4I_{15/2}(Er^{3+})$ → $^2F_{7/2}(Yb^{3+})$ + $^4I_{11/2}(Er^{3+})$) may take place under the excitation of 980 nm owing to the larger absorption cross-section of Yb^{3+} ($^2F_{7/2} \rightarrow {}^2F_{5/2}$) (Balakrishnaiah, 2009). This ET process is dominant for populating the $^4I_{11/2}$ (Er^{3+}) excited level in the Er/Yb-codoped system. For the up-conversion process to populate the $^4F_{7/2}$ (Er^{3+}) excited level, two mechanisms are involved, i.e. ESA1 from $^4I_{11/2}(Er^{3+})$ + photon → $^4F_{7/2}(Er^{3+})$ and ET from $^2F_{5/2}(Yb^{3+})$ + $^4I_{11/2}(Er^{3+})$ → $^2F_{7/2}(Yb^{3+})$ + $^4F_{7/2}(Er^{3+})$. Herein, the ET process is easier to occur in the up-conversion process. However, the emission intensities become saturated at around z = 4, and then slightly decrease with increasing Yb content, which is probable due to the backward ET process from Er^{3+} to Yb^{3+} ion at high Yb contents (Hwang, 2000).

The enhancement of up-conversion red emission is the largest (Fig. 6.13) and the corresponding mechanism is different from that of the blue and green emissions. Some Er^{3+} ions in the $^4I_{11/2}$ level may decay radiatively to the $^4I_{13/2}$ level to produce the 2.7 μm MIR emissions, and other Er^{3+} ions can decay non-radiatively to the $^4I_{13/2}$ level through the MPR process. Both the Er^{3+} ions in $^4I_{11/2}$ and $^4I_{13/2}$ levels may be further excited to the $^4F_{9/2}$ state via one of the following processes (Zhang, 2006): (1) ESA2 from $^4I_{13/2}(Er^{3+})$ + photon → $^4F_{9/2}(Er^{3+})$, (2) phonon-assisted energy transfer (PAET, which contains the ESA2 process) from Yb^{3+}: $^2F_{5/2}(Yb^{3+}) + {}^4I_{13/2}(Er^{3+}) \rightarrow {}^2F_{7/2}(Yb^{3+}) + {}^4F_{9/2}(Er^{3+})$, (3) CR1 from Er^{3+}: $^4I_{11/2}(Er^{3+}) + {}^4F_{7/2}(Er^{3+}) \rightarrow {}^4F_{9/2}(Er^{3+}) + {}^4F_{9/2}(Er^{3+})$ and (4) ET from the $^4I_{11/2}$ level of adjacent Er^{3+}: $^4I_{11/2}(Er^{3+}) + {}^4I_{13/2}(Er^{3+}) \rightarrow {}^4I_{15/2}(Er^{3+}) + {}^4F_{9/2}(Er^{3+})$. As the energy can be efficiently transferred from Yb^{3+} ($^2F_{5/2}$) to Er^{3+} ($^4I_{11/2}$) ions, the ESA2 and PAET processes become dominating, and hence enhancing the red emission.

The above processes for the up-conversion red emission can influence the NIR emission. The efficient ESA2 and PAET processes will greatly decrease the population of Er^{3+} in the $^4I_{13/2}$ level and then the PL intensities of the NIR emission with increasing the Yb content (Fig. 6.13). In addition, the increase in the MIR emission with increasing z ($z \leq 4$) is mainly originated from the ET process from Yb^{3+} ($^2F_{5/2}$) to Er^{3+} ($^4I_{11/2}$). The decrease in the MIR emission at z > 4 should be attributed to the backward ET process from Er^{3+} ($^4I_{11/2}$) to Yb^{3+} ($^2F_{5/2}$).

6.4 Conclusions

The PL properties of the Er/Pr-doped KNN and Er/Yb-doped KNN ceramics have been investigated. For the Er-KNN-Pr-y ceramics, under the excitation of 980 nm, all the ceramics exhibit strong green and weak red up-conversion emissions as well as NIR and MIR down-conversion emissions. The observed PL intensities of the green, red and NIR emissions decrease, while that of the MIR emission increases with increasing the content of Pr^{3+}. The phenomena have been elucidated in terms of energy transfer processes between Er^{3+} and Pr^{3+} ions. Under the excitation of 450 nm, simultaneous green and red down-conversion emissions of Er^{3+} and Pr^{3+} ions can be realized, and the emission color of the ceramics can be tuned via the concentration of Pr^{3+} in a wider range from yellowish green to yellow. The PL intensities of the ceramics can be enhanced by the lattice distortion and structural asymmetry induced by the alignment of polarization of the ferroelectric host. For the Er-KNN-Yb-z ceramics, the effects of Yb^{3+} on the PL intensities of Er^{3+} have been studied. Under the excitation of 980 nm, Vis blue, green and red emissions, as well as NIR and MIR emissions can be obtained. After the codoping of Yb^{3+} ions, the PL intensities of the Vis and MIR emissions are greatly enhanced due to the efficient energy transfer processes from Yb^{3+} to Er^{3+}. The optimal Yb^{3+} concentration is 4 mol% and the corresponding mechanisms that influence the PL intensities have been elaborated. Both Pr^{3+} and Yb^{3+} ions are effective sensitizers for changing the PL emissions of the Er-doped KNN ceramics.

Chapter 7 Er-Doped KNN-LB Transparent Ceramics

7.1 Introduction

High performance EO materials with both good optical transparency and large EO effects have attracted intensive interest because of the extensive optoelectronic applications including optical switches, filters, modulators and data processing devices (Hartling, 1987). $LiNbO_3$ single crystal, the industry benchmark of EO materials, is used in the telecoms market. However, it has limitations for widespread applications due to the drawbacks containing low EO effect (r_c = 19.9 pm/V), high temperature dependency, small available size and high cost (Jiang, 2005). Compared to the $LiNbO_3$ single crystals, EO ceramics usually feature stronger EO responses, ceramic ruggedness, easy fabrication, large available size and low fabrication cost (Li, 2013b). The EO ceramics possessing strong EO response and good mechanical properties, such as PLZT and PMN-PT, which have been widely studied and applied in various optoelectronic devices. Nevertheless, these EO ceramics are lead-based with the lead content over 60 wt%, so that there is an urgent need to explore lead-free EO ceramics for environmental protection reasons.

It has been recently reported that $(K_{0.5}Na_{0.5})_{1-x}Li_xNb_{1-x}Bi_xO_3$ lead-free ceramics exhibit both good optical transparency and EO responses, giving a large effective linear

EO coefficient (r_c) in the range of 120-200 pm/V (Li, 2013a). To the best of our knowledge, there are no other lead-free transparent ceramics owning comparative EO properties. The $(K_{0.5}Na_{0.5})_{1-x}Li_xNb_{1-x}Bi_xO_3$ transparent ceramics were fabricated by the hot-press sintering method, which is a promising technique and has been used to successfully prepare dense and high performance lead-based EO ceramics (Jaeger, 1962). However, the hot-pressing sintering technique has some disadvantages as compared with the pressureless sintering, such as the requirement of technical pressure furnace with long heating and cooling time, high-cost manufacturing processes and low production volume and efficiency.

In this chapter, $(K_{0.5}Na_{0.5})_{1-x}Li_xNb_{1-x}Bi_xO_3$ (KNN-LB-x, x = 0- 0.10) and 1 mol% Er-doped $(K_{0.5}Na_{0.5})_{1-x}Li_xNb_{1-x}Bi_xO_3$ (Er-KNN-LB-x, x = 0.04-0.08) transparent ceramics have been successfully fabricated by pressureless sintering through the same SSR method mentioned in the previous chapters. After the doping of Er^{3+} ions, the EO, PL and ferroelectric properties of the Er-KNN-LB-x transparent ceramics have been investigated for exploring the multifunctional photonic applications.

7.2 KNN-LB transparent ceramics

7.2.1 XRD

Fig. 7.1 shows the XRD patterns of KNN-LB-x (x = 0-0.10) ceramics. All the ceramics possess a single-phase perovskite structure (Fig. 7.1a), suggesting that Li^+ ions have entered the A-sites ($(K_{0.5}Na_{0.5})^+$ sites) and Bi^{3+} ions have diffused into the B-sites (Nb^{5+} sites) according to the designed formula $(K_{0.5}Na_{0.5})_{1-x}Li_xNb_{1-x}Bi_xO_3$. The enlarged

(220) and (002) peaks at ~45.5 ° of the KNN-LB-*x* ceramics are shown in Fig. 7.1b. As *x* increases, the two peaks merge gradually together, indicating that another phase with similar lattice constants, e.g. pseudo-cubic, may be formed. Similar results have been reported for the SSR-derived Er-doped KNN ceramics (Chapter 3).

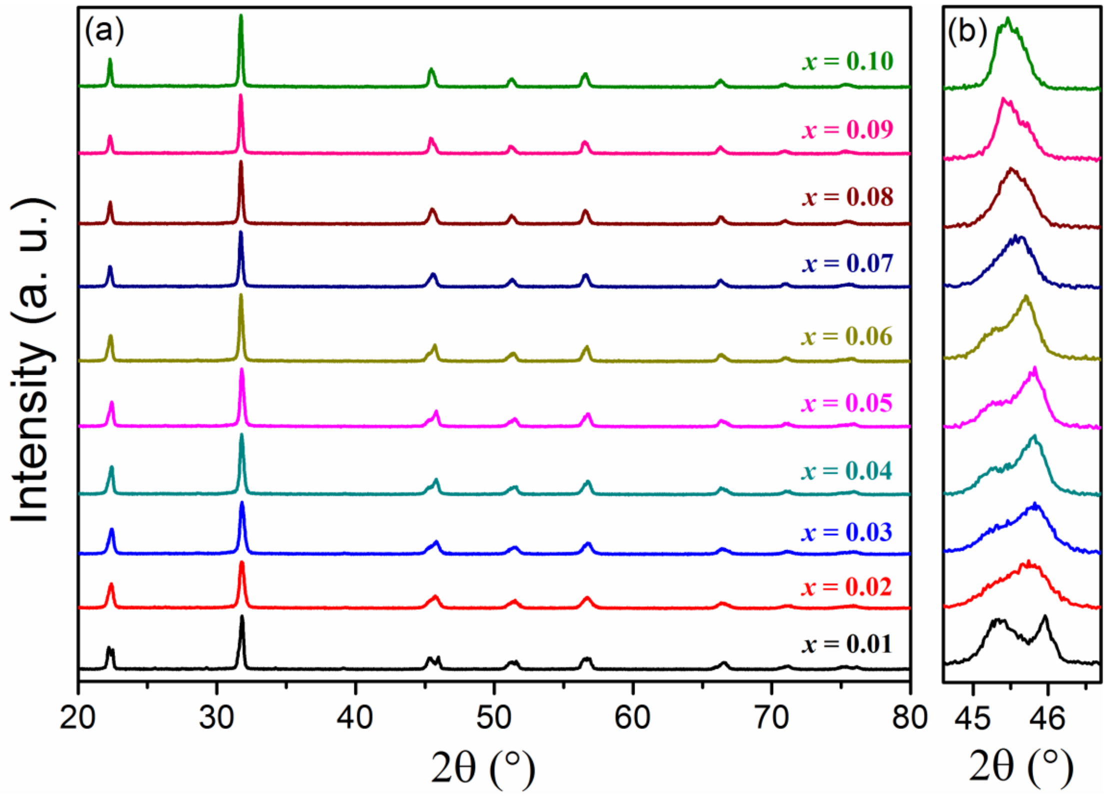

Figure 7.1 (a) XRD patterns of the KNN-LB-*x* ceramics. (b) Enlarged XRD patterns near 45.5 °.

7.2.2 Optical transmittances

A photograph of the KNN-LB-*x* ceramics is shown in Fig. 7.2. The ceramic changes from opaque to translucent as *x* increases from 0.01 to 0.02. As *x* further increases to 0.08, the optical clarity improves and the ceramic becomes transparent.

However, at $x > 0.08$, the optical clarity becomes worse.

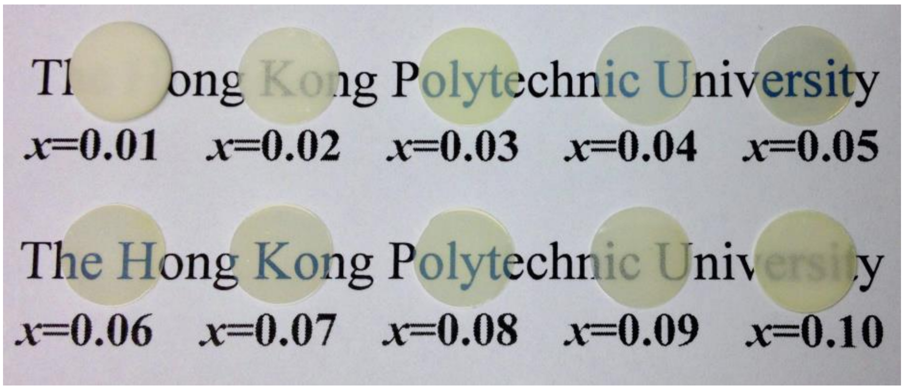

Figure 7.2 Photograph of the KNN-LB-*x* ceramics (t = 0.3 mm).

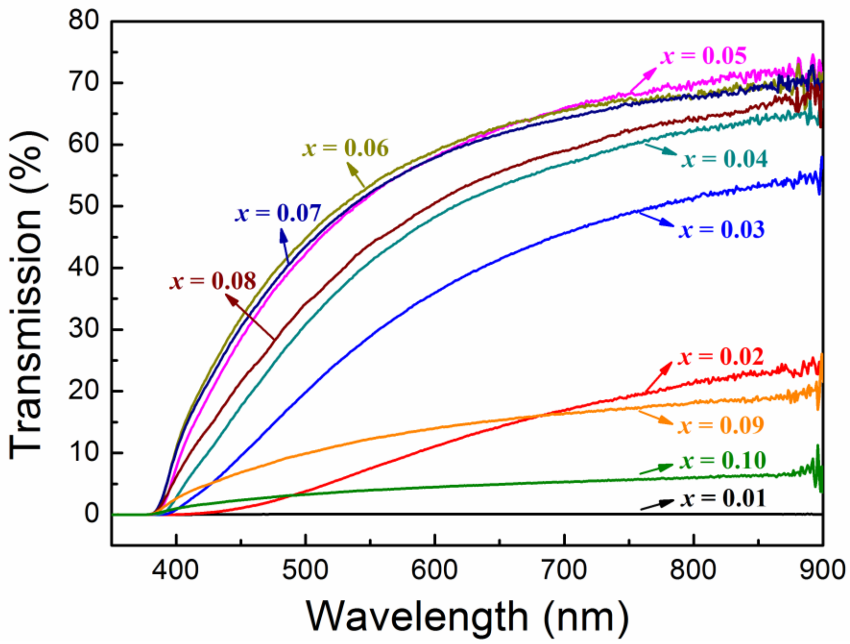

Figure 7.3 Optical transmittance spectra for the KNN-LB-*x* ceramics (t = 0.3 mm).

Fig. 7.3 shows the optical transmittances (T) measured in the range of 300-900 nm. The improvement in transparency is also revealed in the transmittance spectra. It can be seen that the KNN-LB-*x* ceramics with x = 0.05, 0.06 and 0.07 exhibit the highest transmittance. The observed T increases rapidly from zero at ~390 nm, reaches a large value of ~70% in the NIR region, and becomes almost saturated near 900 nm. Probably due to the interband transition, all the ceramics exhibit a zero transmittance at wavelength shorter than 390 nm.

7.3 Er-doped KNN-LB transparent ceramics

7.3.1 XRD

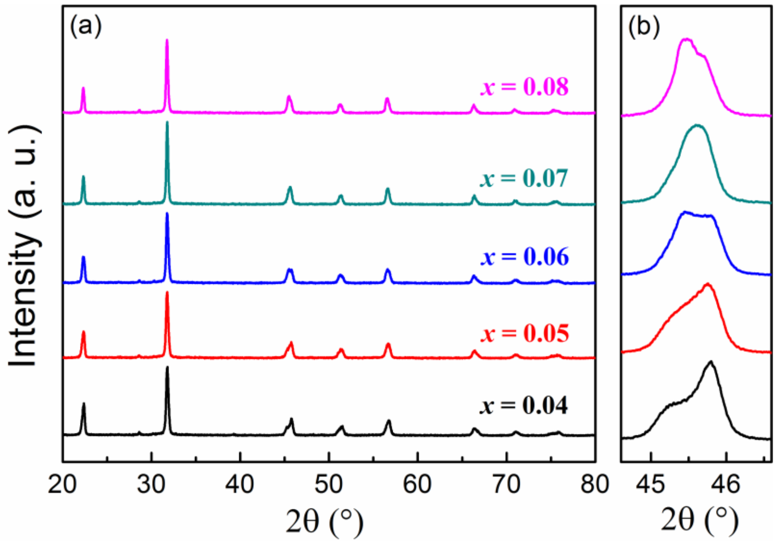

Figure 7.4 (a) XRD patterns of the Er-KNN-LB-*x* ceramics. (b) Enlarged XRD patterns near 45.5 °.

On the basis of the optical transmittance of the KNN-LB-*x* ceramics, 1 mol% Er-doped $(K_{0.5}Na_{0.5})_{1-x}Li_xNb_{1-x}Bi_xO_3$ ceramics with *x* varying from 0.04 to 0.08 (abbreviated as Er-KNN-LB-*x*) have been prepared. The XRD patterns of the Er-KNN-LB-*x* ceramics are shown in Fig. 7.4. Similar to the KNN-LB-*x* ceramics, all the Er-KNN-LB-*x* ceramics possess a single-phase perovskite structure (Fig. 7.4a), suggesting that Li^+, Bi^{3+} and Er^{3+} ions have diffused into the KNN lattice. As shown in the enlarged XRD patterns (Fig. 7.4b), the two diffraction peaks (220) and (002) merge together, and form almost a single peak at $x = 0.07$. This suggests that the ceramics may possess a pseudo-cubic structure or a structure with very similar lattice constants a, b and c, and the structure of the Er-KNN-LB-0.07 ceramic may be nearly cubic.

The lattice constants of the ceramics have been refined using all the diffraction peaks shown in Fig. 7.4 by the Rietveld method. Both the orthorhombic and monoclinic unit cells have been used for the refinement of the KNN cell parameters, and only a small difference between the two structures is noted. In this work, a better fit between the observed and calculated diffraction patterns using the monoclinic model is obtained, giving the results together with the reliability factor R_{wp} and goodness-of-fit indicator S are given in Table 7.1. The low R_{wp} (< 15%) and S (< 2) values reveal a good fit between the observed and calculated patterns. As x increases, the c/a value increases and reaches a maximum value of 0.9988 at $x = 0.07$, and the difference between a and b is only about 0.0221Å. This suggests that the crystal structure has transformed to a pseudo-cubic (or cubic-like) phase, and the Er-KNN-LB-0.07 ceramic has a nearly cubic structure.

Table 7.1 Lattice constants of Er-KNN-LB-*x* ceramics.

x	a (Å)	b (Å)	c (Å)	β (°)	a-b (Å)	c/a	R_{wp} (%)	S
0.04	4.0032	3.9687	3.963	89.38	0.0345	0.99	11.51	1.3080
0.05	3.9964	3.9613	3.9783	89.66	0.0351	0.9955	11.79	1.3263
0.06	3.9959	3.9659	3.9875	89.83	0.03	0.9979	12.97	1.4883
0.07	3.9934	3.9713	3.9886	89.84	0.0221	0.9988	12.73	1.4567
0.08	3.9965	3.9723	3.9833	89.92	0.0242	0.9967	12.82	1.4645

7.3.2 Optical transmittances

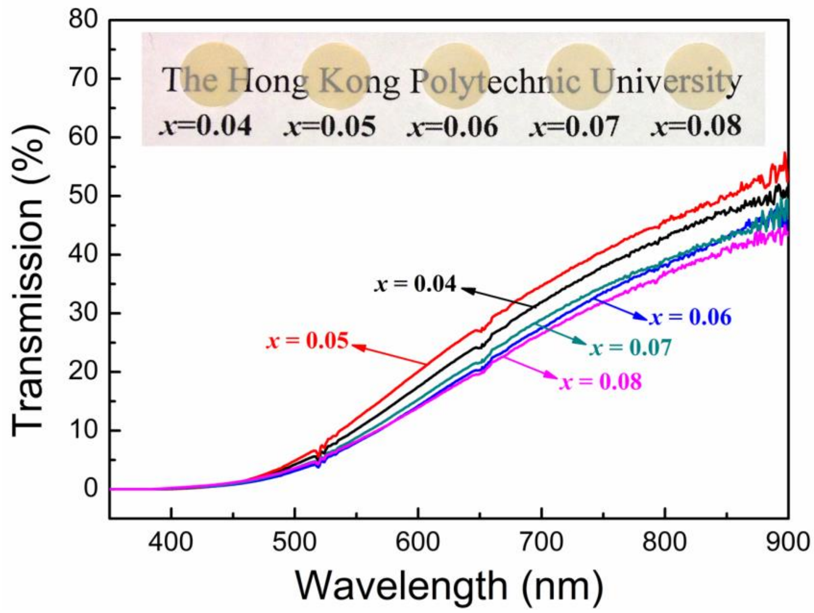

Figure 7.5 Optical transmittance spectra for the Er-KNN-LB-*x* (*x* = 0.04-0.08) ceramics (t = 0.3mm). Inset is a photograph of these transparent ceramics.

The optical transmittances (T) of the Er-KNN-LB-*x* ceramics are shown in Fig. 7.5. All the Er-KNN-LB-*x* ceramics are optically transparent (inset of Fig. 7.5) although the observed transmittances are lower than those of KNN-LB-*x* transparent ceramics. Unlike the KNN-LB-x ceramics, the observed T of the ceramics increases quite steadily from zero in the range of 390 nm to 900 nm. Moreover, two absorption peaks centered at 550 nm and 660 nm are observed in the transmittance spectra of the Er-KNN-LB-x ceramics. These should be attributed to the transitions of Er^{3+} ions $^4I_{15/2} \rightarrow {}^4S_{3/2}$ and $^4I_{15/2} \rightarrow {}^4F_{9/2}$, respectively (Fig. 6.4a). As shown in Fig. 7.5, the Er-KNN-LB-0.05 ceramic exhibits the highest transmittance, giving an observed T of ~55 % at 900 nm. Although the Er-KNN-LB-0.08 ceramic shows the lowest transmittance, the observed T at 900 nm remains reasonably high, about 45 %. As illustrated in the inset of Fig. 7.5, all the ceramics are optically clear in spite of the difference in the observed T values. In agreement with the results of Er-KNN-LB-*x* ceramics, the contents of Li and Bi ($0.04 \leq x \leq 0.08$) do not have significant effects on the optical transmittance.

7.3.3 SEM

Fig. 7.6 shows the SEM micrographs of the Er-KNN-LB-*x* ceramics. It can be seen that all the ceramics exhibit good densification and fine grains (< 700 nm) with the cuboid morphologies (Figs. 7.6a-e). The fine grains are probably resulted from the effective suppression of grain growth by the doping of Bi. As shown in Fig. 7.6f, the average grain size depends almost linearly on the content of Bi. As x increases from 0.04 to 0.08, it increases from ~320 nm to ~640 nm. Besides the larger grains (> 500 nm), some pores are also observed randomly distributed in the ceramics with $x \geq 0.06$. These should be the main reasons for the lower density as well as the poor optical transparence (Fig. 7.5) of these ceramics. The observed densities of the Er-KNN-LB-*x* ceramics are listed in Table 7.2. The transparency of ceramics is generally influenced by three main factors: grain size, grain-boundary phase and pores (Liu, 2008). For lead-based EO transparent ceramics (such as PLZT), the microstructure is dense and grains are large (> 5 μm), so that the grain-boundary is thin, the area of the grain-boundary is small, and thus the optical scattering is reduced and optical transmittance is very high (Jiang, 2005). Unlike the lead-based EO ceramics, the good optical transparency of the lead-free Er-KNN-LB-*x* ceramics should be partly due to the reduced optical scattering by the fine grains (Apetz, 2003).

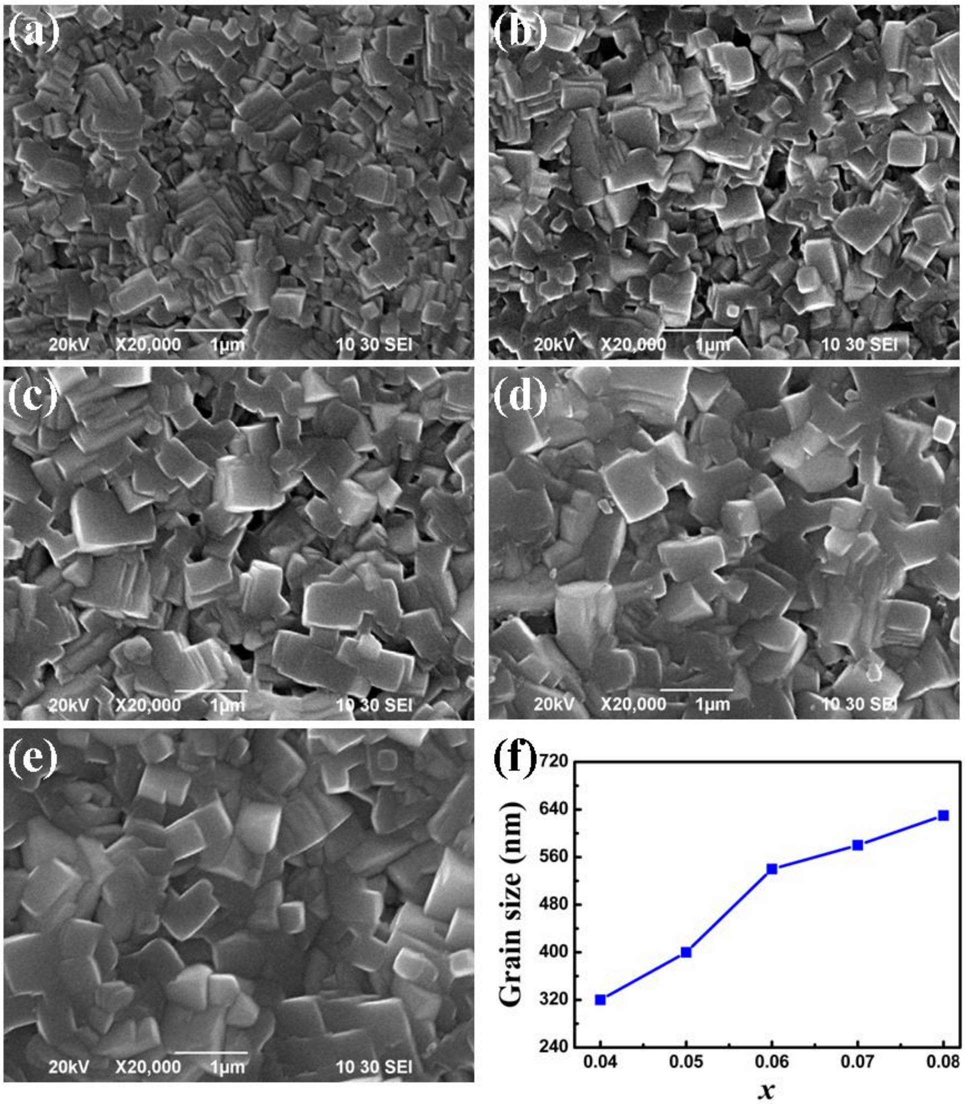

Figure 7.6 SEM micrographs of the Er-KNN-LB-*x* ceramics. (a) $x = 0.04$, (b) $x = 0.05$, (c) $x = 0.06$, (d) $x = 0.07$, (e) $x = 0.08$, (f) the relationship between *x* and grain size.

Table 7.2 Density results for Er-KNN-LB-*x* ceramics.

x	0.04	0.05	0.06	0.07	0.08
ρ (g/cm^3)	4.64	4.62	4.65	4.65	4.67
Relative density (%)	99.1	98.2	98.3	97.8	97.7

7.3.4 Dielectric properties

Fig. 7.7 shows, as examples, the temperature dependences of ε_r measured at 10 kHz, 100 kHz and 1 MHz for the KNN-LB-0.06 and Er-KNN-LB-0.06 ceramics. Similar results have also been observed for the other ceramics ($0.04 \leq x \leq 0.08$). Both the ceramics exhibit a broadened tetragonal-orthorhombic and cubic-tetragonal phase transition peaks, which should be induced by the co-doping of Li^+ and Bi^{3+} ions. As mentioned for the Er-doped KNLN ceramics in Chapter 4, the doping of Li^+ would not enhance the diffuseness of the phase transition because Li^+ has the same valence as K^+ and Na^+. Hence, the diffuse phase transition should be attributed to Bi^{3+}, which replaces Nb^{5+} sites and increases the degree of disorder on the B-sites and the local compositional fluctuation in the ceramics. Similar results have been reported for the hot-pressed based KNN-LB-x transparent ceramics (Li, 2013a). The observed ε_r decreases with increasing frequency. However, unlike the typical relaxor ferroelectrics, an increase in T_c with frequency has not been observed. It has been reported that the change in T_c for KNN-based relaxors is also not large (Du, 2007a, Guo 2004). These indicate that the ceramics (both KNN-LB-x and Er-KNN-LB-x with $0.04 \leq x \leq 0.08$) possess the relaxor-like characteristics.

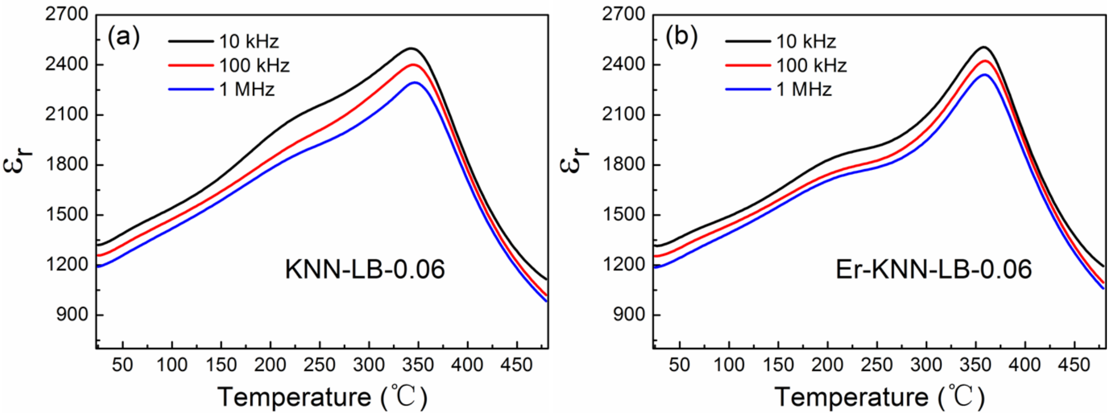

Figure 7.7 Temperature dependences of ε_r at different frequencies for (a) KNN-LB-*x* ceramics and (b) Er-KNN-LB-*x* ceramics.

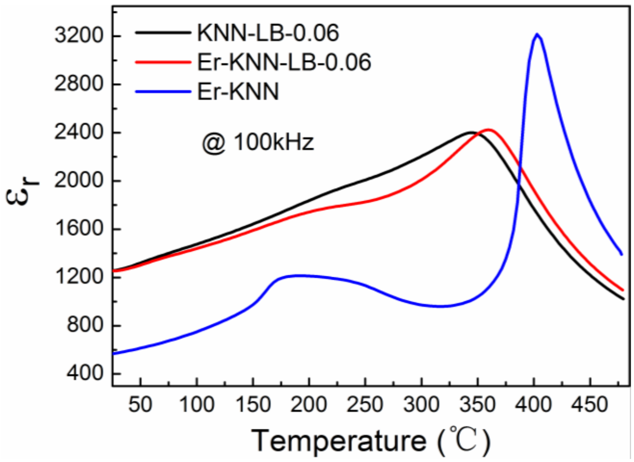

Figure 7.8 Temperature dependences of ε_r for the KNN-LB-0.06, Er-KNN-LB-0.06 and Er-KNN ceramics.

The temperature dependences of ε_r for the KNN-LB-0.06, Er-KNN-LB-0.06 and Er-KNN (1 mol% Er-doped KNN) ceramics are shown in Fig. 7.8 for revealing the effects of Er, Li and Bi on the dielectric properties. It can be seen that the tetragonal-orthorhombic phase transition peak of the Er-KNN-LB-0.06 ceramic is more noticeable than that of the KNN-LB-0.06 ceramic. After the doping of 1 mol% Er, the observed T_c

increases slightly from 345°C to 360°C, while the diffuseness of the phase transition remains almost the same. As compared with the Er-KNN ceramic, the effects of the doping of Li and Bi are observed. The first effect is the induced diffuseness of the two transitions, accompanied with the shifting of the transition temperature T_c and $T_{O\text{-}T}$ to lower and higher temperatures, respectively. The changes of the transition temperatures should be attributed to the doping of Li^+ as discussed in Chapter 4 for the Er-KNLN ceramics. The second effect is the significant increase (more than 100%) in the observed ε_r (before the tetragonal-cubic transition). This should be partly due to the improvement in densification (Figs. 3.2b and 7.6c) (Hollenstein, 2007).

7.3.5 Ferroelectric properties

Fig. 7.9 shows the *P-E* loops of the KNN-LB-0.06 and Er-KNN-LB-0.06 ceramics measured under different electric fields at room temperature. Partly due to the fine grains size and cubic-like symmetry, the ceramics exhibit slim *P-E* loops. As the electric field increases, the observed remnant polarization P_r and coercive field E_c increase and become saturated at 5 kV/mm. For the KNN-LB-0.06 ceramic, the saturated P_r and E_c are 9 μC/cm^2 and 1.5 kV/mm, respectively, while those of the Er-KNN-LB-0.06 ceramic are 8 μC/cm^2 and 1.3 kV/mm, respectively. The decreases in P_r and E_c for the Er-KNN-LB-0.06 ceramic may be partly attributed to the donor doping of Er^{3+} in the A-sites. Combined with the dielectric properties, it is suggested that both the KNN-LB-0.06 and Er-KNN-LB-0.06 ceramics possess relaxor-like characteristics.

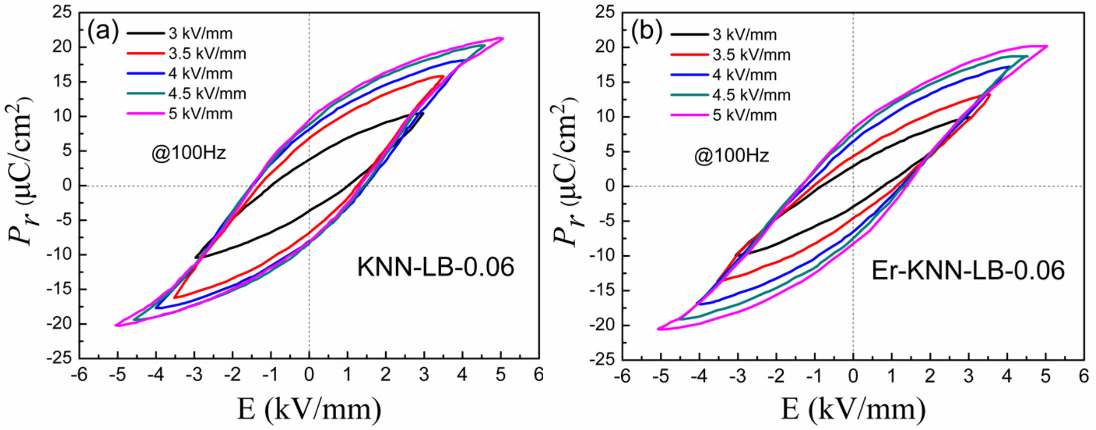

Figure 7.9 *P-E* loops of the (a) KNN-LB-0.06 and (b) Er-KNN-LB-0.06 ceramics under different electric fields at room temperature.

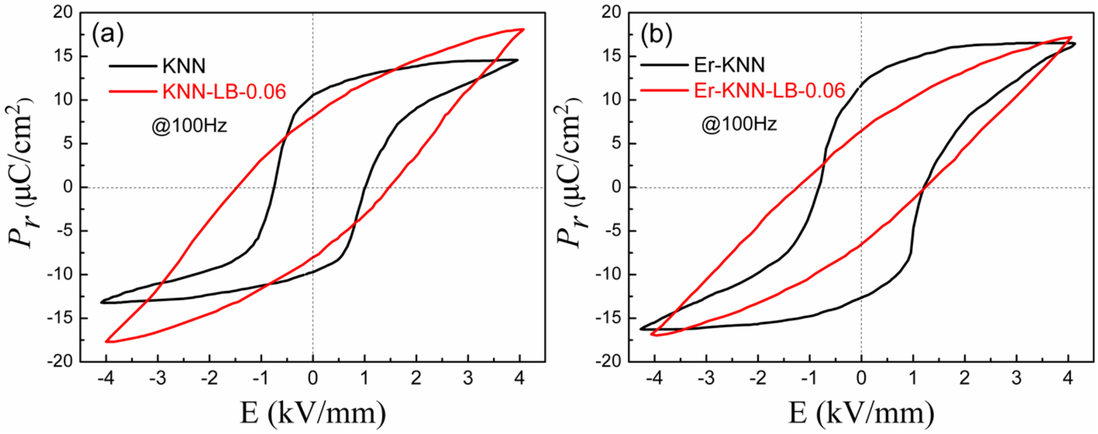

Figure 7.10 *P-E* loops of the ceramics at room temperature, (a) pure KNN and KNN-LB-0.06 ceramics, (b) Er-KNN and Er-KNN-LB-0.06 ceramics.

The *P-E* loops of the KNN, KNN-LB-0.06, Er-KNN and Er-KNN-LB-0.06 ceramics measured under 4 kV/mm at room temperature are shown in Fig. 7.10 for revealing the effects of Li and Bi on the ferroelectric properties. As shown in Figure 7.10a, after the doping of Li and Bi, the *P-E* loop becomes slant and flattened, giving a larger E_c and a smaller P_r. This should be due to the relaxor characteristics induced in the ceramic. Similar changes have also been observed for the other pair of ceramics: Er-

KNN and Er-KNN-LB-0.06 (Fig. 7.10b).

7.3.6 EO properties

Before measuring the EO properties, the KNN-LB-*x* and Er-KNN-LB-*x* ceramics were firstly polarized under a dc electric field of 5 kV/mm at 150 ℃ for 30 min. The poling direction is perpendicular to the parallel spacing of 1 mm in the ceramic specimen. A n_e value of 2.257 (approximated by the value of an un-poled sample) (Li, 2013a) was used to calculate the effective linear EO coefficient r_c (Eq. 2.33). The r_c of the KNN-LB-*x* and Er-KNN-LB-*x* ceramics were measured using the modified Sénarmont system (introduced in Chapter 2). Fig. 7.11 shows the variations of the field-induced phase retardation Γ_m (Eq. 2.28) with the amplitude of an ac voltage at 1 kHz (V_o) for these transparent ceramics. A linear relationship between Γ_m and V_o is observed for each ceramic, suggesting that the ceramics are linear EO materials. By using the fitted slop of the curves, r_c is calculated and the results are listed in Table 7.3. Except for the ceramics with x = 0.04, the observed r_c for both the KNN-LB-*x* and Er-KNN-LB-*x* ceramics increases roughly with increasing the content of Li and Bi, which is in agreement with the results of the hot-pressed ceramics (Li, 2013a). Although the observed r_c (120-200 pm/V) are not as high as that of $Pb_{0.92}La_{0.08}(Zr_{0.65}Ti_{0.35})_{0.98}O_3$ (PLZT) transparent ceramics (612 pm/V), they are about 6-10 times larger than that of $LiNbO_3$ single crystals (19.9 pm/V) (Aillerie, 1989), and comparable to that of PMN-PT single crystals with rhombohedral and tetragonal structures (182 pm/V) (Wan, 2004). The discrepancy for the ceramics with x = 0.04 may be attributed to the variations in composition which may be arisen from the different sintering conditions, e.g. different sintering times: 32 h vs 4 h. It can also be seen that the Er-doping does not affect the EO properties significantly.

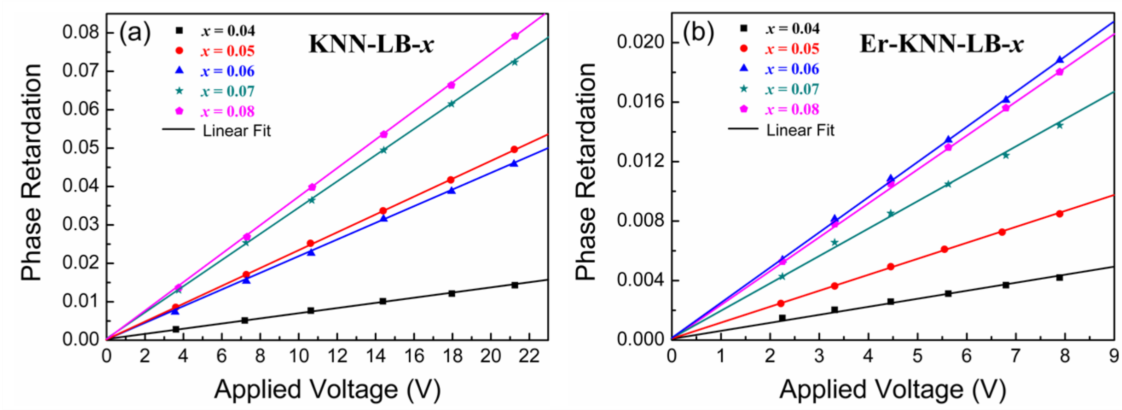

Figure 7.11 The plot of the phase retardations as a function of an ac applied field with a modulation frequency 1 kHz for the (a) KNN-LB-*x* and (b) Er-KNN-LB-*x* ceramics.

Table 7.3 Effective EO coefficient r_c for the KNN-LB-*x* and Er-KNN-LB-*x* ceramics.

KNN-LB-*x*	r_c (pm/V)	Er-KNN-LB-*x*	r_c (pm/V)
$x = 0.04$	20	$x = 0.04$	43
$x = 0.05$	145	$x = 0.05$	128
$x = 0.06$	126	$x = 0.06$	184
$x = 0.07$	182	$x = 0.07$	170
$x = 0.08$	200	$x = 0.08$	182

Shih et al. has shown that, via theoretical calculations, a distorted octahedral structure is a promising mechanism for a strong EO response (Shih, 1982). The large r_c should be partly due to the large distortion of BO_6 octahedron (B = Nb/Bi in the host), which is induced by the doping of Li^+ and Bi^{3+} ions. On the other hand, by considering the ferroelectric phase as a quadratic phase biased with a spontaneous polarization P_s, r_c

can be related to ε_r and P_s via a general equation (DrDomenico, 1969, Burns, 1968):

$$r_c = 2\varepsilon_0\varepsilon_r g_c P_s \tag{7.1}$$

where g_c is the polarization-related quadratic EO coefficient and ε_0 is the permittivity of vacuum. Accordingly, the large r_c should be partly due to the large ε_r of the KNN-LB-*x* and Er-KNN-LB-*x* ceramics, which has been discussed in previous sections (refer to Fig. 7.8). Eq. 7.1 has been shown to be applicable to other oxygen-octahedra materials, such as $LiNbO_3$, $LiTaO_3$, $NaBa_2Nb_5O_{15}$, $KSr_2Nb_5O_{15}$, and $0.88Pb(Zn_{1/3}Nb_{2/3})O_3$-$0.12PbTiO_3$ (DrDomenico, 1969, He, 2012).

7.3.7 PL properties

Apart from the dielectric, ferroelectric and EO properties, the PL properties of the Er-KNN-LB-*x* ceramics have also been investigated, giving the results shown in Figure 7.12. Similar to the Er-KNN and Er-KNLN ceramics, the Er-KNN-LB-*x* ceramics exhibit three main emissions in 510-537 nm (green), 537-570 nm (green) and 640-685 nm (red) under an excitation of 980 nm (Fig. 7.12a). The emissions are attributed to the transitions $^2H_{11/2} \rightarrow {}^4I_{15/2}$, $^4S_{3/2} \rightarrow {}^4I_{15/2}$ and $^4F_{9/2} \rightarrow {}^4I_{15/2}$, respectively. Probably due to the change of crystal field induced by the doping of Li and Bi, the spectral shapes of the Er-KNN-LB-*x* ceramics are quite different from those of the Er-KNN ceramics (Fig. 3.4a). Figure 7.12b shows the variations of the relative (integrated) PL intensity for each emission band. It can be seen that the Er-KNN-LB-0.04 ceramic exhibits the highest PL intensities while those of the Er-KNN-LB-0.07 ceramic are the lowest, showing a decrease of ~20% and ~30% for the green (two green) and red emissions, respectively.

The PL emission is influenced by the crystal field and symmetry of the host. The doping of Li and Bi will change the lattice symmetry of KNN, and thus generating remarkable change on the local field around the activator Er^{3+} ions (Kang, 2009). As discussed in previous sections on the XRD results (Fig. 7.4), the crystal structure has transformed to a pseudo-cubic phase as x increases, and becomes nearly cubic at *x* = 0.07. The highest PL intensity of the Er-KNN-LB-0.04 ceramics should hence be due to the largest asymmetry. The increased asymmetry of Er^{3+} ion sites can enhance the probability for the spontaneous 4f-4f electric dipole transitions, and thus resulting in stronger emissions (Kang, 2009, Du, 2013b).

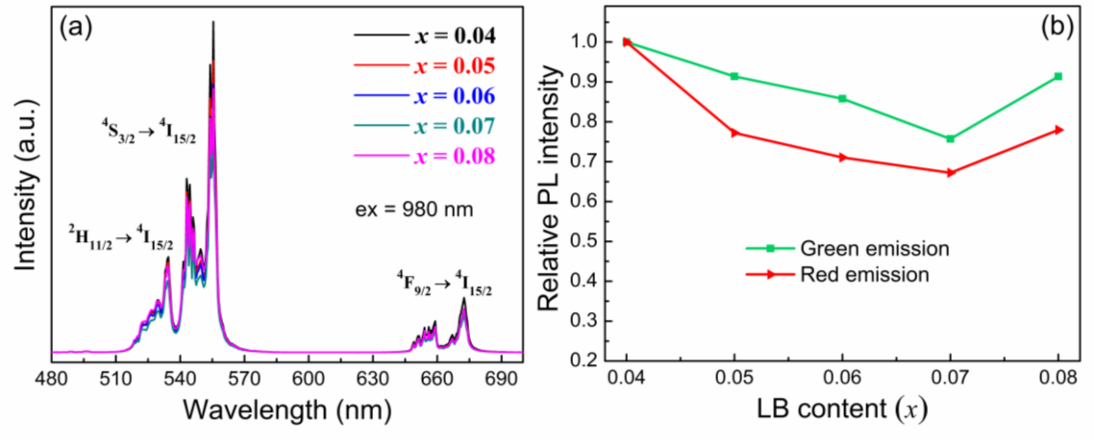

Figure 7.12 (a) Vis up-conversion emissions of the Er-KNN-LB-*x* ceramics. (b) Variations of the relative (integrated) PL intensities with *x*.

7.4 Conclusions

KNN-LB-*x* and Er-KNN-LB-*x* transparent ceramics have been successfully prepared by pressureless sintering through the ordinary SSR method. Due to the effective suppression of grain growth by the doping of Bi, the ceramics possess a dense and fine-grained structure. The doping of Li and Bi also induces a phase transformation into a pseudo-cubic or cubic-like crystal structure. The ceramics are optically clear, exhibiting a high transmittance (~ 70% for KNN-LB-*x* and ~ 50% for Er-KNN-LB-*x*) in the NIR region (~ 900 nm). The good optical transparency should be attributed to the cubic-like crystal structure as well as the relaxor-like characteristics, which have been attested through the temperature dependences of ε_r and *P*-*E* loops. The transparent ceramics exhibit strong EO response, giving a large effective linear EO coefficient, i.e. 120-200 pm/V with *x* in the range of 0.05-0.08. The Vis up-conversion PL properties of the Er-KNN-LB-*x* transparent ceramics have also been investigated together with the explanation of the relationship between PL intensity and crystal structure. The Er-KNN-LB-*x* transparent ceramics possess simultaneously good EO, dielectric, ferroelectric and photoluminescence properties, and hence should have great potential in multifunctional photonic applications, such as optical-electro integrated materials and devices.

Chapter 8 Conclusions

The combination of both photoluminescence (PL) and ferroelectricity into a single entity can provide us a multifunctional material used in various optoelectronic applications. The present work aims to develop new lead-free RE-doped $K_{0.5}Na_{0.5}NbO_3$ (KNN)-based ceramics with outstanding PL performances and good ferroelectric, piezoelectric, dielectric and EO properties. Er^{3+} ions are used as the activator in the KNN host and the PL properties of Er^{3+} (especially the up-conversion) have been systematically investigated. The effect of Pr^{3+} or Yb^{3+} ions (acted as the sensitizers) on the PL properties of Er^{3+} has been studied. The PL mechanism of various Er-doped KNN-based ceramics has been elaborated. Li^{+} and Bi^{3+} ions have been added to the ceramics for modifying the phase structures and properties. Besides the conventional solid-state reaction (SSR) method, the sol-gel method has been applied to prepare the ceramics for study the resulting effects on the microstructure, PL and electrical properties. The relationships between the PL properties and ferroelectric characteristics (e.g., the polarization switching) of KNN have been discussed.

x mol% Er-doped KNN (KNN:Er-x) ceramics have been prepared by the SSR method and their PL and electrical properties have been studied. The Er-doping is effective in changing a phase structure (orthorhombic at $x \leq 2$ and cubic-like at $x \geq 3$) and inhibiting the grain growth to reduce the grain size. Under an excitation of 980 nm, the ceramics exhibit up-conversion green and red emissions, as well as down-conversion near-infrared (NIR) and middle-infrared (MIR) emissions. The relationships between the Vis up-conversion PL and laser power indicate an efficient two-photon process when $x \leq 2$. Except for an abruptly increase at $x = 3$ arisen from the phase transformation from orthorhombic to cubic-like, the lifetimes reduce significantly with increasing x. Both the concentration-quenching effect and change of crystallographic structures affect the energy transfer processes and PL properties, including emission intensities, colors and lifetimes. Our results also reveal that the Er-doping can transform the ceramics from normal ferroelectrics to relaxor-like ones. The ceramics doped with a small amount of Er ($x = 1$ and $x = 2$) manifest relatively good d_{33}, high P_r and ε_r, low tan δ, as well as outstanding PL performances.

2 mol% Er-doped $(K_{0.5}Na_{0.5})_{1-x}Li_xNbO_3$ (Er-KNLN-x) ceramics have been prepared and their dielectric, ferroelectric and PL properties have been investigated. The ceramics possess a single-phase orthorhombic structure at $x < 0.06$. And the structure transforms to tetragonal symmetry at $x \geq 0.06$. Under an excitation of 980 nm, the ceramics exhibit up-conversion luminescent emission bands at 527 nm (green), 548 nm (green), 660 nm (red) as well as down-conversion emission bands at 1.55 μm (NIR) and 2.7 μm (MIR). Probably due to the induced structure distortion and reduced local symmetry, the PL intensities of the green, red as well as MIR emissions are enhanced after the doping of Li^+. The Li-doping is also effective in establishing a dynamic circulatory energy process to further enhance the PL intensity of the MIR emission at the expense of the NIR emission. At the optimum doping level of Li^+ (~6 mol%), the FWHM of the MIR emission also reaches a large value of ~250 nm, demonstrating that the ceramic is a promising candidate for high-power 2.7-μm ceramic lasers. In addition to the good ferroelectric properties, the Er-KNLN-x ceramics should have great

potential for multifunctional optoelectronic applications.

The sol-gel method has been used to prepare Er-doped KNN (KNN:Er-*x*) and 2 mol% Er-doped KNLN (Er-KNLN-0.08) ceramics. The sol-gel-derived ceramics possess a perovskite structure with good compositional homogeneity, and fine and uniform grains. For KNN:Er-*x* ceramics, both the up-conversion emission and luminescent efficiencies of Er^{3+} are improved, leading to very strong green emissions at a low quenching concentration of 2 mol%. Compared to the SSR-derived ceramics, the sol-gel-derived ceramics can be well densified at lower sintering temperatures, and exhibit higher PL intensities, larger d_{33} and ε_r. A moderate amount of Li content is enough for enhancing the Vis up-conversion emissions as well d_{33} and T_c.

The PL properties of 2 mol% Er and y mol% Pr codoped KNN (Er-KNN-Pr-y) and 1 mol% Er and z mol% Yb codoped KNN (Er-KNN-Yb-z) ceramics have been investigated. Pr^{3+} and Yb^{3+} ions are used as the sensitizers for enhancing the PL emissions of Er^{3+}. For the Er-KNN-Pr-y ceramics, under the excitation of 980 nm, all the ceramics exhibit strong green and weak red up-conversion emissions as well as NIR and MIR emissions. The observed PL intensities of the green, red and NIR emissions decrease, while that of the MIR emission increases with increasing the content of Pr^{3+}. The phenomena have been elucidated in terms of energy transfer processes between Er^{3+} and Pr^{3+} ions. Under the excitation of 450 nm, simultaneous green and red down-conversion emissions of Er^{3+} and Pr^{3+} ions can be realized, and the emission color of the ceramics can be tuned via the concentration of Pr^{3+} in a wider range from yellowish green to yellow. The PL intensities of the ceramics can be enhanced by the lattice distortion and structural asymmetry induced by the alignment of polarization of the ferroelectric host. For the Er-KNN-Yb-z ceramics, the effect of Yb^{3+} content on the PL intensities of Er^{3+} have been studied. Under the excitation of 980 nm, Vis blue, green and red emissions, as well as NIR and MIR emissions of Er^{3+} ions can be observed. After codoping with Yb^{3+} ions, the PL intensities (both Vis and MIR emissions) greatly enhance due to the efficient energy transfer processes from Yb^{3+} to Er^{3+}. The optimal Yb^{3+} concentration is 4 mol% and the corresponding mechanisms that influence the PL intensities of Er^{3+} have been elaborated. Both Pr^{3+} and Yb^{3+} ions are proper sensitizers for tuning the PL emissions of Er^{3+} in the KNN ceramics.

The transparent ceramics $(K_{0.5}Na_{0.5})_{1-x}Li_xNb_{1-x}Bi_xO_3$ (KNN-LB-x) and 1 mol% Er-doped $(K_{0.5}Na_{0.5})_{1-x}Li_xNb_{1-x}Bi_xO_3$ (Er-KNN-LB-x) have been successfully fabricated by pressureless sintering through the same SSR method. Due to the effective suppression of grain growth by the doping of Bi, the ceramics possess a dense and fine-grained structure. The ceramics are optically clear, exhibiting a high transmittance (~70% for KNN-LB-x and ~50% for Er-KNN-LB-x) in the NIR region (~900 nm). The good optical transparency should be attributed to the cubic-like crystal structure as well as the relaxor-like characteristics, which have been attested through the temperature dependences of ε_r and P-E loops. The transparent ceramics exhibit strong EO response, giving a large effective linear EO coefficient (120-200 pm/V). The Vis up-conversion PL properties of the Er-KNN-LB-x transparent ceramics have also been investigated and correlated with the crystal structure of the ceramics. The Er-KNN-LB-x transparent ceramics possess simultaneously good EO, dielectric, ferroelectric and photoluminescence properties, and hence should have great potential in multifunctional photonic applications, such as EO integrated materials and devices.

References

http://www.edinst.com/FLSP920.htm.

http://www.ing.unitn.it/~maud/index.html.

Adhikari, R., Joshi, B., García, R. N., Rosa, E. D. L. and Lee, S. W. "Microwave hydrothermal synthesis and infrared to visible upconversion luminescence of Er^{3+}/Yb^{3+} co-doped bismuth molybdate nanopowder," *Journal of Luminescence* 145, 866, 2014.

Ahn, C. W., Park, H. Y., Nahm, S., Uchino, K., Lee, H. G. and Lee, H. J. "Structural variation and piezoelectric properties of $0.95(Na_{0.5}K_{0.5})NbO_3$-$0.05BaTiO_3$ ceramics," *Sensors and Actuators A: Physical* 136, 255, 2007.

Ahn, C. W., Hwang, H. I., Lee, K. S., Jin, B. M., Park, S. M., Park, G. S., Yoon, D. H., Cheong, H. S., Lee, H. J. and Kim, I. W. "Raman Spectra Study of $Na_{0.5}K_{0.5}NbO_3$ Ferroelectric Thin Films," *Japanese Journal of Applied Physics* 49, 095801, 2010.

Ahn, Z. S., Schulze, W. A. "Conventionally sintered $(Na_{0.5}K_{0.5})NbO_3$ with barium additions," *Journal of the American Ceramic Society* 70, C18, 1987.

Ahtee, M. and Glazer, A. M. "Lattice-parameters and tilted octahedra in sodium-potassium niobate solid-solutions," *Acta Crystallographica Section A* 32, 434, 1976.

Aillerie, M., Fontana, M. D., Abdi, F., Carabatos-Nedelec, C., Theofanous, N. and Alexakis, G. "Influence of the temperature-dependent spontaneous birefringence in the electro-optic measurements of $LiNbO_3$," *Journal of Applied Physics* 65, 2406, 1989.

Aillerie, M., Théofanous, N. and Fontana, M. D. “Measurement of the electro-optic coefficients: description and comparison of the experimental techniques,” *Applied Physics B* 70, 317, 2000.

Allain, J. Y., Monerie, M. and Poignant, H. “Energy transfer in Er^{3+}/Pr^{3+}-doped fluoride glass fibres and application to lasing at 2.7 µm,” *Electronics Letters* 27, 445 1991.

Aparna, M. Rachavender, M. Prasad, G. and Kumar, G. S. “Electromechanical characterization of lanthanum-doped sodium bismuth titanate ceramics,” *Modern Physics Letters B* 20, 475, 2006.

Apetz, R. and Bruggen, M. P. B. V. “Transparent Alumina: A Light-Scattering Model,” *Journal of the American Ceramic Society* 86, 480, 2003.

Auzel, F. “Computer quantique par transfert d’energie enttre deux ions de terres rares dans un tungstate mixte et dans un verre,” *Comptes Rendus de l'Académie des Sciences* 262, 1016, 1966.

Auzel, F. “Upconversion and Anti-Stokes Processes with f and d Ions in Solids,” *Chemical Reviews* 104, 139, 2004.

Babu, P., Seo, H. J., Jang, K. H., Balakrishnaiah, R., Jayasankar, C. K., Lim, K. S. and Lavín, V. J. “Optical spectroscopy, 1.5 µm emission, and upconversion properties of Er^{3+}-doped metaphosphate laser glasses,” *The Journal of the Optical Society of America B* 24, 2218, 2007.

Bai, G. X., Ding, J., Tao, L. L., Li, K. F., Hu, L. L. and Tsang, Y. H. “Efficient 2.7 micron emission from Er^{3+}/Pr^{3+} codoped oxyfluorotellurite glass,” *Journal of Non-Crystalline Solids* 358, 3403, 2012.

Bai, X., Song, H. W., Pan, G. H., Lei, Y. Q., Wang, T., Ren, X. G., Lu, S. Z., Dong, B., Dai, Q. L. and Fan, L. "Size-dependent upconversion luminescence in Er^{3+}/Yb^{3+} -codoped nanocrystalline yttria: Saturation and thermal effects," *The Journal of Physical Chemistry C* 111, 13611, 2007.

Bai, Y. F., Wang, Y. X., Yang, K., Zhang, X. R., Peng, G. Y., Song, Y. L., Pan, Z. Y. and Wang, C. H. "The effect of Li on the spectrum of Er^{3+} in Li- and Er-codoped ZnO nanocrystals," *J. Phys. Chem. C*, 112 [32] 12259–5 (2008).

Balakrishnaiah, R., Kim, D. W., Yi, S. S., Kim, K. D., Kim, S. H., Jang, K. W., Lee, H. S. and Jeong, J. H. "Frequency upconversion fluorescence studies of Er^{3+}/Yb^{3+}-codoped $KNbO_3$ phosphors," *Thin Solid Films* 517, 4138, 2009.

Ballato, J., Esmacher, R., Schwartz, R. and Dejneka, M. "Rare-earth-doped ferroelectric PLZT for active electro-optic devices," *Journal of Luminescence* 86, 101, 2000.

Bandi, V. R., Grandhe, B. K., Jang, K., Lee, H. S., Shin, D. S., Yi, S. S. and Jeong, J. H. "Citric based sol-gel synthesis and luminescence characteristics of $CaLa_2ZnO_5$: Eu^{3+} phosphors for blue LED excited white LEDs," *Journal of Alloys and Compounds* 512, 264, 2012.

Berezin, M. Y. and Achilefu, S. "Fluorescence Lifetime Measurements and Biological Imaging," *Chemical Reviews* 110, 2641, 2010.

Berlincourt, D. and Jaffe, H. "Elastic and piezoelectric coefficients of single-crystal barium titanate," *Physical Review* 111, 143, 1958.

Bhatta, H. and Goldys, E. M. "Characterization of yeast strains by fluorescence lifetime imaging microscopy," *FEMS Yeast Research* 8, 81, 2008.

Blasse, G. and Grabmaier, B. C. “Luminescent materials,” *Berlin Heidelberg: Springer Verlag*, 1994.

Brinkmann, R., Sohler, W. and Suche, H. “Continuous-wave erbium-diffused $LiNbO_3$ waveguide-laser,” *Electronics Letters* 27, 415, 1991.

Burns, G. and Smith, A. “Properties of new and useful tungsten-bronze niobates,” *IEEE Journal of Quantum Electronics* 4, 584, 1968.

Capobianco, J. A., Vetrone, F. and Boyer, J. C. “Enhancement of red emission ($^4F_{9/2} \rightarrow {}^4I_{15/2}$) via upconversion in bulk and nanocrystalline cubic Y_2O_3: Er^{3+},” *The Journal of Physical Chemistry B* 106, 1181, 2002.

Catalan, G. and Scott, J. F. “Physics and applications of bismuth ferrite,” *Advanced Materials* 21, 2463, 2009.

Cavalcante, L. S., Anicete-Santos, M., Sczancoski, J. C., Simões, L. G. P., Santos, M. R. M. C., Varela, J. A., Pizani, P. S. and Longo, E. “Intense and broad photoluminescence at room temperature in structurally disordered $Ba[Zr_{0.25}Ti_{0.75}]O_3$ powders: An experimental/theoretical correlation,” *Journal of Physics and Chemistry of Solids* 69, 1782, 2008.

Chai, G. Q., Dong, G. P., Qiu, J. R., Zhang, Q. Y. and Yang, Z. M. “Phase transformation and intense 2.7 μm emission from Er^{3+} doped YF_3/YOF submicron-crystals,” *Scientific Reports* 3, 1598, 2013.

Chattopadhyay, S., Ayyub, P., Palkar, V. R., and Multani, M. “Size-induced diffuse phase transition in the nanocrystalline ferroelectric $PbTiO_3$,” *Physical Review B* 52, 13177, 1995.

Chen, H., Liu, Y. H., Zhou, Y. F. and Jiang, Z. H. “Spectroscopic properties of Er^{3+}-doped tellurite glass for 1.55 μm optical amplifier,” *Journal of Alloys and Compounds* 397, 286, 2005.

Chen, L., Liang, X. L., Long, Z. and Wei, X. H. “Upconversion photoluminescence properties of Er^{3+}-doped $Ba_xSr_{1-x}TiO_3$ powders with different phase structure,” *Journal of Alloys and Compounds* 516, 49, 2012.

Chen, S., Wu, M. J., An, L. Q., Li, Y. X. and Wang, S. W. “Strong green and red upconversion emission in Er^{3+}-doped $Na_{1/2}Bi_{1/2}TiO_3$ ceramics,” *Journal of the American Ceramic Society* 90, 664, 2007.

Chen, Y. and Periasamy, A. “Characterization of two-photon excitation fluorescence lifetime imaging microscopy for protein localization,” *Microscopy Research and Technique* 63, 72, 2004.

Cheng, Z. X., Zhang, S. J., Song, F., Guo, H. C., Han, J. R. and Chen, H. C. “Optical spectroscopy of Yb/Er codoped $NaY(WO_4)_2$ crystal,” *Journal of Physics and Chemistry of Solids* 63, 2011, 2002.

Chivian, J. S., Case, W. E. and Eden, D. D. “The photon avalanche: A new phenomenon in Pr^{3+}-based infrared quantum counters,” *Applied Physics Letters* 35, 124, 1979.

Chu, S. Y., Wen, C. H., Tyan, S. L., Lin, Y. G., Juang, Y. D. and Wen, C. K. “Polarization tuning the Stokes photoluminescence spectra of erbium doped $KNbO_3$ ceramics,” *Journal of Applied Physics* 96, 2552, 2004.

Chu, Y. H., Martin, L. W., Holcomb, M. B. and Ramesh, R. “Controlling magnetism with multiferroics,” *Materials Today* 10, 16, 2007.

Chung, J. H., Ryu, J. H., Mhin, S. W., Kim, K. M. and Shim, K. B. "Controllable white upconversion luminescence in $Ho^{3+}/Tm^{3+}/Yb^{3+}$ co-doped $CaMoO_4$," *Journal of Materials Chemistry* 22, 3997, 2012.

Coats, A. W. and Redfern, J. P. "Thermogravimetric Analysis: A Review," *Analyst* 88, 906, 1963.

De Camargo, A. S., Botero, É. R., Andreeta, É. R., Garcia, D., Eiras, J. A. and Nunes, L. A. O. "2.8 and 1.55 μm emission from diode-pumped Er^{3+}-doped and Yb^{3+} codoped lead lanthanum zirconate titanate transparent ferroelectric ceramic," *Applied Physics Letters* 86, 241112, 2005.

De Wild, J., Meijerink, A., Rath, J. K., Van Sark, W. G. J. H. M. and Schropp, R. E. I. "Upconverter solar cells: materials and applications," *Energy & Environmental Science* 4, 4835, 2011.

Desurvire, E. "The golden age of optical fiber amplifiers," *Physics Today* 47, 20, 1994.

Diallo, P. T., Boutinaud, P., Mahiou, R. and Cousseins, J. C. "Red luminescence in Pr^{3+}-doped calcium titanates," *Physica Status Solidi A* 160, 255, 1997.

Dickinson, B. C., Golding, P. S., Pollnau, M., King, T. A. and Jackson, S. D. "Investigation of a 791-nm pulsed-pumped 2.7-μm Er-doped ZBLAN fibre laser," *Optics Communications* 191, 315, 2001.

Donzella, V., Toccafondo, V., Faralli, S., Pasquale, F. D., Cassagnettes, C., Barbier, D. and Figueroa, H. H. "Ion-exchanged Er^{3+}/Yb^{3+} co-doped waveguide amplifiers longitudinally pumped by broad area lasers," *Optics Express* 18, 12690, 2010.

DrDomenico, M. and Wemple, S. H. “Oxygen-Octahedra Ferroelectrics. I. Theory of Electro-optical and Nonlinear optical Effects,” *Journal of Applied Physics* 40, 720, 1969.

Du, H. L., Luo, F., Qu, S., Pei, Z. B., Zhu, D. M. and Zhou, W. C. “Phase structure, microstructure, and electrical properties of bismuth modified potassium-sodium niobium lead-free ceramics,” *Journal of Applied Physics* 102, 054102, 2007a.

Du, H. L., Zhou, W., Luo, F., Zhu, D., Qu, S. and Pei, Z. “Perovskite lithium and bismuth modified potassium-sodium niobium lead-free ceramics for high temperature applications,” *Applied Physics Letters* 91, 182909, 2007b.

Du, P., Luo, L. H., Li, W. P., Zhang, Y. P. and Chen, H. B. “Photoluminescence and electrical performance of smart material: Pr-doped $(1-x)(Na_{0.5}Bi_{0.5})TiO_3-xCaTiO_3$ ceramics,” *Journal of Alloys and Compounds* 551, 219, 2013a.

Du, P., Luo, L. H., Li, W. P., Zhang, Y. P. and Chen, H. B. “Electrical and luminescence properties of Er-doped $Bi_{0.5}Na_{0.5}TiO_3$ ceramics,” *Materials Science and Engineering: B* 178, 1219, 2013b.

Egerton, L. and Dillon, D. M. “Piezoelectric and Dielectric Properties of Ceramics in the System Potassium-Sodium Niobate,” *Journal of the American Ceramic Society* 42, 438, 1959.

Eitel, R. E., Randall, C. A., Shrout, T. R., Rehrig, P. W., Hackenberger, W. and Park, S. E. “New high temperature morphotropic phase boundary piezoelectrics based on $Bi(Me)O_3-PbTiO_3$ ceramics.” *Japanese Journal of Applied Physics* 40, 5999, 2001.

Etchart, I., Huignard, A., Be′rard, M., Nordin, M. N., Herna′ ndez, I., Curry, R. J., Gillin, W. P. and Cheetham, A. K. “Oxide phosphors for efficient light upconversion: Yb^{3+} and

Er^{3+} co-doped Ln_2BaZnO_5 (Ln = Y, Gd)," *Journal of Materials Chemistry* 20, 3989, 2010.

Fan, C., Wang, J. L., Tang, N., Xu, H. X., Wei, G. K., Xu, H. Z. "Fabrication and photoluminescence of Er^{3+}-doped Al_2O_3 thin films with sol-gel method," *Journal of Nanoscience and Nanotechnology* 11, 11147, 2011.

Fang, J., Wang, X. H. and Li, L. T. "Properties of ultrafine-grained $Na_{0.5}K_{0.5}NbO_3$ ceramics prepared from nanopowder," *Journal of the American Ceramic Society* 94, 1654, 2011.

Feng, Z., Luo, H., Guo, Y., He T. and Xu, H. "Dependence of high electric-field-induced strain on the composition and orientation of $Pb(Mg_{1/3}Nb_{2/3})O_3$ -$PbTiO_3$ crystals," *Solid State Communications* 126, 347, 2003.

Fu, H. and Cohen, R. E. "Polarization rotation mechanism for ultrahigh electromechanical response in single-crystal piezoelectrics," *Nature* 403, 281, 2000.

Gamelin, D. R. and Gudel, H. U. "Design of luminescent inorganic materials: new photophysical processes studied by optical spectroscopy," *Accounts of Chemical Research* 33, 235, 2000.

Gao, D., Kwok, K. W., Lin, D. and Chan, H. L. W. "Microstructure and electrical properties of La-modified $K_{0.5}Na_{0.5}NbO_3$ lead-free piezoelectric ceramics," *Journal of Physics D: Applied Physics* 42, 035411, 2009a.

Gao, D., Kwok, K. W., Lin, D. M. and Chan, H. W. L. "Microstructure, electrical properties of CeO_2-doped $(K_{0.5}Na_{0.5})NbO_3$ lead-free piezoelectric ceramics," *Journal of Materials Science* 44, 2466, 2009b.

Gao, G., Wang, G., Yu, C., Zhang, J. and Hu, L. “Investigation of 2.0 μm emission in Tm^{3+} and Ho^{3+} co-doped oxyfluoride tellurite glass,” *Journal of Luminescence* 129, 1042, 2009.

Gardiner, D. J. “Practical Raman spectroscopy,” *Springer-Verlag*, ISBN 978-0-387-50254-0, 1989.

Ge, W. W., Liu, H., Zhao X. Y., Li X. B., Pan, X. M., Lin, D., Xu, H. Q., Jiang, X. P. and Luo, H. S. “Orientation dependence of electrical properties of $0.96Na_{0.5}Bi_{0.5}TiO3$ - $0.04BaTiO_3$ lead-free piezoelectric single crystal,” *Applied Physics A* 95, 761, 2009.

Gerner, P. and Güdel, H. U. “Absorption and upconversion light emission properties of Er^{3+} and Yb^{3+}/Er^{3+} codoped $NaYS_2$,” *Chemical Physics Letters* 413, 105, 2005.

Gheorghiu, F. P., Ianculescu, A., Postolache, P., Lupu, N., Dobromir, M., Luca, D. and Mitoseriu, L. “Preparation and properties of $(1-x)BiFeO_3$-$xBaTiO_3$ multiferroic ceramics,” *Journal of Alloys and Compounds* 506, 862, 2010.

Golding, P. S., Jackson, S. D., King, T. A. and Pollnau, M. “Energy transfer processes in Er^{3+}-doped and Er^{3+}, Pr^{3+}-codoped ZBLAN glasses,” *Physical Review B* 62, 856, 2000.

Gomes, L., Oermann, M., Heidepriem, H. E., Ottaway, D., Monro, T., Librantz, A. F. H. and Jackson, S. D. “Energy level decay and excited state absorption processes in erbium-doped tellurite glass,” *Journal of Applied Physics* 110, 083111, 2011.

Gottmann, J., Moiseev, L., Vasilief, I. and Wortmann, D. “Manufacturing of Er: ZBLAN ridge waveguides by pulsed laser deposition and ultrafast laser micromachining for green integrated lasers,” *Materials Science and Engineering: B* 146, 245, 2008.

Guillemet-Fritsch S., Valdez-Nava Z., Tenailleau C., Lebey T., Durand B., Chane-Ching J. Y. “Colossal permittivity in ultrafine grain size $BaTiO_{3-x}$ and $Ba_{0.95}La_{0.05}TiO_{3-x}$ materials,” *Advanced Materials* 20, 551, 2008.

Guo, C. F., Li, M., Xu, Y., Li, T., Ren, Z. Y. and Bai, J. T. “A potential green-emitting phosphor $Ca_8Mg(SiO_4)_4Cl_2:Eu^{2+}$ for white light emitting diodes prepared by sol-gel method,” *Applied Surface Science* 257, 8836, 2011.

Guo, Y., Kakimoto, K. and Ohsato, H. “$(K_{0.5}Na_{0.5})NbO_3$-$LiTaO_3$ lead-free piezoelectric ceramics,” *Materials Letters* 59, 241, 2005.

Guo, Y. P., Kakimoto, K. and Ohsato, H. “Phase transitional behavior and piezoelectric properties of $(Na_{0.5}K_{0.5})NbO_3$-$LiNbO_3$ ceramics,” *Applied Physics Letters* 85, 4121, 2004.

Guo, Y. Y., Li, M., Tian, Y., Xu, R. R., Hu, L. L. and Zhang, J. J. “Enhanced 2.7 μm emission and energy transfer mechanism of Nd^{3+}/Er^{3+} co-doped sodium tellurite glasses,” *Journal of Applied Physics* 110, 013512, 2011.

Haase, M. and Schäfer, H. “Up-conversion nanoparticles,” *Angewandte Chemie International Edition* 50, 5808, 2011.

Haertling, G. H. “Properties of hot-pressed ferroelectric alkali niobate ceramics,” *Journal of the American Ceramic Society* 50, 329, 1967.

Hao, J. H., Zhang, Y. and Wei, X. H. “Electric-induced enhancement and modulation of upconversion photoluminescence in epitaxial $BaTiO_3$:Yb/Er thin films,” *Angewandte Chemie International Edition* 123, 7008, 2011.

Haro-González, P., Martín, L. L., Pérez-Rodríguez, C., Martín, I. R. and Mujica, A. “Optical study of the effect of the impurity content on the ferroelectric properties of Er^{3+} doped SBN glass-ceramic samples,” *Journal of Applied Physics* 110, 084113, 2011.

Hartling, G. H. “PLZT electro-optic materials and applications-a review,” *Ferroelectrics* 75, 25, 1987.

He, C. J., Chen, H. B., Sun, L., Wang, J. M., Xu, F., Du, C. L., Zhu, K. J. and Liu, Y. W. “Effective electro-optic coefficient of (1-x)$Pb(Zn_{1/3}Nb_{2/3})O_3$-x$PbTiO_3$ single crystals,” *Crystal Research and Technology* 47, 610, 2012.

Heer, S., Lehmann, O., Haase, M. and Güdel, H. U. “Blue, green, and red upconversion emission from lanthanide-doped $LuPO_4$ and $YbPO_4$ nanocrystals in a transparent colloidal solution,” *Angewandte Chemie International Edition* 42, 3179, 2003.

Heer, S., Kömpe, K., Güdel, H. U. and Haase, M. “Highly Efficient Multicolour Upconversion emission in transparent colloids of lanthanide-doped $NaYF_4$ nanocrystals,” *Advanced Materials* 16, 2102, 2004.

Henderson, B. and Imbusch, G. F. “Optical spectroscopy of inorganic solids,” *Clarendon Press,* Oxyford UK, 1989.

Henke, B., Pientka, F., Johnson, J. Ahrens, B., Miclea, P. and Schweizer, S. “Saturation effects in the upconversion efficiency of Er-doped fluorozirconate glasses,” *Journal of Physics: Condensed Matter* 22, 155107, 2010.

Hiruma, Y. Nagata, H. and Takenaka, T. “Thermal depoling process and piezoelectric properties of bismuth sodium titanate ceramics,” *Journal of Applied Physics* 105, 084112, 2009.

Hollenstein, E., Damjanovic, D. and Setter, N. “Temperature stability of the piezoelectric properties of Li-modified KNN ceramics,” *Journal of the European Ceramic Society* 27, 4093, 2007.

Hou, X. R., Zhou, S. M., Li, W. J., Li, Y. K., Lin, H., Teng, H. and Jia, T. T. “Investigation of up-conversion luminescence in Er^{3+}/Yb^{3+}-codoped yttria transparent ceramic,” *Journal of the American Ceramic Society* 93, 2779, 2010.

Hsu, K., Miller, C. H., Kringlebotn, J. T. and Payne, D. N. “Continuous and discrete wavelength tuning in Er: Yb fiber Fabry-Perot lasers,” *Optical Letters* 20, 337, 1995.

Hu, Y. F., Wang, D. Q., Li, Z. J., Lu, J. J. and Zheng, J. B. “Upconversion luminescence properties of Er^{3+}-Yb^{3+}-codoped titania-zirconia composites,” *Journal of the American Ceramic Society* 93, 374, 2010.

Huang, S. H., Wang, X. J., Chen, B. J., Jia, D. and Yen, W. M. “Photon cascade emission and quantum efficiency of the $^3P_0$ level in Pr^{3+}-doped $SrAl_{12}O_{19}$ system,” *Journal of Luminescence* 102, 344, 2003.

Hui, Y., Zhao, Y., Zhao, S. M., Gu, L. J., Fan, X. Z., Zhu, L., Zou, B. L., Wang, Y. and Cao, X. Q. “Fluorescence of Eu^{3+} as a probe of phase transformation of zirconia,” *Journal of Alloys and Compounds* 573, 177, 2013.

Hwang, B. C., Jiang, S. B., Luo, T., Watson, J., Sorbello G. and Peyghambarian N. “Cooperative upconversion and energy transfer of new high Er^{3+}- and Yb^{3+}-Er^{3+}-doped phosphate glasses,” *The Journal of the Optical Society of America B* 17, 833, 2000.

Inokuti, M. and Hirayama, F. “Influence of Energy Transfer by the Exchange Mechanism on Donor Luminescence,” *The Journal of Chemical Physics* 43, 1978, 1965.

Ishizawa, N., Wang, J., Sakakura, T., Inagaki, Y. and Kakimoto, K. “Structural evolution of $Na_{0.5}K_{0.5}NbO_3$ at high temperatures,” *Journal of Solid State Chemistry* 183, 2731, 2010.

Jackson, S. D., King, T. A. and Pollnau, M. “Modelling of high-power diode-pumped erbium 3-μm fibre lasers,” *Journal of Modern Optics* 47, 1987, 2000.

Jaeger, R. E. and Egerton, L. “Hot-press of potassium sodium niobates,” *Journal of the American Ceramic Society* 45, 209, 1962.

Jha, A., Naftaly, M., Jordery, S., Samson, B. N., Taylor, E. R., Hewak, D., Payne, D. N., Poulain, M. and Zhang, G. “Design and fabrication of Pr^{3+}-doped fluoride glass optical fibres for efficient 1.3 μm amplifiers,” *Pure and Applied Optics: Journal of the European Optical Society Part A* 4, 417, 1995.

Jia, W., Xu, W., Rivera, I., Pérez, A., Fernández, F. “Effects of compositional phase transitions on luminescence of $Sr_{1-x}Ca_xTiO_3$:Pr^{3+},” *Solid State Communications* 126, 153, 2003.

Jia, Y. M., Wei, Y. B., Wu, Z., Zhou, Z. H., Chen, J. R., Jia, Y. K., Zhang, Y. H., Zhou, J. Y., Wang, H. H. “Effects of compositional changes on luminescence of lead-free Eu^{3+}-doped $K_{1-x}Na_xNbO_3$ piezoelectric ceramics,” *Journal of Alloys and Compounds* 586, 66, 2014.

Jiang, H., Zou, Y. K., Chen, Q., Li, K. K., Zhang, R., Wang, Y., Ming, H. and Zheng, Z. Q. “Transparent electro-optic ceramics and devices,” *Proceedings of the SPIE* 5644, 380, 2005.

Jorgensen C. K. and Reisfeld, R. “Judd-Ofelt parameters and chemical bonding,” *Journal of the Less-Common Metals* 93, 107, 1983.

Joubert, M. F. “Photon avalanche upconversion in rare earth laser materials,” *Optical Materials* 11, 181, 1999.

Judd, B. R. “Optical absorption intensities of rare-earth ions,” *Physical Review* 127, 750, 1962.

Kakimoto, K., Akao, K., Guo, Y. and Ohsato. H. “Raman Scattering Study of Piezoelectric ($Na_{0.5}K_{0.5}$)NbO_3-$LiNbO_3$ Ceramics,” *Japanese Journal of Applied Physics* 44, 7064, 2005.

Kang, S. Y., Kim, Y. H., Moon, J., Kang, K. S., Lee, D. J. and Kang, S. G. “Luminescence enhancement by Ga^{3+} codoping of $BaTiO_3$:Pr^{3+} phosphors,” *Japanese Journal of Applied Physics* 48, 052301, 2009.

Kanth, C. L., Ragavaiah, B. V., Rao, B. A. and Veeraiah, N. “Optical absorption, fluorescence and thermoluminescence properties of ZnF_2-MO-TeO_2 (MO = ZnO, CdO and PbO) glasses doped with Er^{3+} ions,” *Journal of Luminescence* 109, 193, 2004.

Kazuo, K., Shiro, Y., Haruki, S. and Akira, M. “Green upconversion fluorescence in Er^{3+}-doped Ta_2O_5 heated gel,” *Applied Physics Letters* 67, 3423, 1995.

Kim, J. S., Ahn, C. W., Lee, S. Y., Ullah, A. and Kim, I. W. “Effects of $LiNbO_3$ substitution on lead-free ($K_{0.5}Na_{0.5}$)NbO_3 ceramics: Enhanced ferroelectric and electrical properties,” *Current Applied Physics* 11, S149, 2011.

Kishi, Y. and Tanabe, S. “Fabrication and efficient infrared-to-visible upconversion in transparent glass ceramics of Er-Yb co-doped CaF_2 nano-crystals,” *Journal of the*

American Ceramic Society 88, 3423, 2005.

Kounga, A. B. Zhang, S. T. Jo, W. Granzow, T. and Rodel, J. "Morphotropic phase boundary in (1-x)$Bi_{0.5}Na_{0.5}TiO_3$-x$K_{0.5}Na_{0.5}NbO_3$ lead-free piezoceramics," *Applied Physics Letters* 92, 222902, 2008.

Kringlebotn, J. T., Archambault, J. L., Reekie, L. and Payne, D. N. "Er^{3+}: Yb^{3+}-codoped fiber distributed-feedback laser," Optical Letters 19, 2101, 1994.

Lee, B. W. and Lee, E. J. "Effects of complex doping on microstructural and electrical properties of PZT ceramics," *Journal of Electroceramics* 17, 597, 2006.

Li, F. L. and Kwok, K. W. "Fabrication of transparent electro-optic $(K_{0.5}Na_{0.5})_{1-x}Li_xNb_{1-x}Bi_xO_3$ lead-free ceramics," *Journal of the European Ceramic Society* 33, 123, 2013a.

Li, F. L. and Kwok, K. W. "$K_{0.5}Na_{0.5}NbO_3$-based lead-free transparent electro-optic ceramics prepared by pressureless sintering," *Journal of the American Ceramic Society* 96, 3557, 2013b.

Li, J. F., Wang, K., Zhang, B. P. and Zhang, L. M. "Ferroelectric and piezoelectric properties of fine-grained $Na_{0.5}K_{0.5}NbO_3$ lead-free piezoelectric ceramics prepared by spark plasma sintering," *Journal of the American Ceramic Society* 89, 706, 2006.

Lin, D. M., Kwok, K. W. and Chan, H. W. L. "Microstructure, dielectric and piezoelectric properties of $(K_{0.5}Na_{0.5})NbO_3$-$Ba(Ti_{0.95}Zr_{0.05})O_3$ lead-free ceramics with CuO sintering aid," *Applied Physics A: Materials Science & Processing* 88, 358 2007a.

Lin, D. M., Kwok, K. W. and Chan, H. W. L. "Structure, piezoelectric and ferroelectric properties of Li- and Sb-modified $K_{0.5}Na_{0.5}NbO_3$ lead-free ceramics," *Journal of Physics D: Applied Physics* 40, 3500, 2007b.

Lin, D. M., Kwok, K. W. and Chan, H. W. L. "Phase structures and electrical properties of $K_{0.5}Na_{0.5}(Nb_{0.925}Ta_{0.075})O_3$-$LiSbO_3$ lead-free piezoelectric ceramics," *Journal of Physics D: Applied Physics* 40, 6060, 2007c.

Lin, D. M., Kwok, K. W. and Chan, H. W. L. "Structure, dielectric and piezoelectric properties of CuO-doped $K_{0.5}Na_{0.5}NbO_3$-$BaTiO_3$ lead-free ceramics," *Journal of Applied Physics* 102, 074113, 2007d.

Lin, D. M., Kwok, K. W. and Chan, H. W. L. "Microstructure, phase transition, and electrical properties of $(K_{0.5}Na_{0.5})_{1-x}Li_x(Nb_{1-y}Ta_y)O_3$ lead-free piezoelectric ceramics," *Journal of Applied Physics* 102, 034102, 2007e.

Lin, D. M., Kwok, K. W. and Chan, H. W. L. "Piezoelectric and ferroelectric properties of $K_xNa_{1-x}NbO_3$ lead-free ceramics with MnO_2 and CuO doping," *Journal of Alloys and Compounds* 461, 273, 2008a.

Lin, D. M., Kwok, K. W. and Chan, H. W. L. "Phase transition and electrical properties of $(K_{0.5}Na_{0.5})(Nb_{1-x}Ta_x)O_3$ lead-free piezoelectric ceramics," *Applied Physics A* 91, 167, 2008b.

Lisiecki, R., Augustyn, E., Romanowski, W. R. and Zelechower, M. "Er-doped and Er, Yb co-doped oxyfluoride glasses and glass-ceramics, structural and optical properties," *Optical Materials* 33, 1630, 2011.

Liu, L., Wang, Y. X., Bai, Y. F., Zhang, X. R., Yang, K., Yang, L. and Song, Y. L. "Effects of Li^+ on structure and spectroscopic properties of Er^{3+}/Li^+ codoped Sb_2O_3-

Na_2O-SiO_2 glasses," *Journal of Applied Physics* 107, 093103, 2010.

Liu, M., Wang, S. W., Zhang, J., An, L. Q. and Chen, L. D. "Upconversion luminescence of $Y_3Al_5O_{12}$ (YAG): Yb^{3+}, Tm^{3+} nanocrystals," *Optical Materials* 30, 370, 2007.

Liu, M., Wang, S. W., Tang, D. Y., Chen, L. D. and Ma, J. "Fabrication and Microstructures of YAG Transparent Ceramics," *Science of Sintering* 40, 311, 2008.

Liu, Y., Tu, D., Zhu, H. and Chen, X. "Lanthanide-doped luminescent nanoprobes: controlled synthesis, optical spectroscopy, and bioapplications," *Chemical Society Reviews* 42, 6924, 2013.

Lobo, R. P. S. M., Mohallem, N. D. S. and Moreira, R. L. "Grain-size effects on diffuse phase transitions of sol-gel prepared barium titanate ceramics," *Journal of the American Ceramic Society* 78, 1343, 1995.

Luo, Y. S., Zhang, J. H., Sun, J. T., Lu, S. Z. and Wang, X. J. "Spectroscopic properties of tungsten-tellurite glasses doped with Er^{3+} ions at different concentrations," *Optical Materials* 28, 255, 2006.

Mahalingam, V., Mangiarini, F., Vetrone, F., Venkatramu, V., Bettinelli, M., Speghini, A. and Capobianco, J. A. "Bright white upconversion emission from Tm^{3+}/Yb^{3+}/Er^{3+}-doped $Lu_3Ga_5O_{12}$ Nanocrystals," *The Journal of Physical Chemistry C* 112, 17745, 2008.

Mahesh, K., Weng, P. S., and Furetta, C. "Thermoluminescence in solids and its applications," *Nuclear Technology Publishing,* Ashford UK, 1989.

Makishima, S., Yamamoto, H., Tomotsu, T. and Shionoya, S. J. “Luminescence spectra of Sm^{3+} in $BaTiO_3$ host lattice,” *Journal of the Physical Society of Japan* 20, 2147, 1965.

Matsubara, M., Yamaguchi, T., Kikuta, K. and Hirano, S. “Sinterability and piezoelectric properties of (K, Na)NbO_3 ceramics with novel sintering aid.” *Japanese Journal of Applied Physics* 10, 7259, 2004.

Merz, W. J. “The electric and optical behavior of $BaTiO_3$ single-domain crystals,” *Physical Review* 76, 1221, 1949.

Miriyala, N., Prashanthi, K. and Thundat, T. “Oxygen vacancy dominant strong visible photoluminescence from $BiFeO_3$ nanotubes,” *Physica Status Solidi-Rapid Research Letters* 7, 668, 2013.

Möbert, P. E. A., Heumann, E., Huber, G. and Chai, B. H. “Green Er^{3+}:$YLiF_4$ upconversion laser at 551nm with Yb^{3+} codoping: a novel pumping scheme,” *Opical Letters* 22, 1412, 1997.

Murty, S. N., Umakantham, K., Bhanumathi, A. “Ferroelectric behaviour of lanthanum doped (Na,K)NbO_3 ceramics,” *Ferroelectrics* 82, 141, 1988.

Murty, S. N. and Bhanumathi, A. “Phase transitions in europium doped (Na,K)NbO_3 ceramics,” *Ferroelectrics* 94, 285, 1989.

Nagata, H., Koizumi, N. and Takenaka, T. “Lead-free piezoelectric ceramics of $(Bi_{1/2}Na_{1/2})TiO_3$-$BiFeO_3$ system,” *Key Engineering Materials* 169, 37, 1999.

Nakashima, Y., Sakamoto, W., Shimura, T. and Yogo, T. “Chemical processing and characterization of ferroelectric (K,Na)NbO_3 thin films,” *Japanese Journal of Applied*

Physics 46, 6971, 2007.

Neaton, J. B., Ederer, C. Waghmare, U. V., Spaldin, N. A. and Rabe, K. M. “First-principles study of spontaneous polarization in multiferroic $BiFeO_3$,” *Physical Review B* 71, 014113, 2005.

Ofelt, G. S. “Intensities of crystal spectra of rare-earth ions,” *The Journal of Chemical Physics* 37, 511, 1962.

Okamoto, S. and Yamomoto, H. “Emission from $BaTiO_3$:Pr controlled by ionic of added trivalent ion,” *Journal of Applied Physics* 91, 5492, 2002.

Orhan, E., Varela, J. A., Zenatti, A., Gurgel, M. F. C., Pontes, F. M., Leite, E. R., Longo, E., Beltràn, A. and Andrès, J. “Room-temperature photoluminescence of $BaTiO_3$: Joint experimental and theoretical study,” *Physical Review B* 71, 085113, 2005.

Ostby, E. P., Yang, L. and Vahala, K. J. “Ultralow-threshold Yb^{3+}: SiO_2 glass laser fabricated by the sol gel process,” *Optical Letters* 32, 2650, 2007.

Pang, M. L., Liu, X. M. and Lin, J. “Luminescence properties of R_2MoO_6:Eu^{3+} (R=Gd, Y, La) phosphors prepared by Pechini sol-gel process,” *Journal of Materials Research* 20, 2676, 2005.

Park, B. H., Kang, B. S., Bu, S. D., Noh, T. W., Lee, J. and Jo, W. “Lanthanum-substituted bismuth titanate for use in non-volatile memories,” *Nature* 401, 682, 1999.

Park, S. E. and Shrout, T. R. “Characteristics of relaxor-based piezoelectric single crystals for ultrasonic transducers,” *IEEE Transactions on Ultrasonics, Ferroelectrics and Frequency Control* 44, 1140, 1997.

Park, S. E. and Hackenberger, W. “High performance single crystal piezoelectrics: applications and issues,” *Current Opinion in Solid State and Materials Science* 6, 11, 2002.

Patra, A., Friend, C. S., Kapoor, R., Prasad, P. N. “Effect of crystal nature on upconversion luminescence in Er^{3+}:ZrO_2 nanocrystals,” *Applied Physics Letters* 83, 284, 2003.

Peng, D. F., Wang, X. S., Xu, C. N., Yao, X., Lin, J. and Sun, T. T. “Bright Upconversion emission, increased T_c, enhanced ferroelectric and piezoelectric properties in Er-doped $CaBi_4Ti_4O_{15}$ multifunctional ferroelectric oxides,” *Journal of the American Ceramic Society* 96, 184, 2013.

Pereira, M., Peixoto, A. G. and Gomes, M. J. M. “Effects of Nb doping on the microstructural and electrical properties of the PZT ceramics,” *Journal of the European Ceramic Society* 21, 1353, 2001.

Phillips, M. L. F., Hehlen, M. P., Nguyen, K., Sheldon, J. M. and Cockroft, N. J. “Upconversion phosphors: recent advances and new applications,” *Proceedings of the Electrochemical Society* 99, 123, 2000.

Piper, W. W., Deluca, J. A. and Ham, F. S. “Cascade fluorescent decay in Pr^{3+}-doped fluorides: Achievement of a quantum yield greater than unity for emission of visible light,” *Journal of Luminescence* 8, 344, 1974.

Pizani, P. S., Leite, E. R., Pontes, F. M., Paris, E. C., Rangel, J. H., Lee, E. J. H., Longo, E., Delega, P. and Varela, J. A. “Photoluminescence of disordered ABO_3 perovskites,” *Applied Physics Letters* 77, 824, 2000.

Pollnau, M., Lüthy, W., Weber, H. P., Jensen, T., Huber, G., Cassanho, A., Jenssen, H. P. and McFarlane, R. A. "Investigation of diode-pumped 2.8 μm laser performance in Er: BaY_2F_8," *Optical Letters* 21, 48, 1996.

Pollnau, M. "The route toward a diode-pumped 1-W erbium 3-μm fiber laser," *IEEE Journal of Quantum Electronics* 33, 1982, 1997.

Pollnau, M., Gamelin, D. R., Luthi, S. R., Güdel, H. U. and Hehlen, M. P. "Power Dependence of Upconversion Luminescence in Lanthanide and Transition-Metal-Ion Systems," *Physical Review B* 61, 3337, 2000.

Pollnau, M. and Jackson, S. D. "Erbium 3-μm fiber lasers," *IEEE Journal of Selected Topics in Quantum Electronics* 7, 30, 2001.

Pollnau, M. and Jackson, S. D. "Advances in mid-infrared fiber lasers, in Mid-Infrared Coherent Sources and Applications," *NATO Science for Peace and Security Series B: Physics and Biophysics,* Springer, 315, 2008.

Polman, A. "Erbium implanted thin film photonic materials," *Journal of Applied Physics* 82, 1, 1997.

Polman, A. "Erbium as a probe of everything?" *Physica B* 300, 78, 2001.

Pronin, I. P., Syrnikov, P. P., Isupov, V. A., Egorov, V. M. and Zaitseva, N.V. "Peculiarities of phase transition in sodium-bismuth titanate," *Ferroelectrics* 25, 395, 1980.

Ramam, K. and Lopez, M. "Ferroelectric and piezoelectric properties of Ba modified lead zirconium titanate ceramics," *Journal of Physics D: Applied Physics* 39, 4466, 2006.

Ren, X. B. “Large electric-field-induced strain in ferroelectric crystals by point-defect-mediated reversible domain switching,” *Nature Materials* 3, 91, 2004.

Ringgaard, E. and Wurlitzer, T. “Lead-free piezoceramics based on alkali niobates,” *Journal of the European Ceramic Society* 25, 2701, 2005.

Rodriguez, R. M., Valiente, R., Polizzi, S., Bettinelli, M., Speghini, A. and Piccinelli, F. “Upconversion luminescence in nanocrystals of $Gd_3Ga_5O_{12}$ and $Y_3Al_5O_{12}$ doped with Tb^{3+}-Yb^{3+} and Eu^{3+}-Yb^{3+},” *The Journal of Physical Chemistry C* 113, 12195, 2009.

Rong, X. S. and Ceng, S. M. “Luminescence and Luminescent Material,” *Chemical Industry Press,* Beijing, 2004.

Ross, S. D. “The vibrational spectra of lithium niobate, barium sodium niobate and barium sodium tantalate,” *Journal of Physics C: Solid State Physics* 3, 1785, 1970.

Russell, H. N. and Saunders, F. A.. New Regularities in the Spectra of the Alkaline Earths. *Astrophysical Journal* 61, 38, 1925.

Saito, Y., Takao, H., Tani, T., Nonoyama, T., Takatori, K., Homma, T., Nagaya, T. and Nakamura, M. “Lead free Piezoceramics,” *Nature* 432, 84, 2004.

Sakata, K. and Masuda, Y. “Ferroelectric and antiferroelectric properties of $(Na_{0.5}Bi_{0.5})TiO_3$-$SrTiO_3$ solid-solution ceramics,” *Ferroelectrics* 7, 347, 1974.

Sanamyan, T., Kanskar, M., Xiao, Y., Kedlaya, D. and Dubinskii, M. “High power diode-pumped 2.7-μm $Er^{3+}:Y_2O_3$ laser with nearly quantum defect-limited efficiency,” *Optics Express* 19, A1082, 2011.

Sawyer, C. B. and Tower, C. H. "Rochelle Salt as a Dielectric," *Physical Review* 35, 269, 1930.

Shannon, R. D. "Revised effective ionic radii and systematic studies of interatomic distances in halides and chalcogenides," *Acta Crystallographica Section A* 32, 751, 1976.

Shih, C. C. and Yariv, A. "A theoretical model of the linear electro-optic effect," *Journal of Physics C: Solid State Physics* 15, 825, 1982.

Shyichuk, A. A. and Lis, S. "Photoluminescence properties of nanosized strontium-yttrium borate phosphor $Sr_3Y_2(BO_3)_4$:Eu^{3+} obtained by the sol-gel Pechini method," *Journal of Rare Earths* 29, 1161, 2011.

Singh, K. C., Jiten, C., Laishram, R., Thakur, O. P. and Bhattacharya, D. K. "Structure and electrical properties of Li- and Ta-substituted $K_{0.5}Na_{0.5}NbO_3$ lead-free piezoelectric ceramics prepared from nanopowders," *Journal of Alloys and Compounds* 496, 717, 2010.

Singh, V., Rai, V. K., Shamery, K. A., Haase, M. and Kim, S. H. "NIR to visible frequency upconversion in Er^{3+} and Yb^{3+} codoped ZrO_2 phosphor," *Applied Physics A* 113, 747, 2013.

Su, W. B., Gu, X., Zou, X. H. and Zhu, R. H. "Luminescence Characteristic and Their Utility of Rare-earth Elements," *Chemical Research* 12, 55, 2001.

Sun, H. Q., Peng, D. F., Wang, X. S., Tang, M. M., Zhang, Q. W. and Yao X. "Green and red emission for $(K_{0.5}Na_{0.5})NbO_3$:Pr ceramics," *Journal of Applied Physics* 111, 046102, 2012.

Sun, J. T., Zhang, J. H., Luo, Y. S., Lu, S. Z., Ren, X. G., Chen, B. J. and Wang, X. J. “Thermal stability and spectral properties of Er^{3+}-doped gadolinium borosilicate glasses,” *Optical Materials* 28, 306, 2006.

Suyver, J. F., Aebischer, A., Biner, D., Gerner, P., Grimm, J., Heer, S., Kramer, K. W., Reinhard, C. and Gudel, H. U. “Novel materials doped with trivalent lanthanides and transition metal ions showing near-infrared to visible photon upconversion,” *Optical Materials* 27, 1111, 2005.

Szachowicz, M., Tascu, S., Joubert, M., Moretti, P. and Nikl, M. “Realization and infrared to green upconversion luminescence in Er^{3+}:$YAlO_3$ ion-implanted optical waveguides,” *Optical Materials* 28, 162, 2006.

Takenaka, T., Maruyama, K. and Sakata, K. “$(Bi_{1/2}Na_{1/2})TiO_3$-$BaTiO_3$ system for lead-free piezoelectric ceramics,” *Japanese Journal of Applied Physics* 30, 2236, 1991.

Tanaka, J., Onoda, Y., Tsukioka, M., Shimazu, M. and Ehara, S. “The NMR study of Li ion motion in $K_3LiNb_6O_{17}$ and $K_3LiTa_6O_{17}$,” *Japanese Journal of Applied Physics* 21, 451, 1982.

Teague, J. R., Gerson, W. J. and James, R. “Dielectric hysteresis in single crystal $BiFeO_3$,” *Solid State Communications* 8, 1073, 1970.

Thiel, C. W., Sun, Y., Macfarlane, R. M., Böttger, T. and Cone, R. L. “Rare-earth-doped $LiNbO_3$ and $KTiOPO_4$ (KTP) for waveguide quantum memories,” *Journal of Physics B: Atomic, Molecular and Optical Physics* 45, 124013, 2012.

Tian, X. L., Wu, Z., Jia, Y. M., Chen, J. R., Zheng, R. K., Zhang, Y. H. and Luo, H. S.Remanent-polarization-induced enhancement of photoluminescence in Pr^{3+}-doped lead-free ferroelectric $(Bi_{0.5}Na_{0.5})TiO_3$ ceramic, *Applied Physics Letters* 102, 042907, 2013.

Tian, Y., Xu, R. R., Hu, L. L. and Zhang, J. J. “Enhanced 2.7 μm emission from $Er^{3+}/Tm^{3+}/Pr^{3+}$ triply doped fluoride glass,” *Journal of the American Ceramic Society* 94, 2289, 2011a.

Tian, Y., Xu, R. R., Zhang, L. Y., Hu, L. L. and Zhang, J. J. “Observation of 2.7 μm emission from diode-pumped Er^{3+}/Pr^{3+}-codoped fluorophosphate glass,” *Optical Letters* 36, 109, 2011b.

Tikhomirov, V. K., Méndez-Ramos, J., Rodríguez, V. D., Furniss, D. and Seddon, A. B. “Laser and gain parameters at 2.7 μm of Er3+-doped oxyfluoride transparent glass-ceramics,” *Optical Materials* 28, 1143, 2006.

Ting, C. C., Chien, Y. C., and Sung, W. F. “Erbium doping effects on the structural and infrared luminescence properties of $Gd_2Ti_2O_7$ nanocrystals,” *Journal of Solid State Science & Technology* 2, R105, 2013.

Tran, D. C., Sigel Jr, G. H., Bendow, B. “Heavy metal fluoride glasses and fibers: a review,” *Journal of Lightwave Technology* 2, 566, 1984.

Uki, D., Ohnishi, H., Yamaguchi, T., Takemori, Y., Koizumi, A., Fuchi, S., Ujihara, T. and Takeda, Y. “Effect of Li doping on photoluminescence from Er, O-codoped GaAs,” *Journal of Crystal Growth* 298, 69, 2007.

Valasek, J. “Piezo-electric and allied phenomena in Rochelle salt,” *Physical Review* 17, 475, 1921.

Van Dijk, J. M. F. and Schuurmans, M. F. H. “On the nonradiative and radiative decay rates and a modified exponential energy gap law for 4f-4f transitions in rare-earth ions,” *The Journal of Chemical Physics* 78, 5317, 1983.

Van Sark, W. G., de Wild, J., Rath, J. K., Meijerink, A. and Schropp, R. E. “Upconversion in solar cells,” *Nanoscale Research Letters* 8, 81, 2013.

Vecht, A., Smith, D. W., Chadha, S. S., Gibbons, C. S., Koh, J. and Morton, D. “New electron excited light-emitting materials,” *Journal of Vacuum Science and Technology* B12, 781, 1994.

Vij, D. R. “Luminescence of solids,” *Plenum Press*, New York, 1998.

Vila, L. D., Aranha, N., Messaddeq, Y., Stucchi, E. B., Ribeiro, S. J. L. and Nunes, L. A. O. “Spectroscopic properties of Er in oxysulfide glasses,” *Journal of Alloys and Compounds* 344, 226, 2002.

Wada, S., Suzuki, S., Noma, T., Suzuki, T., Osada, M., Kakihana, M., Park, S. E., Cross, L. E. and Shrout, T. R. “Enhanced piezoelectric property of barium titanate single crystals with engineered domain configurations,” *Japanese Journal of Applied Physics* 38, 5505, 1999.

Wan, X. M., Luo, H. S., Zhao, X. Y., Wang, D. Y., Chan, H. L. W. and Choy, C. L. “Refractive indices and linear electro-optic properties of (1-x)$Pb(Mg_{1/3}Nb_{2/3})O_3$ - x$PbTiO_3$ single crystals,” *Applied Physics Letters* 85, 5233, 2004.

Wan, X. M., Wang, D. Y., Zhao, X. Y., Luo, H. S., Chan, H. L. W. and Choy, C. L.

“Electro-optic characterization of tetragonal (1-x)Pb($Mg_{1/3}Nb_{2/3}$)O_3-x$PbTiO_3$ single crystals by a modified Sénarmont setup,” *Solid State Communications* 134, 547, 2005.

Wang, C., Hou, Y. D., Ge, H. Y., Zhu, M. K., Wang, H. and Yan, H. “Sol-gel synthesis and characterization of lead-free LNKN nanocrystalline powder,” *Journal of Crystal Growth* 310, 4635, 2008.

Wang, F. and Liu, X. G. “Recent advances in the chemistry of lanthanide-doped upconversion nanocrystals,” *Chemical Society Reviews* 38, 976, 2009.

Wang, F., Han, Y., Lim, C. S., Lu, Y. H., Wang, J., Xu, J., Chen, H. Y., Zhang, C., Hong, M. H. and Liu, X. G. “Simultaneous phase and size control of upconversion nanocrystals through lanthanide doping,” *Nature* 463, 1061, 2010a.

Wang, F., Banerjee, D., Liu, Y. S., Chen, X. Y. and Liu, X. G. “Upconversion nanoparticles in biological labeling, imaging, and therapy,” *Analyst* 135, 1839, 2010b.

Wang, J., Neaton, J. B., Zheng, H., Nagarajan, V., Ogale, S. B., Liu, B., Viehland, D., Vaithyanathan, V., Schlom, D. G., Waghmare, U. V., Spaldin, N. A., Rabe, K. M., Wuttig, M. and Ramesh R. “Epitaxial $BiFeO_3$ Multiferroic Thin Film Heterostructures,” *Science* 299, 1719, 2003.

Wang, R. P., Xie, R. J., Sekiya, T., Shimojo, Y., Akimune, Y., Hirosaki, N. and Itoh, M. “Piezoelectric Properties of Spark-Plasma-Sintered ($Na_{0.5}K_{0.5}$)NbO_3-$PbTiO_3$ Ceramics,” *Japanese Journal of Applied Physics* 41, 7119, 2002.

Wang, X., Kong, X. G., Yu, Y., Sun, Y. J. and Zhang, H. “Effect of annealing on upconversion luminescence of ZnO: Er^{3+} nanocrystals and high thermal sensitivity,” *The Journal of Physical Chemistry C* 111, 15119, 2007.

Wang, X. S., Xu, C. N., Yamada, H., Nishikubo, K. and Zheng, X. G. “Electro-mechano-optical conversions in Pr^{3+}-doped $BaTiO_3$-$CaTiO_3$ ceramics,” *Advanced Materials* 17, 1254, 2005.

Weber, M. J. “Probabilities for radiative and nonradiative decay of Er^{3+} in LaF_3,” *Physical Review* 157, 262, 1967.

Wei, Y. B., Wu, Z. Jia, Y. M., Wu, J., Shen, Y. C. and Luo, H. S. “Dual-enhancement of ferro-/piezoelectric and photoluminescent performance in Pr^{3+} doped $(K_{0.5}Na_{0.5})NbO_3$ lead-free ceramics,” *Applied Physics Letters* 105, 042902, 2014.

Wen, C. H., Chu, S. Y., Tyan, S. L. and Juang, Y. D. “The stokes photoluminescence spectra of erbium-doped $KNbO_3$ polycrystalline,” *Journal of Crystal Growth* 262, 225, 2004.

Wen, C. H., Chu, S. Y., Shin, Y. Y., Lee, C. T. and Juang, Y. D. “Red, green and blue photoluminescence of erbium doped potassium tantalate niobate polycrystalline,” *Journal of Alloys and Compounds* 459, 107, 2008.

Werts, M. H. V. “Making Sense of Lanthanide Luminescence,” *Science Progress* 88, 101, 2005.

Wiedemann, E. “Ueber Fluorescenz und Phosphorescenz I. Abhandlung (On fluorescence and phosphorescence),” *Annalen der Physik* 270, 446, 1888.

Wu, B. T., Qiu, J. R., Jiang, N., Zhou, S. F., Ren, J. J., Chen, D. P., Jiang, X. W. and Zhu, C. S. “Optical properties of transparent alkali gallium silicate glass-ceramics containing Ni^{2+}-doped beta-Ga_2O_3 nanocrystals,” *Journal of Materials Research* 22, 3410, 2007.

Xu, R. R., Tian, Y., Hu, L. L., Zhang, J. J., "Enhanced emission of 2.7 μm pumped by laser diode from Er^{3+}/Pr^{3+}-codoped germanate glasses," *Optical Letters* 36, 1173, 2011.

Xu, Y. H. "Ferroelectric materials and their applications," *Elsevier Science Publishers,* Amsterdam, 1991.

Yamamoto, H., Makishima, S. and Shionoya, S. "Vibronic structure in luminescence spectra of rare earth ions in $SrTiO_3$, $BaTiO_3$ and other perovskites," *Journal of the Physical Society of Japan* 23, 1321, 1967.

Yang, J., Zhang, C. M., Peng, C., Li, C. X., Wang, L. L., Chai, R. T. and Lin, J. "Controllable Red, Green, Blue (RGB) and bright white upconversion luminescence of Lu_2O_3: $Yb^{3+}/Er^{3+}/Tm^{3+}$ nanocrystals through single laser excitation at 980 nm," *Chemistry - A European Journal* 15, 4649, 2009.

Yao, Q. R., Wang, F. F., Jin, C. C., Tang, Y. X., Wang, T. and Shi, W. Z. "Piezoelectric/photoluminescence effects in rare-earth doped lead-free ceramics," *Applied Physics A* 113, 231, 2013.

Ye, S., Xiao, F., Pan, Y. X., Ma, Y. Y. and Zhang, Q. Y. "Phosphors in phosphor-converted white light-emitting diodes: Recent advances in material, techniques and properties," *Materials Science and Engineering: R: Reports* 71, 1, 2010.

Yen, W. M., Shionoya, S. and Yamamoto, H. "Phosphor handbook," *CRC press,* Taylor and Francis, 2007.

Yi, G. S., Lu, H. C., Zhao, S. Y., Yue, G., Yang, W. J., Chen, D. P. and Guo, L. H. "Synthesis, characterization, and biological application of size-controlled nanocrystalline $NaYF_4$: Yb,Er infrared-to-visible up-conversion phosphors," *Nano*

Letters 4, 2191, 2004.

Yi, G. S. and Chow, G. M. “Synthesis of hexagonal-phase NaYF4:Yb, Er and NaYF4:Yb, Tm nanocrystals with efficient up-conversion fluorescence,” *Advanced Functional Materials* 16, 2324, 2006.

Yilmaz, H., Trolier-Mckinstry, S. Messing, G. L. “(Reactive) Templated grain growth of textured sodium bismuth titanate ($Na_{1/2}Bi_{1/2}TiO_3$-$BaTiO_3$) ceramics. II. Dielectric and piezoelectric properties,” *Journal of Electroceramics* 11, 217, 2003.

You, F. T. Huang, S. H. Meng, C. X. Wang, D. W. Xu, J. H. Huang, Y and Zhang, G. B. “4f5d configuration and photon cascade emission of Pr^{3+} in solids,” *Journal of Luminescence* 122, 58, 2007.

Zeng, J. T., Wei, Z. H., Huang, Y. L., Tsuboi, T., Zheng, L. Y., Ruan, W., Wang, S. W. and Li, G. R. “NIR to visible up-conversion luminescence of Er^{3+}-doped PMN-PT transparent ceramics,” *Journal of the American Ceramic Society* 95, 2573, 2012.

Zhan, H., Zhou, Z. G., He, J. L. and Lin, A. X. “Intense 2.7 μm emission of Er^{3+}-doped water-free fluorotellurite glasses,” *Optical Letters* 37, 3408, 2012.

Zhang, D. L., Wong, W. H. and Pun, E. Y. B. “Characterization of vapour-transport-equilibrated Yb(/Er):$LiNbO_3$ crystals,” *Journal of Physics: Condensed Matter* 16, 7793, 2004.

Zhang, H. X., Kam, C. H., Zhou, Y., Han, X. Q., Xiang, Q., Buddhudu, S., Lam, Y. L. and Chan, Y. C. “Photoluminescence at 1.54 μm in sol-gel-derived, Er-doped $BaTiO_3$ films,” *Journal of Alloys and Compounds* 308, 134, 2000.

Zhang, J., Wang, S. W., Rong, T. J. and Chen, L. D. “Upconversion luminescence in Er^{3+} doped and Yb^{3+}/Er^{3+} codoped yttria nanocrystalline powders,” *Journal of the American Ceramic Society* 87, 1072, 2004.

Zhang, L. Y., Yang, Z. H., Tian, Y., Zhang, J. J. and Hu, L. L. “Comparative investigation on the 2.7 μm emission in Er^{3+}/Ho^{3+} codoped fluorophosphate glass,” *Journal of Applied Physics* 110, 093106, 2011.

Zhang, Q. Y., Feng, Z. M., Yang, Z. M. and Jiang, Z. H. “Energy transfer and infrared-to-visible upconversion luminescence of Er^{3+}/Yb^{3+}-codoped halide modified tellurite glasses,” *Journal of Quantitative Spectroscopy & Radiative Transfer* 98, 167, 2006.

Zhang, S. T., Kounga, A. B., Aulbach, E., Granzow, T., Jo, W., Kleebe, H. J. and Rodel, J. “Lead-free piezoceramics with giant strain in the system $Bi_{0.5}Na_{0.5}TiO_3$-$BaTiO_3$-$K_{0.5}Na_{0.5}NbO_3$. I. Structure and room temperature properties,” *Journal of Applied Physics* 103, 034107, 2008.

Zhang, X., Yang, P. P., Wang, D., Xu, J., Li, C. X., Gai, S. L. and Lin, J. “$La(OH)_3$: Ln^{3+} and La_2O_3: Ln^{3+} (Ln = Yb/Er, Yb/Tm, Yb/Ho) microrods: synthesis and up-conversion luminescence properties,” *Crystal Growth & Design* 12, 306, 2012.

Zhao, S. L., Wang, X. L., Xu, S. Q. and Hu, L. L. “Frequency upconversion fluorescence of Er^{3+}-doped TeO_2-WO_3 glass,” *Chalcogenide Letters* 2, 99, 2005.

Zheng, W., Huang, P., Tu, D. T., Ma, E., Zhu, H. M. and Chen, X. Y. “Lanthanide-doped upconversion nano-bioprobes: electronic structures, optical properties, and biodetection,” *Chemical Society Reviews* 2014, in press.

Zhou, H., Wu, G. H., Qin, N. and Bao, D. H. “Improved electrical properties and strong red emission of Pr^{3+}-doped $xK_{0.5}Bi_{0.5}TiO_3$-$(1-x)Na_{0.5}Bi_{0.5}TiO_3$ lead-free ferroelectric thin films," *Journal of the American Ceramic Society* 95, 483, 2012.

Zhu, X. and Jain, R. "10-W-level diode-pumped compact 2.78 μm ZBLAN fiber laser," *Optical Letters* 32, 26, 2007.

Zhu, X. S. and Peyghambarian, N. "High-power ZBLAN glass fiber lasers: Review and prospect," *Advances in OptoElectronics* 2010, 501956, 2010.

Zou, H., Peng, D. F., Wu, G. H., Wang, X. S., Bao, D. H., Li, J., Li, Y. X. and Yao, X. "Polarization-induced enhancement of photoluminescence in Pr^{3+} doped ferroelectric diphase $BaTiO_3$-$CaTiO_3$ ceramics," *Journal of Applied Physics* 114, 073103, 2013.